The Influence of Specific Ions and System Architecture on the Recognition and Reactivity of Two Charged Materials:

DNA-Modified Gold Nanoparticle Aggregates and Planar Silica

by

Md Delwar Hossain Sikder

A thesis submitted in partial fulfillment of the requirements for the degree of

Doctor of Philosophy

Department of Chemistry
University of Alberta

Abstract

DNA functionalized gold nanoparticles (GNP–DNA) offer simple colorimetric nucleic acid sensing with high selectivity and sensitivity. Consequently, they are promising in genetic profiling, disease diagnostics, and forensic applications. In the presence of a target nucleic acid, GNP–DNA forms reversible aggregates, which undergo sharp thermal melting transitions. The abrupt transition is associated with cooperativity, which provides selectivity in GNP-DNA based assays, important for the detection of single base-pair mismatches. Therefore, we have studied the effect of DNA structure and ion polarizability on cooperativity, and the thermodynamics and kinetics of aggregation.

We first explore a three-strand system where a linker or target DNA strand hybridized to two different GNP–DNA resulting in duplex-linked aggregates. We find that the presence of single stranded DNA gaps in the linker strand has a strong influence on all of these parameters. For example, upon inserting one unhybridized base on the target sequence such that the hybridizing strands on the GNP–DNA formed a gap rather than a nick, the extent of cooperative interactions was significantly reduced. We also observe a stark decrease in the rate of aggregation with the one-base gap compared with the nicked system. The aggregation rate and the size of the aggregates are also found to be inversely proportional to the length of the gap present in the target-linked aggregate.

Next, we evaluate the effect of loop and stem size on the properties of GNP–DNA assemblies using a linker strand that possessed a hairpin at the nicked site rather than a gap sequence as in the previous experiments. We observe that increasing the stem length increases cooperativity but decreases the thermodynamic stability, aggregation kinetics and aggregate size. However, increasing the loop size decreases the thermodynamic stability, cooperativity, rate of aggregation and the aggregate size. These results strongly indicate that bulky secondary structures can significantly modulate the behavior of the aggregates.

We then explore the influence of specific ions on aggregate behavior in a two-strand system with a complementary mixture of GNP–DNA. We find that the ion identity has a dramatic effect on the aggregate properties. Specifically, we observe that the largest unhydrated cation cesium greatly increases the number of cooperative DNA duplexes in the aggregates. On the other hand, the smallest cation explored, lithium, is found to enhance the thermal stability and aggregation rate as well as increase the size of the aggregates. Regarding anions, our results also show that iodide causes irreversible aggregation, consistent with previous reports. However, bromide completely prevents aggregation. The very interesting effect of Br^- is not seen with unmodified duplexes and requires further investigation to understand on the molecular level.

Finally, we extend the specific ion effect study from nanoparticle surfaces to planar silica surfaces due to their importance in DNA microarray based detection. We observe a dramatic increase in the binding affinity of Ca^{2+} and Mg^{2+} at higher pH, which is strongly suggestive of silica surface charge neutralization and charge reversal unlike the simple screening effects observed for monovalent cations under similar conditions. These results impact not just biodiagnostics but are also relevant in the oil–sands processing.

Acknowledgements

At first, I express my indebtedness and gratitude to my research advisor, Dr. Julianne Gibbs-Davis, who sensibly supervised my research work. Her keen intuition, enthusiasm, constructive criticism, and supportive attitude inspired me to enrich my graduate career and overcoming life's challenges. She inspired me to realize the ultimate competition and motivated me to build my academic, administrative and interpersonal skills, accordingly. I am grateful for her extremely valuable support in completion of my doctoral studies.

I sincerely thank Dr. Jonathan Veinot and Dr. Gabriel Hanna for serving on my supervisory committee. I am also thankful to Dr. Alex Brown for serving on my candidacy and Ph.D. defense committee. I gratefully acknowledge their advice and criticism that helped me to learn wisely.

I am grateful to my research colleagues, especially, Azam, Kausar, Julian, Champika, Mike, Rosalie, Jade, Katie, Zhiguo, Akemi, Eiman, Safeenaz, Yimeng, Rohan and Alex for their cooperative attitudes in the group.

I am thankful to Anita Weiler for her administrative support during the entire course of my doctoral studies. She, indeed, is an invaluable resource for the graduate students at the Department of Chemistry. I would also like to thank Gareth Lambkin of the Biological Services and Wayne Moffat of the Analytical & Instrumentation Laboratory at the Department of Chemistry for allowing me to use the facilities in their laboratories.

I am grateful to my friends at the University of Alberta, particularly, in the Department of Chemistry and Bangladeshi Student Association at the University of Alberta for making my monotonous and stressful graduate life more enjoyable. They made my work a fun job with their hilarious jokes, surprising treats and constructive conversations. Getting along with them taught me how to build a perfect administrative and strong interpersonal skills. I sincerely acknowledge their contribution in my academic, social and personal life.

I am grateful to my parents who constantly motivated me from overseas during my graduate studies at the University of Alberta. Special thanks to my Mom, who helped me to see the beautiful earth and raised me with her priceless motherhood.

I would like to take this as another opportunity to express my gratefulness to my beloved wife, Mansura Khatun, for being part of me and supporting my life in all aspects for many years.

Finally, I express my heartfelt gratitude to almighty Allah, who blessed me with strength and patience, and helped me to achieve all successes in my life.

This thesis is dedicated to my dearest wife

Mansura Khatun

We held our hands over 12 years in all journeys.

It’s hard to think of a step alone now.

Table of Contents

Introduction

Effect of Single-Stranded DNA Gap Structures on Cooperativity and the Rate of Association in DNA–Modified Gold Nanoparticle Aggregates

Chapter 3

The Influence of Loop and Stem on the Behavior of DNA Hairpin–Linked Gold Nanoparticle Aggregates

Chapter 4……………………………………………………………...120

Specific Ion Effects on Cooperativity and the Rate of Association in DNA–Modified Gold Nanoparticle Assemblies

Chapter 5..…..……..……………………………………………………..160

The Influence of Divalent Cations on the Acid-Base Behavior of the Silica/Water Interface

General Conclusions

List of Tables

List of Figures

Chapter 1.

Chapter 2.

Chapter 3.

Chapter 4.

Chapter 5.

Chapter 6.

Abbreviations/Symbols

A : Adenine or deoxyadenosine

$\beta^{(2)}$: Molecular hyperpolarizability

C : Cytosine or deoxycytidine

$\chi^{(2)}$: Second order susceptibility

DLS : Dynamic light scattering

DNA : Deoxyribonucleic acid

E : Electric field

Ext : Extinction

Φ_0 : Interfacial potential

G : Guanine or deoxyguanosine

GNP : Gold nanoparticle

GNP–DNA : DNA modified gold nanoparticle

ΔH : Enthalpy change of melting transition

Δi : Number of released cations per DNA duplex dissociation

λ_{max} : Maximum wavelength

LSPR : Localized surface plasmon resonance

μL : Microliter

N : Cooperative Unit

nm : Nanometer

nM : Nanomolar

ω : Frequency of electric field

PBS : Phosphate buffered saline

PCR : Polymerase chain reaction

Poly-A : Polydeoxyadenosine

Poly-T : Polydeoxythymidine

R : Molar gas constant

R_h : Hydrodynamic radius

RNA : Ribonucleic acid

ΔS : Entropy change of melting transitions

SFG : Sum frequency generation

SHG : Second harmonic generation

SNP : Single nucleotide polymorphism

T : Thymine or deoxythymidine

TEM : Transmission Electron Microscopy

Temp. : Temperature

T_m : Melting temperature of uDNA or GNP–DNA aggregates

uDNA : Unmodified or free DNA

UV-vis : Ultraviolet-visible

List of DNA

GNP–DNA-I : GNP–3′-TTTTTTTTTT-GAA TAG TTA-5′

GNP–DNA-II : GNP–5′-TTTTTTTTTT-TTG TTA AAT-3′

GNP-DNA-III : GNP–5′-TTTTTTTTTT-TTG TTA AAT AAA AAA AAA A-3′

GNP-DNA-IV : GNP–5′-AAAAAAAAAA-GAA TAG TTA TAA ATT GTT-3′

GNP-DNA-V : GNP–5′-AAAAAAAAAA-CTT ATC AAT ATT TAA CAA-3′

GNP-DNA-VI : Au–3′-TTTTTTTTTT-GAA TAG TAT-5′

T_n-Gap Linkers: 5′-CTT ATC AAT $(T)_n$ ATT TAA CAA-3′

$A_1C_7T_1$ Hairpin: 5′-CTT ATC ATA A CCCCCCC T ATT TAA CAA-3′

$A_3C_4T_3$ Hairpin: 5′-CTT ATC ATA AAA CCCC TTT ATT TAA CAA-3′

$A_3C_7T_3$ Hairpin: 5′-CTT ATC ATA AAA CCCCCCC TTT ATT TAA CAA-3′

$A_3C_{10}T_3$ Hairpin: 5′-CTT ATC ATA AAA CCCCCCCCCC TTT–
–ATT TAA CAA-3′

$A_6C_7T_6$ Hairpin: 5′-CTT ATC ATA AAAAAA CCCCCCC TTTTTT–
–ATT TAA CAA-3′

CHAPTER 1

Introduction

1.1 DNA: A Tool for Molecular Recognition

Deoxyribonucleic acid or DNA is the genetic blueprint of life where the form and function of the living world is encoded in the combination of nucleic acid bases: adenine (A), guanine (G), cytosine (C) and thymine (T). The structure of DNA possesses a negatively charged phosphodiester backbone composed of a sugar molecule and phosphate group. The nucleic acid bases, attached to the sugar molecule, can basepair (A:T and G:C) through hydrogen bonding and π–π base stacking and form a spiral DNA double helix, or duplex.[1] The process of a DNA single strand with a combination of nucleic acid bases forming such interactions with its complementary strand is called DNA hybridization. Because of this unique sensing property, DNA can be used as a generic polymeric moiety for very specific molecular recognition such as RNA, DNA,[2-3] protein,[4-5] and heavy metal[6] detection. As this molecular recognition depends on the nucleic acid bases, DNA is also utilized as a highly "programmable" object to construct many nanotechnological structures in material synthesis[7-10] and therapeutics.[11] Moreover, synthetic single strands of DNA can be modified with fluorescent and quencher tags for detection purposes. Such modifications can be performed with a large variety of functional groups such as thiols, primary amines, and alkyne moieties that can be conveniently used for attachment to metallic nanoparticles surfaces,[12] polymers,[13] and organic molecules[14] in the laboratory for sensing, diagnostics, therapeutics and other functional devices. The advancement of DNA solid–state synthesis has also made it possible to synthesize oligonucleotides on much larger scale, which is readily employed in laboratory research in diverse chemical and biological fields everyday (*vide supra*). The highly predictable and highly specific interactions of DNA with other molecules such as RNA, peptides, cells, lipids, proteins, polymers, organic molecules, metal ions and nanomaterials allow for the precise engineering of DNA structures. These unique features make DNA a very useful tool in nanotechnology.[3, 12, 15-21]

1.2 DNA-Functionalized Gold Nanoparticles (GNP–DNA Conjugates)

Gold nanoparticles (GNP) are very well known for their use as glass coloring materials since the ancient times.[22] They are perhaps the most promising materials in the wide field of nanotechnology.[23-24] Controlled synthesis of gold nanoparticles was achieved in the mid twentieth century when Turkevich et al. reported the preparation of small sized gold nanoparticles from the reduction of chlorauric acid with sodium citrate.[25] This synthetic route attracted much attention and became a very popular technique of making nanoparticles because of its simplicity where the citrate acts both as a reducing agent and a stabilizer.[26-27] Later in the early 90s, Brust et al. reported the synthesis of GNP < 10 nm size, which required the reduction of chlorauric acid with sodium borohydride and subsequent stabilization by tetraoctylammonium bromide.[28] The color observed from the colloidal nanoparticle solutions changed with the size or shape of the metallic nanoparticle. These particles also possessed high extinction coefficients, on the order of 10^8 $M^{-1}cm^{-1}$, which produced intense colors even with very low amounts of material in solution. The intense color for gold nanoparticles is due to the absorption of a specific wavelength of visible light, which leads to the collective oscillation of loosely bound electrons in the conduction band called the surface plasmon oscillation. Surface plasmon resonance absorption coefficients are orders of magnitude higher than strongly absorbing organic dyes, which makes these nanomaterials very popular in analyte detection. As the frequency of oscillation for GNPs is usually in the visible region of the electromagnetic spectrum, these materials can be used in colorimetric sensing. Moreover, changing the environment around the GNP leads to a change in the plasmon oscillation frequency, which can result in a stark colorimetric transition.[29]

Mirkin et al.[30] and Alivisatos et al.[31] first described the preparation of DNA/nanoparticle hybrid materials. Assembling these materials through DNA recognition resulted in a surprising change in their optical properties (Figure 1.1). In Mirkin's work, two non-complementary thiol-modified DNA single strands were functionalized with GNP. Those sequences were allowed to react with double stranded DNA overhangs, complementary to the tethered DNA sequences on the nanoparticle. Such a reaction yielded macroscopic aggregates. Alivisatos et al. in their studies used thiol-modified single stranded DNA of several different sequences, which were conjugated to GNP. By adding the respective complementary DNA single strands, they were able to assemble the GNPs into various dimeric and trimeric conformations. The distance between the particles largely regulated the optical properties of the GNP–DNA assemblies. Such interparticle distance was tuneable by selection of length and structure of the linking DNA strands. This invention pioneered the use of DNA nanoparticle assemblies for important applications such as colorimetric sensing of targets.[32]

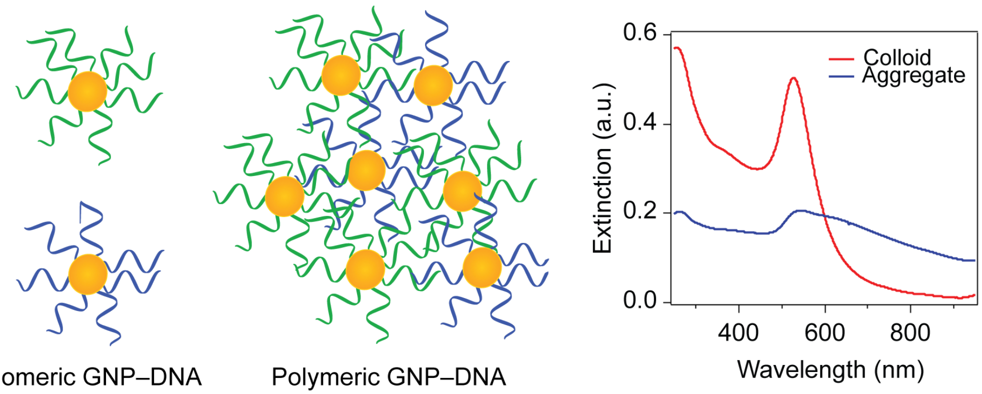

Monomeric GNP–DNA Conjugates

Polymeric GNP–DNA Aggregates

Spectral red-shift on aggregation

Figure 1.1. Polymeric GNP–DNA aggregate formation from monomeric GNP–DNA conjugates. This process takes place through hybridization of complementary DNA strands on the nanoparticle surface. An associated red-shift in the nanoparticles' absorption is also observed when aggregates are formed.

1.3. Synthesis of GNP–DNA Conjugates

Gold–thiol chemistry is very well known for the adsorption of thiolated hydrocarbon chains on gold.[33] Similarly, treatment of GNPs with thiol-modified DNA strands can lead to dense DNA coverage on the nanoparticle. Achieving a high number of DNA strands is ideal as such modification leads to more stable conjugates. Specifically, the negative charges on the DNA strands cause strong repulsive interactions, which prevents the self-aggregation of gold nanoparticles. Usually thiolated DNA strands in the form of disulphide-modified DNA are prepared using solid-phase synthesis. The disulphide functional group is less reactive at room temperature and provides protection for storage. Prior to synthesizing GNP–DNA, the disulphide-modified DNA is reduced yielding highly reactive strands with terminal thiol functional groups ready to be attached to the nanoparticle surface. As DNA is loaded on the surface, repulsion between adjacent strands becomes prominent due to closely packed negative charges. As a result, to increase the density of DNA strands on the gold, the addition of salt is important as the cations screen the phosphate groups allowing more DNA to occupy the nanoparticle surface. Hurst et al.[34] reported that sonication can further improve the surface loading by removing non-specifically bound oligonucleotides to make room for oncoming thiolated strands. Indeed, DNA undergoes a fair degree of non-specific interactions with gold nanoparticles, particularly the adenine. Therefore, to make the anchored sequences most available for hybridization with target DNA strands in assays, an extended spacer sequence (usually poly-T or poly-A) or a polyethylene glycol spacer is used.

1.4 Optical Properties of GNP–DNA Conjugates

As mentioned, free electrons that are loosely bound to the metal atoms are referred to as surface plasmons and are highly responsive to incident light. The origin of the bright red color of small (13-nm) gold nanoparticles is the localized surface plasmon resonance (LSPR) that occurs in metal structures with sizes much smaller than the wavelength of the excitation wavelength. Under an electromagnetic field, the electron cloud is displaced relative to the nuclei, giving rise to a restoring force from the coulombic attraction resulting in oscillation of the electron cloud with respect to the nuclei (Figure 1.2). This restoring force leads the resonance to occur in the presence of incident light at a specific frequency that is characteristic of the particle size, shape, dielectric environment and proximity between particles.[29, 35] This oscillation results in the unusually strong scattering and absorption of light.

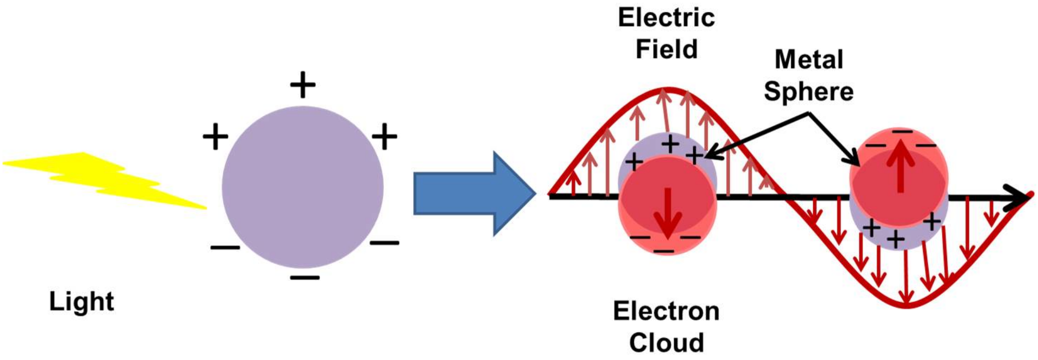

Figure 1.2. Incident light induces plasmon oscillation when size of the metal structure is much smaller than the wavelength of incident light resulting in strong absorption and scattering. Figure adapted and modified with permission from reference 29.[29]

The interaction of nanoparticles with light results in some photons being absorbed and some being scattered. Therefore, the extinction cross-section $C_{ext} = C_{abs} + C_{scat}$ where C_{abs} and C_{scat} are the absorption and scattering cross sections, respectively. These extinction cross-sections are up to five orders of magnitude greater than the cross-section of an organic dye,[36] therefore, utilizing nanomaterials is particularly advantageous in colorimetric platforms. Moreover, nanoparticles do not undergo photobleaching that is a common problem in fluorophore-incorporated biosensors making them robust labels. The extremely intense localized electromagnetic fields induced by plasmon resonance make the nanoparticles highly sensitive to very small changes in the refractive index around the nanoparticle and interparticle distances, both of which are observed as spectral shifts (Figure 1.1). Indeed, the covalent modification of 13-nm GNP with thiolated DNA strands led to a ~ 5 nm red-shift in the absorption maximum of the nanoparticles.[37]

1.5 Melting Properties and Applications of GNP–DNA

The stability of colloidal dispersions of gold nanoparticles in solution is provided by the ligand corona around the nanoparticle surface. Ligands with a head and tail group facilitate attachment to the surface by electrostatic interactions or covalent bond formation and provide colloidal stability in solution. Ligand–stabilized nanoparticles are promising materials for numerous assays using the molecular recognition properties of the DNA, RNA, or peptide corona (Figure 1.3).[38]

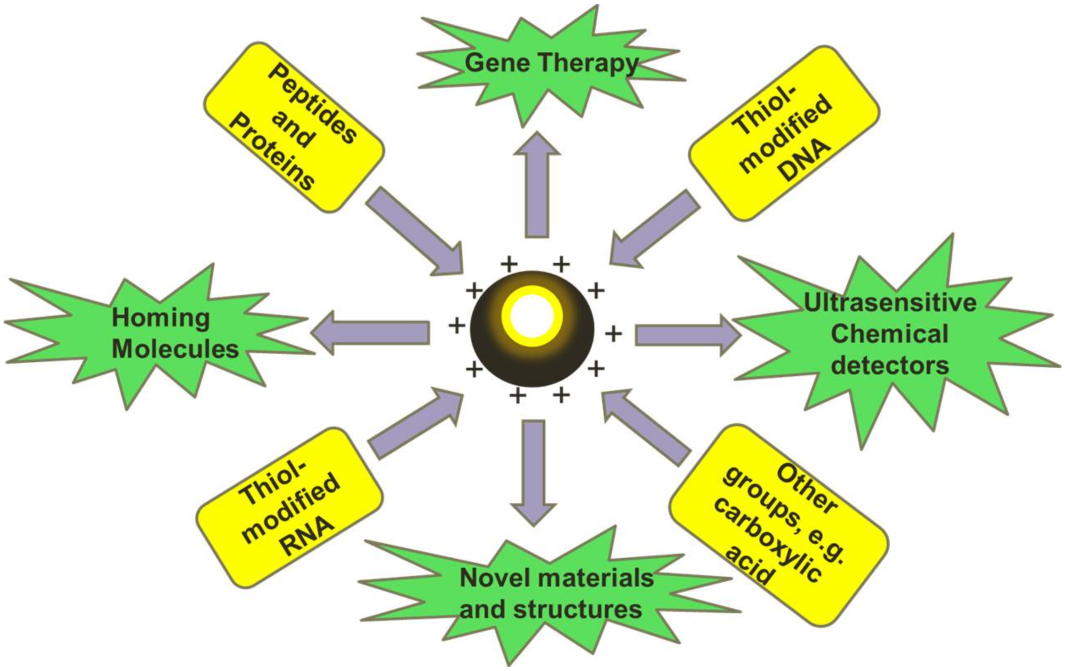

Figure 1.3. Gold nanoparticles with different kinds of macromolecule conjugates, such as thioalkylated DNA, RNA, proteins, peptides, carboxylic acids, and

poly(amidoamine) dendrimers. Figure adapted and modified with permission form reference 38.[38]

Simple colorimetric assays for DNA detection can be constructed using these GNP–DNA conjugates as probes where a target nucleic acid can link pairs of nanoparticles eventually resulting in aggregate formation. Indeed, Elghanian et al. reported selective colorimetric detection of DNA using GNP–DNA conjugates at low target DNA concentrations (femtomoles) in a sandwich type assay.[39] These sandwich type assays involve DNA capture strands attached to a solid support (generally glass or gold) and GNP–DNA that are complementary to adjacent regions on a target nucleic acid sequence thereby sandwiching the target nucleic acid. Using amplification methods like silver enhancement increased the sensitivity of these assays based on the catalytic ability of gold nanoparticles to reduce silver ions.[3]

The target-linked GNP–DNA assemblies in solution and on surfaces undergo temperature induced melting transitions over a very narrow temperature range compared to unmodified (uDNA) duplexes (Figure 1.4). Consequently with simple thermal stringency washes, GNP–DNA probes are far more selective and cost effective compared to molecular fluorophore assays.[40-43] The abrupt dissociation of GNP–DNA aggregates in particular is attributed to different features of the system depending on the model used.

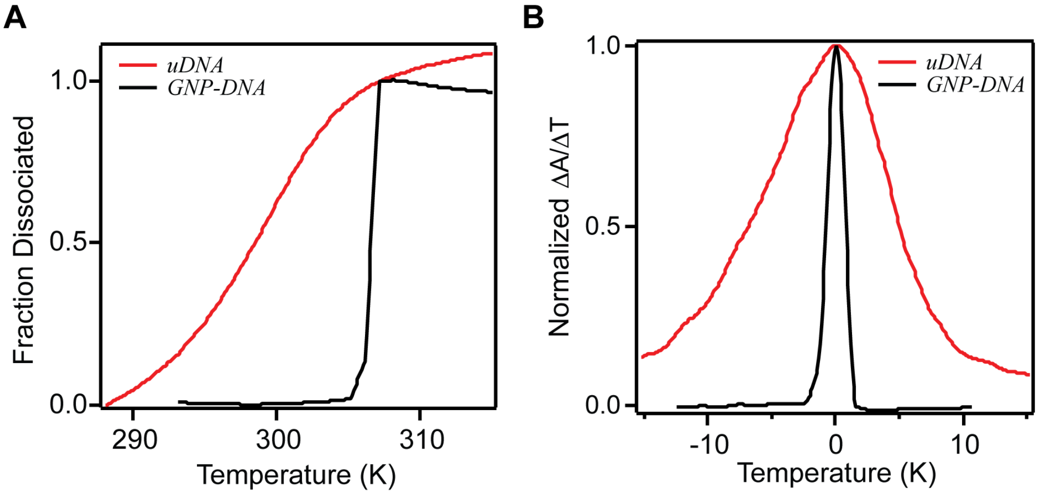

Figure 1.4. A.) The black transition curve represents a sharp thermal melting transition of DNA modified gold nanoparticle aggregates whereas the red curve represents the corresponding DNA duplex melting transition in the absence of gold nanoparticles (uDNA). B.) The first derivatives of the melting transitions from part A. It is clear that the GNP–DNA aggregates dissociate over a much narrower temperature range compared to their unmodified analogs.

1.6 Theories of GNP–DNA Aggregate Melting

The origin of the sharp thermal dissociation of GNP–DNA over a narrow temperature range is yet a matter of debate. The proposed theoretical models to explain this sharp dissociation can be divided into two groups and the postulates of these groups are as follows:

(1) The theories of the first group assume that these aggregates contain many linked particles, which undergo a phase transition that takes place in bulk materials.

(2) The second group assumes that sharp melting arises from dissociation that takes place through melting of particles in pairs within an aggregate that are linked by multiple DNA strands.

The first group explains that the sharp dissociation associated with the GNP–DNA aggregate melting is a bulk phase transition of macroscopic quantity. This sharp dissociation theory does not consider the effect of cations or the contribution of individual DNA linker strands.[44-47] According to the theories of the second group, the sharp melting of GNP–DNA aggregate is a cooperative effect that results from either cation release or a change in entropy derived from dissociation of multiple DNA duplex linkers or a combination of both effects. These theories consider the high local electrolyte concentration and the structural rigidity of the linked particles within the closely packed environment of the duplex-linked GNP–DNA.[13, 48-51]

1.6.1 Phase Transition Model of Aggregate Dissociation

The phase transition theory of aggregate melting assumes that the aggregate is one large collection of identical gold nanoparticles at low temperatures, which forms a dispersed colloid at high temperature.[52-54] The arrangement of the gold nanoparticles in the aggregate can be thought of as a simple cubic lattice. In this simple cubic lattice each nanoparticle is surrounded by n number of neighboring nanoparticles and carries N number of DNA single strands available for hybridization. Therefore, the number of available single strands to hybridize with each neighbour will be a maximum of N/n. The dissociation of the hybridized DNA duplex linked aggregates can be represented by,

$$D \rightleftharpoons S + S \tag{1.1}$$

where D and S are hybridized and single-stranded DNA on the nanoparticles, respectively.

The fraction of DNA that is hybridized $p(\mathrm{T})$ is a function of temperature as the duplex dissociation to single strands is a temperature dependent process. If the neighbouring nanoparticles are linked with a minimum of one duplex, the fraction of linked GNP–DNA $p_\mathrm{f}(\mathrm{T})$ can be related to $p(\mathrm{T})$:

$$1 - p_\mathrm{f}(\mathrm{T}) = [1 - p(\mathrm{T})]^{\mathrm{N/n}} \tag{1.2}$$

The sharp melting of these aggregates to dispersed colloids is described by percolation theory where the melting temperature $\mathrm{T_c}$ corresponds to the bond percolation threshold for the lattice, at which an infinite connected path of the hybridized DNA duplex linked nanoparticles is formed, p_c. Therefore, at percolation ($\mathrm{T} = \mathrm{T_c}$):

$$[1 - p(\mathrm{T_c})]^{\mathrm{N/n}} = 1 - p_\mathrm{c} \tag{1.3}$$

To understand the percolation threshold, let us consider a large array of squares filled with dots as shown in figure 1.5. A certain fraction of the squares are filled with particles, which results in formation of clusters. From Figure 1.5, the dot-filled squares that have one side in common are called nearest neighbours and dot-filled squares touching corners are called the next nearest neighbours. Percolation theory deals with the number and properties of these nearest neighbours and next nearest neighbours. These nearest neighbours in this model lattice correspond to the adjacent nanoparticles in the DNA–linked gold nanoparticle aggregates.[55]

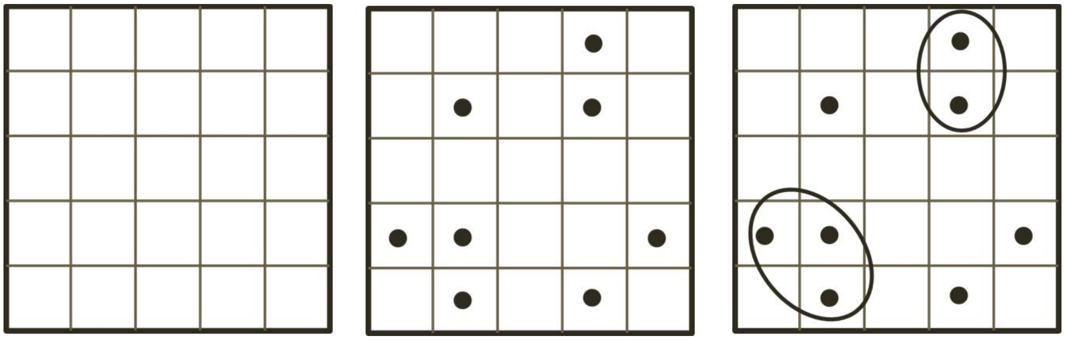

Figure 1.5. Left: Schematic of an empty square lattice. Middle: A square lattice partially occupied with particles. Right: Groups of neighbours for the partially filled square lattice (shown in circles). Figure reproduced with permission from reference 55.[55]

Using percolation theory, the sharp transition of an aggregate can be related to a forest fire if the lattice represents a forest and a single tree is denoted by the single squares occupied by the dots. The empty white squares represent empty spaces. The probability for a square to be filled with a dot is p and for it to be empty is $1–p$. Therefore, $p = 1$ when all squares are filled with dots, which corresponds to a completely ordered forest occupied by infinite rows and columns of trees in our analogy. The $p < 1$ corresponds to a disordered forest with a lower density of trees represented by randomly occupied spaces. To spread the forest fire a tree can only ignite its nearest neighbour, not the ones further away. If probability $p << 1$, most of the burning trees have no neighbours at all and the fire stops as soon as those trees burns out. On the other hand, if p is large, at some critical value, $p = p_c$, a path of neighbouring trees is connected from the very first row to the very last, called a percolating cluster. The rate of the forest fire depends on the arrangement of the occupied squares. At probabilities p slightly above p_c, burning out the entire forest is a fast and cooperative process. For p slightly below p_c, the fire needs longer time to penetrate into the forest due to gaps between clusters of trees. Very similarly, an aggregate phase transition is observed when p transitions from p_c to $p < p_c$.

1.6.2 Theory of Entropy Driven Sharp Melting

In contrast to the aggregation model, Schatz, Nguyen and coworkers[14, 49] attributed the sharp melting transition to an entropically driven process arising from the difference in effective concentration of hybridized DNA duplex linkers connecting a pair of molecules. To understand this model let us assume a GNP–DNA dimer linked with up to three DNA duplexes (Figure 1.6). The two GNP–DNA monomers responsible for the formation of the dimer have complementary DNA sequences x and y. Therefore the first hybridization event will result in the formation of an xy_1-duplex linked dimer followed by the formation of xy_2, and xy_3. If the concentrations of the monomers are [x] and [y], that of the fully hybridized dimer can be represented as $[xy_3]$ and the ones with one and two DNA duplex linkers will be $[xy_1]$ and $[xy_2]$, respectively. The total concentration of DNA is C_{total}, where

$$C_{total} = 3\left(\left[x\right]+\left[y\right]+2\left[xy_3\right]+2\left[xy_2\right]+2\left[xy_1\right]\right). \tag{1.4}$$

and the fraction of DNA single strand *f* can be determined from,

$$1-f=\frac{2\left[xy_3\right]+2\left[xy_2\right]+2\left[xy_1\right]}{C_{total}} \tag{1.5}$$

The intermediate species [xy_3], [xy_2] and [xy_1] can be related to effective concentration terms that take into account the fact that the second and third hybridization events occur intramolecularly with two GNP–DNA that are tethered together through the first duplex. The determination of configurational entropy[56] from the differences in these effective concentrations due to multiple hybridization events showed that there is a large change in entropy, ΔS when two monomer molecules form a dimer from the hybridization of the first pairs of DNA single strands to make DNA duplex linker. However, the change in entropy in the second hybridization event was found to be smaller than the first one. Similarly, ΔS for the third hybridization event was smaller than the second duplex formation too. This gradual decrease in the dissociation ΔS was attributed to the main source of cooperativity between the three hybridized DNA duplex linkers in a dimer.

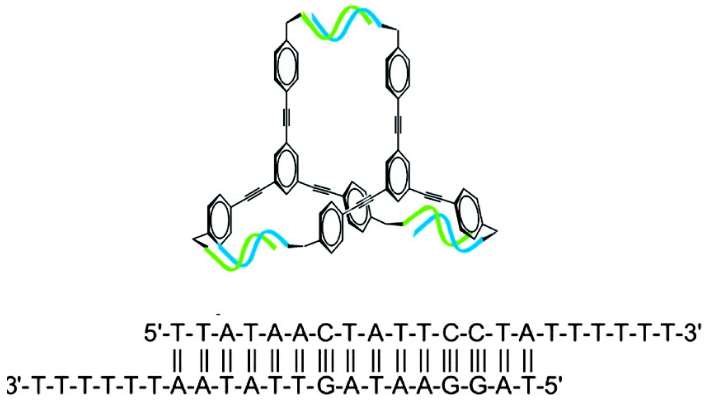

Figure 1.6. Figure shows small molecule-DNA hybrid (SMDH) dimer formation through hybridization of three complementary DNA strands chemically bonded to

the small molecule. This model represents a GNP–DNA dimer with three DNA duplex linkers in section 1.6.2. Figure adapted with permission reference 49.[49]

1.6.3 Shared Ion-Cloud Model of Cooperative Melting

Another model put forth by the Schatz and Mirkin groups that considered the molecular environment around two GNP–DNA as contributing to the sharp melting is the shared ion-cloud model.[48] Similar to the previous model, the melting of GNP–DNA aggregates can be depicted as a series of DNA duplex linker dissociation steps whose dissociation constants are highly dependent on the melting of their neighbouring duplexes.

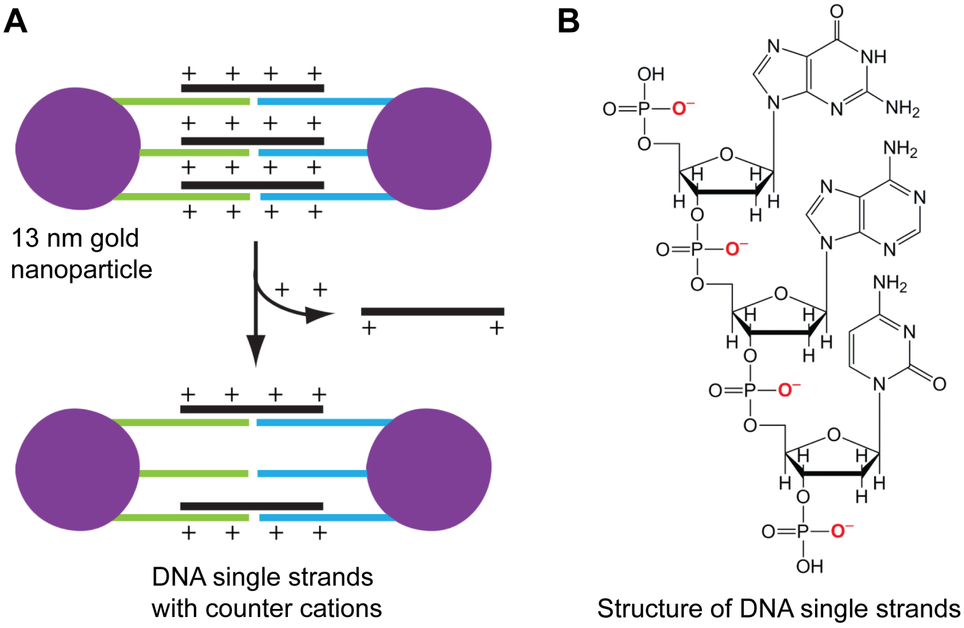

Figure 1.7. A.) Dissociation of a GNP–DNA dimer, a zoom in view at the molecular level of an aggregate. B.) Structure of DNA showing the origin of negative charges on the backbone that causes recruitment of cations during DNA hybridization.

The key feature of this melting model is the presence of many single strands on each particle that result in a crowded DNA environment from the dense packing. Upon hybridization with complementary GNP–DNA, the resulting DNA duplexes condense additional cations along their backbone that screen their charge. Due to the dense packing of DNA on the nanoparticle surface, each duplex can interact with its neighbours by sharing the condensed cation cloud around its backbone. The result of this interaction is cooperativity whereby multiple duplexes melt in conjunction (Figure 1.8). The cooperativity in these systems is quantified by the cooperative unit, or the number of DNA duplexes that shares a common cation cloud.

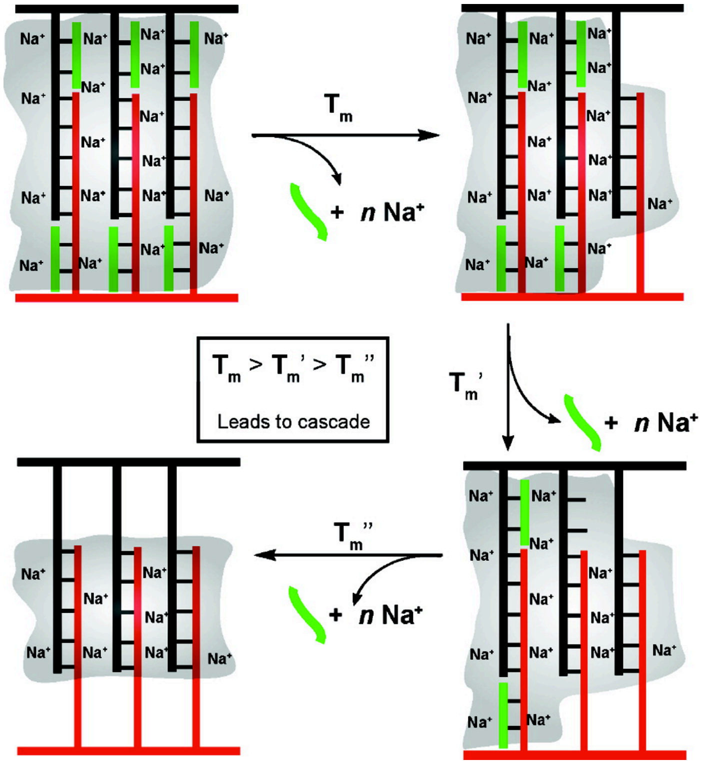

Figure 1.8. Cooperative interactions between neighbouring DNA strands from a crowded environment of linker DNA duplexes in a DNA–polymer hybrid that

leads to recruiting more cations. These cations become shared in a common ion cloud. Figure adapted with permission from reference 57.[57]

Each pair of particles can be linked by many DNA duplexes, so the dissociation process involves a series of melting steps derived from the duplex linker dissociation and the associated nanoparticles (Figure 1.9). To derive the thermodynamic quantities and cooperativity of a three-strand system where two GNP–DNA are each complementary to a different half of a linker strand (like the sandwich assay where a target DNA binds to complementary GNP tethered probes), let us assume the aggregate releases a target linker B along with its recruited salt cations S in each melting step. The series of dissociation of all duplex linkers can therefore be expressed as,

$$\begin{aligned} A_N &= A_{N-1} + B + nS \\ A_{N-1} &= A_{N-2} + B + nS \\ &------------ \\ A_2 &= A_1 + B + nS \\ A_1 &= A_0 + B + nS \end{aligned} \qquad (1.6)$$

where, n is the number of cations released (S) during a single melting step, A_i is the instantaneous concentration of the nanoparticles and i is the number of linker duplexes remaining that link two nanoparticles in the GNP–DNA dimer within the aggregate, and N is the number of linker duplexes per nanoparticle.

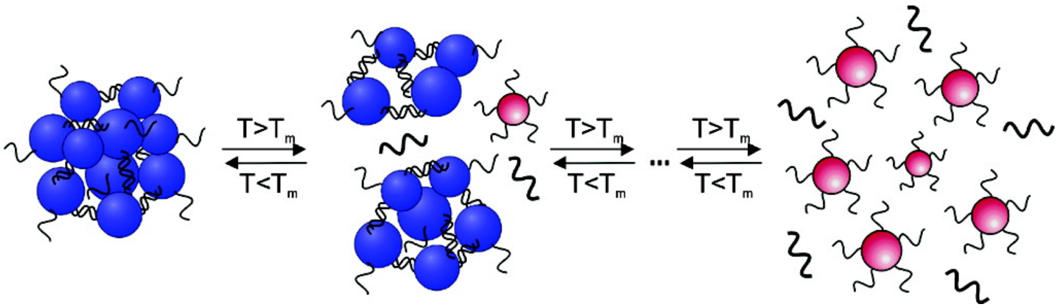

Figure 1.9. Figure shows the GNP–DNA aggregate dissociates in a series of melting steps. Figure adapted with permission from reference 48.[48]

The entire dissociation process can, therefore, be expressed as:

$$A_N = A_0 + NB + nNS \tag{1.7}$$

The overall dissociation equilibrium constant K of equation 1.7 can be related to the equilibrium constants K$_i$ of all the individual dissociation steps in equation 1.6 as:[50]

$$\frac{1}{K} = \frac{BS^n}{K_1} + \frac{B^2S^{2n}}{K_1K_2} + \cdots\cdots + \frac{B^NS^{nN}}{K_1K_2\cdots\cdots K_N} \tag{1.8}$$

Due to the cooperative interaction, thermal melting of one DNA linker duplex will decrease the melting temperature of the remaining linkers. Therefore, the first melting duplex will have the highest melting temperature and the last melting duplex will possess the lowest melting temperature or

$$K_N < K_{N-1} < \cdots\cdots < K_1$$

This makes the $\frac{B^NS^{nN}}{K_1K_2\cdots\cdots K_N}$ term dominant in equation 1.8. Consequently,

$$\frac{1}{K} \approx \frac{B^NS^{nN}}{K_1K_2\cdots\cdots K_N} \tag{1.9}$$

Combining equation 1.9 with the van't Hoff expression, $\Delta H = -R\left[\frac{d\ln K}{d(1/T)}\right]$, a dissociation curve for the entire GNP–DNA aggregate can be obtained as:[50]

$$f = \frac{1}{1+\exp\left[\frac{\Delta H_{total}}{R}\left(\frac{1}{T}-\frac{1}{T_m}\right)\right]} \tag{1.10}$$

where $\Delta H_{total} = \sum_i \Delta H_i$ and f is the fraction of dissociated DNA-linked nanoparticles. From equation 1.10, it is clear that the sharpness of the sigmoidal melting tansition is determined by the total change in enthalpy of melting, ΔH_{total}.

1.7 Experimental Support for Cooperative Models of DNA Dissociation in Dense Materials

Gibbs-Davis et al. reported that DNA dissociation was sharp in a DNA–linked polymer aggregate even though the aggregate remained intact after DNA dissociation.[57] In this study, DNA was designed for two hybridization events in the same polymer structure where two tethered complementary DNA sequences linked the polymers in the hybridized structure and a small A_{10} sequence was hybridized to the T_{10} spacer sequence (Figure 1.10). (Such spacer sequences are particularly helpful in preventing nonspecific interaction of the tethered DNA with the polymer or metal nanoparticle surface). In the thermal dissociation experiment two melting transitions were observed. One of the transitions was due to the dissociation of the complementary linker sequences whereas the other transition belonged to the A_{10}:T_{10} duplex melting. If a phase transition was responsible for sharp melting, the duplex dissociations that do not result in breaking the aggregate should give rise to thermal dissociation over a broad temperature range like unmodified DNA duplexes. On the contrary, the A_{10}:T_{10} melting transitions in this system were seen to be much narrower compared to that of unmodified DNA. Such an observation weakens the phase transition theory of sharp dissociation where it is clear that aggregate dissociation is not required for abrupt transitions.

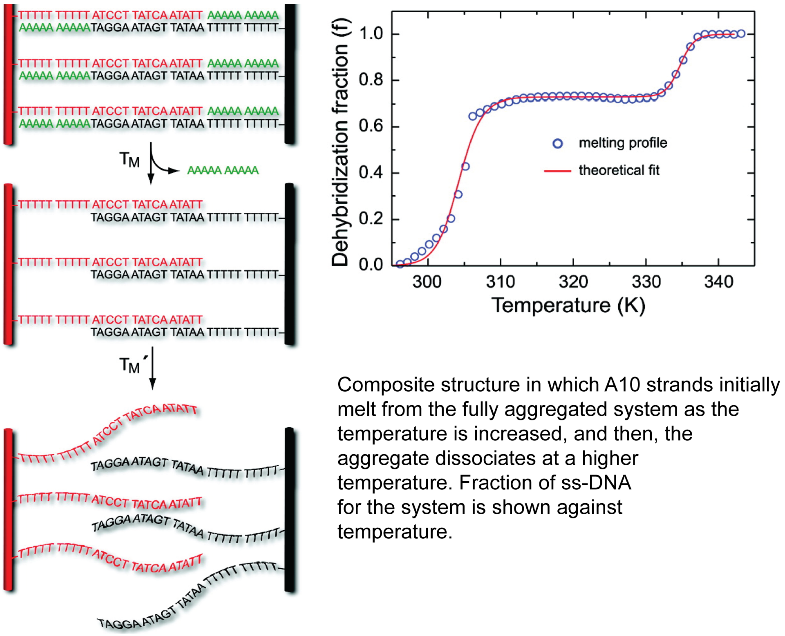

Composite structure in which A10 strands initially melt from the fully aggregated system as the temperature is increased, and then, the aggregate dissociates at a higher temperature. Fraction of ss-DNA for the system is shown against temperature.

Figure 1.10. Two sharp melting transitions in DNA functionalized polymeric assemblies. The first transition does not lead to aggregate dissolution and yet is sharp, which supports that cooperativity can lead to sharp melting. This figure was adapted and modified with permission from reference 57.[57]

Eryazici et al. reported sharp dissociation in small molecule–DNA hybrid dimers (Figure 1.11).[14] Such melting over a narrow temperature range also contradicts the bulk phase transition theory. In this molecular assembly dimers of organic molecule were formed with the aid of two DNA strands chemically bonded to the molecules. These two examples clearly support that sharp transition in these small molecule dimer systems stemmed from the condensed DNA packing where each duplex melting is cooperatively affected by its neighbour duplexes.

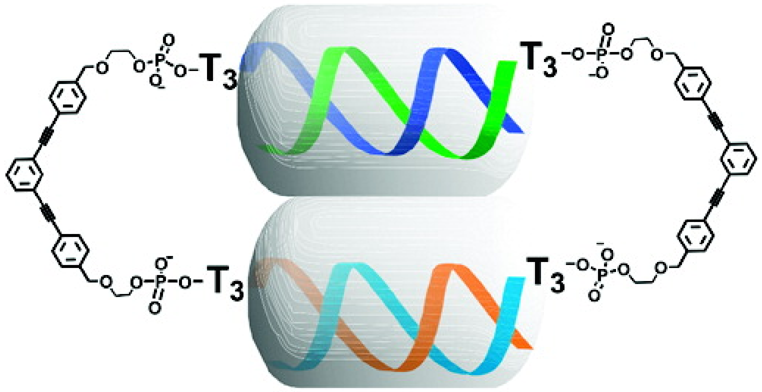

Figure 1.11. Small molecule DNA hybrid (SMDH) with two DNA linker duplexes. Temperature induced dissociation of this SMDH gives rise to melting transition over narrow temperature range unlike a single DNA duplex dissociation. Figure adapted with permission from reference 14.[14]

Because of the support for the cooperative model, particularly the shared ion-cloud model over the conventional phase transition concept, we have used this model to analyze the GNP–DNA assemblies in our projects and determined cooperativity and salt dependent behaviour in the presence of structural diversity and various electrolytes.

1.8 Overview of This Thesis

The advances in the nanoparticle modification with DNA or RNA molecules have made it possible to develop many exciting diagnostic assays in the past few decades. More specifically, colorimetric methods have been applied in large number of biomolecule and ion detection assays. These DNA modified gold nanoparticle conjugates have also been proven to show advantages in selectivity and sensitivity over conventional methods. This success of GNP–DNA materials in diagnostics[17] motivated us to investigate the thermodynamic, kinetic and cooperative behaviour of the conjugates at the molecular level.

The research aim of Chapter 2 was to understand the effect of the structure of the aggregates on cooperativity and aggregation kinetics by inserting single stranded gaps in the linker DNA three-strand system. As cooperativity is proposed to originate from the presence of densely packed DNA strands on the nanoparticles and their structural rigidity, a negative impact on detection assays regarding long and flexible DNA targets was expected. Such flexibility can also slow down detection by increasing the time for aggregation, which is also a drawback in preparation of these aggregates in diagnostic assays. The outcome of this project will be discussed in detail in chapter 2.

In the second project we designed GNP–DNA aggregates linked by duplexes that possessed DNA hairpins with varying stem and loop lengths at the nicked site or junction where the two nanoparticle strands met on the linker strand. Similar to the first project, we wanted to determine the effect of secondary structures on the GNP–DNA aggregates. Such secondary structures can affect the selectivity of diagnostic assays by decreasing cooperativity. Indeed, we observed a noticeable change in thermodynamic and kinetic behaviour as we increased the size of stem and loop systematically on the DNA hairpin linkers, which is important in diagnostic assays regarding DNA or RNA hairpins. The results will be discussed in chapter 3.

In the third project, we studied the effect of ion polarizability on the cooperativity and thermodynamic and kinetic behaviour of GNP–DNA aggregates. As cations play an important role in hybridization of complementary DNA stands, we hypothesized that a change in the size of the cation would also change the cooperative interactions in the assemblies. We report that the most polarizable cation examined increases cooperativity by forming a larger shared cation cloud. Such a phenomenon is surprising as smaller cations are able to interact more strongly than larger cations with polyelectrolytes in solution. The details of this project and results will be discussed in chapter 4.

In the fourth project, we extended this investigation of cation interactions from a nanoparticle surface to a bulk planar silica surface. In this work we have explored the effect of divalent cations on the electrostatic properties of surface charges on silica in the presence of water over a broad pH range. The outcome of this project showed a stark difference in properties compared to those in the presence of monovalent cations. The results will be discussed in chapter 5.

The final chapter includes a summary of results and future directions for this work.

1.8 References

1. Chris R. Calladine, H. D., Ben Luisi, Andrew Travers, *Understanding DNA: The Molecule and How it Works*. 3rd ed.; Elsevier Academic Press.

2. Drummond, T. G.; Hill, M. G.; Barton, J. K., Electrochemical DNA sensors. *Nature Biotechnology* **2003,** *21* (10), 1192-1199.

3. Taton, T. A.; Mirkin, C. A.; Letsinger, R. L., Scanometric DNA Array Detection with Nanoparticle Probes. *Science* **2000,** *289* (5485), 1757-1760.

4. Dai, N.; Kool, E. T., Fluorescent DNA-based enzyme sensors. *Chemical Society Reviews* **2011,** *40* (12), 5756-5770.

5. Xiang, Y.; Lu, Y., DNA as Sensors and Imaging Agents for Metal Ions. *Inorganic Chemistry* **2013,** *53* (4), 1925-1942.

6. Zhang, X.-B.; Kong, R.-M.; Lu, Y., Metal Ion Sensors Based on DNAzymes and Related DNA Molecules. *Annual Review of Analytical Chemistry* **2011,** *4* (1), 105-128.

7. Storhoff, J. J.; Mirkin, C. A., Programmed Materials Synthesis with DNA. *Chemical Reviews* **1999,** *99* (7), 1849-1862.

8. Mao, X.; Liu, G., Nanomaterial based electrochemical DNA biosensors and bioassays. *Journal of Biomedical Nanotechnology* **2008,** *4* (4), 419-431.

9. Seeman, N. C., Nanomaterials based on DNA. *Annual Review of Biochemistry* **2010,** *79*, 65-87.

10. Park, S. Y.; Lytton-Jean, A. K. R.; Lee, B.; Weigand, S.; Schatz, G. C.; Mirkin, C. A., DNA-programmable nanoparticle crystallization. *Nature* **2008,** *451* (7178), 553-556.

11. Andersen, E. S.; Dong, M.; Nielsen, M. M.; Jahn, K.; Subramani, R.; Mamdouh, W.; Golas, M. M.; Sander, B.; Stark, H.; Oliveira, C. L. P.; Pedersen, J. S.; Birkedal, V.; Besenbacher, F.; Gothelf, K. V.; Kjems, J., Self-assembly of a nanoscale DNA box with a controllable lid. *Nature* **2009,** *459* (7243), 73-76.

12. Niemeyer, C. M.; Simon, U., DNA-Based Assembly of Metal Nanoparticles. *European Journal of Inorganic Chemistry* **2005,** *2005* (18), 3641-3655.

13. Park, S. Y.; Gibbs-Davis, J. M.; Nguyen, S. T.; Schatz, G. C., Sharp Melting in DNA-Linked Nanostructure Systems: Thermodynamic Models of DNA-Linked Polymers. *The Journal of Physical Chemistry B* **2007,** *111* (30), 8785-8791.

14. Eryazici, I.; Prytkova, T. R.; Schatz, G. C.; Nguyen, S. T., Cooperative Melting in Caged Dimers with Only Two DNA Duplexes. *Journal of the American Chemical Society* **2010,** *132* (48), 17068-17070.

15. Ellington, A. D.; Szostak, J. W., In vitro selection of RNA molecules that bind specific ligands. *Nature* **1990,** *346* (6287), 818-822.

16. Ellington, A. D.; Szostak, J. W., Selection in vitro of single-stranded DNA molecules that fold into specific ligand-binding structures. *Nature* **1992,** *355* (6363), 850-852.

17. Rosi, N. L.; Mirkin, C. A., Nanostructures in Biodiagnostics. *Chemical Reviews* **2005,** *105* (4), 1547-1562.

18. Giljohann, D. A.; Seferos, D. S.; Patel, P. C.; Millstone, J. E.; Rosi, N. L.; Mirkin, C. A., Oligonucleotide loading determines cellular uptake of DNA-modified gold nanoparticles. *Nano Letters* **2007,** *7* (12), 3818-3821.

19. Chiu, T.-C.; Huang, C.-C., Aptamer-Functionalized Nano-Biosensors. *Sensors* **2009,** *9* (12), 10356-10388.

20. Giljohann, D. A.; Seferos, D. S.; Daniel, W. L.; Massich, M. D.; Patel, P. C.; Mirkin, C. A., Gold Nanoparticles for Biology and Medicine. *Angewandte Chemie International Edition* **2010,** *49* (19), 3280-3294.

21. Zhao, W.; Brook, M. A.; Li, Y., Design of Gold Nanoparticle-Based Colorimetric Biosensing Assays. *ChemBioChem* **2008,** *9* (15), 2363-2371.

22. Quinten, M., *Optical Properties of Nanoparticle Systems: Mie and Beyond*. Wiley-VCH, Weinheim, Germany: 2011.

23. Daniel, M.-C.; Astruc, D., Gold nanoparticles: assembly, supramolecular chemistry, quantum-size-related properties, and applications toward biology, catalysis, and nanotechnology. *Chemical reviews* **2004,** *104* (1), 293-346.

24. Cai, W.; Gao, T.; Hong, H.; Sun, J., Applications of gold nanoparticles in cancer nanotechnology. *Nanotechnology, science and applications* **2008,** *1*, 17.

25. Turkevich, J.; Stevenson, P. C.; Hillier, J., A study of the nucleation and growth processes in the synthesis of colloidal gold. *Discussions of the Faraday Society* **1951,** *11* (0), 55-75.

26. Frens, G., Particle size and sol stability in metal colloids. *Kolloid-Zeitschrift und Zeitschrift für Polymere* **1972,** *250* (7), 736-741.

27. Frens, G., Controlled Nucleation for the Regulation of the Particle Size in Monodisperse Gold Suspensions. *Nature* **1973,** *241* (105), 20-22.

28. Brust, M.; Walker, M.; Bethell, D.; Schiffrin, D. J.; Whyman, R., Synthesis of thiol-derivatised gold nanoparticles in a two-phase Liquid-Liquid system. *Journal of the Chemical Society, Chemical Communications* **1994,** (7), 801-802.

29. Kelly, K. L.; Coronado, E.; Zhao, L. L.; Schatz, G. C., The Optical Properties of Metal Nanoparticles: The Influence of Size, Shape, and Dielectric Environment. *The Journal of Physical Chemistry B* **2002,** *107* (3), 668-677.

30. Mirkin, C. A.; Letsinger, R. L.; Mucic, R. C.; Storhoff, J. J., A DNA-based method for rationally assembling nanoparticles into macroscopic materials. *Nature* **1996,** *382* (6592), 607-609.

31. Alivisatos, A. P.; Johnsson, K. P.; Peng, X.; Wilson, T. E.; Loweth, C. J.; Bruchez, M. P.; Schultz, P. G., Organization of 'nanocrystal molecules' using DNA. *Nature* **1996,** *382* (6592), 609-611.

32. Song, Y.; Wei, W.; Qu, X., Colorimetric Biosensing Using Smart Materials. *Advanced Materials* **2011,** *23* (37), 4215-4236.

33. Love, J. C.; Estroff, L. A.; Kriebel, J. K.; Nuzzo, R. G.; Whitesides, G. M., Self-Assembled Monolayers of Thiolates on Metals as a Form of Nanotechnology. *Chemical Reviews* **2005,** *105* (4), 1103-1170.

34. Hurst, S. J.; Lytton-Jean, A. K. R.; Mirkin, C. A., Maximizing DNA Loading on a Range of Gold Nanoparticle Sizes. *Analytical Chemistry* **2006,** *78* (24), 8313-8318.

35. Storhoff, J. J.; Lazarides, A. A.; Mucic, R. C.; Mirkin, C. A.; Letsinger, R. L.; Schatz, G. C., What Controls the Optical Properties of DNA-Linked Gold Nanoparticle Assemblies? *Journal of the American Chemical Society* **2000,** *122* (19), 4640-4650.

36. Jain, P. K.; Lee, K. S.; El-Sayed, I. H.; El-Sayed, M. A., Calculated Absorption and Scattering Properties of Gold Nanoparticles of Different Size, Shape, and Composition: Applications in Biological Imaging and Biomedicine. *The Journal of Physical Chemistry B* **2006,** *110* (14), 7238-7248.

37. Stoeva, S. I.; Lee, J.-S.; Thaxton, C. S.; Mirkin, C. A., Multiplexed DNA Detection with Biobarcoded Nanoparticle Probes. *Angewandte Chemie International Edition* **2006,** *45* (20), 3303-3306.

38. De Long, R. K.; Reynolds, C. M.; Malcolm, Y.; Schaeffer, A.; Severs, T.; Wanekaya, A., Functionalized gold nanoparticles for the binding, stabilization, and delivery of therapeutic DNA, RNA, and other biological macromolecules. *Nanotechnology, Science and Applications* **2010,** *3*, 53-63.

39. Elghanian, R.; Storhoff, J. J.; Mucic, R. C.; Letsinger, R. L.; Mirkin, C. A., Selective Colorimetric Detection of Polynucleotides Based on the Distance-Dependent Optical Properties of Gold Nanoparticles. *Science* **1997,** *277* (5329), 1078-1081.

40. Tyagi, S.; Kramer, F. R., Molecular Beacons: Probes that Fluoresce upon Hybridization. *Nature Biotechnology* **1996,** *14* (3), 303-308.

41. Lander, E. S., Array of hope. *Nature Genetics* **1999,** *21*, 3-4.

42. Duggan, D. J.; Bittner, M.; Chen, Y.; Meltzer, P.; Trent, J. M., Expression profiling using cDNA microarrays. *Nature Genetics* **1999,** *21* (1, Suppl.), 10-14.

43. Fang, X.; Liu, X.; Schuster, S.; Tan, W., Designing a Novel Molecular Beacon for Surface-Immobilized DNA Hybridization Studies. *Journal of the American Chemical Society* **1999,** *121* (12), 2921-2922.

44. Lee, O.-S.; Prytkova, T. R.; Schatz, G. C., Using DNA to Link Gold Nanoparticles, Polymers, and Molecules: A Theoretical Perspective. *The Journal of Physical Chemistry Letters* **2010,** *1* (12), 1781-1788.

45. Park, S. Y.; Stroud, D., Theory of melting and the optical properties of gold/DNA nanocomposites. *Physical Review B* **2003,** *67* (21), 212202.

46. Lukatsky, D. B.; Frenkel, D., Phase Behavior and Selectivity of DNA-Linked Nanoparticle Assemblies. *Physical Review Letters* **2004,** *92* (6), 068302.

47. Lukatsky, D. B.; Frenkel, D., Surface and bulk dissolution properties, and selectivity of DNA-linked nanoparticle assemblies. *The Journal of Chemical Physics* **2005,** *122* (21), 214904/214901-214904/214911.

48. Jin, R.; Wu, G.; Li, Z.; Mirkin, C. A.; Schatz, G. C., What Controls the Melting Properties of DNA-Linked Gold Nanoparticle Assemblies? *Journal of the American Chemical Society* **2003,** *125* (6), 1643-1654.

49. Prytkova, T. R.; Eryazici, I.; Stepp, B.; Nguyen, S.-B.; Schatz, G. C., DNA Melting in Small-Molecule−DNA-Hybrid Dimer Structures: Experimental Characterization and Coarse-Grained Molecular Dynamics Simulations. *The Journal of Physical Chemistry B* **2010,** *114* (8), 2627-2634.

50. Long, H.; Kudlay, A.; Schatz, G. C., Molecular Dynamics Studies of Ion Distributions for DNA Duplexes and DNA Clusters: Salt Effects and Connection to DNA Melting. *The Journal of Physical Chemistry B* **2006,** *110* (6), 2918-2926.

51. Kudlay, A.; Gibbs, J. M.; Schatz, G. C.; Nguyen, S. T.; Olvera de la Cruz, M., Sharp Melting of Polymer−DNA Hybrids: An Associative Phase Separation Approach. *The Journal of Physical Chemistry B* **2007,** *111* (7), 1610-1619.

52. Park, S. Y.; Stroud, D., Theory of melting and the optical properties of gold/DNA nanocomposites. *Physical Review B: Condensed Matter and Materials Physics* **2003,** *67* (21), 212202/212201-212202/212204.

53. Park, S. Y.; Stroud, D., Theory of the optical properties of a DNA-modified gold nanoparticle system. *Physica B (Amsterdam, Neth.)* **2003,** *338* (1-4), 353-356.

54. Park, S. Y.; Stroud, D., Structure formation, melting, and optical properties of gold/DNA nanocomposites: Effects of relaxation time. *Physical Review B: Condensed Matter and Materials Physics* **2003,** *68* (22), 224201/224201-224201/224211.

55. Stauffer, D.; Aharony, A., *Introduction to Percolation Theory*. Revised Second Edition ed.; Taylor & Francis: 1994.

56. Karplus, M.; Kushick, J. N., Method for estimating the configurational entropy of macromolecules. *Macromolecules* **1981,** *14* (2), 325-332.

57. Gibbs-Davis, J. M.; Schatz, G. C.; Nguyen, S. T., Sharp Melting Transitions in DNA Hybrids without Aggregate Dissolution: Proof of Neighboring-Duplex Cooperativity. *Journal of the American Chemical Society* **2007,** *129* (50), 15535-15540.

CHAPTER 2

Effect of Single-Stranded DNA Gap Structures on Cooperativity and the Rate of Association in DNA-Modified Gold Nanoparticle Aggregates

Portions of this chapter are reproduced in part with permission from the
American Chemical Society

Sikder, M. D. H. and Gibbs-Davis, J. M. "The Influence of Gap Length on Cooperativity and Rate of Association in DNA-Modified Gold Nanoparticle Aggregates," *J. Phys. Chem. C*, **2012**, 116 (21), 11694-11701.

2.1 Introduction

Gold nanoparticle–DNA conjugates are one of the most successful examples of DNA hybrid materials.[1] By combining the molecular recognition properties of DNA with the optical and catalytic properties of gold nanoparticles, these new materials are widely implemented in diagnostics[2-3] and more recently in therapeutic applications.[4] One of the most noteworthy properties of gold nanoparticle–DNA conjugates (GNP–DNA) is the increased cooperativity and stability of DNA hybridized in GNP–DNA aggregates or films.[5-7] As a result of this cooperativity, GNP–DNA probes are far more selective in detection applications. For example, using a simple sandwich-type assay, single basepair mismatches can be discriminated with three times greater selectivity than molecular probes.[5]

The cooperativity of GNP–DNA is displayed during the sharp thermal dissociation, or melting, of GNP–DNA aggregates linked through hybridization by a third complementary strand (Figure 2.1A, *linker sequence*). Figure 2.1B illustrates a typical sharp melting profile, which is unlike those profiles exhibited by unmodified DNA duplexes that dissociate over a broad temperature range. Because of this sharp transition, temperature can be used to discriminate between perfectly complementary DNA duplexes and those containing a single basepair mismatch. As a consequence, simple thermal stringency washes are sufficient to achieve very high selectivity in assays designed for detecting single nucleotide polymorphisms using GNP–DNA probes.[5]

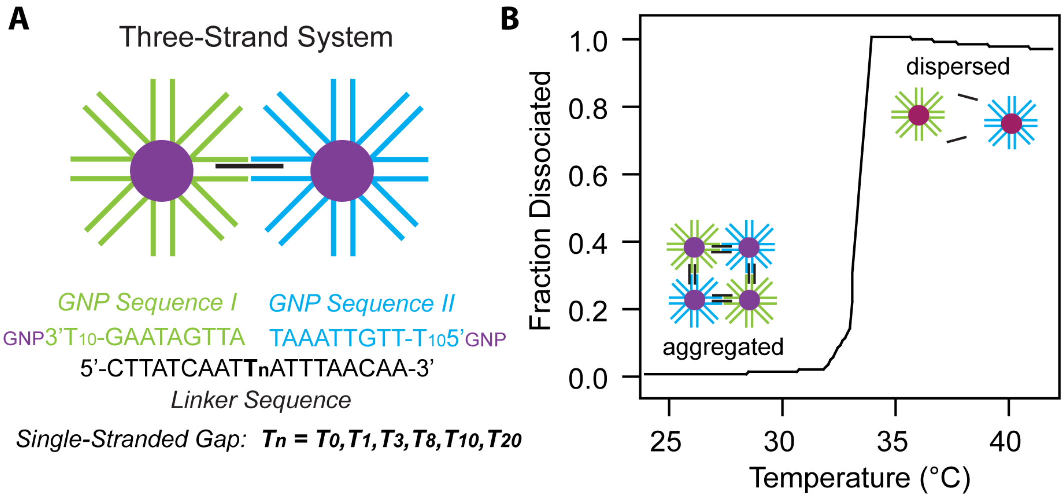

Figure 2.1. A.) A three-strand duplex hybridization system using two sets of gold nanoparticles modified with *GNP sequence I* and *II* that are each complementary to half of a *linker sequence* containing single-stranded gaps of polythymidine (T_n where $n = 0$, 1, 8, 10 and 20). B.) Because each GNP–DNA contains many DNA strands, hybridization of the GNP–DNA and the *linker sequence* leads to a network, or aggregate, of duplex-linked GNP–DNA. For the aggregate lacking any gap (T_0), the dissociation of the aggregate occurs over a narrow temperature range. This sharpness is attributed to cooperative dissociation arising from interactions between neighboring duplexes (to illustrate, a cooperative number of two is shown).

As new applications of DNA-modified gold nanoparticles emerge an important question that remains is how sensitive cooperativity and other GNP–DNA properties are to changes in the hybridization structure or environment. For example, placing mismatches[8] or long spacer sequences adjacent to the GNP surface[6] was shown to actually enhance aggregate stability but the effect on cooperativity was not determined. In contrast to the aggregate enhancement observed with increasing spacer sequences at the nanoparticle surface, single-stranded gaps on the *linker* sequence have been shown to decrease aggregate stability.[9] These single-stranded gaps can arise in genomic DNA detection when GNP–DNA probes are designed to hybridize to two unique regions on a target sequence that do not fall adjacent to one another.[9-13] Such gaps may also be found in GNP–DNA conjugates with aptamer or hairpin sequences,[14-15] which have promise in small molecule and ion detection,[3] or in switchable GNP assemblies.[16] Most recently, gaps have been used to tune the crystallization process for assemblies of GNP–DNA linked through DNA duplexes.[17-19] However, despite their importance the influence of these gaps on cooperativity has not yet been explored. Understanding the influence of single-stranded gaps on GNP–DNA cooperativity is critical to optimize real-world assays using genomic DNA targets and GNP–DNA probes as selectivity is strongly reliant on aggregate cooperativity.[5] Moreover, determining how cooperativity is influenced by adding flexible, single-stranded gaps into the GNP–DNA aggregate structure provides insights into what principles are most important in maintaining GNP–DNA cooperativity.

The current state of understanding concerning the origin of cooperativity in GNP–DNA and other cooperative organic–DNA hybrid materials maintains that the presence of multiple DNA strands on the scaffold material is critical to induce sharp melting transitions.[7] In addition to polyvalency, the rigidity of the scaffold structure also appears to be critical to induce cooperative melting transitions in DNA materials. For example, other types of flexible polyvalent DNA materials like DNA modified dendrimers have not been reported to induce sharp melting behavior.[20] Additionally, DNA hybridized to a single nanoparticle does not display significantly sharp melting indicating that these duplexes are not placed in the proper orientation to exhibit sharp transitions indicative of highly cooperative behavior.[21-22]

The physical origin of cooperative neighboring duplex interactions has been attributed to the greater number of cations condensed on DNA duplexes compared with their single stranded analogues.[6-7, 23] The salt dependence of DNA hybridization makes sense from a simple charge-screening argument: duplex formation requires the association of two polyanionic strands, so screening the charges is critical for overcoming repulsion between the two oligonucleotides.[24] For polyvalent DNA materials like DNA-modified gold nanoparticles, one could imagine that repulsive effects become even more significant since hybridization of two DNA-modified nanoparticles results in duplexes in close proximity to one another. However, when neighboring duplexes are rigidly held within 5 nm of one another, molecular simulations suggest that the individual condensed cation clouds associated with each DNA duplex coalesce to form one shared cloud.[23] As a result, when the first duplex dissociates leading to a concomitant loss of condensed cations, the cation cloud of all of the neighboring duplexes sharing the ion cloud is perturbed. Consequently, the neighboring duplexes are destabilized, which is manifested in an increasing K_d for each subsequent dissociation. This increasing K_d results in a melting cascade, whereby the melting of the first duplex causes the melting of all the subsequent duplexes sharing the cation cloud.[6-7]

As the rigidity of the scaffold structure influences the ability of neighboring duplexes to dissociate cooperatively, we were interested to see how the introduction of flexible single-strand gaps in the middle of each duplex forming the aggregate would influence this behavior (Figure 2.1A). We reasoned that such flexibility might perturb the formation of the condensed cation cloud between neighboring duplexes that contributes to cooperativity. In addition to the decrease in rigidity, we also reasoned that the single-stranded gaps would perturb cooperativity by decreasing the density of condensed cations in the aggregate structure as single-stranded DNA does not condense as many cations as the duplex form.[24]

In this chapter, we examine the role of single-stranded DNA gaps in the linker strand on the thermodynamic and kinetic properties of duplex-linked GNP–DNA aggregates using absorbance spectroscopy and dynamic light scattering. Cooperativity persists in all of the GNP–DNA aggregates investigated, but the extent of cooperativity was found to depend heavily on the size of the gap sequence. Owing to the significance of condensed cations in the cooperative interactions between neighboring duplexes, the change of condensed cation density was determined for gap-linked duplexes to rationalize the changes in cooperativity. The kinetics of hybridization were also found to depend on the gap length, which is consistent with the recent report by Liu and co-workers.[13] Unlike simply focusing on comparing aggregate melting temperatures and association for a large range of gap sizes and overhangs, we aimed to quantify the thermodynamic parameters, cooperativity, salt dependence, and aggregate size associated with different gap lengths, which provides greater insight as to the influence of gaps on GNP–DNA aggregate behavior.

2.2 Experimental Section

2.2.1 General Data

The DNA was synthesized on an Applied Biosystems Model 392 DNA/RNA solid-phase synthesizer. DNA reagents were purchased from Glen Research, and standard phosphoramidites were used for all of the nucleotides. For attachment to the gold nanoparticles, we used 3′- and 5′-thiolated DNA strands synthesized using 3′-Thiol-Modifier C6 S–S CPG and 5′-Thiol-Modifier C6 S–S phosphoramidite, respectively. All thermal denaturation analyses of DNA-containing materials were performed using an HP 8453 diode-array spectrophotometer equipped with a HP 89090A Peltier temperature controller. Gold nanoparticles with an average diameter of 13 nm were prepared following the literature procedure[25] and size measured using transmission electron microscopy (Figure 2.2A). DNA modification of the gold nanoparticles was performed using sonication to maximize DNA loading according to previous reports.[26] The diameter of the gold nanoparticles was further confirmed by the presence of an absorbance peak at 519 nm (Figure 2.2B), characteristic of 13-nm gold nanoparticles. Concentrations of DNA-modified gold nanoparticle solutions (λ_{max} = 525 nm) were determined from the corresponding extinction coefficient of 2.4×10^8 $M^{-1}cm^{-1}$.[27] DNA concentrations were determined from the molar absorptivity at 260 nm calculated for each sequence using Oligo Calculator (version 3.26).[28]

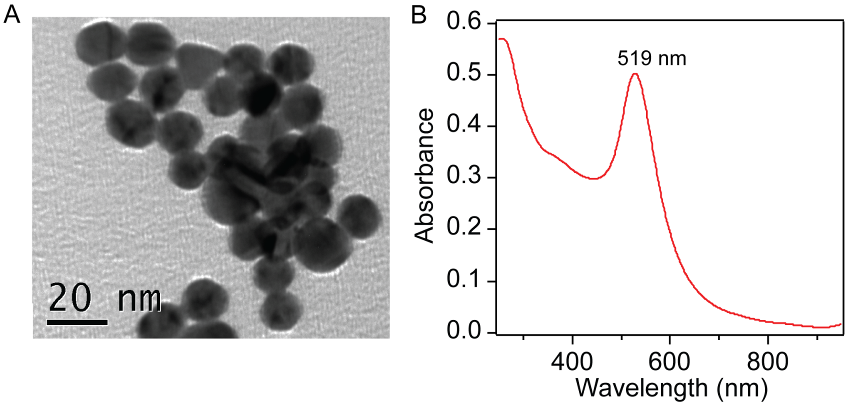

Figure 2.2. A.) Transmission electron microscopic image of synthesized citrate stabilized 13 nm gold nanoparticles. B.) UV-vis spectrum of nanoparticles shows a sharp absorption peak with a maximum of 519 nm.

2.2.2 Thermal Dissociation Experiments

For the unmodified DNA experiments, we combined 1.3 nmol of each DNA sequence in PBS buffer (1.0 mL, 10 mM PBS, pH 7.0) with varying NaCl concentration (0.1–0.5 M). The mixture was allowed to equilibrate for at least 15 min while the instrument cooled to initial temperatures. The melting experiments were performed using UV–vis ChemStation Software with absorbance readings at 260 nm taken at 1 °C intervals from 10 to 60 °C, with 1 min hold time at each temperature. The samples were stirred at 250 rpm during the temperature-variation experiment. The resulting profiles were baseline corrected by subtracting the absorbance at 600 nm. For the GNP–DNA experiments, we combined GNP–DNA-I (1.5 pmol), GNP–DNA-II or GNP–DNA-III (1.5 pmol) and linker (60 pmol) in PBS buffer (1.0 mL, 0.3 M NaCl, 10 mM PBS, pH 7.0). Unless otherwise noted in the text, the mixture was allowed to sit overnight at room temperature and then cooled to 4 °C for 2 h immediately prior to running the melting experiments. The melting experiments were performed using UV–vis ChemStation Software with absorbance readings at 525 nm taken at 1 °C intervals from 10 to 60 °C, with 1 min hold time at each temperature. The samples were stirred at 250 rpm during the temperature-variation experiment. The resulting profiles were baseline corrected by subtracting the absorbance at 925 nm.

2.2.3 Thermal Denaturation Profile Analysis

The maximum of the first derivative of the melting profile is often used to determine the melting temperature (T_m). However, for the unmodified three-strand duplexes we observed that the steepest part of the melting curve that the thermal denaturation software assigned to the melting temperature was often not at the center of the transition (Figure 2.3). Therefore, we determined the melting temperature from fitting a Gaussian function to the first derivative in Igor Pro (WaveMetrics, Inc., Version 6.20A).

$$f'(T) = f'(0) + \mathrm{A}\exp\left[-\left(\frac{\mathrm{T}-\mathrm{T_m}}{\mathrm{width}}\right)^2\right] \tag{2.1}$$

where f' is the first derivative of the melting profile as a function of temperature, T is the temperature in K, A is the amplitude, width is the width of the Gaussian peak and T_m is the melting temperature.

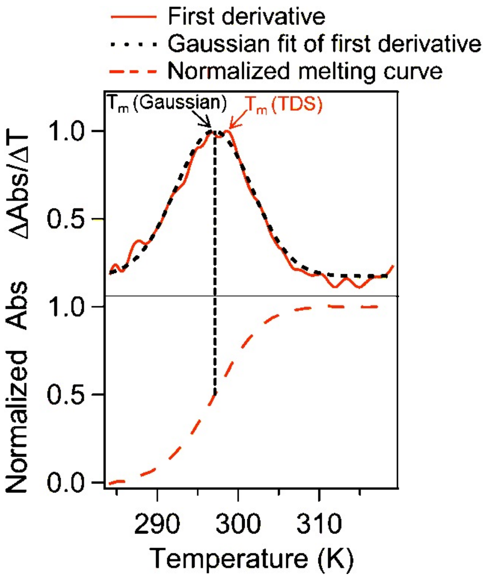

Figure 2.3. Figure illustrates how the peak of a Gaussian fit to the first derivative of the melting curve (upper graph) results in better agreement with the temperature at which half of the DNA has melted (lower graph). In contrast, the maximum of the first derivative is often used by thermal denaturation software (TDS) to assign the melting temperature, which for our system leads to poor agreement with the temperature of half dissociation. Consequently the peak temperature from the Gaussian fit as the melting temperature was used.

For the unmodified DNA system, the reported T_m values are the average of two measurements on different hybridization mixtures, and the error represents the range of measured values (Table 2.1). For the GNP–DNA experiments, the T_m was determined by fitting the baseline subtracted and normalized melting profile to equation 2.5.[6] To ensure that the DNA density of the GNP–DNA was constant in the experiments, we used one purified batch of DNA-modified gold nanoparticles for all of the experiments shown in Table 2.1. The error bars for T_m

and ΔH represent ±1 standard deviation as reported in the fit of equation 2.5 to the data using Igor Pro.

2.2.4 Dynamic Light Scattering

The aggregate or particle size was measured on a Zetasizer Nano S series dynamic light scatterer (Malvern Instruments Ltd.) with a 633 nm laser. Three measurements were done for each sample, and each measurement was obtained from an average of at least 14 scans. Samples were prepared as described in the thermal denaturation section and allowed to sit at room temperature. The first set of DLS measurements was done after 30 min of hybridization on one set of samples. The second set of measurements was conducted after 180 min of hybridization on another set of samples. To obtain the reference particle size, DLS measurements were also performed on the citrate-stabilized and DNA-modified gold nanoparticles. The intensity distribution and particle size in hydrodynamic radius were obtained using Zetasizer software (version 6.2). All hybridization mixtures were made and DLS measurements conducted at room temperature.

2.3 Thermodynamics of Aggregates Containing Single-Stranded Gaps

2.3.1 Thermal Denaturation Profile Analysis

One common strategy for GNP–DNA-based detection is based on a colorimetric change that occurs when a target DNA sequence hybridizes with two different GNP–DNA probes.[2] In these assays, the probe sequences on the GNP–DNA are complementary to two regions on the target (linker) sequence; when the two regions are immediately adjacent a *nicked duplex* results (Figure 2.4, where

$T_n = T_0$). As previously discussed, each nanoparticle contains many probe sequences so hybridization with multiple target strands leads to an aggregate of duplex-linked nanoparticles. The proximity of neighboring nanoparticles in the aggregate decreases the energy requirement for exciting surface plasmons thus the color of the nanoparticle suspension changes when target DNA is added and the GNP–DNA aggregates form.[29]

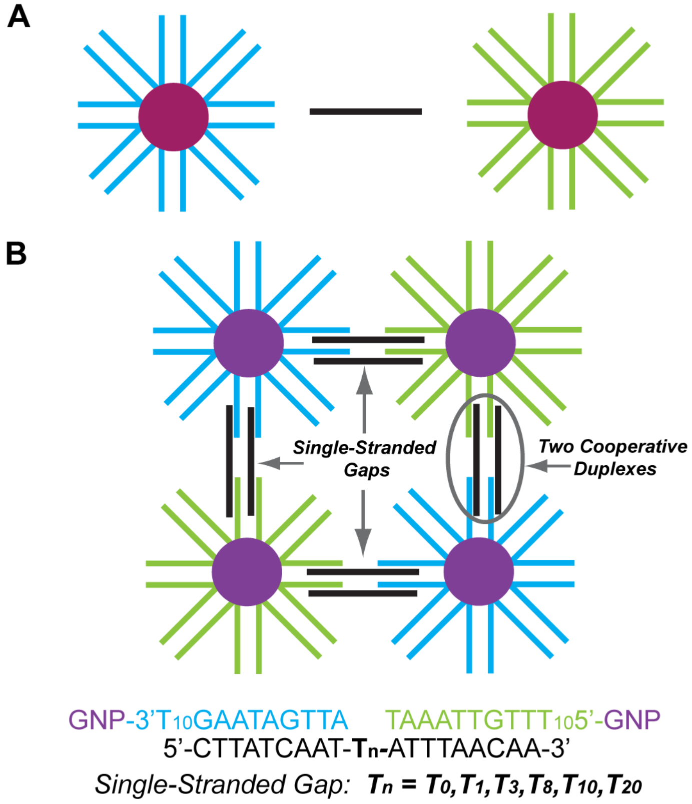

Figure 2.4. A.) Above the melting temperature (T_m), the DNA-modified gold nanoparticles (GNP-DNA) and the target strand are unhybridized. The dispersed GNP-DNA appears red due to surface-plasmon resonant absorbance (λ_{max} = 525 nm). B.) Hybridization leads to aggregate formation with cooperative interactions between neighboring duplexes. To illustrate, a cooperative unit of two duplexes

is depicted. The proximity of the GNPs also leads to a red shift of the SPR λ_{max}, which causes the aggregates to appear purple. Target sequences containing single-stranded gaps of polythymidine (T_n where n = 0, 1, 3, 8, 10 and 20) were used in this investigation.

Figure 2.5B illustrates the corresponding thermal dissociation observed from the change in absorbance at 525 nm as a hybridized mixture of complementary GNP–DNA and linker DNA with varying gap sequences (T_n) is heated (1.5 nM and 60 nM of GNP–DNA and linker, respectively, in 0.3 M NaCl, 10 mM PBS). The full-width half-maximum of the first derivative (fwhm) is proportional to the cooperativity of the aggregate dissociation[6] and, as shown in Figure 2.5C, is very narrow for the nicked duplexes in the GNP–DNA system (fwhm =1.6 °C, where T_n = T_0). In comparison, unmodified DNA complexes of the same sequence exhibit a broad transition over more than 10–20 °C (Figure 2.5A).

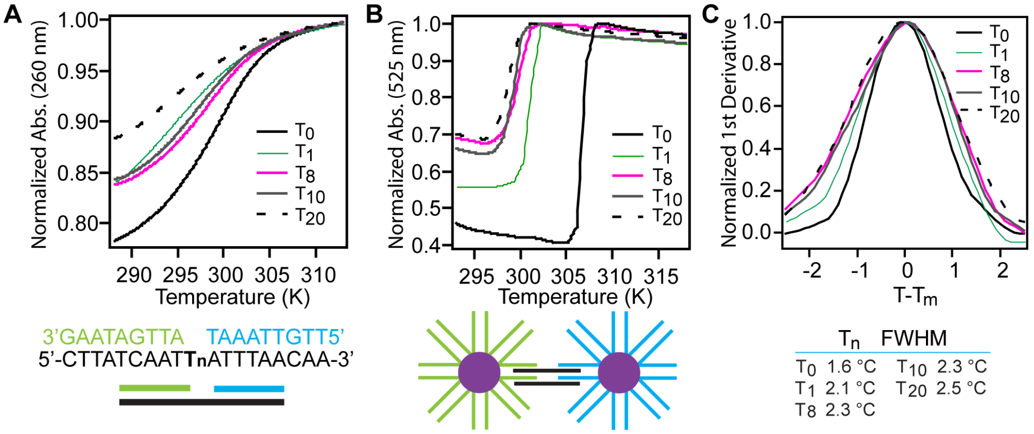

Figure 2.5. A.) Melting profiles of the unmodified three-strand duplex system with varying length *n* of polythymidine gaps (T_n) on the target, or linker, strand.

B.) Melting profiles of the GNP–DNA three-strand duplex system with varying length *n* of polythymidine gaps (T_n) on the linker strand. C.) First derivative of the melting profiles in part B. To compare the width of the transitions, the T_m for each curve was subtracted from the temperature. The full-width half-maximum values (fwhm) correspond to the first derivatives.

We selected polythymidine gaps since they are known to exhibit minimal self-stacking[30] and are consequently ideal for introducing flexibility at the GNP–DNA binding site. Indeed, gel electrophoresis[31] and scanning force microscopy[32] studies have shown that adding a gap of as few as two or five unhybridized thymidines, respectively, saturates the flexibility of the gap. Figure 2.5B illustrates the melting behavior of GNP–DNA linked with a linker sequence containing a nick (where $T_n = T_0$) or a gap of 1–20 thymidine groups ($T_1 - T_{20}$). As a point of comparison, similar experiments were performed on unmodified DNA of the same sequence (Figure 2.5A). (Note higher concentrations of unmodified DNA were needed to observe hyperchromic absorbance changes at 260 nm due to weaker DNA optical activity compared with the GNPs).

For T_0 (the nicked duplex), the melting temperature, or the temperature at which half the GNP–DNA aggregate had melted (T_m) was 306.6 ± 0.1 K (Figure 2.5B). Upon adding one thymidine gap, the T_m became lower than that of the T_0 system, indicating that π-stacking at the three-strand junction was disrupted with the addition of one base (Figure 2.5B, T_1).[33] As the number of thymidines in the gap sequence was increased to 20, we observed a decrease in melting temperature, until the T_m leveled off at 300 K (Table 2.1, Figure 2.6C). In contrast, the unmodified DNA system demonstrated a nonmonotonic relationship between the gap length and the melting temperature, indicating that the aggregate or the multivalent structure of the GNPs uniquely influenced the melting behavior (Figure 2.6C). The lack of trend in gap length and T_m for the unmodified system also suggested that larger gaps formed secondary structures that increased the adjacent duplex stability. Consistent with previous results, the GNP–DNA aggregates exhibited greater T_m values than the analogous unmodified duplex, despite the higher DNA concentration for the unmodified DNA experiment.[7]

2.3.2 Quantifying Cooperativity in Gap-Linked Aggregates

To quantify the extent of cooperativity as a function of T_n length, we determined the cooperative unit, or number of duplexes that interacted during dissociation, from the ratio of the enthalpy change for the GNP–DNA aggregates and the unmodified system,

$$N = \frac{\Delta \mathrm{H}_{\mathrm{GNP}}}{\Delta \mathrm{H}_{\mathrm{uDNA}}} \tag{2.2}$$

where N represents the number of DNA duplexes that melt cooperatively and ΔH_{GNP} and ΔH_{uDNA} are the change in enthalpy for dissociation of the GNP–DNA aggregates and unmodified DNA duplexes, respectively.[5, 34]

2.3.2.1 Using the Van't Hoff Method with Varying DNA Concentration for ΔH Determination

For the unmodified DNA system, we chose to use the van't Hoff method for determining the ΔH_{uDNA} from melting profiles acquired at different DNA concentrations according to the work of Marky and Breslauer.[35] This approach relies on the sensitivity of the melting temperature to the change in DNA concentration and is a commonly used method.[26] From the plot of $1/T_m$ versus ln [DNA] (Figure 2.6B) the slope was used to determine ΔH of association according to:

$$\frac{dT_m^{-1}}{d\ln[\mathrm{DNA}]} = \frac{2R}{\Delta H} \tag{2.3}$$

and ΔS of association was then determined from the *y*-intercept:

$$y - \text{intercept} = \frac{\Delta S - 2R\ln 6}{\Delta H} \tag{2.4}$$

These thermodynamic values were determined from the average T_m from two separate samples, while the error was determined from the error in T_m and the standard deviation in the slope and y-intercept values determined from the fitting software.

As shown in equation 2.3, systems with a greater absolute ΔH value should exhibit very small changes in $1/T_m$ (or T_m) as a function of DNA concentration. Indeed, we observed that changing the concentration of GNP–DNA did not lead to a discernible change in T_m over the concentration range in which we could observe GNP–DNA melting by changes in absorbance. Consequently, we chose to use the established method for determining the GNP–DNA change in enthalpy developed by Schatz and Mirkin (equation 2.5).[6]

2.3.2.2 Using the Schatz-Mirkin Model for ΔH Determination

To determine the value of ΔH_{GNP} of dissociation according to this method,[6] we related the absorbance change at 525 nm (Abs) to the fraction of melted GNP–DNA, *f*, as a function of temperature. Next, a sigmoidal function was fit to *f*:

$$f = \frac{\mathrm{Abs}_{\max} - \mathrm{Abs}}{\mathrm{Abs}_{\max} - \mathrm{Abs}_{\min}} = \frac{1}{1+\exp\left[\frac{\Delta H_{\mathrm{GNP}}}{\mathrm{R}}\left(\frac{1}{\mathrm{T}}-\frac{1}{\mathrm{T_m}}\right)\right]} \qquad (2.5)$$

where R is the ideal gas constant. The fit of equation 2.5 to the experimental data for the nicked duplex (T_0) is shown in Figure 2.6A, and the resulting ΔH values are given in Table 2.1 with the corresponding T_m values for the GNP–DNA hybridization mixtures in 0.3 M NaCl buffer (10 mM PBS, pH 7). The fit of equation 2.5 to the unmodified DNA melting profiles did not show good agreement for the gap-linked systems. Consequently, the van't Hoff method using varying DNA concentration was only used to assess the ΔH for the unmodified DNA.

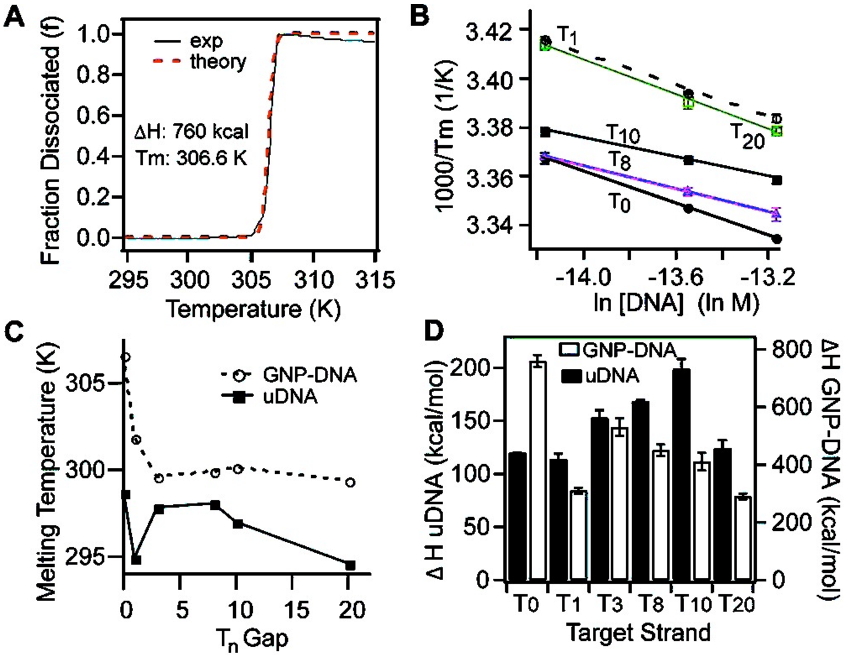

Figure 2.6. A.) The fraction of GNP–DNA dissociated as a function of temperature for the nicked duplex (where $T_n = T_0$). The theoretical fit is based on Jin et al.[6] (equation 2.5) and was used to determine ΔH and T_m. B.) Van't Hoff plots of T_m^{-1} versus natural log DNA concentration for unmodified gap-linked DNA duplexes mixtures ranging from 700 nM to 1.9 μM where T_n is the gap

length. C.) Melting temperature as a function of T_n gap length for the GNP–DNA and unmodified DNA (uDNA) systems. D.) ΔH of dissociation as a function of T_n gap length for the unmodified DNA (uDNA, left axis) and GNP–DNA (right axis).

Table 2.1. Thermodynamic Values Corresponding to the Dissociation of T_n Gap-Linked Aggregates of GNP–DNA and Unmodified DNA Duplexes (uDNA).

	GNP		uDNA				
Gap	**ΔH_{GNP} (kcal/mol)**	**T_m (K)**	**ΔH_{uDNA} (kcal/mol)**	**T_m (K)**	**ΔS_{uDNA} (cal/mol·K)**	**Δi**	**N**
T_0	760(20)	306.6(1)	120.0(2)	298.7(1)	360(1)	3.7(1)	6.3(2)
T_1	320(10)	301.8(1)	114(6)	294.9(3)	340(20)	3.3(2)	2.8(2)
T_3	540(30)	299.6(1)	153(7)	297.8(1)	470(20)	4.9(3)	3.5(3)
T_8	460(20)	299.9(1)	168(1)	298.1(2)	517(3)	6.0(1)	2.7(1)
T_{10}	410(30)	300.1(3)	200(10)	297.0(1)	620(30)	6.8(4)	2.0(2)
T_{20}	290(10)	299.4(1)	124(8)	294.6(1)	380(20)	3.4(3)	2.4(2)

Numbers shown in the parenthesis are the standard deviations calculated from two or more sets of data (except for ΔH_{GNP} that was derived from the fit function using equation 2.5). Therefore, ΔH_{GNP} = 760(20) means 760 ± 20 kcal/mol and Δi = 3.7(1) denotes 3.7 ± 0.1.

The thermodynamic values corresponding to the dissociation of GNP–DNA aggregates and the unmodified duplexes are presented in Table 2.1, and a comparison of the ΔH values for the unmodified DNA and GNP–DNA system is shown in Figure 2.6D. The results for a T_3 linker system were also determined, but the data were not included in Figures 2.6B, 2.7B, and 2.8 for clarity. For the GNP–DNA aggregates, ΔH_{GNP} was highest for the nicked system (T_0 = 760 ± 20 kcal/mol) and much lower for the system with one base insertion (T_1 = 320 ± 10 kcal/mol), while the T_3, T_8, and T_{10} gaps exhibited similar ΔH_{GNP} values of 400–500 kcal/mol. Upon introducing a T_{20} gap, ΔH_{GNP} dropped again to the lowest value for all of the T_n gaps (290 ±10 kcal/mol). These results supported that increasing the flexibility of the linker strand linking the GNP–DNA together decreased the stability of the aggregate, but the large effect of the single base insertion suggested that perturbation of the duplex was as important as increased flexibility. For the unmodified DNA, the T_1 system exhibited the lowest ΔH_{uDNA} of dissociation, 114 ± 6 kcal/mol, but it was within error of the value for the T_0 system (Figure 2.6D). The T_{10} system, however, had the highest ΔH_{uDNA} value compared with the other T_n gaps (200 ± 10 kcal/mol, Table 2.1). This increase in enthalpy upon dissociation of the T_{10} system was not expected and suggested that a stabilizing secondary structure formed for this gap size. The increase in ΔH, however, was compensated for by an increase in entropy upon DNA dissociation (ΔS_{uDNA} = 620 ±30 cal/(mol K), Table 2.1). The lower entropy of the hybridized T_{10} system could also be explained by the formation of a secondary structure for this gap. Moreover, previous studies have found that a T_2 gap resulted in a larger melting ΔS_{uDNA} than that of the T_0 duplex consistent with the trend observed for the T_n series (Table 2.1).[33] It would be interesting to observe the trends in ΔS for the GNP–DNA system and compare them with the unmodified DNA duplexes, but as previously discussed the large ΔH values should lead to small changes in T_m as a function of DNA concentration (equation 2.3), which makes determining the y-intercept proportional to ΔS difficult (equation 2.4). With our current thermal denaturation experimental setup, we were unable to resolve such small changes in T_m.

2.3.2.3 Calculating the Cooperative Unit N

Comparing the ΔH values for the two systems allowed us to determine *N* for each GNP–DNA system, where *N* is the number of DNA duplexes that melt cooperatively (equation 2.2). As the two methods for calculating ΔH for the GNP–DNA and unmodified DNA were different, we focus our discussion on the trend in cooperative unit as a function of the T_n gap length rather than the absolute values of *N*.

For the nicked GNP–DNA system (T_0), the cooperative unit was 6.3 ± 0.2 duplexes indicating that the aggregated GNP–DNA contained a high density of DNA duplexes (Table 2.1). Upon introducing one T insertion, there was a significant reduction in the cooperative unit of the GNP–DNA from 6 to 3. This result suggested that cooperativity was very sensitive to perturbations of the duplex structure, which supported that the rigidity of the DNA duplexes was important to maintain cooperative interactions. Upon increasing the gap further, however, from 3–20 oligothymidines the cooperative unit decreased only slightly from 3.5(3) to 2.4(2). These results were surprising since we expected the proposed source of cooperativity, sharing of the condensed cation cloud, to decrease systematically as the gap increased, as the single-stranded gap was expected to contain less condensed ions than the adjacent hybridized regions.[36] We also anticipated that the amount of these condensed ions at the gap would not vary during dissociation of the adjacent duplexes.[36] As a result, we expected the cooperative unit to decrease as the unhybridized gap length increased.

2.3.3 Determining the Number of Released Cations Upon Thermal Dissociation

The release of cations upon melting of the gap-linked duplex is illustrated schematically in Figure 2.7A. This number of released cations, Δi, can be determined from the melting profiles for the unmodified three-strand duplexes at different NaCl concentrations (Figure 2.7B).[6, 37] Specifically, the slope of T_m versus ln [NaCl] can be related to the number of released cations Δi according to

$$\frac{dT_m}{d\ln[\text{NaCl}]} = \Delta i \frac{RT_m^2}{\Delta H} \qquad (2.6)$$

where T_m and ΔH_{uDNA} correspond to the values at 0.3 M NaCl.[24]

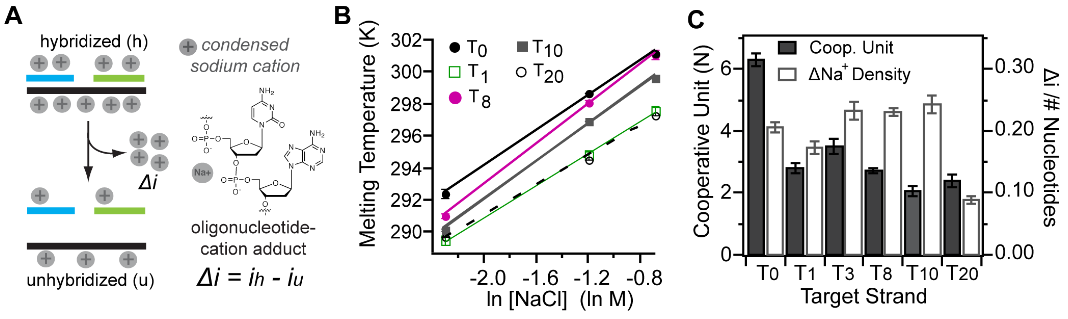

Figure 2.7. A.) Scheme illustrating the change in the number of condensed cations (Δi) upon dissociating an unmodified DNA duplex. An oligonucleotide-

cation adduct representing a condensed cation is shown. B.) Melting temperatures were determined from the unmodified DNA three-strand duplex system with different T_n gap sequences at various salt concentrations ranging from 0.1 to 0.5 M NaCl (10 mM PBS, 1.3 μM [DNA]). The slope can be used to determine the number of released cations during duplex dissociation. (C) Cooperative unit for T_n-gap-linked GNP–DNA aggregates versus the number of released cations per nucleotide for the corresponding gap-linked duplexes.

The resulting values of Δi are included in Table 2.1 and indicate that the number of released cations varied greatly with the length of the gap, contrary to our initial hypothesis. Specifically, the nicked duplex (where $T_n = T_0$) released on average 3.7 ± 0.1 cations for each dissociating duplex. Upon introducing a one-nucleotide T insertion, the number of released cations decreased to 3.3 ± 0.2, which was consistent with the decrease in cooperative number for the T_1 GNP–DNA system. However, the number of released cations then rose as the gap increased, exhibiting the largest value of 6.8 ± 0.4 for the T_{10} gap. This increase in the number of released cations as a function of gap length indicated that the unhybridized gap recruited more condensed cations when the adjacent sequences were hybridized rather than dissociated. Consequently, the larger amount of condensed cations associated with the single-stranded gap might also participate in a condensed cation cloud with neighboring strands. Indeed, the largest number of condensed cations observed for the T_{10} gap duplex could explain why cooperativity persists in this GNP–DNA system despite the highest melting ΔS.

To see how well the *density* of released cations correlated with the cooperative unit N, we took the ratio of Δi and the number of phosphates per duplex (36 bases + gap length). The increase in Δi for T_{10} led to a change in cation (Na^+) density of 0.243 ± 0.003 cations/nucleotide, which is slightly higher than the change in cation density for even the T_0 system that did not contain a single-stranded gap (Figure 2.7C, 0.206 ± 0.002). Overall, there is a correlation of the change in cation density with cooperative unit, particularly for T_1, but it cannot completely explain the lesser degree of cooperativity for the T_{10} system. We infer from these results that the T_{10} system had a greater number of condensed cations to stabilize the duplex structure, which helped maintain cooperative interactions, but could not entirely compensate for the impact of the T_{10} gap on lowering the ΔS of association. Importantly, this data indicated that the gap-linked duplexes had a similar influx of cations per nucleotide than the nicked duplex.

2.4 Kinetics of Aggregates Containing Single-Stranded Gaps

2.4.1 Kinetic Analysis Based on Extinction of GNP-DNA Suspensions

The recent report on hybridization behavior of gap-linked DNA-gold nanoparticle aggregates found that the hybridization rates decreased as the gap sequence increased in length.[13] This is in contrast to the influence of spacer sequences at the GNP surface that enhanced hybridization rates.[38] We were interested to see if slower aggregate formation could also be observed in our T_n-gap systems. First, we observed that the relative absorbance change at 525 nm decreased upon adding gaps (Figure 2.5B). Figure 2.8A illustrates the *absolute* change in absorbance at 525 nm for GNP–DNA before and after the abrupt melting transitions. Increasing the length of the T_n gap led to a monotonic decrease in delta absorbance after hybridization at room temperature, followed by a 2 h incubation at 4 °C. Previous work by the groups of Schatz and Mirkin indicated that the magnitude of the absorbance change correlates with the aggregate size.[29] From this we inferred that increasing the gap length resulted in the formation of smaller aggregates.

One reason for smaller aggregates with increasing T_n length is a slower rate of aggregate formation.[13] Tracking the change in absorbance at 525 nm after mixing both GNP–DNA and linker illustrated that the amount of hybridization varied at short reaction times (2.8B). Specifically, the time it took to reach 20% hybridization based on the relative changes in absorbance was 2 h for the nicked duplex ($n = 0$), 3 h for the duplex containing one gap nucleotide ($n = 1$) and more than 6 h for the duplex containing several thymidines ($n = 8$, 10, and 20).

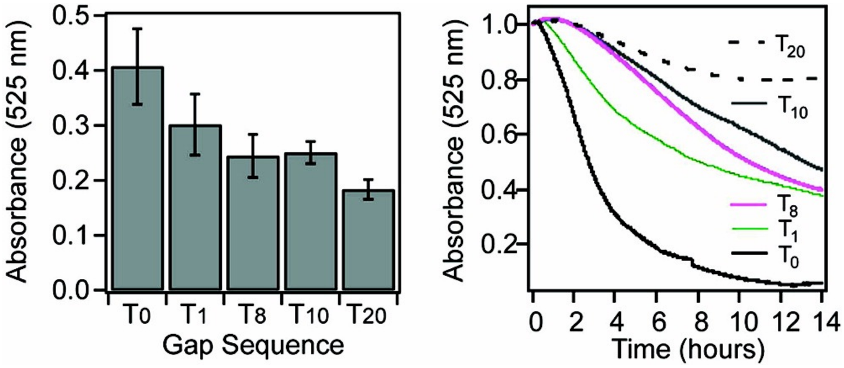

Figure 2.8. A.) Absolute change in absorbance at 525 nm upon dissociating the GNP–DNA aggregates linked with linker strands containing various gap sequences (T_n). The magnitude of the absorbance change corresponds to the size

of the aggregate. B.) Kinetic profile for GNP–DNA aggregate formation. At 24 h, the absorbance readings for the T_1- and T_8-linked aggregates was 0.4 au.

2.4.2 Kinetic Analysis Based on Dynamic Light Scattering of GNP-DNA Suspensions

Using dynamic light scattering we characterized the aggregates at 30 min and 3 h (Figure 2.9A and B, respectively), which confirmed that increasing the gap size led to smaller GNP–DNA clusters at short reaction times. The bare 13 nm gold nanoparticles showed up 12 nm of hydrodynamic radius (R_h) in the dynamic light scattering measurement. The DNA functionalized gold nanoparticles were measured 23 nm. DLS measures the radius of the water-coordinated particles, which is proportional to the actual size of the bare particles. The largest hydrodynamic radius was found for the aggregates derived from the T_0 system. We measured the size to be 390 nm at 30 min and 640 nm at 3 hours of hybridization. This suggests fast initial aggregation, which is consistent with its hybridization kinetics. For T_1 gap linked aggregates, R_h was found to be 130 nm at 30 min and 440 nm at 3 hours. These radii are significantly smaller than those of T_0 system and are also consistent with their aggregation kinetics. The R_h for the T_8, T_{10} and T_{20} gap linked aggregates were also measured and they reflected their hybridization kinetics too as those values were very similar within the experimental time frame. The measured values, 80 nm, 90 nm, and 80 nm at 30 min and 200 nm, 120 nm, and 90 nm correspond to the T_8, T_{10} and T_{20} systems respectively.

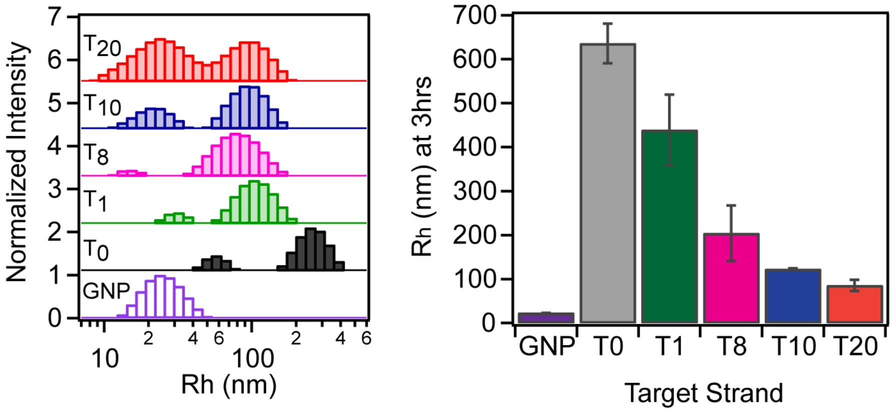

Figure 2.9. A.) Normalized fractional intensity vs hydrodynamic radius (Rh) determined from dynamic light scattering for GNP–DNA mixtures after 30 min of hybridization at room temperature with T_n linkers. (--) No linker was added. B.) Average hydrodynamic radius (Rh) for GNP–DNA hybridized with different linker strands after 3 h at room temperature, where (---) was the GNP–DNA mixture without linker. Error bars show the standard deviation from three sets of scans, where one set represents at least 14 light scattering correlation functions.

2.4.3 Comparison of the Rate of Hybridization at a Gap vs Nicked Site

Even without gaps, the hybridization kinetics of DNA immobilized on gold nanoparticles is known to be slower than the hybridization of unmodified DNA owing to the confined environment of the nanoparticle-bound DNA strand.[39-41] Previous work by Gang and co-workers[39] demonstrated that one way to increase GNP–DNA aggregate formation involved prehybridizing small oligonucleotides complementary to a portion of the GNP-tethered sequence that bridged the nanoparticle surface and the region complementary to the linker. These smaller strands were also shown to increase hybridization rates of linker

DNA to GNP–DNA that did not afford aggregates.[40] In both cases, the increased rate of aggregation or hybridization was attributed to the improved access to the GNP-bound DNA after rigidifying it through hybridization with the small oligonucleotides. The strong dependence of the rate of aggregate formation in our system, however, where the single-stranded region is far from the nanoparticle surface, suggests other possible effects. We infer from our kinetic data that the hybridization state of the DNA in GNP–DNA aggregates is not only important because it can direct the DNA away from the nanoparticle surface but also because it imparts rigidity into the aggregate structure that is critical to form multiple GNP–DNA linkages.

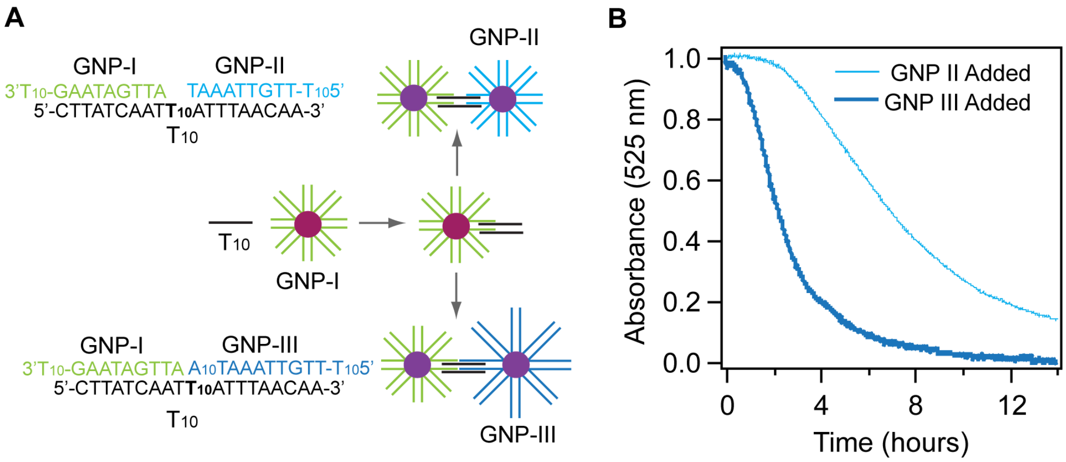

Figure 2.10. A.) Schematic for the comparison of nicked versus gap GNP–DNA aggregation formation. GNP–DNA-I is first mixed with the linker T_{10} and then either GNP–DNA-II or GNP–DNA-III is added resulting in a gap or nick-linked aggregate, respectively. B.) Kinetic hybridization profiles for GNP–DNA-I and T_{10} linker hybridized for several hours followed by the addition of GNP–DNA-II and GNP–DNA-III at time zero.

To confirm that the kinetics were influenced by whether or not an incoming GNP–DNA was hybridizing at a nicked or gapped site, we measured the formation of a nick-linked GNP–DNA aggregate and gap-linked GNP–DNA aggregate in a stepwise manner (Figure 2.10). First, a GNP–DNA was hybridized to a linker containing a T_{10} track in the middle of the sequence (Figure 2.10A, GNP–DNA-I and T_{10}). Next, a completely complementary GNP–DNA was added (GNP–DNA-III) or a GNP–DNA that was only partially complementary resulting in a T_{10} gap (GNP–DNA-II). As shown in Figure 2.10B, the GNP–DNA that hybridized to form a nicked duplex displayed more rapid hybridization rates, despite the longer hybridization sequence (Figure 2.10B, GNP–DNA-III). This result is interesting in light of the previous kinetic studies that attributed the enhanced hybridization rates of partially hybridized GNP–DNA to greater accessibility of the DNA bound to the nanoparticle surface. Our data suggest that hybridization at a nicked site is inherently faster even without changing the accessibility of the DNA bound to the gold nanoparticle, which is consistent with previous observations for the hybridization of DNA adjacent to hairpin structures.[42-43] Moreover, this comparison also suggests that the length of the gap-containing linker is not the main reason for slower kinetics as suggested recently.[13] The question remains whether this signals more rapid DNA hybridization based on stabilization of the transition state by the flanking nick site or a decreased energy barrier for GNP–DNA cluster and aggregate formation for rigid DNA linkages between particles. Monitoring the hybridization of an unmodified DNA to the GNP–DNA-I:T_{10} complex should elucidate the reason for the enhanced rates, but such studies are outside the scope of this investigation.

Interestingly, based on the absorbance changes we found that larger aggregates were formed after 14 h when the linker and one GNP–DNA were prehybridized. Specifically, when the linker was first hybridized to one GNP–DNA followed by the addition of the other GNP–DNA (Figure 2.10B, GNP–DNA-II), the relative change in absorbance was greater than when both GNP–DNA and the linker were simultaneously mixed (Figure 2.10B, T_{10}). This supports that the aggregate structure is under kinetic control at this temperature and also indicates that prehybridization promotes aggregation.

2.5 Conclusions

In this chapter, we have systematically studied the effect of DNA gaps on the thermodynamic and kinetic properties of GNP–DNA aggregates. We found that the presence of polythymidine gaps still resulted in relatively sharp melting behavior in GNP–DNA aggregates, which has important implications for genomic DNA detection with thermal stringency washes. However, increasing the gap sequence decreased the cooperativity, the melting temperature, and the aggregation rate. On the basis of the thermodynamic and salt-dependent analysis, the cooperative unit could be correlated with the change in cation density, balanced by the increase in melting entropy, for gap-linked unmodified DNA duplexes. Unexpectedly to us, the number of released cations increased with increasing gap length from T_1–T_{10} for the unmodified DNA duplexes, even though the number of dehybridizing bases was the same in all systems. As a result the change in condensed ion density was similar for most gap lengths, which was consistent with the persistence of cooperativity in the gap-linked DNA aggregates through a shared ion cloud between neighboring duplexes. Finally, as in previous reports we observed that hybridization is much slower for gap-linked duplexes.[13] Our work indicates that aggregation of GNP–DNA is inherently faster at a nick site, even when the increasing linker length and accessibility of the DNA are taken into account. Although gap-linked GNP–DNA aggregates still exhibit cooperativity, for optimal selectivity and speed, assays should be designed to form nicked GNP–DNA complexes whenever possible.[12, 44]

2.6 References

1. Niemeyer, C. M.; Simon, U., DNA-Based Assembly of Metal Nanoparticles. *European Journal of Inorganic Chemistry* **2005,** *2005* (18), 3641-3655.

2. Rosi, N. L.; Mirkin, C. A., Nanostructures in Biodiagnostics. *Chemical Reviews* **2005,** *105* (4), 1547-1562.

3. Chiu, T.-C.; Huang, C.-C., Aptamer-Functionalized Nano-Biosensors. *Sensors* **2009,** *9* (12), 10356-10388.

4. Giljohann, D. A.; Seferos, D. S.; Daniel, W. L.; Massich, M. D.; Patel, P. C.; Mirkin, C. A., Gold Nanoparticles for Biology and Medicine. *Angewandte Chemie International Edition* **2010,** *49* (19), 3280-3294.

5. Taton, T. A.; Mirkin, C. A.; Letsinger, R. L., Scanometric DNA Array Detection with Nanoparticle Probes. *Science* **2000,** *289* (5485), 1757-1760.

6. Jin, R.; Wu, G.; Li, Z.; Mirkin, C. A.; Schatz, G. C., What Controls the Melting Properties of DNA-Linked Gold Nanoparticle Assemblies? *Journal of the American Chemical Society* **2003,** *125* (6), 1643-1654.

7. Lee, O.-S.; Prytkova, T. R.; Schatz, G. C., Using DNA to Link Gold Nanoparticles, Polymers, and Molecules: A Theoretical Perspective. *The Journal of Physical Chemistry Letters* **2010,** *1* (12), 1781-1788.

8. Harris, N. C.; Kiang, C.-H., Defects Can Increase the Melting Temperature of DNA–Nanoparticle Assemblies. *The Journal of Physical Chemistry B* **2006,** *110* (33), 16393-16396.

9. Y. Paul Bao, M. H., Tai-Fen Wei, Sudhakar S. Marla, James J. Storhoff, and Uwe R. Müller, SNP identification in unamplified human genomic DNA with gold nanoparticle probes. *Nucleic Acids Research* **2005,** *33(2)*.

10. Storhoff, J. J.; Lucas, A. D.; Garimella, V.; Bao, Y. P.; Muller, U. R., Homogeneous detection of unamplified genomic DNA sequences based on colorimetric scatter of gold nanoparticle probes. *Nature Biotechnology* **2004,** *22* (7), 883-887.

11. Zhao, J.; Tang, S.; Storhoff, J.; Marla, S.; Bao, Y. P.; Wang, X.; Wong, E.; Ragupathy, V.; Ye, Z.; Hewlett, I., Multiplexed, rapid detection of H5N1 using a PCR-free nanoparticle-based genomic microarray assay. *BMC Biotechnology* **2010,** *10* (1), 74.

12. Hill, H. D.; Vega, R. A.; Mirkin, C. A., Nonenzymatic Detection of Bacterial Genomic DNA Using the Bio Bar Code Assay. *Analytical Chemistry* **2007,** *79* (23), 9218-9223.

13. Smith, B. D.; Dave, N.; Huang, P.-J. J.; Liu, J., Assembly of DNA-Functionalized Gold Nanoparticles with Gaps and Overhangs in Linker DNA. *The Journal of Physical Chemistry C* **2011,** *115* (16), 7851-7857.

14. Liu, J.; Lu, Y., A Colorimetric Lead Biosensor Using DNAzyme-Directed Assembly of Gold Nanoparticles. *Journal of the American Chemical Society* **2003,** *125* (22), 6642-6643.

15. Liu, J.; Lu, Y., Accelerated Color Change of Gold Nanoparticles Assembled by DNAzymes for Simple and Fast Colorimetric Pb2+ Detection. *Journal of the American Chemical Society* **2004,** *126* (39), 12298-12305.

16. Maye, M. M.; Kumara, M. T.; Nykypanchuk, D.; Sherman, W. B.; Gang, O., Switching binary states of nanoparticle superlattices and dimer clusters by DNA strands. *Nature Nanotechnology* **2010,** *5* (2), 116-120.

17. Park, S. Y.; Lytton-Jean, A. K. R.; Lee, B.; Weigand, S.; Schatz, G. C.; Mirkin, C. A., DNA-programmable nanoparticle crystallization. *Nature* **2008,** *451* (7178), 553-556.

18. Hill, H. D.; Macfarlane, R. J.; Senesi, A. J.; Lee, B.; Park, S. Y.; Mirkin, C. A., Controlling the Lattice Parameters of Gold Nanoparticle FCC Crystals with Duplex DNA Linkers. *Nano Letters* **2008,** *8* (8), 2341-2344.

19. Macfarlane, R. J.; Lee, B.; Hill, H. D.; Senesi, A. J.; Seifert, S.; Mirkin, C. A., Assembly and organization processes in DNA-directed colloidal crystallization. *Proceedings of the National Academy of Sciences* **2009,** *106* (26), 10493-10498.

20. Shchepinov, M. S.; Mir, K. U.; Elder, J. K.; Frank-Kamenetskii, M. D.; Southern, E. M., Oligonucleotide dendrimers: stable nano-structures. *Nucleic Acids Research* **1999,** *27* (15), 3035-3041.

21. Lytton-Jean, A. K. R.; Mirkin, C. A., A Thermodynamic Investigation into the Binding Properties of DNA Functionalized Gold Nanoparticle Probes and Molecular Fluorophore Probes. *Journal of the American Chemical Society* **2005,** *127* (37), 12754-12755.

22. Xu, J.; Craig, S. L., Thermodynamics of DNA Hybridization on Gold Nanoparticles. *Journal of the American Chemical Society* **2005,** *127* (38), 13227-13231.

23. Long, H.; Kudlay, A.; Schatz, G. C., Molecular Dynamics Studies of Ion Distributions for DNA Duplexes and DNA Clusters: Salt Effects and Connection to DNA Melting. *The Journal of Physical Chemistry B* **2006,** *110* (6), 2918-2926.

24. Anderson, C. F.; Record, M. T., Polyelectrolyte Theories and their Applications to DNA. *Annual Review of Physical Chemistry* **1982,** *33* (1), 191-222.

25. Grabar, K. C.; Freeman, R. G.; Hommer, M. B.; Natan, M. J., Preparation and Characterization of Au Colloid Monolayers. *Analytical Chemistry* **1995,** *67* (4), 735-743.

26. Hurst, S. J.; Lytton-Jean, A. K. R.; Mirkin, C. A., Maximizing DNA Loading on a Range of Gold Nanoparticle Sizes. *Analytical Chemistry* **2006,** *78* (24), 8313-8318.

27. Stoeva, S. I.; Lee, J.-S.; Thaxton, C. S.; Mirkin, C. A., Multiplexed DNA Detection with Biobarcoded Nanoparticle Probes. *Angewandte Chemie International Edition* **2006,** *45* (20), 3303-3306.

28. Kibbe, W. A., OligoCalc: an online oligonucleotide properties calculator. *Nucleic Acids Research* **2007,** *35* (suppl 2), W43-W46.

29. Storhoff, J. J.; Lazarides, A. A.; Mucic, R. C.; Mirkin, C. A.; Letsinger, R. L.; Schatz, G. C., What Controls the Optical Properties of DNA-Linked Gold Nanoparticle Assemblies? *Journal of the American Chemical Society* **2000,** *122* (19), 4640-4650.

30. Aalberts, D. P.; Parman, J. M.; Goddard, N. L., Single-Strand Stacking Free Energy from DNA Beacon Kinetics. *Biophysical Journal* **2003,** *84* (5), 3212-3217.

31. Mills, J. B.; Cooper, J. P.; Hagerman, P. J., Electrophoretic Evidence that Single-Stranded Regions of 1 or More Nucleotides Dramatically Increase the Flexibility of DNA. *Biochemistry* **1994,** *33* (7), 1797-1803.

32. Rivetti, C.; Walker, C.; Bustamante, C., Polymer chain statistics and conformational analysis of DNA molecules with bends or sections of different flexibility. *Journal of Molecular Biology* **1998,** *280* (1), 41-59.

33. Lane, M. J.; Paner, T.; Kashin, I.; Faldasz, B. D.; Li, B.; Gallo, F. J.; Benight, A. S., The Thermodynamic Advantage of DNA Oligonucleotide 'Stacking Hybridization' Reactions: Energetics of a DNA Nick. *Nucleic Acids Research* **1997,** *25* (3), 611-616.

34. Gibbs-Davis, J. M.; Schatz, G. C.; Nguyen, S. T., Sharp Melting Transitions in DNA Hybrids without Aggregate Dissolution: Proof of Neighboring-Duplex Cooperativity. *Journal of the American Chemical Society* **2007,** *129* (50), 15535-15540.

35. Marky, L. A.; Breslauer, K. J., Calculating thermodynamic data for transitions of any molecularity from equilibrium melting curves. *Biopolymers* **1987,** *26* (9), 1601-1620.

36. Tan, Z.-J.; Chen, S.-J., Nucleic Acid Helix Stability: Effects of Salt Concentration, Cation Valence and Size, and Chain Length. *Biophysical Journal* **2006,** *90* (4), 1175-1190.

37. Korolev, N. I.; Vlasov, A. P.; Kuznetsov, I. A., Thermal denaturation of Na- and Li-DNA in salt-free solutions. *Biopolymers* **1994,** *34* (9), 1275-1290.

38. Oh, J.-H.; Lee, J.-S., Designed Hybridization Properties of DNA–Gold Nanoparticle Conjugates for the Ultraselective Detection of a Single-Base Mutation in the Breast Cancer Gene BRCA1. *Analytical Chemistry* **2011,** *83* (19), 7364-7370.

39. Maye, M. M.; Nykypanchuk, D.; van der Lelie, D.; Gang, O., A Simple Method for Kinetic Control of DNA-Induced Nanoparticle Assembly. *Journal of the American Chemical Society* **2006,** *128* (43), 14020-14021.

40. Prigodich, A. E.; Lee, O.-S.; Daniel, W. L.; Seferos, D. S.; Schatz, G. C.; Mirkin, C. A., Tailoring DNA Structure To Increase Target Hybridization Kinetics on Surfaces. *Journal of the American Chemical Society* **2010,** *132* (31), 10638-10641.

41. Chen, C.; Wang, W.; Ge, J.; Zhao, X. S., Kinetics and thermodynamics of DNA hybridization on gold nanoparticles. *Nucleic Acids Research* **2009,** *37* (11), 3756-3765.

42. O'Meara, D.; Nilsson, P.; Nygren, P.-Å.; Uhlén, M.; Lundeberg, J., Capture of Single-Stranded DNA Assisted by Oligonucleotide Modules. *Analytical Biochemistry* **1998,** *255* (2), 195-203.

43. Riccelli, P. V.; Merante, F.; Leung, K. T.; Bortolin, S.; Zastawny, R. L.; Janeczko, R.; Benight, A. S., Hybridization of single-stranded DNA targets to immobilized complementary DNA probes: comparison of hairpin versus linear capture probes. *Nucleic Acids Research* **2001,** *29* (4), 996-1004.

44. Akamatsu, K.; Kimura, M.; Shibata, Y.; Nakano, S.-i.; Miyoshi, D.; Nawafune, H.; Sugimoto, N., A DNA Duplex with Extremely Enhanced Thermal Stability Based on Controlled Immobilization on Gold Nanoparticles. *Nano Letters* **2006,** *6* (3), 491-495.

CHAPTER 3

The Influence of Loop and Stem on the Behavior of DNA Hairpin–Linked Gold Nanoparticle Aggregates

3.1 Introduction

DNA functionalized gold nanoparticles (GNP–DNA) are very attractive materials due to their highly programmable structures and striking molecular recognition properties that give rise to numerous applications in nanomaterial synthesis, therapeutics and diagnostics.[1-7] These materials can be used to form a range of assemblies from discrete oligomers to macroscopic aggregates of functionalized gold nanoparticles (GNP), interconnected by virtue of a complementary linker DNA's interactions with the nanoparticle-bound DNA strands. Such aggregate formation is easily visualized from a color change that takes place when the colloidal dispersion of the GNP–DNA aggregates form a network of DNA–duplex linked nanoparticles. Specifically, a red to purple color transition is observed due to the changes in plasmon excitation energy of GNPs upon forming an aggregate. This distinct color change makes it possible to construct colorimetric sensors for detection of ions, small molecules, proteins, polymers and nucleic acids.[8-12] Indeed, numerous assays have been already developed based on this platform that lead to the detection of a large variety of substances such as cocaine,[13-14] glucose,[15] lectin,[16-17] thrombin,[18] cytokine,[19] glutathione,[20] cysteine,[8, 20] UO_2^{2+},[21] Hg^{2+},[22-25] Cd^{2+},[25] Pb^{2+},[25-28] K^+,[29] ATP,[30] kinase,[31] endo-nuclease,[32] DNAase,[33] antibodies,[34] viruses,[35-36] and cholera toxin.[37] Additionally, owing to its simplicity and versatility, a GNP-DNA colorimetric assay exhibits promise in cancer diagnosis.[7, 38] In related work, GNP-conjugated aptamers have been shown to assemble on cell membranes providing direct visualization and detection of cancer cells.[38] GNP–aptamer conjugates have also been successful in small molecule and ion detection while hairpin linker strands have proven useful in switchable GNP–DNA assemblies.[26-27, 39] Regarding the latter, DNA hairpins were also found to be useful in protein detection based on GNP–DNA aggregation[40] and in discrete nanoparticle assemblies for the detection of single base mismatches[41] and intercellular mRNA.[42]

When a DNA-linked GNP aggregate is formed, it can be reversibly converted to a dispersed colloid by means of heat,[43-46] electromagnetic radiations,[47] pH,[48] enzymatic cleavage[49] or a change in the DNA structure.[14, 18] The disintegration, or disassembly, upon heating the aggregates can be monitored by observing their absorption spectra that corresponds to surface plasmon resonance. Such thermal-induced transitions from aggregate to dispersed colloid, referred to as melting transitions, are unusually sharp occurring over a narrow temperature range. This sharp melting is a major advantage of these GNP–DNA materials in diagnostic applications (*vide supra*).

One common strategy to detect nucleic acid biomarkers involves hybridizing complementary probe DNA strands modified with molecular fluorophores to the target sequence. Such techniques suffer two distinct drawbacks. Firstly, a high concentration of DNA is required for a suitable response, therefore, amplification using expensive techniques such as polymerase chain reaction becomes unavoidable; secondly, these molecular probes lack high selectivity due to their thermal dissociation over a broad temperature range, which makes it difficult to use thermal stringency washes to detect mutations with very subtle anomalies like single nucleotide polymorphisms. Although slightly less common, GNP-DNA probes compare favourably with molecular probes. In part this stems from the extraordinarily sharp transitions of DNA–linked gold nanoparticles that make them advantageous over their molecular counterparts. Using thermal stringency washes one can differentiate mutant linker DNA with much higher selectivity compared to their wild type analogs owing to the thermal sensitivity of the target DNA-linked GNP aggregates.

The sharp dissociation of GNP–DNA aggregates is reasoned to arise from the presence of cooperativity in the DNA linkers within the aggregates.[46, 50-52] This cooperativity is associated with the densely packed DNA on the nanoparticle surface, but it is affected by the architecture of the target (linker) DNA:GNP-DNA complex. For example, the presence of flexible gap sequences in the DNA linker has been shown to have a great effect on the thermal stability, transition enthalpy, entropy, and cooperativity in the GNP–DNA aggregates.[43] These assemblies have been also reported to be highly affected when the associated nanoparticle size, interparticle distance, electrolyte density of the medium, surface functionalized DNA density and the architecture of the assemblies are changed.[46] Mutations in the DNA linkers[53] and presence of spacer sequences on the GNP surface[46] have also been reported to have a positive effect on the aggregate stability whereas single-stranded gaps on the DNA linker have been shown to decrease aggregate stability.[43, 54-55]

Earlier in this thesis, we have demonstrated that cooperativity is highly influenced by the presence of flexibility in the GNP–DNA structure[43] (Chapter 2). In another study (Chapter 4), we will also reveal that changing the polarizability of the electrolytes in the buffer solution can modulate cooperativity. These results support that there is a strong dependence of cooperativity on the architecture, conformation and ionic environment of these GNP–DNA assemblies. In this work we aimed to design nanomaterials consisting of GNP–DNA linked with DNA hairpins, and study their cooperative behavior as well as their thermodynamic and kinetic properties. The hairpin loop has been used to detect single base pair mismatches in GNP-linked hairpin probes.[41] More recently, colorimetric assays using DNA hairpin induced GNP–DNA aggregation have been applied for protein and small molecule sensing.[56] Moreover, short hairpin RNA bound to GNPs has been shown to be important molecules in gene therapy.[57] The optimal use of these molecules to construct GNP–DNA based colorimetric methods requires a thorough understanding of the effect of hairpin structure on the nanoparticle assemblies. Determining the influence of such DNA hairpin structures on cooperativity by changing the stem and loop length in the GNP–DNA aggregates provides fundamental insight into the selectivity in molecular recognition derived from these materials.

The general structure of a DNA hairpin consists of a loop region and a stem region (Figure 3.1). The stability of the helix formed by these hairpins is highly affected by the stem and loop structures. For example, a hairpin with a loop of two nucleic acid bases experiences high strain,[58] whereas a long loop size will promote further secondary structures formation making them thermodynamically less stable.[59] Therefore, the optimum length of these regions is very important for the DNA hairpin stability.

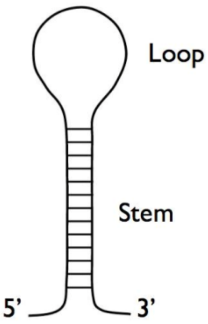

Figure 3.1. Structure of a DNA hairpin consists of a hybridized stem region and an unhybridized loop region. The single-stranded 5´ and 3´ ends are available to hybridize with their complementary sequences on the gold nanoparticles.

In this work, we designed non-complementary GNP–DNA–I and GNP–DNA–IV and a series of DNA hairpin linkers based on a $A_nC_mT_n$ system with deoxyadenosine (A)-thymidine (T) basepair-induced stems and polydeoxycytidine (C) loops (Figure 3.2). We also included in our design a 5´ and 3´ single-stranded region that was available to hybridize to GNP-DNA-I and GNP–DNA-VI. To study the individual influence of stem and loop, we systematically varied their lengths by changing n = 1, 3, and 6; and m = 4, 7, and 10. As a point of comparison, we introduced two unmodified strands with similar sequences to GNP-I and GNP-VI to determine the unique role of the GNP aggregate on the recognition properties.

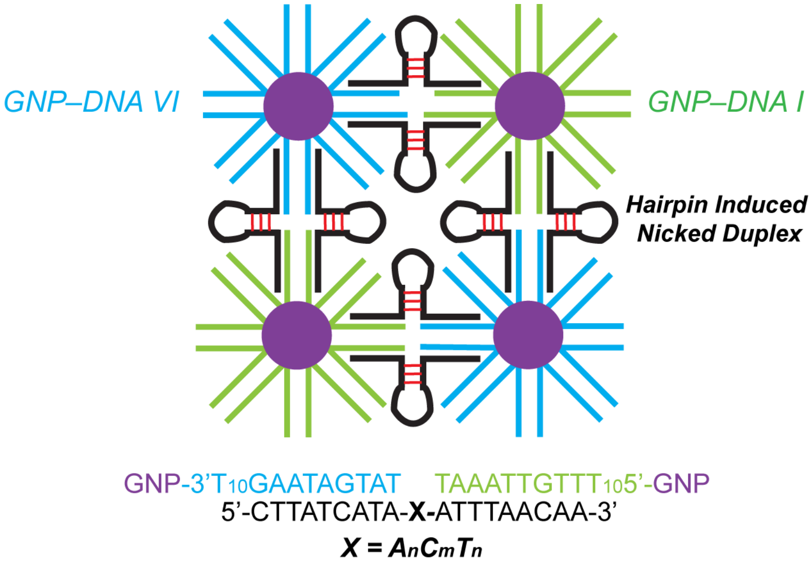

Figure 3.2. GNP–DNA aggregates linked with an $A_nC_mT_n$ hairpin system; n is the number of nucleic acid basepairs in the stem and varied from 1 to 7 and m is the number of bases in the loop, which varied from 4 to 10.

3.2 Experimental Section

3.2.1 DNA Design and Synthesis

All DNA hairpins and thiolated strands used for GNP functionalization (disulfide functionalized DNA) were synthesized in the laboratory using solid-phase synthesis. Details of the DNA synthesis and attachment to the GNPs appeared in section 2.2.1 of chapter 2 of this thesis. The probe DNA strand used for synthesizing GNP–DNA-I contained a 3′- thiol, whereas a 5′- thiol terminated DNA strand was used for GNP–DNA-VI synthesis. These GNP–DNA probe sequences were non-complementary to each other but complementary to the corresponding 5′ and 3′ end of the linker DNA hairpin strands. The synthesized thiolated DNA contained polythymidine spacer sequences were placed between the probe sequence and the thiol functional group to avoid non-specific interaction between GNP and the tethered probe strands.[46] Polythymidines were also chosen particularly for their advantage in loading higher DNA density on the nanoparticle surface over polyadenosine spacers.[60] All synthesized DNA strands were purified and lyophilized in aliquots and stored in the freezer to avoid possible degradation in solution. One lyophilized aliquot of DNA samples was dissolved in 10 mM PBS buffer at pH 7 in the presence of 0.1 M NaCl as DNA stabilizer electrolyte. High concentrations of the DNA stock solutions were prepared so that ~ 3 – 5 μL of DNA could be used in all experiments. The reason for the use of low volume of DNA was to keep the electrolyte concentration constant when experiments were performed at high NaCl concentrations in 1.0 mL volume. Potential enzymatic degradation of DNA was avoided by always using fresh and clean gloves while handling the samples.

3.2.2 GNP-DNA Synthesis and Characterization

Gold nanoparticles of 13-nm diameter were synthesized[61] in the laboratory for DNA functionalization and the size confirmed using transmission electron microscopy (Figure 3.3A). The size of the synthesized citrate-stabilized GNP was further confirmed by the presence of an absorbance peak at 519 nm (Figure 3.3B), characteristic of 13-nm gold nanoparticles.[61] Maximum loading of DNA on the gold surface was promoted by sonication and aging the functionalized GNP–DNA conjugates in 0.7 M NaCl.[60] The concentration of the synthesized citrate stabilized aqueous GNP was 6.1×10^{12} particles/mL, which was diluted by a factor of four by adding ultra pure Milli-Q water prior to the addition of DNA. The concentration of the citrate-stabilized nanoparticles was determined from absorption at 519 nm with an extinction coefficient of 2.7×10^{8} M^{-1} cm^{-1}.[62]

The disulfide terminated probe strands were reduced with 0.01 M aqueous dithiothreitol (DTT) solution at pH 8.0 and ~ 3 μM of the freshly reduced and purified thiol functionalized DNA was used for nanoparticle modification. The reduction, purification and functionalization processes were completed within two hours time frame to avoid potential dimerization of the thiol functional DNA strands that prevents covalent modification of the GNP. The functionalized GNP–DNA was dispersed in 0.05 M NaCl solution for about one hour followed by gradual increase of the NaCl concentration every 30 minutes using concentrate 2 M NaCl solution in a step-wise manner. The salt concentration of the resulting GNP–DNA colloidal dispersion was increased up to 0.7 M and the process completed over 3 hours. These GNP–DNA conjugates in 0.7 M NaCl were aged for at least three days to obtain high DNA density on the GNP surface. Immobilization of thiolated DNA strands onto the GNP caused a red-shift of the absorption maximum to 525 nm (Figure 3.3B and 3.3C), which was also expected.[63] The hairpin-linked aggregates absorbed at 545 nm with decreased absorption maximum due to the coupling of surface plasmon oscillation for proximity of GNP that decreased the energy needed to excite the particles (Figure 3.2C). The concentrations of all DNA were determined from their corresponding UV absorption at λ_{max} = 260 nm using Oligo Calculator (version 3.26)[64] and that of the functionalized gold nanoparticles from their extinction at λ_{max} = 525 nm using extinction coefficient of 2.4×10^{8} M^{-1} cm^{-1}.[63]

Prior to hybridization of the GNP–DNA conjugates for thermal denaturation and kinetics experiments, a purification by centrifugation was performed on all the GNP–DNA conjugates to avoid interference from untethered DNA thiol strands.[63] The centrifugation followed by decantation of the supernatant was done multiple times to reduce the NaCl concentration to the experimental conditions and remove the excess DNA. Only freshly purified GNP–DNA conjugates were used for all thermal denaturation and kinetics experiments and in samples for recording absorption spectra. The aggregates for thermal denaturation experiments were stored at 4 °C, and all DNA strands were stored at the same temperature in a custom-made aluminum metal block designed to hold 0.6 – 2.0 μL microtubes.

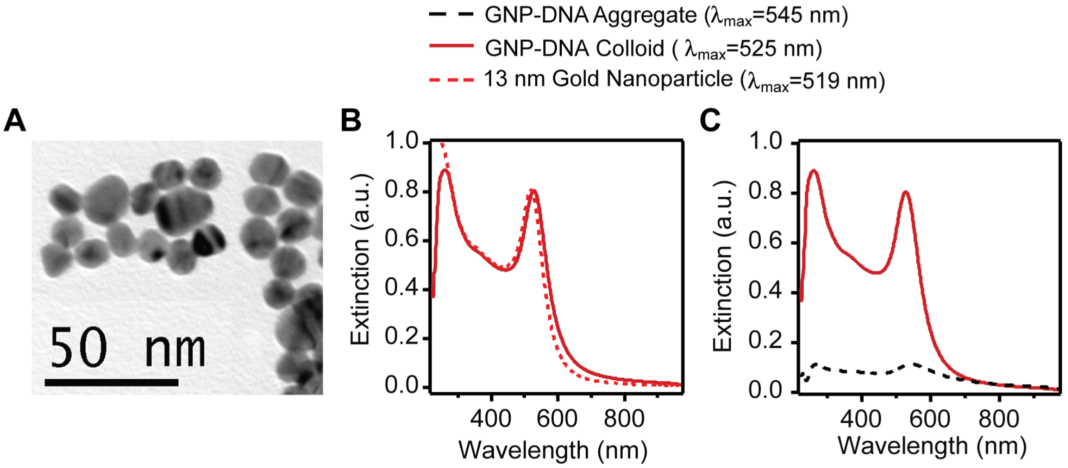

Figure 3.3. A.) Transmission electron microscopic image of citrate stabilized 13-nm GNP prepared for this study. B.) The UV-vis extinction spectrum of 13-nm GNP exhibits a sharp peak with a maximum of 519 nm. DNA modification of the nanoparticles resulted in a red-shift of the absorption maximum to 525 nm. C.) The GNP–DNA colloidal dispersion in 0.5 M NaCl absorbs at 525 nm. Hairpin

linked GNP-DNA aggregates absorb at 545 nm with a decrease in the overall extinction compared with the dispersed colloid.

3.2.3 Thermal Dissociation Experiments

All thermal denaturation and kinetics experiments were performed on an HP 8453 diode-array spectrophotometer equipped with an HP 89090A Peltier temperature controller. The thermal dissociation or melting experiments were performed on the hairpin linked three strand duplexes containing unmodified DNA (uDNA) and GNP–DNA aggregates. For the uDNA experiments, we combined 1.3–2.2 nmol of each DNA sequence, depending on the desired final concentration, in PBS buffer (1.0 mL, 10 mM PBS, pH 7.0) at 0.5 M NaCl concentration. The mixture was hybridized at 4 °C for at least 1 hour. Prior to performing a thermal denaturation experiment, the spectrometer cell holder temperature was set to the initial values using the Peltier temperature controller coupled to the spectrometer. The sample was allowed to equilibrate at this temperature for at least 15 min and melting experiments performed using UV–vis ChemStation Software by increasing the temperature in a step-wise manner followed by recording the absorption spectra. All experiments were performed in a Varian PTFE stopper top quartz cuvette containing 7 mm magnetic stir bar. For experiments involving uDNA duplexes, the temperature was varied from 15 °C to 75 °C by an increment of 1 °C with 1 min hold time at each temperature. The samples were stirred at 250 rpm using the HP 89090A Peltier temperature controller's built-in stirring system. The thermal denaturation profile was obtained from the software plotted absorbance at $\lambda_{max} = 260$ nm for each temperature. An increased temperature resulted in a scattering of the DNA solution, which was observed in their absorption spectra. Therefore, the thermal denaturation profiles were baseline corrected by subtracting the absorbance at 350 nm where all the spectra showed a constant absorbance over a broad range of wavelengths.

For the GNP–DNA experiments, we combined GNP–DNA–I (1.5 pmol with respect to GNPs), GNP–DNA–VI (1.5 pmol with respect to GNPs), and the linker DNA hairpin (60 pmol) in PBS buffer (1.0 mL, 10 mM PBS, pH 7.0) at varying NaCl concentrations (0.2 – 0.5 M). Unless otherwise noted in the text, the mixture was allowed to hybridize at 4 °C for 16 hours prior to running the thermal denaturation or melting experiments. The melting experiments were performed using UV–vis ChemStation Software with absorbance readings at 525 nm taken at 1 °C intervals from 20 to 50 °C, with 1 min hold time at each temperature. The stirring speed of all samples was maintained at 250 rpm for each experiment. The resulting profiles were baseline corrected by subtracting the absorbance at 920 nm.

3.2.4 Thermal Denaturation Profile Analysis

The steepest part of a sigmoidal melting transition corresponds to the 50 – 50 population of DNA duplexes and single strands or GNP–DNA aggregates and dispersed colloids. The temperature corresponding to this part of the melting profile is defined as the melting temperature or thermal denaturation temperature, T_m and is a measure of the thermodynamic stability of the duplexes or aggregates.[46] A detailed description of challenges in T_m determination and the solutions appeared in section 2.2.3 of chapter 2 of this thesis. Some hairpin-linked uDNA in our experiments formed low temperature duplexes. Hence it required us to fit the first derivative of these transitions to a Gaussian fit function (equation 3.1) as described previously in chapter 2.

$$f'(\mathrm{T}) = f'(0) + \mathrm{A}\exp\left[-\left(\frac{\mathrm{T}-\mathrm{T_m}}{\mathrm{width}}\right)^2\right] \tag{3.1}$$

where $\mathrm{T_m}$ is the melting temperature, f' is the first derivative of the melting profile as a function of temperature, T is the temperature in K, A is the amplitude, and width is the width of the Gaussian peak. The reported $\mathrm{T_m}$ (Table 3.1) values for both uDNA duplexes and GNP–DNA aggregates are the average of at least two measurements on different samples, and the error represents the range of measured values with a minimum 0.1 °C that corresponds to the resolution of the instrument.

The ΔH values reported (Table 3.1) for the GNP–DNA aggregates were determined by fitting the baseline subtracted and normalized melting profile to a sigmoidal function using equation 3.2.[46]

$$f = \frac{\mathrm{Abs_{max}} - \mathrm{Abs}}{\mathrm{Abs_{max}} - \mathrm{Abs_{min}}} = \frac{1}{1+\exp\left[\frac{\Delta \mathrm{H_{GNP}}}{\mathrm{R}}\left(\frac{1}{\mathrm{T}} - \frac{1}{\mathrm{T_m}}\right)\right]} \tag{3.2}$$

where f is the dissociated fraction of aggregates, $\Delta\mathrm{H_{GNP}}$ represents the dissociation enthalpy, $\mathrm{T_m}$ is the melting temperature, and R is the molar gas constant. The DNA density influences the ΔH for the GNP–DNA melting transitions. Therefore, to maintain a constant density of DNA on the GNP–DNA conjugates we used one purified batch of DNA-modified gold nanoparticles for all ΔH determination (Table 3.1). The error bars for ΔH represent ±1 standard deviation as reported in the fit of equation 3.2 to the data using Wavemetrics Igor Pro (version 6.30). As in chapter 2, the ΔH of the unmodified DNA systems was determined differently than the GNP–DNA aggregates using a concentration-dependent method (section 2.3.2.1).[65]

3.3 Thermodynamics of Aggregates Containing $A_nC_7T_n$ Hairpin Linkers with Varying Stem Size

Figure 3.4 illustrates hybridization of two distinct and non-complementary GNP–DNA probes with a DNA hairpin linker strand. As described in section 3.2.1, the 5′- thiol modified GNP–DNA probe sequence was complementary to the nine terminal nucleic acids at the 3′- end of all hairpin strands, whereas the 3′- thiol modified GNP–DNA probe sequence was complementary to the nine terminal nucleic acids at the 5′- end of the same DNA hairpin. The high DNA density on the GNP allowed hybridization of more than one strand between two nanoparticles. This results in close proximity of DNA duplexes between two adjacent nanoparticles. Each DNA duplex in such a nanoparticle dimer is associated with a particular number of cations that screen the negative charges of the DNA phosphate groups. A close packing configuration of these duplexes results in sharing the cation cloud associated with each strand by multiple neighboring DNA duplexes. Moreover, due to the presence of a high number of DNA strands on each nanoparticle, these dimers undergo a further oligomerization in the presence of available linker DNA strands resulting in the formation of a three-dimensional network of nanoparticles linked by DNA single strands, or more simply GNP–DNA aggregates.

Cooperativity that leads to sharpness of the temperature induced aggregate dissociation is proposed to originate from this shared ion cloud.[46, 66] When one DNA duplex linker dissociates due to temperature increase, it decreases the local cation concentration resulting in an increase in the dissociation constants of the remaining interacting duplexes. This increase in the dissociation constant further decreases the thermal stability of the remaining duplexes resulting in a melting cascade. It is obvious that any factor that disrupts this shared ion cloud will have an impact on the cooperativity in GNP–DNA dissociation. Our study was focused on the effect of secondary structures in the linker DNA strand, more specifically DNA hairpins on this cooperativity. The number of DNA duplexes sharing a common ion cloud is called the cooperative unit. For simplicity, a cooperative unit of two is shown in Figure 3.4.

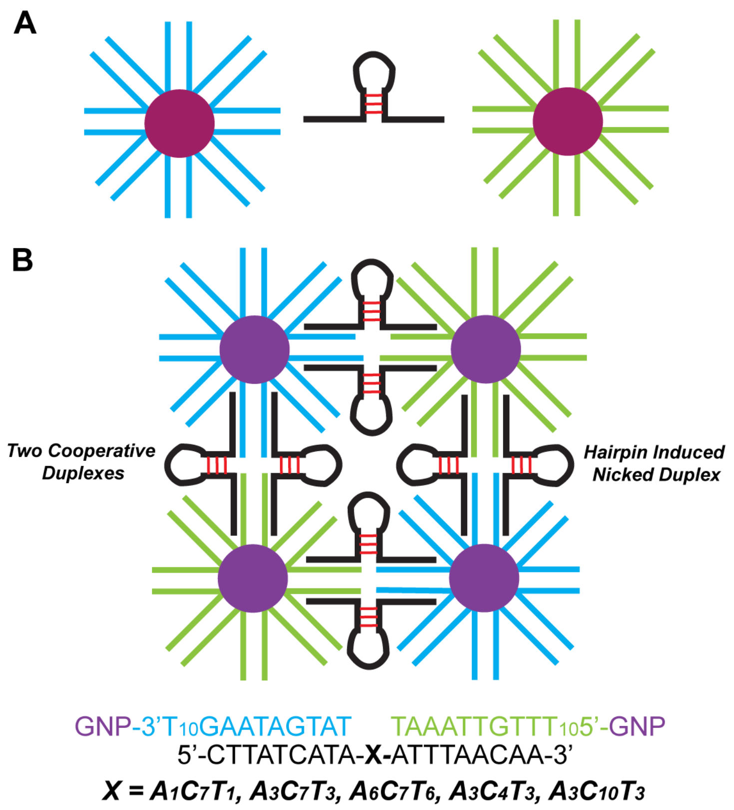

Figure 3.4. A.) The 3′- GNP–DNA probe is shown in blue and the 5′- GNP–DNA probe in green. The linker DNA hairpins have varying A:T basepair stems and polydeoxycytidine loops. **B.)** Hybridization of the two GNP–DNA probes with the linker DNA hairpin leads to the formation of aggregates with hypothetical two cooperative unit. The linker contains a hairpin (X) based on a $A_nC_mT_n$ sequence (n = 1, 3 and 6; m = 4, 7, and 10) used in this investigation.

Figure 3.5A illustrates the corresponding thermal dissociation observed from the change in absorbance at 525 nm upon heating a hybridized mixture of complementary GNP–DNA and linker hairpin DNA with varying stem lengths (hairpin $A_nC_mT_n$, where n = 1, 3, and 6; m = 7). The concentrations were 1.5 nM (with respect to GNPs) and 60 nM of GNP–DNA and linker, respectively, in 0.5

M NaCl, 10 mM PBS. The thermal dissociation of the corresponding uDNA consisting of the same sequences described in Figure 3.5 but lacking any GNPs was also measured to determine the influence of the GNP on the melting transition (2.2 μM per strand, Figure 3.5B). The melting temperature (T_m) of the uDNA and the GNP–DNA aggregates are shown in Figure 3.5C. The T_m is higher for the GNP–DNA aggregates compared to the unmodified DNA duplexes, consistent with our previous observations (Chapter 2) and other reports.[67] Moreover, the thermal stability of all the hairpin-linked GNP–DNA aggregates varied a small amount with stem size, whereas that of the unmodified three-strand duplexes showed more significant variation in T_m. Specifically, the unmodified $A_6C_7T_6$ three-strand (or nicked) duplex exhibited a higher melting temperature compared with the $A_3C_7T_3$ and $A_1C_7T_1$ containing duplexes. Such dependence of the thermal stability has been seen for hairpin DNA with longer stem sequences.[68] We attribute the increase in thermal stability to the greater number of hybridizing bases that contribute to the total stability of the hairpin. These results indicate that the hairpin stability strongly influences the stability of the nicked duplex for the unmodified system, but not the hairpin-linked GNP aggregates. Finally, in comparison to the GNP–DNA melting transitions, the unmodified DNA complexes of the same sequence exhibited a broad transition over more than 10 – 20 °C (Figure 3.5).

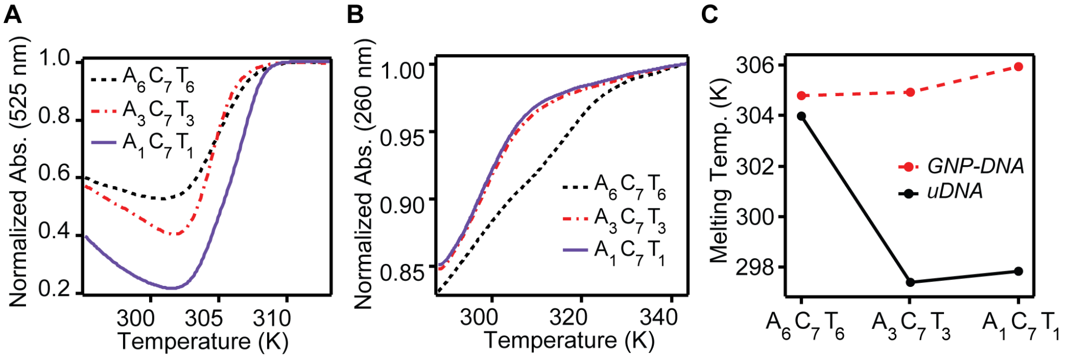

Figure 3.5. A.) Melting profiles of the hairpin-linked GNP–DNA aggregates with varying length of the stem in the linker hairpin strand. B.) Melting profiles of the unmodified three-strand duplex system with varying lengths of the stem on the hairpin linker strand. C.) Thermal denaturation temperatures of the GNP-DNA aggregates with varying hairpin stem size and the corresponding unmodified three–strand duplex system.

For $A_1C_7T_1$ (the shortest possible stem on the hairpin linker), the melting temperature was 305.9 ± 0.1 K for the hairpin-linked GNP-DNA aggregates (Figure 3.5C). Upon adding two more deoxyadenosine and thymidine basepairs on the stem of the DNA hairpin (resulting in the $A_3C_7T_3$ system), the T_m became lower than that of the $A_1C_7T_1$ system (Figure 3.6C, $A_3C_7T_3$, T_m = 304.9 ± 0.1 K). As the number of adenosine and thymidine basepairs in the stem sequence was further increased to six (resulting in the $A_6C_7T_6$ system), we observed a thermal stability very similar to that of the $A_3C_7T_3$ system (Table 3.1, Figure 3.5C). This result was surprising as the trend in the melting temperatures of the GNP–DNA aggregates was opposite to that of the unmodified DNA nicked duplexes. This indicates that the aggregate or the multivalent structure of the GNPs uniquely influenced the melting behavior (Figure 3.5C).

Table 3.1. Thermodynamic Values Corresponding to the Dissociation of $A_nC_mT_n$ Systems (n = 1, 3, and 6; m = 4, 7, and 10) of GNP–DNA and Unmodified DNA Duplexes (uDNA).

	GNP–DNA		**uDNA**				
Hairpin Systems	**ΔH_{GNP} (kcal/mol)**	**T_m (K)**	**ΔH_{uDNA} (kcal/mol)**	**T_m (K)**	**ΔS_{uDNA} (cal/mol·K)**	**Δi (GNP–DNA)**	**N (GNP–DNA)**
A_1 C_7 T_1	190(10)	305.9(1)	89(3)	297.8(1)	249(8)	4.9(3)	2.1(2)
A_3 C_7 T_3	250(20)	304.9(3)	88(2)	297.4(1)	252(5)	4.3(4)	2.9(2)
A_6 C_7 T_6	182(9)	304.8(2)	62(1)	304.0(1)	159(3)	3.9(2)	2.9(2)
A_3 C_4 T_7	290(30)	305.4(1)	87(2)	297.5(1)	248(7)	4.0(5)	3.3(4)
A_3 C_7 T_3	250(20)	304.9(3)	88(2)	297.4(1)	252(5)	4.3(4)	2.9(2)
A_3 $C_{10}T_3$	250(20)	304.1(1)	160(10)	297.4(1)	500(40)	7.5(5)	1.5(2)

Numbers shown in the parenthesis are the standard deviations calculated from two or more sets of data (except for ΔH_{GNP} that was derived from the fit function using equation 3.2). Therefore, $\Delta H_{GNP} = 250(20)$ means 250 ± 20 kCal/mol and Δi = 2.9(2) denotes 2.9 ± 0.2.

3.3.1 Quantifying Cooperativity in $A_nC_7T_n$ Hairpin-Linked Aggregates

As described at length in Chapter 2, to quantify the extent of cooperativity as a function of $A_nC_mT_n$ length in the linker DNA hairpin, we determined the cooperative unit, equivalent to the number of duplexes that interact in the aggregate such that their dissociation equilibria are coupled, from the ratio of the enthalpy change for the GNP–DNA aggregates and the unmodified system.

$$N = \frac{\Delta H_{GNP}}{\Delta H_{uDNA}} \tag{3.3}$$

where N represents the cooperative number, and ΔH_{GNP} and ΔH_{uDNA} correspond to the dissociation of the GNP–DNA aggregates and unmodified DNA duplexes, respectively.[46, 66] Just as for the gap-linked system (Chapter 2), the value of ΔH_{GNP} was determined directly from the melting profiles according to the model of Schatz and Mirkin (using equation 3.2).[46] Details are described in section 2.3.2.2. The fit of equation 3.2 to the experimental data for the $A_6C_7T_6$ aggregate system is shown in Figure 3.6A, and the resulting ΔH values are given in Table 3.1 with the corresponding T_m values for the GNP–DNA hybridization mixtures in 0.5 M NaCl buffer (10 mM PBS, pH 7). Also described in that chapter, the ΔH for the unmodified three-strand system (ΔH_{uDNA}) was determined from the slope of $1/T_m$ versus ln [DNA] (Figure 3.6B), while the y-intercept and this ΔH_{uDNA} value were used to find ΔS_{uDNA} as described in section 2.3.2.1.[65] The data shown in Figure 3.6 is the average T_m from two separate samples and the error represents the range of values.

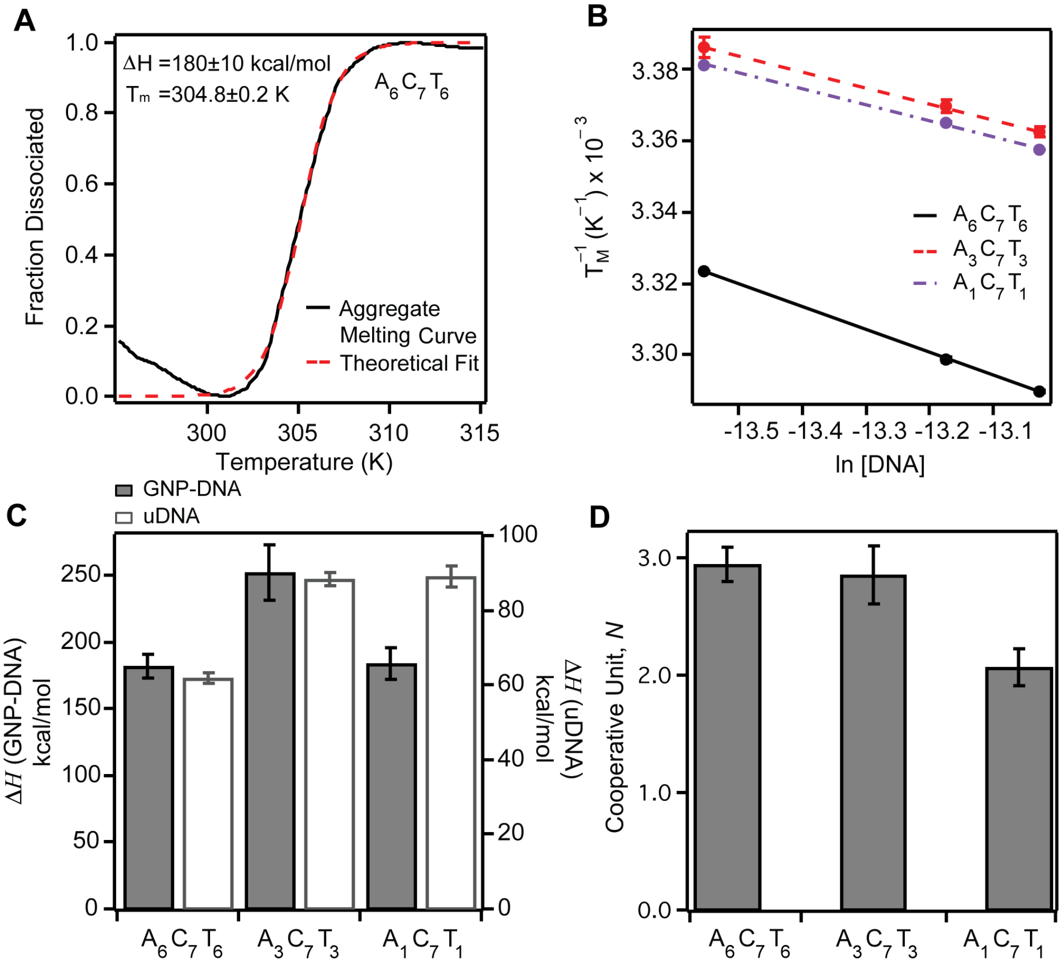

Figure 3.6. A.) The fraction of GNP–DNA dissociated as a function of temperature for the six A:T base paired stem on the hairpin linker, (where X = $A_6C_7T_6$). The theoretical fit is based on the work of Jin *et al*[46] (equation 3.2) and was used to determine ΔH. B.) Van't Hoff plots of T_m^{-1} versus natural log DNA concentration for unmodified hairpin linked DNA duplexes ranging from 1.3 μM to 2.2 μM where the size of the stem on the hairpin was varied from one to six A:T basepairs. C.) ΔH of dissociation as a function of stem length on the hairpin linker for the unmodified DNA (uDNA, left axis) and GNP–DNA (right axis). D.) Cooperative unit for hairpin linked GNP–DNA aggregates with varying stem size.

The thermodynamic values corresponding to the dissociation of GNP–DNA aggregates and the unmodified duplexes are presented in Table 3.1. A comparison of the ΔH values as a function of stem length ($A_nC_7T_n$; n = 1, 3, and 6) for the unmodified DNA and the GNP–DNA system is shown in Figure 3.6C. For the $A_nC_7T_n$-linked GNP–DNA aggregates, ΔH_{GNP} was highest for the $A_3C_7T_3$ system (ΔH_{A3C7T3} = 250 ± 20 kcal/mol) and lower for the systems with one and six A:T basepair stem on the hairpin (ΔH_{A1C7T1} = 190 ± 10 kcal/mol and ΔH_{A6C7T6} = 180 ± 10 kcal/mol). These results supported that an optimum size of the stem is crucial in the formation of hairpin-linked aggregates. Such behavior of these aggregates can be attributed to a balanced contribution of the bulkiness of the hairpin stem and the strength of the associated stem as the hairpin must form in the dense environment of the GNP–DNA aggregate. For the unmodified DNA, the $A_1C_7T_1$ system exhibited the highest ΔH_{uDNA} of dissociation, 89 ± 3 kcal/mol, but it was within the error of the value for the $A_3C_7T_3$ system (Figure 3.6C). The $A_6C_7T_6$ system, however, had the lowest ΔH_{uDNA} value compared with the other $A_nC_7T_n$ hairpin systems (62 ± 1 kcal/mol, Table 3.1). This decrease in dissociation enthalpy of the $A_6C_7T_6$ system suggested that the stem of this hairpin linker was already hybridized when exposed to the two complementary short probe sequences (Figure 3.7). Therefore, the number of hybridizing bases upon hybridization with the unmodified DNA for this hairpin strand was less than $A_3C_7T_3$ and $A_1C_7T_1$, which involved the hybridization of the stem while binding to the probes to form a three-strand duplex.

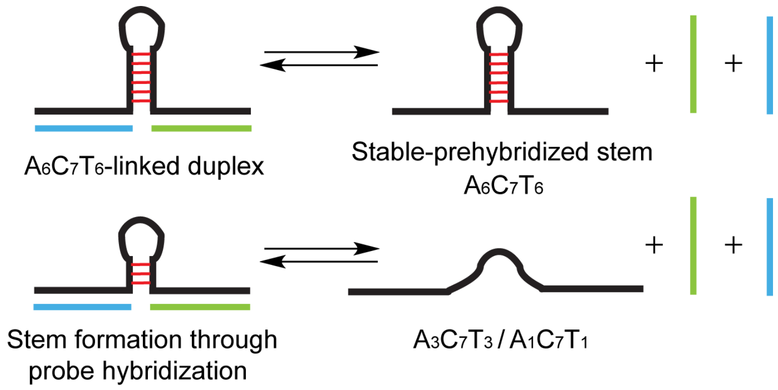

Figure 3.7. The lower dissociation ΔH for the six A:T basepairs stem on the $A_6C_7T_6$ based hairpin linker is indicative of more stable prehybridized stem in this hairpin. For $A_6C_7T_6$ and $A_6C_7T_6$ systems, the number of hybridizing bases were three and one A:T basepairs respectively. The higher ΔH and low number of basepairs on the stem in these hairpin linkers suggested that the stem hybridized during duplex formation with the short probe sequences.

3.3.2 Calculating the Cooperative Unit, N

Comparing the ΔH values for the two systems allowed us to determine *N* for each GNP–DNA system, where *N* is the number of DNA duplexes that melt cooperatively (equation 3.3). For the $A_1C_7T_1$ GNP–DNA system, the cooperative unit was 2.1 ± 0.2 duplexes indicating that the aggregated GNP–DNA contained on average two DNA strands cooperatively interacting with each other while holding the GNP–DNA probes in the aggregate network (Table 3.1). Such cooperative behavior can only arise with a high density of DNA on the nanoparticle surface. Upon increasing the stem size from A:T to $(A:T)_3$ and $(A:T)_6$ ($X = A_3C_7T_3$ and $A_6C_7T_6$, respectively) the cooperative number increased to 2.9 ± 0.2, which indicated that the flexible nature of the $A_1C_7T_1$ hairpin in the aggregate decreased cooperative interactions between the neighboring three-strand duplexes. These results suggested that cooperativity was very sensitive to perturbations of the duplex structure, which supported that the rigidity of the DNA duplexes was important to maintain cooperative interactions. Moreover, these results were surprising since we expected that increasing the bulkiness of the stem would reduce cooperativity in the aggregates because of steric effects. The similar cooperative number for $A_6C_7T_6$ and $A_3C_7T_3$ indicated, however, that cooperativity in these hairpin-linked aggregates was a compromise between the rigidity of the aggregate structure and the bulkiness of the hairpin linker. As discussed earlier in section 3.3, the proposed source of cooperativity is the sharing of a common ion cloud by multiple neighboring linker duplexes. Therefore, we anticipated that the amount of these condensed ions at the $A_nC_7T_n$ systems would also vary with increased number of A:T basepairs during dissociation of the adjacent duplexes.[69]

3.3.3 Determining the Number of Released Cations Upon Thermal Dissociation

The release of cations upon melting of a DNA duplex is illustrated schematically in Chapter 2. The number of released cations, Δi, can be determined from the melting profiles of the GNP–DNA aggregates at different NaCl concentrations (Figure 3.8B).[46, 70-71] Specifically, the slope of T_m versus ln [NaCl] can be related to the number of released cations Δi according to:

$$\frac{\mathrm{dT_m}}{\mathrm{d\,ln[NaCl]}} = \Delta i \frac{N\mathrm{RT_m^2}}{\Delta \mathrm{H}} \tag{3.4}$$

where T_m and ΔH_{GNP} correspond to the values at 0.5 M NaCl (Table 3.1).[46]

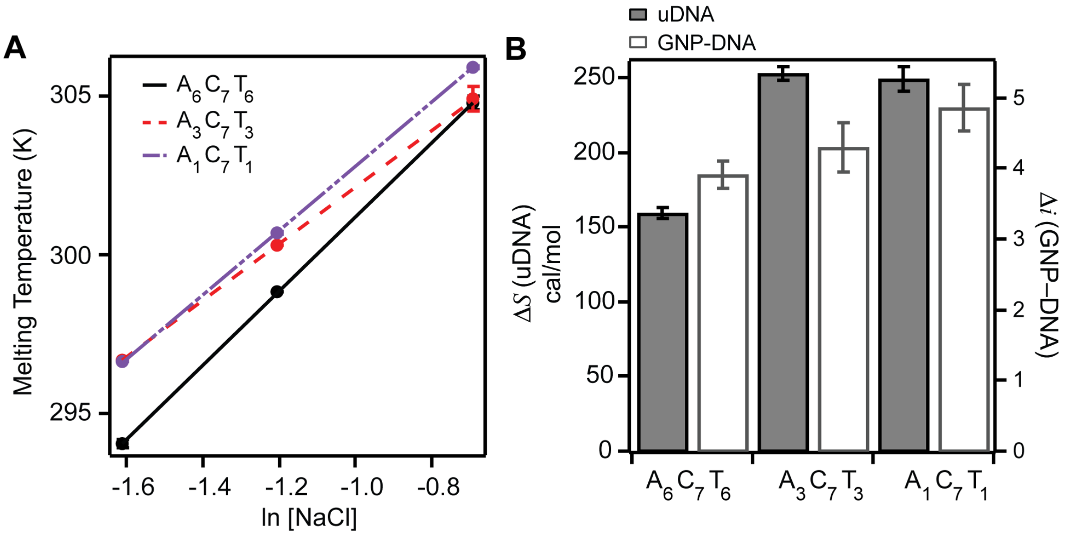

Figure 3.8. A.) The plot of T_m vs. ln [NaCl] for the GNP-DNA systems with varying stem size on the linker hairpin strand. The slopes of the linear fit to the data were used to determine the number of released cations per duplex dissociation. B.) ΔS of dissociation as a function of varying linker hairpin stem size for the GNP-DNA systems (ΔS_{uDNA}, left axis) and the number of released cations during the aggregate dissociation from each duplex melting ($\Delta i_{GNP\text{-}DNA}$ right axis).

The resulting values of Δi are included in Table 3.1. The $A_1C_7T_1$ GNP–DNA system recruited a higher number of cations during hybridization ($\Delta i = 4.9 \pm 0.3$) compared to the $A_3C_7T_3$ ($\Delta i = 4.3 \pm 0.4$) and $A_6C_7T_6$ ($\Delta i = 3.9 \pm 0.2$) systems. This further suggested that the $A_1C_7T_1$ and $A_3C_7T_3$ systems required to hybridize the hairpin linker stems while binding to the probe strands whereas in $A_6C_7T_6$ system the stem of the hairpin linker was already pre-hybridized. Although the differences in Δi in these systems were quite subtle within the error of the values, a smaller number for the $A_6C_7T_6$ system was expected in accordance with the maintenance of this stable A:T basepaired stem after dissociation of the aggregate. The trend in Δi and N were directly opposite of one another, indicating that the changes in cooperativity were not exclusively from changes in the ionic environment of the aggregate.

In our previous investigation on gap-linked aggregates, we proposed that an increased flux of ions manifested in Δi could be offset by a decrease in entropy upon forming the gap-linked duplexes (Chapter 2). Consequently, we compared the Δi values with ΔS of the unmodified DNA system determined from the y-intercepts of the van't Hoff plots, which were used to calculate the ΔH_{uDNA} values (Figure 3.8A). The resulting ΔS values were shown in table 3.1. The largest dissociation ΔS was measured for the $A_3C_7T_3$ system (252 ± 5 cal/mol·K) followed by $A_1C_7T_1$ (249 ± 8 cal/mol·K). The change in entropy in the $A_6C_7T_6$ GNP–DNA system was determined to be the lowest (159 ± 3 cal/mol·K) in this series. This again indicated that the change in disorder upon hybridizing the $A_6C_7T_6$ linker hairpin to the unmodified strands was much less compared to the $A_3C_7T_3$ and $A_1C_7T_1$ systems due to its prehybridized stem (Figure 3.7). Assuming the trend in ΔS for the unmodified system was the same for ΔS in the GNP–DNA aggregate, which we cannot measure, provides insight into the disagreement between Δi and N. As shown in Figure 3.8, ΔS and Δi follow a similar trend. This supports that the increased number of ions recruited by $A_1C_7T_1$ was compensated for by a large decrease in entropy upon association of the hairpin-linked GNP–DNA aggregate. Consequently, N does not follow the trend in Δi.

We note that the gap-linked systems also exhibited increased dissociation entropy with increased number of ions released, which could suggest that one source of the contribution to the lower entropy stemmed from the condensation of additional ions onto the duplex (Chapter 2).

3.4 Kinetics of Aggregates Containing $A_nC_7T_n$ Hairpin Linkers

In Chapter 2, we reported slower aggregation for flexible gap-linked systems and also observed that aggregation was inherently faster in the presence of a nicked site.[43] In this study, a nicked site is present in all the GNP-DNA aggregates but it lies adjacent to a hairpin. We compared the aggregation rate for the hairpin linkers of different stem lengths and found that the $A_3C_7T_3$ and $A_1C_7T_1$ systems aggregation rates were quite competitive, whereas that of the $A_6C_7T_6$ system was much slower than its shorter versions (Figure 3.9A). Specifically, we observed after 12 hours $A_3C_7T_3$ and $A_1C_7T_1$ reached 80% hybridization based on the relative absorbance changes whereas that of the $A_6C_7T_6$ was only 30% within that time frame. We expected a more rigid structure at the nicked site would impart faster kinetics compared to more flexible counterparts. These results indicated that the presence of a nicked site is important for faster kinetics, but a bulky rigid structure at the nicked site (i.e., a long stem) can significantly reduce the aggregation kinetics.

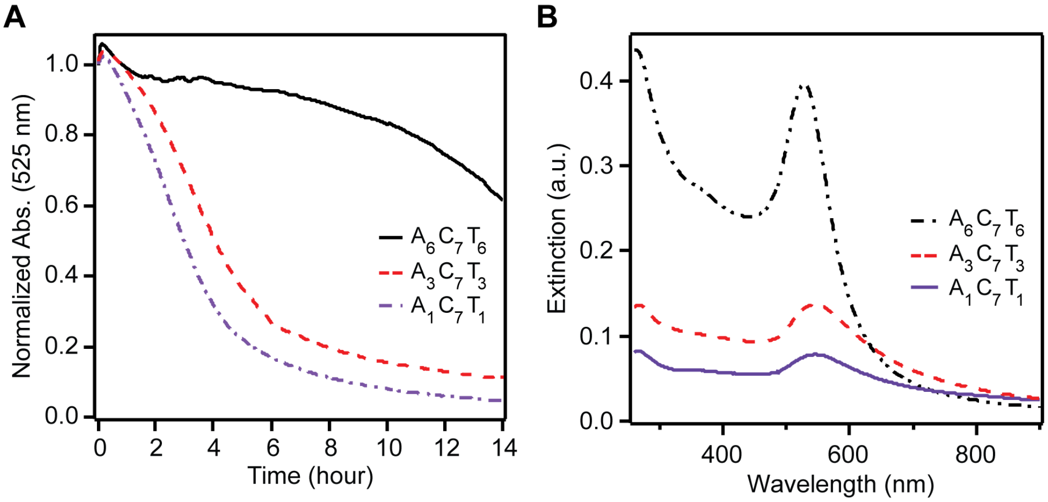

Figure 3.9. A.) Kinetic profile for GNP–DNA aggregate formation. The plots were obtained by taking an absorption spectrum every 30 seconds for 14 hours and plotting the absorption maximum (525 nm) with respect to time. The kinetics of hybridizing were greatly slowed when the stem size was longer than three AT base pairs. B.) Absorption spectra of GNP-DNA aggregates with varying linker hairpin stem size after 16 hours. The absorbance is inversely proportional to the size of aggregates formed. Larger aggregates were formed with smaller stems of the linker hairpin also in agreement with their corresponding kinetic profiles.

3.5 Thermodynamics of Aggregates Containing $A_3C_mT_3$ Loop Size Linkers

3.5.1 Thermal Denaturation Profile Analysis

Thus far, we have found that the stem size greatly impacts the cooperativity of the aggregate and the rate of its association as well as the thermal stability of the aggregate but to a lesser extent. We next performed the same kind of thermodynamic and kinetic analysis on hairpin-linked aggregates with varying loop size by varying the length of the polydeoxycytidine loop. Figure 3.10A illustrates the corresponding thermal dissociation observed from the change in absorbance at 525 nm as a hybridized mixture of complementary GNP–DNA and linker DNA hairpins with varying loop sequences ($X = A_3C_mT_3$, where m = 4, 7, and 10) was heated (1.5 nM and 60 nM of GNP–DNA and linker, respectively, in 0.5 M NaCl, 10 mM PBS). Figure 3.10B shows the thermal dissociation of the corresponding unmodified DNA duplex dissociation curves. The melting temperatures, T_m, as shown in Figure 3.10C, were higher for the GNP-DNA aggregates compared to the unmodified DNA duplexes. Unlike the stem-variation experiments, the thermal stability of all the unmodified duplexes was very similar whereas that of the nanoparticle versions showed a monotonic decrease with the size of the loop. For $A_3C_4T_3$ (the shortest loop on the linker DNA hairpin), the melting temperature was 305.4 ± 0.1 K (Figure 3.10C). Upon adding three more cytidine bases on the loop of the DNA hairpin (resulting in the $A_3C_7T_3$ system), the T_m became lower than that of the $A_3C_4T_3$ system (Figure 3.5C, $T_{m,\ A3C7T3}$ = 304.9 ± 0.1 K). As the number of cytidine bases in the loop sequence was increased to ten (that resulted in the $A_3C_{10}T_3$ system), we observed a further decrease in thermal stability compared to the other loop systems (Table 3.1, Figure 3.10C, $T_{m,\ A3C10T3}$ = 304.1 ± 0.1 K). Such dependence of T_m on the loop size has been reported previously for hairpin dissociation.[72] Therefore, we attribute the lower thermal stability of the three-strand duplex in the $A_3C_{10}T_3$ system to the flexibility of the long hairpin. This decreased thermal stability due to flexible DNA structure was also reported for DNA gap-linked assemblies,[43] which was discussed in Chapter 2 of this thesis. Once again, in comparison to the

GNP-DNA melting transitions, the unmodified DNA complexes of the same sequence exhibited a broad transition over more than 10–20 °C (Figure 3.10B).

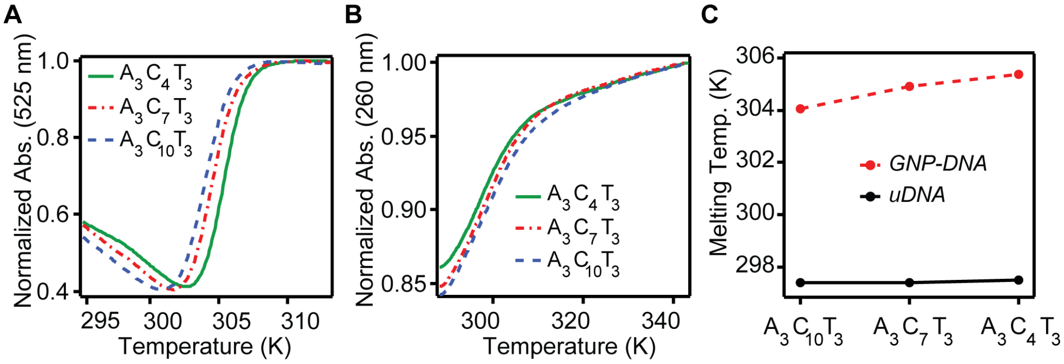

Figure 3.10. A.) Melting profiles of the GNP–DNA three-strand duplex system with varying length of the loop in the hairpin linker. B.) Melting profiles of the unmodified three-strand duplex system with varying length of the loop on the hairpin linker strand. C.) Thermal denaturation temperature of the GNP-DNA aggregates with varying loop size on the linker hairpin strands and the corresponding unmodified three–strand duplex system.

In contrast, the unmodified DNA system demonstrated very similar thermal stability in the corresponding duplexes, indicating that the aggregate highly influenced the thermal stability (Figure 3.10C). The thermodynamic analysis below will reveal the competing changes in ΔS and ΔH that resulted in similar thermal stabilities for the unmodified system. Consistent with previous results, the GNP–DNA aggregates also exhibited greater T_m values than the analogous unmodified duplex, despite the higher DNA concentration for the unmodified DNA experiment.[67]

3.5.2 ΔH of GNP–DNA Aggregates and Unmodified Duplexes

The thermodynamic values corresponding to the dissociation of hairpin-linked GNP–DNA aggregates and the unmodified duplexes are presented in Table 3.1, and a comparison of the ΔH values for the unmodified DNA and GNP–DNA systems with varying loop size is shown in Figure 3.12C. For the $A_3C_mT_3$ GNP–DNA aggregates, ΔH_{GNP} was highest for the $A_3C_4T_3$ system (ΔH_{A3C4T3} = 290 ± 30) kcal/mol), and lower identical values were determined for the systems with 7 and 10 deoxycytidine loops on the hairpin (ΔH_{A3C7T3} = 250 ± 20 kcal/mol and $\Delta H_{A3C10T3}$ = 250 ± 20 kcal/mol). These results indicated that the change in enthalpy for the aggregate dissociation was directly proportional to the rigidness of the loop on the linker DNA hairpin. Therefore, the hairpin loop has a large effect on the formation and stability of the associated GNP–DNA assemblies. For the unmodified DNA, the trend in the ΔH was completely opposite to that of the GNP–DNA versions (Figure 3.12C). The $A_3C_{10}T_3$ system exhibited the highest ΔH_{uDNA} of dissociation, 160 ± 10 kcal/mol, which was almost twice the value for $A_3C_7T_3$ and $A_3C_4T_3$ (ΔH_{A3C7T3} = 88 ±2 kcal/mol and ΔH_{A3C4T3} = 87 ± 2 kcal/mol). The smaller ΔH for the $A_3C_4T_3$ can be attributed to the rigid structure of the shorter looped hairpin linker. We attribute the largest dissociation ΔH for the $A_3C_{10}T_3$ system to its more flexible loop that in turn stabilized the stem better in the hairpin. The decreased ΔH for the $A_3C_7T_3$ and $A_3C_4T_3$ systems were possibly due to the presence of high strain in the hairpins that did not lead to stable and complete A:T basepair formation in their respective stems (Figure 3.11).

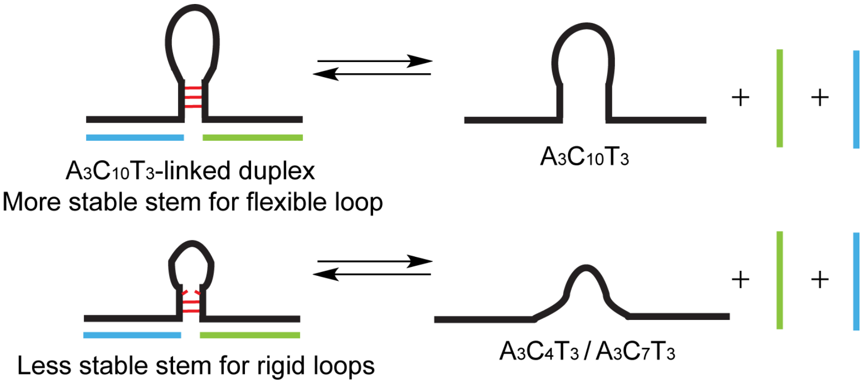

Figure 3.11. The lower dissociation ΔH for the 4 and 7 deoxycytidine loop on the $A_3C_4T_3$ and $A_3C_7T_3$ based hairpin linkers is indicative of less stable stem formation in these hairpins. For $A_3C_{10}T_3$ system, the ten deoxycitidine loop was flexible enough to stabilize A:T basepairs on the stem and was reflected in its higher ΔH value.

3.5.3 Calculating the Cooperative Unit N

Comparing the ΔH values for the two systems allowed us to determine N for each GNP–DNA system, where N is the number of DNA duplexes that melt cooperatively (equation 3.2). For the $A_3C_{10}T_3$ GNP–DNA system, the cooperative unit was determined to be 1.5 ± 0.2 (Figure 3.12D, Table 3.1), whereas that of the $A_3C_4T_3$ aggregate system was 3.3 ± 0.4 (Figure 3.12D). The cooperative number for the $A_3C_7T_3$ system was found to be 2.9 ± 0.2 (Figure 3.12D). Such a two-fold decrease in cooperativity upon approximately doubling the loop length indicated an indirect relationship of cooperative number with the loop length. More specifically, decrease in cooperative number with increasing loop length suggested that the largest, floppiest loop disrupted neighboring duplex interactions. The proposed source of cooperativity, sharing of the common cation cloud, is dependent on the condensed ions recruited during a hybridization event.[46, 69] So once again we focused on determining the number of cations released during dissociation for the hairpin-linked systems as a function of loop length.

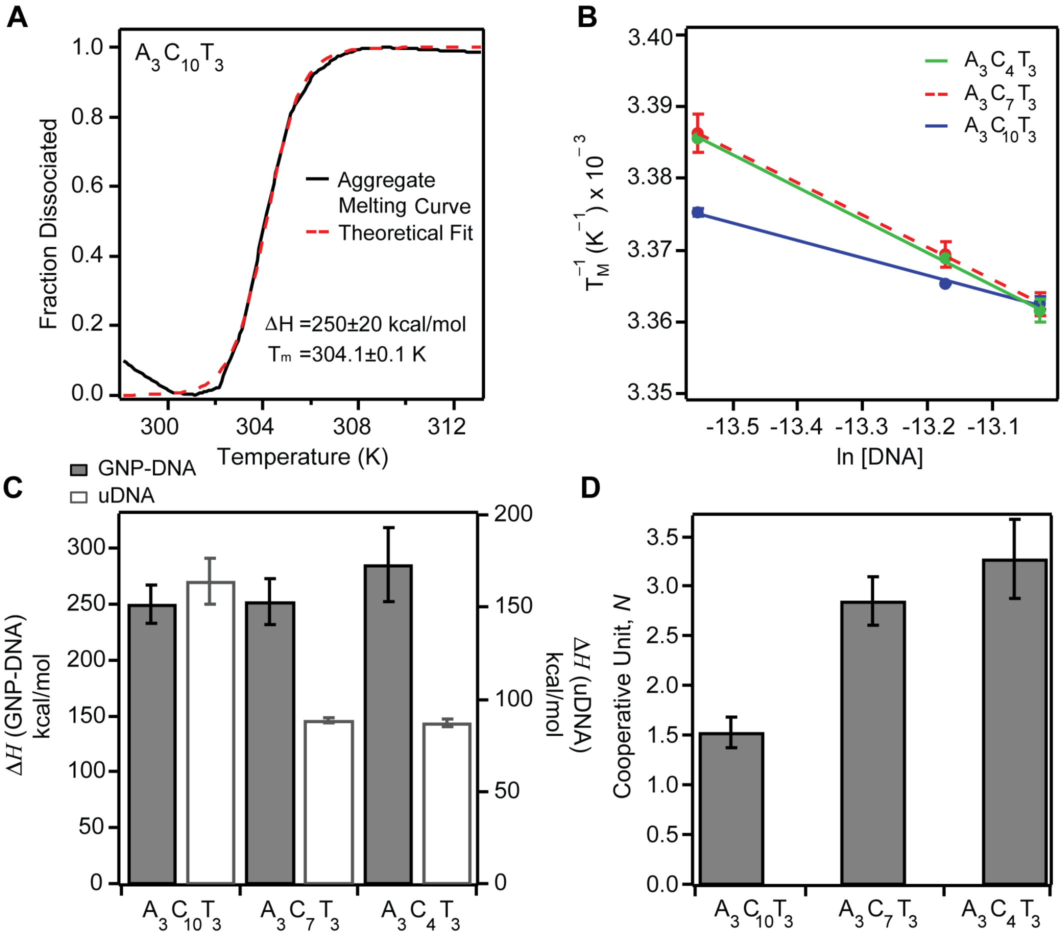

Figure 3.12. A.) The fraction of GNP–DNA dissociated as a function of temperature for the ten deoxycytidine loop on the linker hairpin system, (where X = $A_3C_{10}T_3$). The theoretical fit is based on Jin *et al.*[46] (equation 3.2) and was used to determine ΔH and T_m. B.) Van’t Hoff plots of T_m^{-1} versus natural log DNA concentration for unmodified hairpin linked DNA duplexes mixtures ranging from 1.3 µM to 2.2 µM where the size of the loop on the hairpin was varied from 4 to

10 deoxycytidine bases. C.) Δ*H* of dissociation as a function of loop size on the hairpin linker for the unmodified DNA (*uDNA*, left axis) and GNP–DNA (right axis). D.) Cooperative unit for hairpin linked GNP–DNA aggregates with varying loop size.

3.5.4 Determining the Number of Released Cations Upon Thermal Dissociation

Figure 3.13 exhibits the measured values of Δ*i* from the $A_3C_mT_3$ GNP–DNA aggregate dissociation experiments and the ΔS of the corresponding unmodified DNA duplexes. Like the stem length variation study, we observed a strong correlation between the Δ*i* of the aggregates and the ΔS of the unmodified DNA duplexes. The $A_3C_{10}T_3$ GNP–DNA system recruited the highest number of cations during hybridization (Δ*i* = 7.5 ± 0.5) within this $A_3C_mT_3$ series. The ion recruitment by $A_3C_7T_3$ (Δ*i* = 4.3 ± 0.4) and $A_3C_4T_3$ (Δ*i* = 4.0 ± 0.5) systems indicated that such change in Δ*i* was directly proportional to the size of the loop. An increased number of ions recruited by the $A_3C_mT_3$ systems was also compensated for by a large increase in their ΔS. The largest ΔS was measured for the $A_3C_{10}T_3$ system (500 ± 40 cal/mol·K), which we attribute to the decreased conformational entropy of a long loop as well as the increased number of condensed cations. The Δ*S* for $A_3C_7T_3$ and $A_3C_4T_3$ systems were 252 ± 5 cal/mol·K and 248 ± 7 cal/mol·K, which suggested that the influence of cation condensation on ΔS was more significant than the loop size.

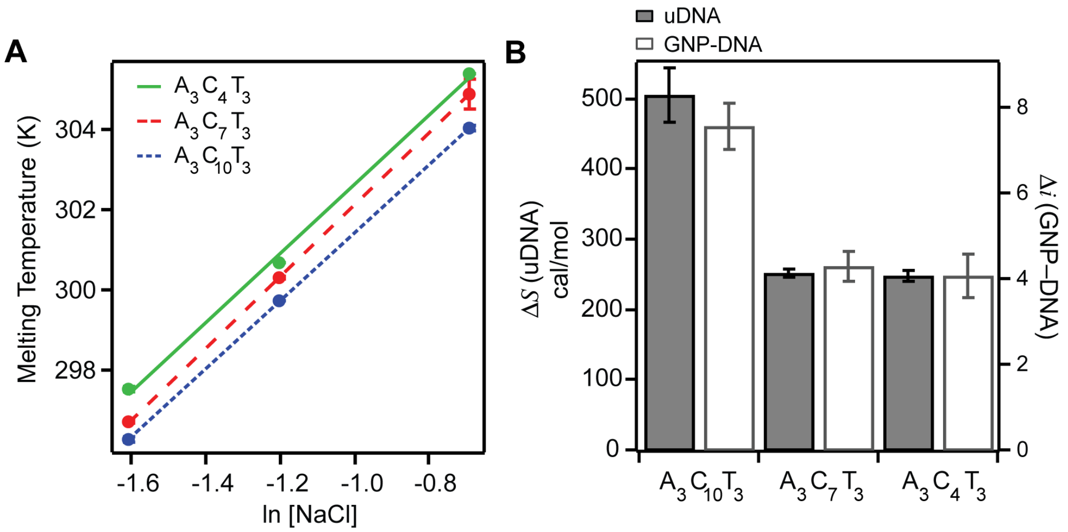

Figure 3.13. A.) Plot of T_m vs. ln [NaCl] for the GNP–DNA systems with varying loop size on the linker hairpin strand. The slopes of these plots were used to determine the number of released cations per duplex dissociation. B.) ΔS of dissociation as a function of varying linker hairpin loop size for the GNP–DNA systems (ΔS_{uDNA}, left axis) and the number of released cations during the aggregate dissociation from each duplex melting ($\Delta i_{GNP\text{-}DNA}$ right axis).

3.6 Kinetics of Aggregates Containing $A_3C_mT_3$ Hairpin Linkers

Aggregation kinetics of $A_3C_mT_3$ hairpin linked GNP–DNA conjugates showed a stark difference in the rate of hybridization when the length of the loop in the hairpin linker is varied particularly to long loop sequences. The $A_3C_{10}T_3$ hairpin system aggregation rate was much slower than its shorter versions, $A_3C_4T_3$ and $A_3C_7T_3$ (Figure 3.14A). However, the difference between the $A_3C_4T_3$ and $A_3C_7T_3$ hybridization rates was not observed, as they were very similar. After 12 hours of aggregation, we observed that the $A_3C_4T_3$ and $A_3C_7T_3$ systems reached 80% hybridization based on the relative absorbance changes whereas that of the $A_3C_{10}T_3$ was only 50% within that time frame. These results indicated a bulky flexible loop can significantly reduce the aggregation kinetics, consistent with the slow kinetics observed for large single-stranded gaps in Chapter 2.

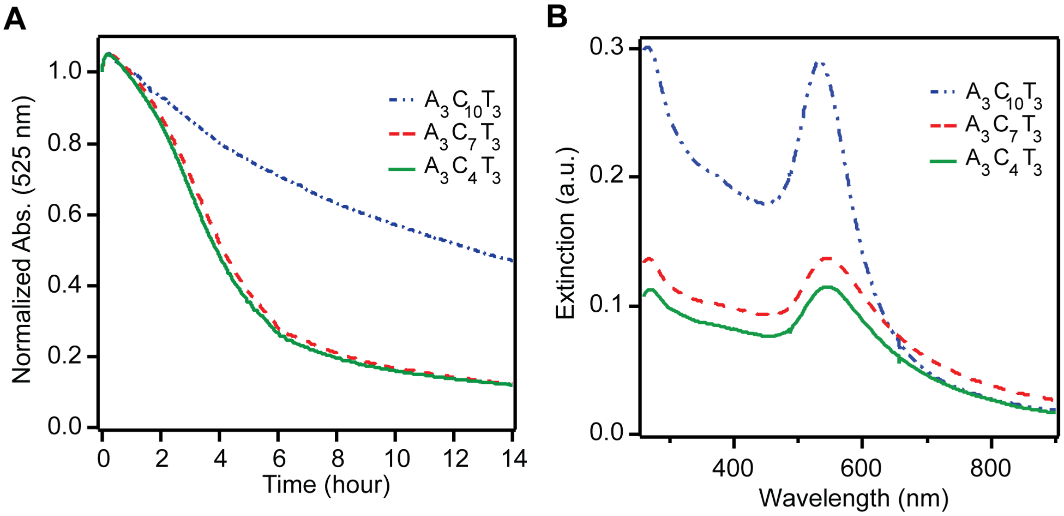

Figure 3.14. A.) Kinetic profile for GNP–DNA aggregate formation. The plots were obtained by taking absorption spectrum every 30 seconds for 14 hours and plotting the absorption maximum (525 nm) with respect to time. Figure shows significantly slow kinetics when the loop size was longer than seven deoxycytidine bases. B.) Absorption spectra of GNP-DNA aggregates with varying linker hairpin loop size after 16 hours. The absorbance was proportional to the size of aggregates formed. Larger aggregates were formed when the loop length of the linker hairpin decreased, consistent with their corresponding kinetic profiles.

3.7 Conclusions

In this chapter, we have systematically studied the effect of DNA hairpin loop and stem size on the thermodynamic, kinetic and cooperative properties of GNP–DNA aggregates. We found that the presence of a rigid stem or a flexible loop can significantly change the thermodynamic, kinetic and cooperative behavior of DNA–linked gold nanoparticles assemblies. Increasing the size of the stem had a positive impact on the cooperativity and a slight negative impact on the thermal stability of the GNP-DNA assemblies. For the length of the loop, the trend was completely opposite; the systems with smaller loops contributed to higher cooperative numbers. The salt dependent behavior of these hairpin-linked aggregates had a direct relationship with the change in entropy of their unmodified analogs. Such a relationship indicated that the recruitment of a larger number of cations resulted in larger decreases in entropy; in other words the cations recruitment was achieved at the cost of the corresponding entropy of the hybridized system. Finally, we observed that both larger stems and loops slowed down the aggregation process. The former results were surprising for the longer stem sequence, as a more stable stem was expected to enhance the aggregation kinetics by stabilizing the nicked site.

3.7 References

1. Niemeyer, C. M.; Simon, U., DNA-Based Assembly of Metal Nanoparticles. *European Journal of Inorganic Chemistry* **2005,** *2005* (18), 3641-3655.

2. Rosi, N. L.; Mirkin, C. A., Nanostructures in Biodiagnostics. *Chemical Reviews* **2005,** *105* (4), 1547-1562.

3. Giljohann, D. A.; Seferos, D. S.; Patel, P. C.; Millstone, J. E.; Rosi, N. L.; Mirkin, C. A., Oligonucleotide loading determines cellular uptake of DNA-modified gold nanoparticles. *Nano Letters* **2007,** *7* (12), 3818-3821.

4. Chiu, T.-C.; Huang, C.-C., Aptamer-Functionalized Nano-Biosensors. *Sensors* **2009,** *9* (12), 10356-10388.

5. Giljohann, D. A.; Seferos, D. S.; Daniel, W. L.; Massich, M. D.; Patel, P. C.; Mirkin, C. A., Gold Nanoparticles for Biology and Medicine. *Angewandte Chemie International Edition* **2010,** *49* (19), 3280-3294.

6. Taton, T. A.; Mirkin, C. A.; Letsinger, R. L., Scanometric DNA Array Detection with Nanoparticle Probes. *Science* **2000,** *289* (5485), 1757-1760.

7. Zhao, W.; Brook, M. A.; Li, Y., Design of Gold Nanoparticle-Based Colorimetric Biosensing Assays. *ChemBioChem* **2008,** *9* (15), 2363-2371.

8. Lee, J. S.; Ulmann, P. A.; Han, M. S.; Mirkin, C. A., A DNA-gold nanoparticle-based colorimetric competition assay for the detection of cysteine. *Nano Letters* **2008,** *8* (2), 529-533.

9. Han, M. S.; Lytton-Jean, A. K. R.; Mirkin, C. A., A Gold Nanoparticle Based Approach for Screening Triplex DNA Binders. *Journal of the American Chemical Society* **2006,** *128* (15), 4954-4955.

10. Han, M. S.; Lytton-Jean, A. K. R.; Oh, B.-K.; Heo, J.; Mirkin, C. A., Colorimetric Screening of DNA-Binding Molecules with Gold Nanoparticle Probes. *Angewandte Chemie* **2006,** *118* (11), 1839-1842.

11. Hurst, S. J.; Han, M. S.; Lytton-Jean, A. K. R.; Mirkin, C. A., Screening the Sequence Selectivity of DNA-Binding Molecules Using a Gold Nanoparticle-Based Colorimetric Approach. *Analytical Chemistry* **2007,** *79* (18), 7201-7205.

12. Thanh, N. T. K.; Rosenzweig, Z., Development of an Aggregation-Based Immunoassay for Anti-Protein A Using Gold Nanoparticles. *Analytical Chemistry* **2002,** *74* (7), 1624-1628.

13. Zhang, J.; Wang, L.; Pan, D.; Song, S.; Boey, F. Y. C.; Zhang, H.; Fan, C., Visual Cocaine Detection with Gold Nanoparticles and Rationally Engineered Aptamer Structures. *Small* **2008,** *4* (8), 1196-1200.

14. Liu, J.; Lu, Y., Fast Colorimetric Sensing of Adenosine and Cocaine Based on a General Sensor Design Involving Aptamers and Nanoparticles. *Angewandte Chemie International Edition* **2006,** *45* (1), 90-94.

15. Li, W.; Feng, L.; Ren, J.; Wu, L.; Qu, X., Visual Detection of Glucose Using Conformational Switch of i-Motif DNA and Non-Crosslinking Gold Nanoparticles. *Chemistry – A European Journal* **2012,** *18* (40), 12637-12642.

16. Hone, D. C.; Haines, A. H.; Russell, D. A., Rapid, Quantitative Colorimetric Detection of a Lectin Using Mannose-Stabilized Gold Nanoparticles. *Langmuir* **2003,** *19* (17), 7141-7144.

17. Otsuka, H.; Akiyama, Y.; Nagasaki, Y.; Kataoka, K., Quantitative and Reversible Lectin-Induced Association of Gold Nanoparticles Modified with α-

Lactosyl-ω-mercapto-poly(ethylene glycol). *Journal of the American Chemical Society* **2001,** *123* (34), 8226-8230.

18. Pavlov, V.; Xiao, Y.; Shlyahovsky, B.; Willner, I., Aptamer-Functionalized Au Nanoparticles for the Amplified Optical Detection of Thrombin. *Journal of the American Chemical Society* **2004,** *126* (38), 11768-11769.

19. Nam, J.-M.; Wise, A. R.; Groves, J. T., Colorimetric Bio-Barcode Amplification Assay for Cytokines. *Analytical Chemistry* **2005,** *77* (21), 6985-6988.

20. Sudeep, P. K.; Joseph, S. T. S.; Thomas, K. G., Selective Detection of Cysteine and Glutathione Using Gold Nanorods. *Journal of the American Chemical Society* **2005,** *127* (18), 6516-6517.

21. Wu, P.; Hwang, K.; Lan, T.; Lu, Y., A DNAzyme-Gold Nanoparticle Probe for Uranyl Ion in Living Cells. *Journal of the American Chemical Society* **2013,** *135* (14), 5254-5257.

22. Xue, X.; Wang, F.; Liu, X., One-Step, Room Temperature, Colorimetric Detection of Mercury (Hg^{2+}) Using DNA/Nanoparticle Conjugates. *Journal of the American Chemical Society* **2008,** *130* (11), 3244-3245.

23. Lee, J.-S.; Han, M. S.; Mirkin, C. A., Colorimetric Detection of Mercuric Ion (Hg^{2+}) in Aqueous Media using DNA-Functionalized Gold Nanoparticles. *Angewandte Chemie* **2007,** *119* (22), 4171-4174.

24. Chung, C. H.; Kim, J. H.; Jung, J.; Chung, B. H., Nuclease-resistant DNA aptamer on gold nanoparticles for the simultaneous detection of Pb^{2+} and Hg^{2+} in human serum. *Biosensors and Bioelectronics* **2013,** *41* (0), 827-832.

25. Kim, Y.; Johnson, R. C.; Hupp, J. T., Gold Nanoparticle-Based Sensing of "Spectroscopically Silent" Heavy Metal Ions. *Nano Letters* **2001,** *1* (4), 165-167.

26. Liu, J.; Lu, Y., A Colorimetric Lead Biosensor Using DNAzyme-Directed Assembly of Gold Nanoparticles. *Journal of the American Chemical Society* **2003,** *125* (22), 6642-6643.

27. Liu, J.; Lu, Y., Accelerated Color Change of Gold Nanoparticles Assembled by DNAzymes for Simple and Fast Colorimetric $Pb2^+$ Detection. *Journal of the American Chemical Society* **2004,** *126* (39), 12298-12305.

28. Wang, Z.; Lee, J. H.; Lu, Y., Label-Free Colorimetric Detection of Lead Ions with a Nanomolar Detection Limit and Tunable Dynamic Range by using Gold Nanoparticles and DNAzyme. *Advanced Materials* **2008,** *20* (17), 3263-3267.

29. Zhao, W.; Chiuman, W.; Lam, J. C. F.; McManus, S. A.; Chen, W.; Cui, Y.; Pelton, R.; Brook, M. A.; Li, Y., DNA Aptamer Folding on Gold Nanoparticles: From Colloid Chemistry to Biosensors. *Journal of the American Chemical Society* **2008,** *130* (11), 3610-3618.

30. Huang, Y.-F.; Chang, H.-T., Analysis of Adenosine Triphosphate and Glutathione through Gold Nanoparticles Assisted Laser Desorption/Ionization Mass Spectrometry. *Analytical Chemistry* **2007,** *79* (13), 4852-4859.

31. Wang, Z.; Sun, N.; He, Y.; Liu, Y.; Li, J., DNA Assembled Gold Nanoparticles Polymeric Network Blocks Modular Highly Sensitive Electrochemical Biosensors for Protein Kinase Activity Analysis and Inhibition. *Analytical Chemistry* **2014**.

32. Song, G.; Chen, C.; Ren, J.; Qu, X., A Simple, Universal Colorimetric Assay for Endonuclease/Methyltransferase Activity and Inhibition Based on an Enzyme-Responsive Nanoparticle System. *ACS Nano* **2009,** *3* (5), 1183-1189.

33. Zhao, W.; Lam, J. C. F.; Chiuman, W.; Brook, M. A.; Li, Y., Enzymatic Cleavage of Nucleic Acids on Gold Nanoparticles: A Generic Platform for Facile Colorimetric Biosensors. *Small* **2008,** *4* (6), 810-816.

34. Wang, C.; Chen, Y.; Wang, T.; Ma, Z.; Su, Z., Biorecognition-Driven Self-Assembly of Gold Nanorods: A Rapid and Sensitive Approach toward Antibody Sensing. *Chemistry of Materials* **2007,** *19* (24), 5809-5811.

35. Beissenhirtz, M. K.; Elnathan, R.; Weizmann, Y.; Willner, I., The Aggregation of Au Nanoparticles by an Autonomous DNA Machine Detects Viruses. *Small* **2007,** *3* (3), 375-379.

36. Souza, G. R.; Christianson, D. R.; Staquicini, F. I.; Ozawa, M. G.; Snyder, E. Y.; Sidman, R. L.; Miller, J. H.; Arap, W.; Pasqualini, R., Networks of gold nanoparticles and bacteriophage as biological sensors and cell-targeting agents. *Proceedings of the National Academy of Sciences of the United States of America* **2006,** *103* (5), 1215-1220.

37. Schofield, C. L.; Field, R. A.; Russell, D. A., Glyconanoparticles for the Colorimetric Detection of Cholera Toxin. *Analytical Chemistry* **2007,** *79* (4), 1356-1361.

38. Medley, C. D.; Smith, J. E.; Tang, Z.; Wu, Y.; Bamrungsap, S.; Tan, W., Gold Nanoparticle-Based Colorimetric Assay for the Direct Detection of Cancerous Cells. *Analytical Chemistry* **2008,** *80* (4), 1067-1072.

39. Huang, C.-C.; Huang, Y.-F.; Cao, Z.; Tan, W.; Chang, H.-T., Aptamer-Modified Gold Nanoparticles for Colorimetric Determination of Platelet-Derived Growth Factors and Their Receptors. *Analytical Chemistry* **2005,** *77* (17), 5735-5741.

40. Wu, Z.-S.; Lu, H.; Liu, X.; Hu, R.; Zhou, H.; Shen, G.; Yu, R.-Q., Inhibitory Effect of Target Binding on Hairpin Aptamer Sticky-End Pairing-Induced Gold Nanoparticle Assembly for Light-up Colorimetric Protein Assay. *Analytical Chemistry* **2010,** *82* (9), 3890-3898.

41. Dubertret, B.; Calame, M.; Libchaber, A. J., Single-mismatch detection using gold-quenched fluorescent oligonucleotides. *Nature Biotechnology* **2001,** *19* (4), 365-370.

42. Harry, S. R.; Hicks, D. J.; Amiri, K. I.; Wright, D. W., Hairpin DNA coated gold nanoparticles as intracellular mRNA probes for the detection of tyrosinase gene expression in melanoma cells. *Chemical Communications* **2010,** *46* (30), 5557-5559.

43. Sikder, M. D. H.; Gibbs-Davis, J. M., The Influence of Gap Length on Cooperativity and Rate of Association in DNA-Modified Gold Nanoparticle Aggregates. *The Journal of Physical Chemistry C* **2012,** *116* (21), 11694-11701.

44. Elghanian, R. J. J., Selective colorimetric detection of polynucleotides based on the distance-dependent optical properti. *Science* **1997,** *277* (5329), 1078.

45. Mucic, R. C.; Storhoff, J. J.; Mirkin, C. A.; Letsinger, R. L., DNA-Directed Synthesis of Binary Nanoparticle Network Materials. *Journal of the American Chemical Society* **1998,** *120* (48), 12674-12675.

46. Jin, R.; Wu, G.; Li, Z.; Mirkin, C. A.; Schatz, G. C., What Controls the Melting Properties of DNA-Linked Gold Nanoparticle Assemblies? *Journal of the American Chemical Society* **2003,** *125* (6), 1643-1654.

47. Sidhaye, D. S.; Kashyap, S.; Sastry, M.; Hotha, S.; Prasad, B. L. V., Gold Nanoparticle Networks with Photoresponsive Interparticle Spacings. *Langmuir* **2005,** *21* (17), 7979-7984.

48. Seela, F.; Budow, S., pH-Dependent Assembly of DNA–Gold Nanoparticles Based on the i-Motif: A Switchable Device with the Potential of a Nanomachine. *Helvetica Chimica Acta* **2006,** *89* (9), 1978-1985.

49. Liu, J.; Lu, Y., Stimuli-Responsive Disassembly of Nanoparticle Aggregates for Light-Up Colorimetric Sensing. *Journal of the American Chemical Society* **2005,** *127* (36), 12677-12683.

50. Long, H.; Kudlay, A.; Schatz, G. C., Molecular Dynamics Studies of Ion Distributions for DNA Duplexes and DNA Clusters: Salt Effects and Connection to DNA Melting. *The Journal of Physical Chemistry B* **2006,** *110* (6), 2918-2926.

51. Park, S. Y.; Gibbs-Davis, J. M.; Nguyen, S. T.; Schatz, G. C., Sharp Melting in DNA-Linked Nanostructure Systems: Thermodynamic Models of DNA-Linked Polymers. *The Journal of Physical Chemistry B* **2007,** *111* (30), 8785-8791.

52. Kudlay, A.; Gibbs, J. M.; Schatz, G. C.; Nguyen, S. T.; Olvera de la Cruz, M., Sharp Melting of Polymer−DNA Hybrids: An Associative Phase Separation Approach. *The Journal of Physical Chemistry B* **2007,** *111* (7), 1610-1619.

53. Harris, N. C.; Kiang, C.-H., Defects Can Increase the Melting Temperature of DNA−Nanoparticle Assemblies. *The Journal of Physical Chemistry B* **2006,** *110* (33), 16393-16396.

54. Y. Paul Bao, M. H., Tai-Fen Wei, Sudhakar S. Marla, James J. Storhoff, and Uwe R. Müller, SNP identification in unamplified human genomic DNA with gold nanoparticle probes. *Nucleic Acids Research* **2005,** *33(2).*

55. Smith, B. D.; Dave, N.; Huang, P.-J. J.; Liu, J., Assembly of DNA-Functionalized Gold Nanoparticles with Gaps and Overhangs in Linker DNA. *The Journal of Physical Chemistry C* **2011,** *115* (16), 7851-7857.

56. Li, J.; Fu, H.-E.; Wu, L.-J.; Zheng, A.-X.; Chen, G.-N.; Yang, H.-H., General Colorimetric Detection of Proteins and Small Molecules Based on Cyclic Enzymatic Signal Amplification and Hairpin Aptamer Probe. *Analytical Chemistry* **2012,** *84* (12), 5309-5315.

57. Xiang, S.; Fruehauf, J.; Li, C. J., Short hairpin RNA-expressing bacteria elicit RNA interference in mammals. *Nature Biotechnology* **2006,** *24* (6), 697-702.

58. Davison, A.; Leach, D. R. F., Two-base DNA hairpin-loop structures in vivo. *Nucleic Acids Research* **1994,** *22* (21), 4361-4363.

59. Rentzeperis, D.; Alessi, K.; Marky, L. A., Thermodynamics of DNA hairpins: Contribution of loop size to hairpin stability and ethidium binding. *Nucleic Acids Research* **1993,** *21* (11), 2683-2689.

60. Hurst, S. J.; Lytton-Jean, A. K. R.; Mirkin, C. A., Maximizing DNA Loading on a Range of Gold Nanoparticle Sizes. *Analytical Chemistry* **2006,** *78* (24), 8313-8318.

61. Grabar, K. C.; Freeman, R. G.; Hommer, M. B.; Natan, M. J., Preparation and Characterization of Au Colloid Monolayers. *Analytical Chemistry* **1995,** *67* (4), 735-743.

62. Lai, Y.-J.; Tseng, W.-L., Role of 5-thio-(2-nitrobenzoic acid)-capped gold nanoparticles in the sensing of chromium(vi): remover and sensor. *Analyst* **2011,** *136* (13), 2712-2717.

63. Stoeva, S. I.; Lee, J.-S.; Thaxton, C. S.; Mirkin, C. A., Multiplexed DNA Detection with Biobarcoded Nanoparticle Probes. *Angewandte Chemie International Edition* **2006,** *45* (20), 3303-3306.

64. Kibbe, W. A., OligoCalc: an online oligonucleotide properties calculator. *Nucleic Acids Research* **2007,** *35* (suppl 2), W43-W46.

65. Marky, L. A.; Breslauer, K. J., Calculating thermodynamic data for transitions of any molecularity from equilibrium melting curves. *Biopolymers* **1987,** *26* (9), 1601-1620.

66. Gibbs-Davis, J. M.; Schatz, G. C.; Nguyen, S. T., Sharp Melting Transitions in DNA Hybrids without Aggregate Dissolution: Proof of Neighboring-Duplex Cooperativity. *Journal of the American Chemical Society* **2007,** *129* (50), 15535-15540.

67. Lee, O.-S.; Prytkova, T. R.; Schatz, G. C., Using DNA to Link Gold Nanoparticles, Polymers, and Molecules: A Theoretical Perspective. *The Journal of Physical Chemistry Letters* **2010,** *1* (12), 1781-1788.

68. Antao, V. P.; Tinoco, I. J., Thermodynamic parameters for loop formation in RNA and DNA hairpin tetraloops. *Nucleic Acids Research* **1992,** *20* (4), 819-824.

69. Tan, Z.-J.; Chen, S.-J., Nucleic Acid Helix Stability: Effects of Salt Concentration, Cation Valence and Size, and Chain Length. *Biophysical Journal* **2006,** *90* (4), 1175-1190.

70. Korolev, N. I.; Vlasov, A. P.; Kuznetsov, I. A., Thermal denaturation of Na- and Li-DNA in salt-free solutions. *Biopolymers* **1994,** *34* (9), 1275-1290.

71. Anderson, C. F.; Record, M. T., Polyelectrolyte Theories and their Applications to DNA. *Annual Review of Physical Chemistry* **1982,** *33* (1), 191-222.

72. Groebe, D. R.; Uhlenbeck, O. C., Characterization of RNA hairpin loop stability. *Nucleic Acids Research* **1988,** *16* (24), 11725-11735.

CHAPTER 4

Specific Ion Effects on Cooperativity and the Rate of Association in DNA–Modified Gold Nanoparticle Assemblies

4.1 Introduction

The interaction of cations with polyelectrolytes has attracted much attention in the past few decades.[1-4] Such interactions in oligonucleotides are of particular interest for biological processes such as hybridization,[5] DNA condensation[6-8] and secondary structure formation.[9] The structure of DNA comprised of the purine and pyrimidine bases and the phosphate-sugar backbone is very sensitive to ions and solvents, and the thermodynamics of interactions involve important contributions from dehydration and counterion release.[1, 4, 10-12] A single experimental method is not sufficient to provide a comprehensive description of DNA–ion interactions. Therefore, the interactions with DNA and cations have been studied theoretically and experimentally in the solid state and solution by multiple techniques focused on specific ion effects of monovalent and divalent cations on the DNA backbone over the past three decades.[13-31]

The ability of DNA to hybridize with its complement is central to many assays used in biodiagnostics. Many of the applications require amplification of the target DNA sequence before detection can be successfully performed. However, some methods are sensitive enough to not necessitate amplification. In particular gold nanoparticles have been incorporated into a number of novel DNA sensor strategies, which has the potential to eliminate expensive DNA amplification techniques such as PCR.[32-34] Gold nanoparticles possess optical and catalytic properties that make them very useful in the detection of DNA with higher selectivity and sensitivity than most molecular-based probes.[35] Moreover small sized gold nanoparticles have a large surface to volume ratio and are also highly controllable in size and shape. The chemical affinity of the surface of gold for thiols and amines makes it also very useful and easy for covalently attaching oligonucleotides.

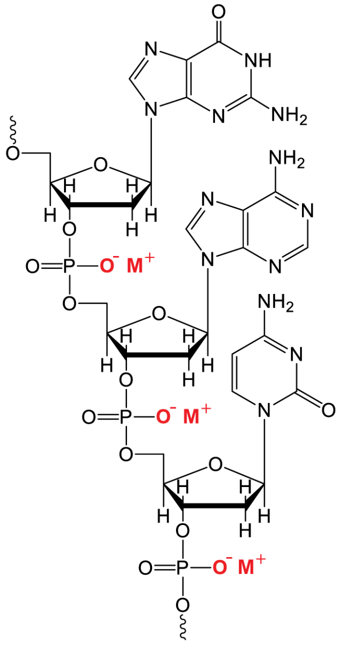

Figure 4.1. The chemical structure of single-stranded DNA. Interactions can take place between the phosphate negative charges with monovalent or multivalent cations. Their interactions can be more complex than it is shown.

In 1996, it was first shown that aggregates of gold nanoparticles functionalized with DNA can form reversibly by DNA hybridization.[36-37] These reversible aggregates can be used to discriminate single nucleotide polymorphisms with greater selectivity using thermal or salt stringency washes. The origin of this selectivity has been attributed to the presence of cooperativity in these materials, which arises from a common ion cloud formed during hybridization that is shared by neighboring DNA duplexes tethered to the gold surface. Studies have shown that the cooperative behavior is highly dependent on the DNA structure such as the presence of gap sequences[38] as well as the DNA density on the gold nanoparticle surface.[39] The effect of ion identity on the thermodynamic, kinetic and cooperative behavior of these aggregates, however, remains unexplored to this date. Garnering a comprehensive understanding of the specific ion effects on the DNA functionalized gold nanoparticle aggregates may help to improve the design and efficiency of DNA detection assays as well as shed light on their fundamental behavior. In this chapter, we have explored the effect of the chloride salts of the alkali ions Li^+, Na^+, K^+, and Cs^+ on the thermodynamic, kinetic and cooperative properties of GNP–DNA assemblies. Near the end of the chapter, we also explore the influence of the monovalent anions on GNP–DNA behavior.

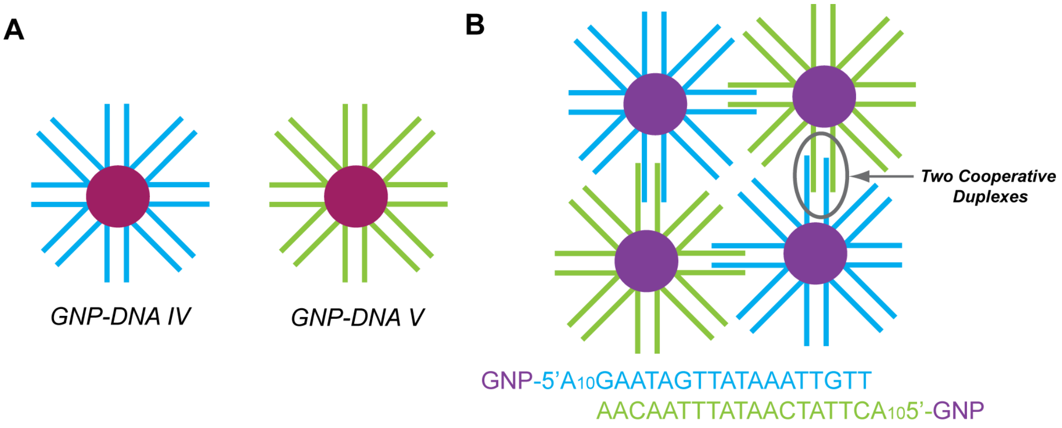

Figure 4.2. (A) DNA functionalized 13-nm gold nanoparticles (GNP–DNA) prepared using gold thiol chemistry. (B) DNA directed assembly of GNP–DNA aggregates formed from complementary mixtures of GNP–DNA conjugates.

4.2 Experimental Section

4.2.1 General Data

A detailed description of the DNA syntheses and attachment to the gold nanoparticle appeared in section 2.2.1 of chapter 2 of this thesis. All the DNA strands used in this work were synthesized using solid-phase synthesis technique. Thiol-modified DNA strands were used for attachment to the gold nanoparticle. Since we have used two completely complementary DNA sequences on the nanoparticles, only 5′-thiolated DNA strands were synthesized and used for the functionalization. The synthesized thiolated DNA contained polyadenosine spacer sequences,[39] which promotes $\pi-\pi$ self-stacking[40] and non-covalent binding to the gold nanoparticles,[41] results in higher thermodynamic stability and better stabilization of GNP–DNA conjugates over polythymidine spacers, although polythymidines are advantageous for higher DNA density over polyadenosine spaces.[42] DNA-modified 13-nm gold nanoparticles were prepared and analyzed as described in Chapter 3 including salting the samples as described with NaCl containing buffer. The DNA functionalized gold nanoparticle conjugates were purified by centrifugation followed by decantation of untethered extra thiolated DNA and the addition of 10 mM PBS (no salt buffer).[43] A high extent of purity of the GNP–DNA conjugates was very important for precise understanding of their assembly properties. Therefore, this centrifugation technique was performed multiple times and the final purified GNP–DNA was dispersed in the final buffer containing LiCl, NaCl, KCl, or CsCl at specific experimental concentrations. The DNA solutions were stored in custom-made aluminum metal blocks designed to hold 1.7 μL microtubes. The freshly purified GNP–DNA conjugates were used for kinetic experiments or hybridization for preparing aggregates.

4.2.2 Thermal Dissociation Experiments

The thermal denaturation analyses were performed on an HP 8453 diode-array spectrophotometer equipped with an HP 89090A Peltier temperature controller using Varian PTFE stopper top quartz cuvette containing 7 mm magnetic stir bar. The unmodified thermal DNA dissociation experiments, called melting experiments or thermal denaturation experiments, were performed on 1.0 mL duplex DNA solutions at 1.3 μM concentration. This concentration was optimal to obtain a smooth sigmoidal transition. Experiments with nanomolar concentrations of DNA were also performed, but a smooth transition curve was not observed. To prepare the DNA duplexes, we hybridized the complementary DNA strands by combining 1.3 nmols of each DNA sequence in PBS buffer (1.0 mL, 10 mM PBS, pH 7.0). For determining specific cation effects, we prepared distinct 10 mM PBS buffers containing LiCl, NaCl, KCl, or CsCl at 0.1 M, 0.2 M. 0.3 M, and 0.5 M concentrations. The hybridization mixtures dispersed in specific electrolytes were stored at 4 °C temperature prior to performing the thermal denaturation experiments. A thermal denaturation experiment comprised setting the temperature of the spectrometer cell holder to the initial values followed by increasing the temperature and recording the absorption spectra. The DNA duplex or GNP–DNA aggregate samples were allowed to equilibrate at the initial temperature for at least 15 min and melting experiments performed using UV–vis ChemStation Software. The absorption spectra were recorded for each temperature and λ_{max} = 260 nm selected for transition profiles. For experiments involving DNA duplexes, the initial temperature was set at 30 °C and increased to 80 °C by an increment of 1 °C with 1 min hold time at each temperature. A 7 mm magnetic stir bar was used to stir the samples during all thermal denaturation and kinetics experiments, and the stirring speed was set at 250 rpm using the HP 89090A Peltier temperature controller's built-in stirring system. An increase in the temperature caused enhanced scattering observed in the DNA absorption spectra. Therefore, the resulting thermal denaturation profiles were baseline corrected by subtracting the absorbance at 600 nm where all the spectra showed a flat region. To prepare the GNP–DNA aggregates, we hybridized GNP–DNA–IV (1.5 pmols with respect to the GNPs) and GNP–DNA–V (1.5 pmols with respect to the GNPs) in specific PBS buffers containing distinct electrolytes and concentrations. The mixtures were hybridized at room temperature for 16 hours. For the thermal denaturation experiments, the initial temperature was set to 40 °C and the aggregates allowed to equilibrate at that temperature for at least 15 min. The temperature was increased to 80 °C by an interval of 1 °C with 1 min hold time at each temperature. The stirring speed was set at 250 rpm, and λ_{max} was selected 525 nm for transition profiles. The melting transition profiles were baseline corrected by subtracting the absorbance at 925 nm.

4.2.3 Melting Profile Analysis

The melting temperature (T_m) determines the thermodynamic stability of both DNA duplex and GNP–DNA aggregate and is defined as the temperature at which half of the DNA duplexes denature into DNA single strands or half of the

GNP–DNA aggregates dissociate into colloidal dispersions of GNP–DNA conjugates. A melting transition curve has a sigmoidal shape and the steepest part of the melting curve corresponds to the T_m. A smooth transition curve is not always observed at particularly low DNA and electrolyte concentrations, hence the instrument assigned T_m sometimes varies from the actual value. A detailed description of this problem and its solution appeared in section 2.2.3 of chapter 2 of this thesis (Figure 2.3). Therefore, we determined the T_m of each transition for the NaCl concentration variation experiments by fitting the first derivative of the transition curves to a Gaussian function (equation 4.1) using Igor Pro (WaveMetrics, Inc., Version 6.20A) as described in chapter 2.

$$f'(T) = f'(0) + \mathrm{A}\exp\left[-\left(\frac{\mathrm{T}-\mathrm{T_m}}{\mathrm{width}}\right)^2\right] \tag{4.1}$$

where f' is the first derivative of the melting profile as a function of temperature, T is the temperature in K, A is the amplitude, width is the width of the Gaussian peak and T_m is the melting temperature. The reported T_m (Table 4.1) values are an average of at least two measurements on different samples in 0.2 M NaCl and the error represents the range of measured values with a minimum value of 0.1 °C, which is the resolution of the instrument. The T_m presented in Table 4.1 for both DNA duplex and the GNP–DNA experiments, were determined by fitting the baseline subtracted and normalized melting profile to equation 4.2,[39] a sigmoidal function used for the determination of ΔH of the transitions. These average T_m values were the same when determined from equation 4.1. Two sets of GNP–DNA experiments were performed on two freshly purified batches. The reported error bars (Table 4.1) for ΔH are the range of values obtained from at least two sets of data.

4.2.4 Aggregation Kinetics Experiments

The aggregation kinetics experiments were performed on the HP 8453 diode-array spectrophotometer in a time based experiment mode. The instrument temperature was set to 25 °C and absorption spectra recorded every 30 seconds for 15 hours. The experiments were performed on two sets of GNP–DNA samples to obtain reproducible kinetic profiles. Only freshly purified GNP–DNA probes were used for one single kinetic experiment. All experiments were done in 0.2 M electrolyte concentration.

4.2.5 Dynamic Light Scattering

A detailed description of the dynamic light scattering (DLS) experiments appeared in section 2.2.4 of chapter 2 of this thesis. Two sets of samples were prepared for the DLS and the values reported (section 4.4) are the average of two measurements with error bars representing the range of values from two sets of data. The samples were prepared as described in section 4.2.2, and the DLS measurements were performed 4 hours after hybridization at room temperature.

4.3 The Effect of Alkali Chloride Identity on the Thermodynamics of GNP–DNA Aggregates

The unusual molecular recognition properties of GNP–DNA, particularly of duplex-linked aggregates of these materials, have been attributed to the ionic environment within the aggregates that allows for cooperative interactions between neighboring duplexes.[39] To see if the identity of the cations influenced this cooperativity, the thermal dissociation profiles of the GNP–DNA assemblies were measured from the change in absorbance at 525 nm with varying alkali chlorides (Li^+, Na^+, K^+, and Cs^+) as electrolytes (Figure 4.3A). The thermally induced aggregate–to-colloid transitions occurred over a very narrow temperature window (~ 2 °C), which was highly indicative of the presence of cooperativity in all the systems.[38-39, 44] The full-width half-maximum of the first derivative (fwhm) is a useful parameter for quantifying how narrow the temperature window is for a particular transition. The measured fwhm values for the GNP–DNA Na^+, K^+, and Cs^+ systems were 1.6 °C while that of the Li^+ system was 1.9 °C.

The corresponding unmodified DNA duplex melting profiles obtained from the absorbance changes at 260 nm for systems lacking GNPs are shown in Figure 4.3B. (Note that higher concentrations of DNA were required to observe a hyperchromic absorbance changes due to weaker DNA optical activity compared with the GNPs). Compared to the GNP–DNA transitions, all DNA duplex melting took place over a broad temperature range (~ 10–20 °C).

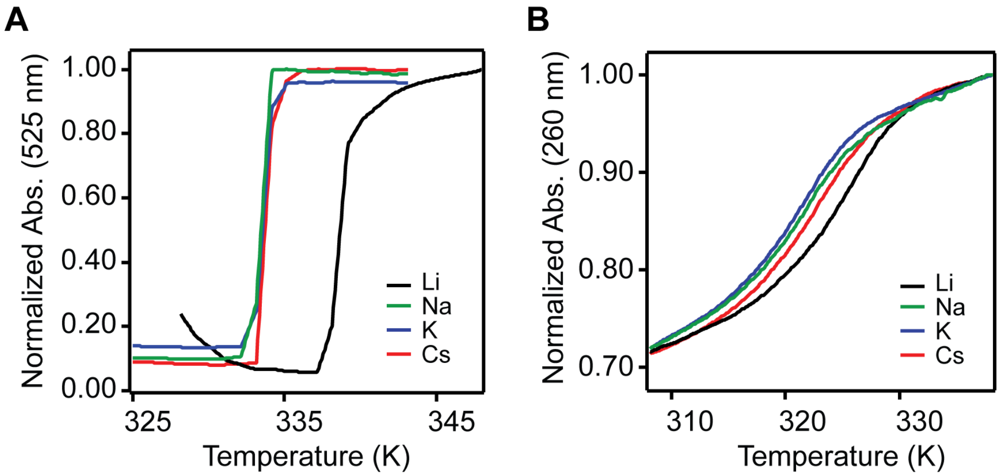

Figure 4.3. (A) Thermal dissociation, or melting, profiles of the GNP–DNA two-strand duplex linked aggregate systems with varying cations Li^+, Na^+, K^+, and Cs^+

in the hybridized samples. (B) Thermal melting profiles of the two-strand duplex systems with varying cations Li^+, Na^+, K^+, and Cs^+ in the hybridized samples.

The highest melting temperature among all the GNP–DNA aggregates was observed for Li^+ (338.3 ± 0.5 K) similar to the system with the unmodified DNA duplex. Such increased T_m has been also reported for DNA duplex dissociation in Li^+ as an electrolyte previously.[45] This increased thermal stability of DNA duplexes is due to specific binding of Li^+ to the DNA double helix, which has been attributed to Li^+'s strong affinity towards phosphate groups and complexation with nitrogenous nucleic acid bases.[46] The Na^+, K^+, and Cs^+ induced thermal stability of the GNP–DNA aggregates were very similar, and the T_m values for Na^+, K^+ and Cs^+ systems were found to be 333.6 ± 0.1 K, 333.6 ± 0.6 K, and 333.7 ± 0.1 K, respectively. The melting temperatures of the corresponding unmodified DNA duplexes (uDNA) were lower than those of the aggregates by ~ 11–13 °C. This increase in T_m upon incorporating GNPs was ~ 40% higher than that observed for the three strand ternary complex systems (Chapter 2, Table 2.1, T_0–*nicked duplex*), which also indicates that the structure of DNA has a unique influence on the GNP–DNA aggregates (which was discussed in chapters 2 and 3). The T_m values for the unmodified DNA duplexes in the presence of Na^+ and K^+ were both 321.0 K whereas that of the Cs^+ system was found to be slightly higher (322.5 K) but lower than Li^+ (325.2 K).

The dissociation ΔH of GNP–DNA aggregates and the corresponding DNA duplexes are shown in Figure 4.4B. For the determination of the change in enthalpy due to aggregate or duplex dissociation, we used the method developed by Schatz and Mirkin (equation 4.2) that required normalization of the dissociation curves to generate the fraction of dissociated aggregate or duplex as a function of temperature.[39] After this normalization, these traces were fit with a sigmoidal function (equation 4.2) to determine ΔH and the T_m of each transition. This method required the melting transition to possess a clear baseline and a plateau. For many of the gap–linked DNA duplexes (described in chapter 2), we could not observe a well-defined baseline due to the low stability of these three-strand duplexes. Therefore, the *van't Hoff* method for ΔH determination was used for unmodified DNA duplexes in our previous studies.[47] In this work the thermal stability of the duplexes for all the unmodified systems was well above room temperature, therefore, it allowed us to use the Schatz and Mirkin model for the corresponding DNA duplexes, too:

$$f = \frac{\mathrm{Abs_{max}} - \mathrm{Abs}}{\mathrm{Abs_{max}} - \mathrm{Abs_{min}}} = \frac{1}{1 + \exp\left[\frac{\Delta H}{R}\left(\frac{1}{T} - \frac{1}{T_m}\right)\right]} \qquad (4.2)$$

where *f is* the dissociated fraction of aggregate or duplex, ΔH represents the dissociation enthalpy of either GNP–DNA aggregates or unmodified DNA duplexes, T_m is the melting temperature, and R is the molar gas constant. The resulting ΔH values are given in Table 4.1 with the corresponding T_m values for the hybridization mixtures in 0.2 M electrolyte concentration. A detailed description of these models appeared in section 2.3.2.2 of chapter 2 of this thesis.

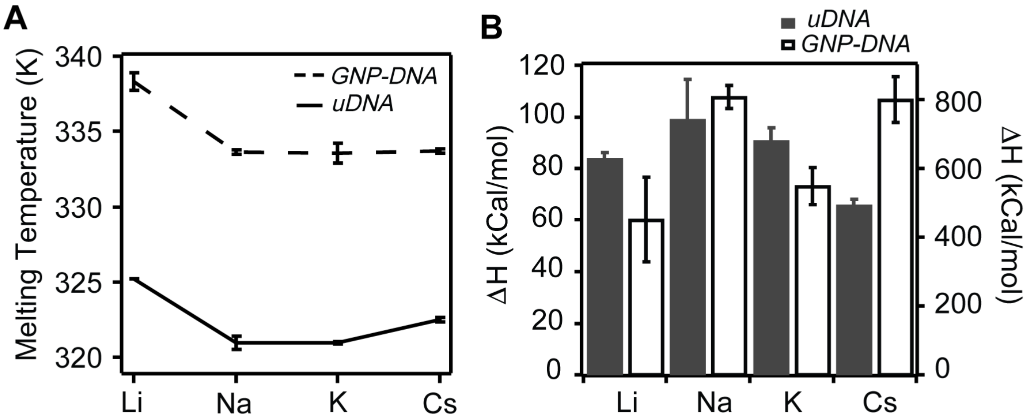

Figure 4.4. (A) Melting temperatures, T_m, of GNP–DNA aggregates (GNP–DNA) and the corresponding DNA duplexes (uDNA) for specific cation systems. (B) Dissociation ΔH of the GNP–DNA aggregates and the corresponding DNA duplexes (uDNA) for specific cation systems.

The thermodynamic values corresponding to the GNP–DNA aggregate and the DNA duplex dissociations are presented in Table 4.1. The highest Δ*H* value for the GNP–DNA aggregate dissociations was observed for the aggregate dissociations in the presence of Na^+ (ΔH_{GNP} = 800 ± 30 kcal/mol) and Cs^+ (ΔH_{GNP} = 800 ± 70 kcal/mol). The lowest ΔH was obtained for the aggregate that contained Li^+ (ΔH_{GNP} = 450 ± 120 kcal/mol) as the electrolyte, whereas that of the K^+ system was found to be 550 ± 50 kcal/mol. The ΔH of the corresponding DNA duplexes were significantly lower than those of the GNP–DNA aggregates. The highest dissociation ΔH within all the unmodified systems was found for Na^+ (ΔH_{uDNA} = 100 ± 16 kcal/mol) consistent with its nanoparticle-modified version. The K^+ unmodified duplex system possessed a similar value within the error range of the DNA duplex with Na^+ electrolyte present (ΔH_{uDNA} = 90 ± 5 kcal/mol). The lowest dissociation ΔH was observed for Cs^+ (ΔH_{uDNA} = 66 ± 2 kcal/mol) whereas that of Li^+ was found to be 84 ± 2 kcal/mol. The low dissociation ΔH values for both the GNP–DNA and unmodified DNA systems in the presence of LiCl were interesting given the highest observed melting temperature for the hybridization mixtures containing Li^+. These opposing trends in ΔH and T_m revealed that the duplex stabilization by Li^+ was due to a smaller decrease in entropy upon hybridization in comparison with the other alkali chlorides.

4.3.1 Cooperativity in Aggregates with Varying Alkali Identity

Cooperativity, *N*, is the extent of cooperative interactions between neighboring DNA duplexes in the GNP–DNA aggregates. As described in section 2.3.2 of chapter 2 this value could be determined from the ratio of the dissociation enthalpy changes according to:

$$N = \frac{\Delta \mathrm{H_{GNP}}}{\Delta \mathrm{H_{uDNA}}} \quad (4.3)$$

The greatest *N* value was observed for the Cs^+ system (Figure 4.5A, 12.2 ± 0.1) whereas the lowest value was measured for the Li^+ aggregate system (5.4 ± 0.2). This two-fold increase in *N* was found to be inversely proportional to their ionic radius of the hydrated ions from 3.40 Å to 2.28 Å (Figure 4.5B). The cooperative unit for Na^+ was found to be an intermediate value between Li^+ and Cs^+ (8.2 ± 0.2) that almost linearly related their hydrated ionic radius to *N*. The value observed for K^+ was 6.1 ± 0.3 and did not follow the expected linearity.

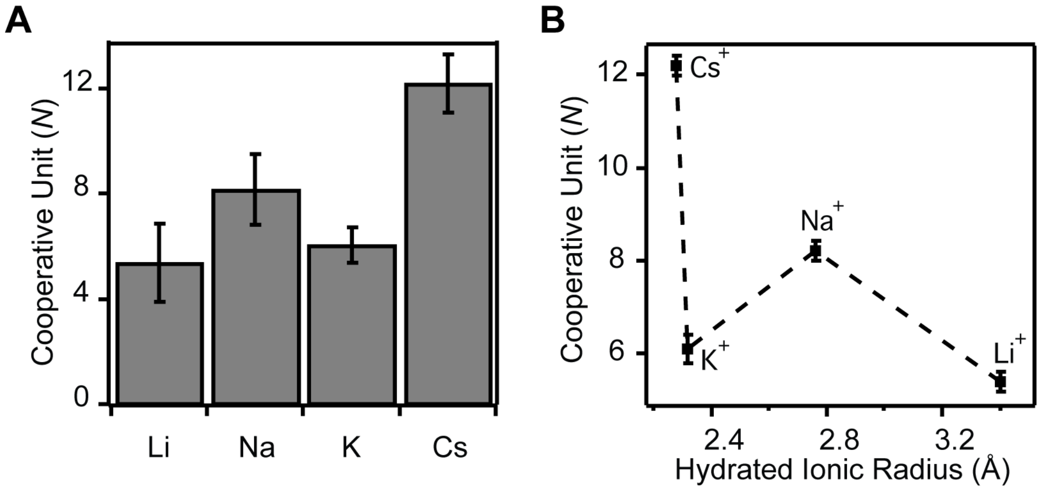

Figure 4.5. A.) The cooperative unit determined for GNP–DNA aggregates in the presence of Li^+, Na^+, K^+, and Cs^+. B.) The cooperative unit as a function of ionic radius of the hydrated cations. Li^+, Na^+, and Cs^+ exhibited a nearly linear relationship whereas K^+ deviated from the linearity due to its smaller cooperative unit.

Table 4.1. Thermodynamic Values Corresponding to the Dissociation of GNP–DNA Aggregates and the Unmodified DNA Duplexes (uDNA) with Varying Alkali Chloride.

	GNP–DNA			uDNA			
Cations	ΔH_{GNP} (kcal/mol)	T_m (K)	Δi	ΔH_{uDNA} (kcal/mol)	T_m (K)	Δi	N
Li^+	450(120)	338.3(5)	3.2(1)	84(2)	325.2(1)	2.2(1)	5.4(2)
Na^+	800(30)	333.6(1)	4.3(7)	100(16)	321.0(4)	2.8(5)	8.2(2)
K^+	548(50)	333.6(6)	4.0(6)	90(5)	321.0(1)	2.5(2)	6.1(3)
Cs^+	800(70)	333.7(1)	3.0(4)	66(2)	322.5(2)	2.3(1)	12.2(1)

4.3.2 Effect of Cation Polarizability on Thermodynamic Stability and Cooperativity

The highest thermal stability of the DNA duplexes and their corresponding GNP–DNA aggregates in the presence of Li^+ is attributed to its specific binding interactions with the phosphate groups and the bases that result in a decrease in repulsion between the two complementary strands in the duplex.[46, 48] Indeed, it has been reported that in the solid state small and hard monovalent and divalent cations can interact more effectively with the nitrogenous bases through the nitrogen atoms of purines and pyrimidines besides electrostatic interactions with the phosphate groups on the DNA backbone.[49] Yet how can these interactions be rationalized given the smaller dissociation ΔH values? We reason that the enhanced stabilization of lithium in comparison with the other salts is due to the entropic contribution to the free energy. Specifically, the strong electrostatic interactions of Li^+ with the negatively charged DNA occur with partial dehydration of hydrated Li^+ [50] (Figure 4.6). This dehydration causes a decrease in magnitude of the ΔH of DNA duplex formation, as the number of water molecules associated with Li^+ in its hydration sphere is less when Li^+ binds with the duplexes. More simply, a less negative ΔH of duplex formation (or a less positive ΔH of dissociation) is derived from the positive $\Delta H_{dehydration}$. Hence, a smaller T_m would be expected for such single strand to duplex transitions. However, the dehydration of hydrated Li^+ causes an increase in ΔS, which results in an overall less negative ΔS for association that provides the higher thermodynamic stability of the duplexes in the presence of Li^+. As lithium is much more strongly hydrated than the other ions, the entropic contribution (i.e., the loss of water) is more significant.

For the unmodified DNA duplexes, we observed a decrease in T_m by ~3 K when Li^+ was replaced with Na^+ and K^+. However, Cs^+ increased the thermal stability of the DNA duplexes by ~ 1.5 K compared to Na^+ and K^+, which was not observed for the aggregates. This order of selectivity of alkali cations for DNA in water has been also reported previously.[46] Although Cs^+ exhibited the second highest thermal stability, it had the lowest dissociation enthalpy change, which once again indicated that the decrease in entropy upon hybridizing in the presence of Cs^+ was less than for Na^+ and K^+. We attribute this apparent less negative ΔS of duplex formation in the presence of Cs^+ to cesium's weak interactions with water that allow it to become easily dehydrated. Moreover, the more polarizable cesium may also release more water bound to the phosphate groups upon binding to the DNA. We conclude that the influence of the ions on duplex stability is a balance between the strength of electrostatic screening of the duplexes and the ability to become dehydrated and dehydrate the DNA.

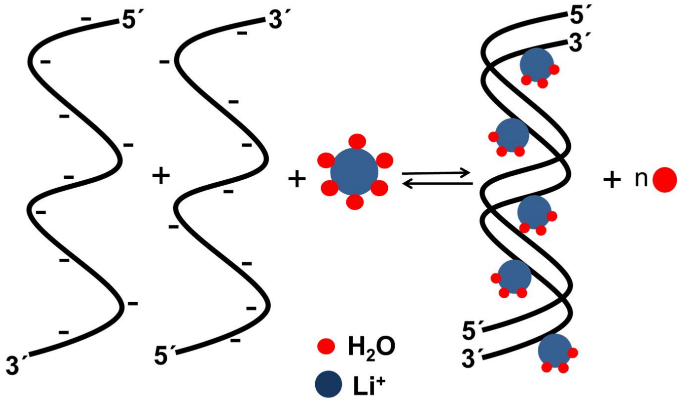

Figure 4.6. Schematic representation of partial dehydration of Li^+ when a DNA duplex is formed. This dehydration results in a less negative ΔH and ΔS for both Li^+ and Cs^+ for duplex formation. The number of water molecules and size of Li^+ do not reflect their actual numbers and size and is used as representation only.

For the GNP–DNA systems, the trend in T_m differed from the unmodified duplexes, which is indicative of the unique influence of densely packed DNA strands on the nanoparticle surface on the T_m of corresponding aggregates. Specifically, replacing Li^+ with any of the other cations decreased the T_m by ~5 K. Unlike the unmodified system, the thermal stability remained the same, as the size of the hydrated cations decreased from Na^+ to K^+ and Cs^+.

Despite the lower ΔH, we maintain that lithium stabilized the duplex through stronger ion-ion interactions and specific interactions with the nucleic acid bases, both of which may contribute to the ion cloud formation, responsible for the cooperative effect in GNP–DNA melting transitions.[38-39, 44] We initially hypothesized that the largest shared cation cloud would be formed in the presence of the strongest interacting cations with the phosphate oxygens and the purine and pyrimidine nitrogens. Therefore, we expected Li^+ to enhance the cooperativity in GNP–DNA aggregates better relative to the other alkali metal monovalent cations.

Surprisingly, our experimental results showed that cooperativity was significantly decreased in the presence of Li^+ and increased in the presence of Cs^+ (Figure 4.5A). To explain the enhanced effect of Cs^+ on cooperative interactions between DNA duplexes in GNP–DNA assemblies we propose an ion cloud model that considers ion polarizability. Assuming that the shared ion cloud has a cylindrical shape, two different phenomena can take place during formation of the GNP–DNA aggregates:

(1) The size of the ion cloud remains the same for all the cations. Hence the density of ions will be greater for the smaller cations Li^+ and Na^+ (assuming they become partially dehydrated) compared to the larger ones. In this case, it is expected that the higher cation density in the ion cloud would increase the cooperative effect by increasing the number of duplexes in the ion cloud (Figure 4.7A).

(2) The size of the ion cloud varies to maintain a constant density of the cations and is non-specific to their sizes. In such case, larger, diffused and polarizable cations will create a larger ion cloud allowing for interactions among more neighboring DNA duplexes (Figure 4.7B).

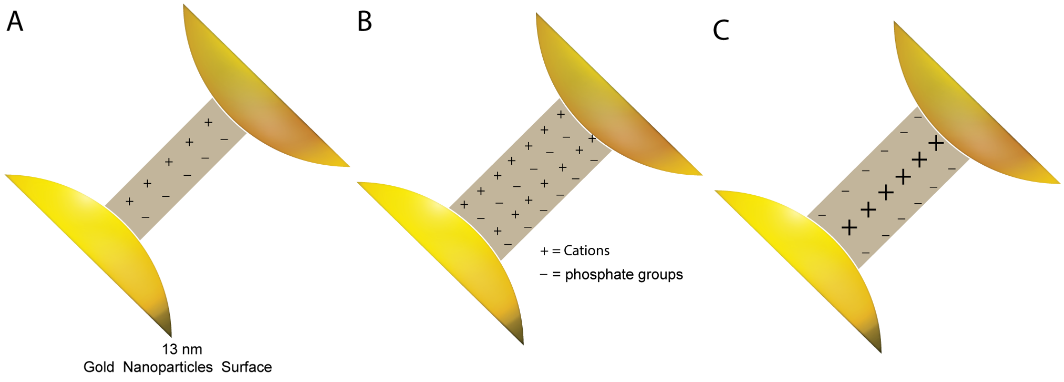

Figure 4.7. Hypothetical cylindrical shape of the shared ion cloud formed from the cooperative interactions of neighboring DNA duplexes because of the closely packed monolayer of DNA single strands on the gold nanoparticle surface. (A) The size of the ion cloud is smaller due to less number of small size cations associated with the linker DNA strands; (B) the ion cloud is larger due to more cations bound to DNA linkers resulting in a higher ion density; (C) the size of the ion cloud is larger due to a similar number of larger cations to **A** associated with the DNA linkers. The ion cloud was depicted for the presence of monovalent cations only.

Two factors can contribute to cooperativity in the GNP–DNA systems: firstly, the density of ions and their polarizability. Based on the greatest cooperativity for the aggregates in the presence of Cs^+, we propose that the more polarizable the ion, the more it will be able to interact with a higher number of DNA strands (in agreement with the second proposed scenario). To verify that a change in ion density was not responsible for the cooperative effects, we applied Manning Theory to determine the number of cations that were recruited during duplex formation and were released when the duplex dissociates (Δi). Not only did we determine the number of cations released upon GNP–DNA aggregate dissociation in the presence of Li^+, Na^+, K^+ and Cs^+, we also did similar experiments to evaluate the number of cations released upon melting the corresponding unmodified DNA duplexes to compare how they differed from the GNP–DNA aggregates. Such experiments in both unmodified and GNP–DNA aggregates should clarify if there was any contribution of the cation polarizability to the cooperativity in the GNP–DNA aggregates.

4.3.3 Quantifying the Number of Released Cations, Δi, in GNP–DNA Aggregates

A detailed description of Δi determination appeared in section 2.3.3 of chapter 2 of this thesis. A series of experiments was performed with both GNP–DNA aggregates and the corresponding unmodified DNA duplexes at varying electrolyte concentrations. The slope of the plot of T_m vs. ln [MCl] was used to determine Δi using equation 4.4[39] (M = Li^+, Na^+, K^+, or Cs^+, Figure 4.8B and C):

$$\frac{\mathrm{dT_m}}{\mathrm{d\,ln[NaCl]}} = \Delta i\,\frac{N\mathrm{RT_m^2}}{\Delta \mathrm{H}} \qquad (4.4)$$

Figure 4.8A compares the calculated Δi for the GNP–DNA aggregate dissociation and the corresponding DNA duplex melting. The trend for the number of cations associated with each duplex in the unmodified DNA and the aggregates were identical, however, the Δi values for the aggregates were higher than those of the unmodified DNA. We attribute this increase in the Δi to the high density of closely packed DNA on the gold nanoparticles causing more cation recruitment than the unmodified duplexes. This increased number of cations released per duplex dissociation also indicates why the GNP–DNA aggregates are more thermally stable than the unmodified DNA.

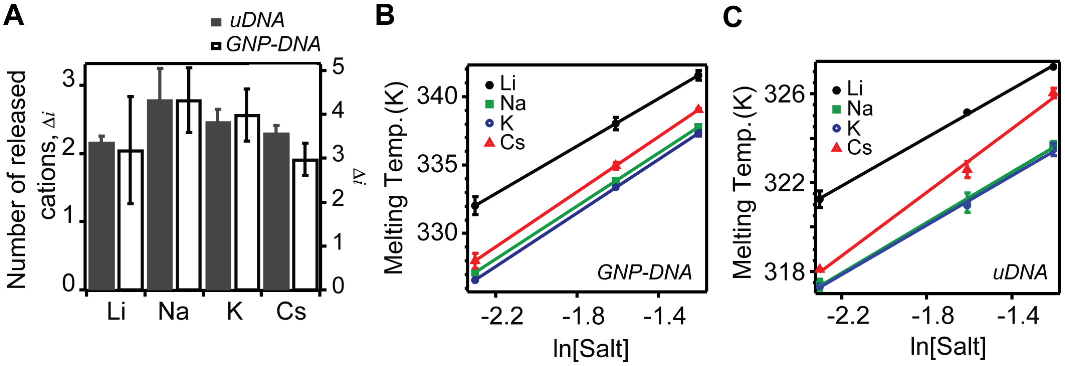

Figure 4.8. A.) Number of released cations per duplex dissociation for GNP–DNA aggregates (right axis) and DNA duplexes (left axis). B.) Plot of T_m vs. ln [MCl] for the GNP–DNA aggregates. Thermal denaturation experiments were performed at 0.2 M, 0.3 M and 0.5 M Li^+, Na^+, K^+, and Cs^+ concentrations as described in section 4.2.2. Melting temperatures were determined for each experiment using equation 4.1 as described in section 4.2.3. C.) Plot of T_m vs. ln [MCl] for the corresponding DNA duplexes. Similar to the GNP–DNA aggregates, T_m was measured for different concentrations of the monovalent cations (*vide supra*).

The resulting values of Δ*i* are included in Table 4.1 and indicate that the changes in the number of released cations were very subtle with the size of the cations. Specifically, the unmodified Li^+ system released 2.2 ± 0.1 cations for each dissociating duplex. Increasing the size of the cation to Na^+, the number of released cations increased to 2.8 ± 0.5. The values for K^+ and Cs^+ were 2.5 ± 0.2 and 2.3 ± 0.1, respectively. This result was unexpected for Li^+ due to its specificity in interactions with DNA duplexes. From these subtle changes in the Δi, it indicated the number of cations associated with a duplex was the same regardless of the charge density of the monovalent cations. For the GNP–DNA systems, we found Δi for Li^+ to be 3.2 ± 0.1, as expected to be higher than that of the unmodified DNA duplex. The values for the Na^+, K^+, and Cs^+ were 4.3 ± 0.7, 4.0 ± 0.6 and 3.0 ± 0.4, respectively. These Δi values were also similar within the error range. Hence it was obvious that varying the identity of the monovalent cations did not affect the number of ions associated with a duplex in the unmodified DNA or in the aggregate. Therefore, the effect of cation identity on the cooperativity was not derived from the cation density in the shared ion cloud, but rather resulted from the increased polarizability of Cs^+ (Figure 4.7C) that facilitated interactions of neighboring DNA within the aggregate.

4.4 The Kinetics of Aggregation of GNP–DNA with Varying Alkali Chloride Electrolyte

In the previous chapters (chapter 2 and 3), we discussed how the rate of GNP–DNA aggregation depended on the DNA structures (the presence of flexible gaps and DNA hairpins). A noticeable disadvantage of these GNP–DNA aggregates in DNA detection applications is their slower aggregation rate. The known factors that influence the rate of GNP–DNA aggregation are the presence of spacer sequences that make the hybridizing portion of the strands more accessible on the GNP surface, flexible single-stranded gaps present in the target sequence, the temperature, salt concentration and DNA concentration.[38, 51-52]

Another important factor that remains unexplored is the effect of type of cations present during aggregation. The aggregation of DNA functionalized gold nanoparticles depends on the hybridization of the complementary DNA sequences that link the gold nanoparticles into a three-dimensional network. It is important that the repulsive interactions derived from the presence of negatively charged phosphate groups on the DNA backbone are screened prior to a stable duplex forming. Therefore, the identity of the cations is also an important parameter that should influence the rate of hybridization of the complementary DNA strands in the GNP–DNA aggregates.

We hypothesized that, regardless of forming highly cooperative aggregates, the rate of aggregation in the presence of Cs^+ should be slower because of its weaker interactions with the phosphate groups compared to the other monovalent ions in this series. Therefore, the greatest enhancement on the aggregation kinetics in these GNP–DNA assemblies should occur in the presence of Li^+ due to its more effective neutralization of the repulsive forces between negatively charged phosphate groups on two complementary DNA strands. Since the extent of base stacking and hydrogen bonding remains the same for all cations, the aggregation kinetics will be solely dependent on the cation identity.

Figure 4.9A shows the kinetic profile of GNP–DNA aggregate formation in the presence of Li^+, Na^+, K^+, and Cs^+. These results indicated that the kinetics of aggregation was faster for Li^+ followed by Na^+, K^+ and Cs^+, consistent with our expectations. To probe the size of the aggregates after a certain period, we hybridized GNP–DNA-IV and GNP–DNA-V probe conjugates and measured their absorption spectrum after 12 hours of hybridization (Figure 4.9B). The larger the aggregate, the lower will be the absorption at 525 nm, which is the characteristic absorption maximum of the 13-nm GNP–DNA conjugates.[53] After 12 hours of aggregation the size of the aggregates was the largest in the presence of Li^+, followed by Na^+, K^+ and Cs^+ respectively, which we attributed to the faster rate of aggregation for the former.

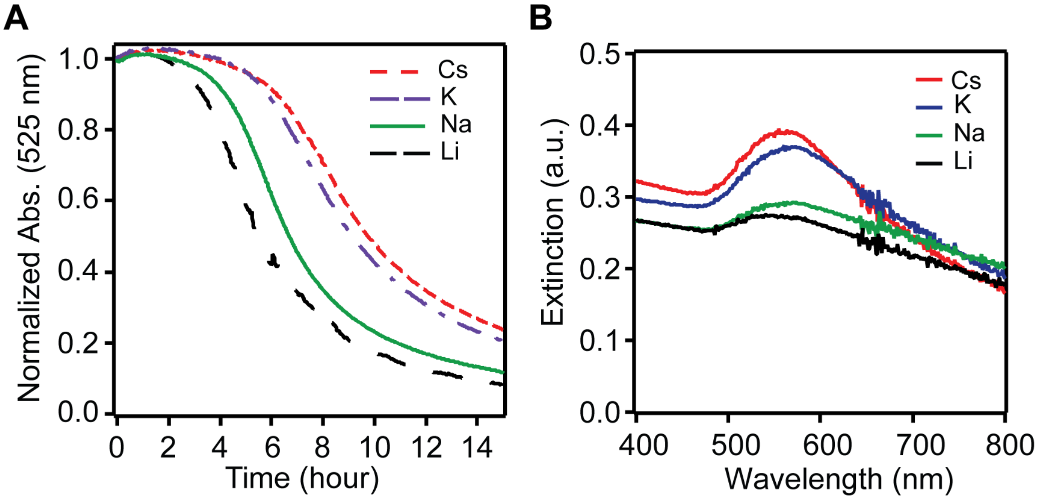

Figure 4.9. A.) Kinetic profile of GNP–DNA aggregate formation in the presence of Li^+, Na^+, K^+, and Cs^+. B.) Absorption spectrum of hybridized GNP–DNA samples at 12 hours.

Clearly, the aggregation kinetics of GNP–DNA probes had a strong effect on the GNP–DNA aggregates size. This can be useful in developing materials for DNA detection assays, where the aggregate size can be a key-determining factor for discriminating a wild type DNA sequences from its mutants.[54] Based on this correlation between the aggregation kinetics and the aggregate size, lithium should be used in the buffer with GNP–DNA probes in colorimetric assays. It would be interesting to see how the divalent cations behave in terms of aggregation and dissociation, which will further clarify the effect of counter ion charge to size ratio on the GNP–DNA aggregate behavior. That work is not relevant to this chapter, therefore, will be the future goal of this current project.

Since the UV-vis study on the aggregation kinetics only depended on the fact that the surface plasmon resonance was dampened and shifted to lower energies due to the formation of larger assemblies of particles, we required a microscopic method to probe the various aggregate sizes by visualization. Transmission electron microscopic (TEM) images revealed the formation of the complementary DNA linked aggregates of 13-nm gold nanoparticles (Figure 4.10A and B). Consistent with our UV-vis absorbance analysis, the aggregates formed in the presence of Li^+ were much larger than that of the Cs^+ based on the TEM images after hybridizing the GNP–DNA complementary probes for 8 hours. We also performed dynamic light scattering to study these aggregates after 4 hours of GNP–DNA hybridization, which gave the hydrodynamic radius of the resulting aggregates. Figure 4.10C shows the average hydrodynamic radius of Li^+ induced aggregates was ~ 450 nm whereas that of the Cs^+ was ~ 300 nm.

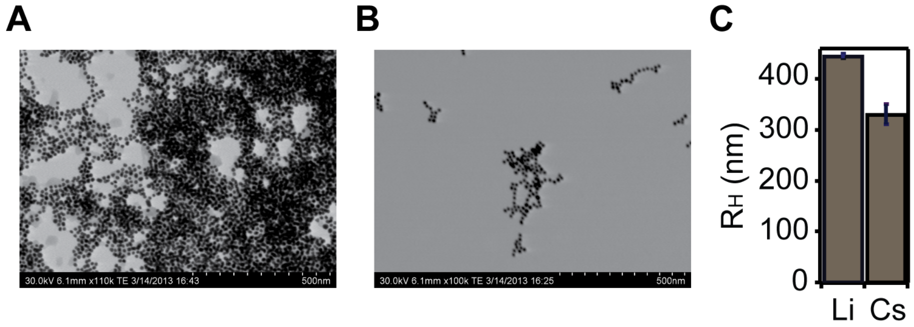

Figure 4.10. A.) Transmission electron microscopic image of GNP–DNA aggregates in Li^+. The image was obtained after 8 hours of hybridization of the complementary conjugates. B.) Transmission electron microscopic image of GNP–DNA aggregates in Cs^+. Similar to Li^+, the Cs^+ induced aggregate image was obtained after 8 hours of hybridization of the complementary conjugates. B.) Hydrodynamic radius of GNP–DNA aggregates in Li^+ and Cs^+ after 4 hours of hybridization.

4.5 The Effect of Monovalent Anions on GNP–DNA Assemblies

Thus far, we have explored the influence of cations on the behavior of negatively charged GNP–DNA. However, other work in our group has shown that anions can have dramatic effects in the surface properties of negatively charged surfaces.[55] To study the effect of monovalent anions, we prepared buffer solutions containing 0.1 M NaBr and 0.1 M NaI and monitored their aggregation and thermal dissociation. The effect of the anions on GNP–DNA hybridization was more dramatic compared to the monovalent cations. We observed irreversible GNP–DNA aggregation in the presence of I^- (Figure 4.11A), which was confirmed by thermal dissociation experiment (Figure 4.11B). Such I^- induced aggregation of gold nanoparticles has been reported[56-58] and attributed to I^- adsorption onto the gold nanoparticle surface that results in a stark drop in the surface potential. This decrease in the surface potential of gold nanoparticle was proposed to decrease the interparticle repulsive force of interaction facilitating irreversible aggregation.

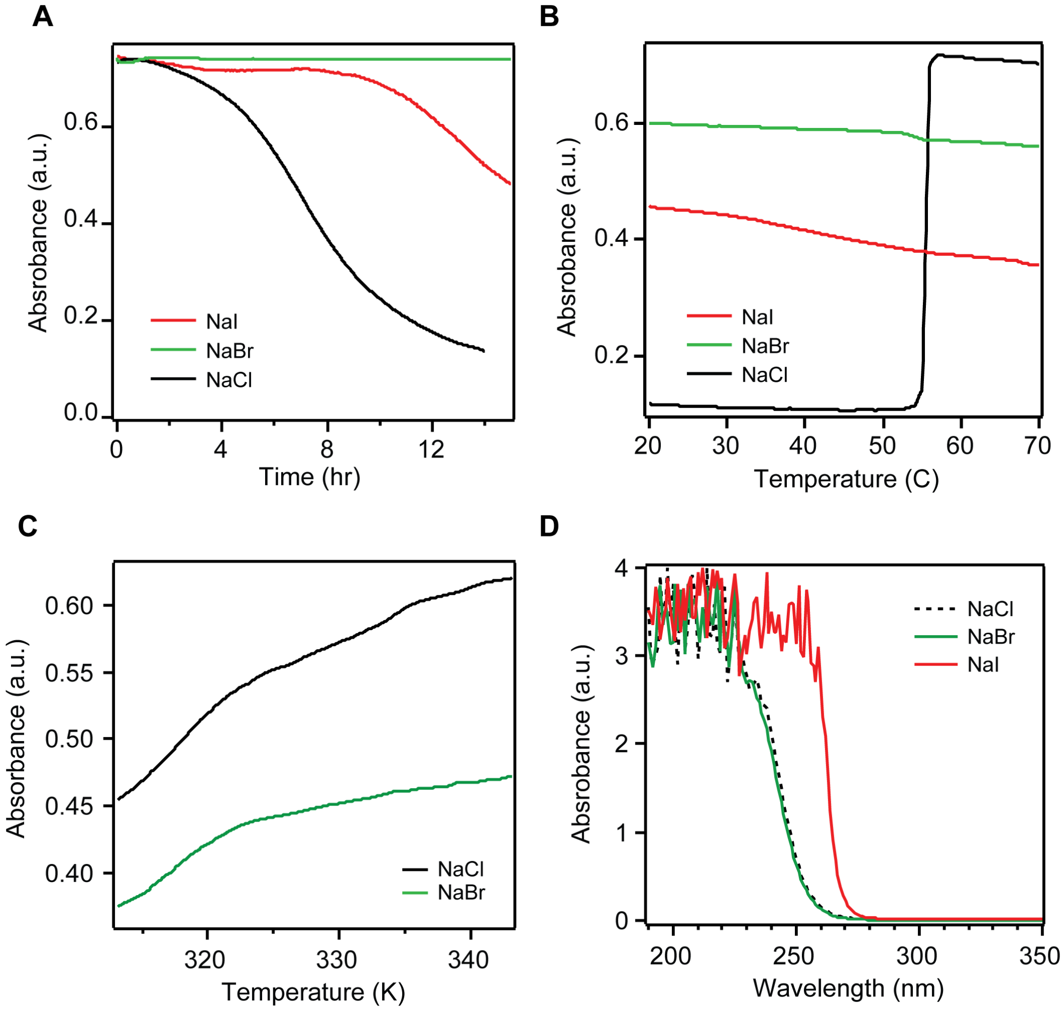

Figure 4.11. A.) Hybridization kinetics of GNP–DNA probes in the presence of Cl^-, Br^-, and I^-. Iodide promoted irreversible aggregate formation whereas no aggregates were formed in the presence of bromide. B.) Thermal denaturation profile of GNP–DNA aggregates in the presence of Cl^-, Br^-, and I^-. No melting

transitions were observed for Br^- and I^-. This confirmed irreversible aggregation by iodide. C.) Thermal denaturation profile of unmodified DNA duplex in the presence of Cl^- and Br^-. Melting transitions were observed for both anions and possessed identical thermodynamic stability. D.) Absorption spectra of the Cl^-, Br^-, and I^- containing buffers. I^- strongly absorbed in the DNA's absorption region, therefore, the unmodified duplex dissociation could not be observed for iodide.

The effect of Br^- was even more dramatic (Figure 4.11A and B) as it did not allow GNP–DNA hybridization. Such an effect of Br^- was not seen for unmodified DNA duplexes (Figure 4.11C) as we observed dissociation of unmodified DNA duplexes in the presence of Br^-. Moreover, the thermodynamic stability of unmodified DNA duplexes in the presence of Br^- was exactly similar to the stability in the presence of Cl^-. The effect of Br^- on the GNP–DNA probes is unknown and requires further investigation to provide greater insight. The unmodified DNA dissociation could not be observed for I^- as the buffer solution strongly absorbed at 260 nm, which is characteristic absorption maximum of DNA (Figure 4.11D).

4.6 Conclusions

In this study, we found that the size of the cation affected cooperativity and thermodynamic stability in GNP–DNA probes and their aggregate size. The aggregate size increased with decreasing size of the dehydrated cations, whereas the cooperativity was largest for Cs^+. The rate of aggregation was also heavily influenced by cation size, which would be interesting to explore further for electrolyte ions with greater charge to size ratios. We explained the increase in cooperativity for the larger cesium as arising from the interaction of a more polarizable cation with more DNA neighboring duplexes. It would also be interesting to see how the entropy of the GNP–DNA systems varied due to the fact that water in the DNA duplexes influenced the cooperative dissociation in free DNA. Such studies require microcalorimetry experiments that we, unfortunately, did not have access to during pursuit of this work.

4.7 References

1. Record, M. T.; Anderson, C. F.; Lohman, T. M., Thermodynamic analysis of ion effects on the binding and conformational equilibria of proteins and nucleic acids: the roles of ion association or release, screening, and ion effects on water activity. *Quarterly Reviews of Biophysics* **1978,** *11* (02), 103-178.

2. Sabbagh, I.; Delsanti, M., Solubility of highly charged anionic polyelectrolytes in presence of multivalent cations: Specific interaction effect. *The European Physical Journal E* **2000,** *1* (1), 75-86.

3. Hugerth, A.; Sundelöf, L.-O., The effect of polyelectrolyte counterion specificity, charge density, and conformation on polyelectrolyte–amphiphile interaction: The carrageenan/furcellaran–amitriptyline system. *Biopolymers* **2001,** *58* (2), 186-194.

4. Ludwig, H.; Loebel, K. H., Interaction of polyelectrolytes with mono- and divalent cations. *Berichte der Bunsengesellschaft für physikalische Chemie* **1996,** *100* (6), 863-868.

5. Springer, T.; Sipova, H.; Vaisocherova, H.; Stepanek, J.; Homola, J., Shielding effect of monovalent and divalent cations on solid-phase DNA hybridization: surface plasmon resonance biosensor study. *Nucleic Acids Research* **2010,** *38* (20), 7343-7351.

6. Plum, G. E.; Arscott, P. G.; Bloomfield, V. A., Condensation of DNA by trivalent cations. 2. Effects of cation structure. *Biopolymers* **1990,** *30* (5-6), 631-643.

7. He, S.; Arscott, P. G.; Bloomfield, V. A., Condensation of DNA by multivalent cations: experimental studies of condensation kinetics. *Biopolymers* **2000,** *53* (4), 329-341.

8. Bloomfield, V. A., Condensation of DNA by multivalent cations: considerations on mechanism. *Biopolymers* **1991,** *31* (13), 1471-1481.

9. Soto, A. M.; Misra, V.; Draper, D. E., Tertiary Structure of an RNA Pseudoknot Is Stabilized by "Diffuse" Mg^{2+} Ions. *Biochemistry* **2007,** *46* (11), 2973-2983.

10. Anderson, C. F.; Record, M. T., Polyelectrolyte Theories and their Applications to DNA. *Annual Review of Physical Chemistry* **1982,** *33* (1), 191-222.

11. Anderson, C. F.; Record, M. T., Salt-Nucleic Acid Interactions. *Annual Review of Physical Chemistry* **1995,** *46* (1), 657-700.

12. Misra, V. K.; Sharp, K. A.; Friedman, R. A.; Honig, B., Salt Effects on Ligand-DNA Binding: Minor Groove Binding Antibiotics. *Journal of Molecular Biology* **1994,** *238* (2), 245-263.

13. Chu, V. B.; Bai, Y.; Lipfert, J.; Herschlag, D.; Doniach, S., Evaluation of ion binding to DNA duplexes using a size-modified Poisson-Boltzmann theory. *Biophysical Journal* **2007,** *93* (9), 3202-3209.

14. Tan, Z.-J.; Chen, S.-J., Nucleic Acid Helix Stability: Effects of Salt Concentration, Cation Valence and Size, and Chain Length. *Biophysical journal* **2006,** *90* (4), 1175-1190.

15. Hud, N. V.; Feigon, J., Localization of divalent metal ions in the minor groove of DNA A-tracts. *Journal of the American Chemical Society* **1997,** *119* (24), 5756-5757.

16. Young, M. A.; Jayaram, B.; Beveridge, D. L., Intrusion of counterions into the spine of hydration in the minor groove of B-DNA: Fractional occupancy of electronegative pockets. *Journal of the American Chemical Society* **1997,** *119* (1), 59-69.

17. Shui, X.; McFail-Isom, L.; Hu, G. G.; Williams, L. D., The B-DNA dodecamer at high resolution reveals a spine of water on sodium. *Biochemistry* **1998,** *37* (23), 8341-8355.

18. Berger, I.; Tereshko, V.; Ikeda, H.; Marquez, V. E.; Egli, M., Crystal structures of B-DNA with incorporated 2'-deoxy-2'-fluoro-arabino-furanosyl thymines: Implications of conformational preorganization for duplex stability. *Nucleic Acids Research* **1998,** *26* (10), 2473-2480.

19. Feig, M.; Pettitt, B. M., Sodium and chlorine ions as part of the DNA solvation shell. *Biophysical Journal* **1999,** *77* (4), 1769-1781.

20. Chiu, T. K.; Kaczor-Grzeskowiak, M.; Dickerson, R. E., Absence of minor groove monovalent cations in the crosslinked dodecamer C-G-C-G-A-A-T-T-C-G-C-G. *Journal of Molecular Biology* **1999,** *292* (3), 589-608.

21. Minasov, G.; Tereshko, V.; Egli, M., Atomic-resolution crystal structures of B-DNA reveal specific influences of divalent metal ions an conformation and packing. *Journal of Molecular Biology* **1999,** *291* (1), 83-99.

22. Tereshko, V.; Minasov, G.; Egli, M., A 'Hydrat-ion' spine in a B-DNA minor groove. *Journal of the American Chemical Society* **1999,** *121* (15), 3590-3595.

23. Hud, N. V.; Sklenář, V.; Feigon, J., Localization of ammonium ions in the minor groove of DNA duplexes in solution and the origin of DNA A-tract bending. *Journal of Molecular Biology* **1999,** *286* (3), 651-660.

24. Tereshko, V.; Minasov, G.; Egli, M., The Dickerson-Drew B-DNA dodecamer revisited at atomic resolution. *Journal of the American Chemical Society* **1999,** *121* (2), 470-471.

25. Hamelberg, D.; McFail-Isom, L.; Williams, L. D.; David Wilson, W., Flexible structure of DNA: Ion dependence of minor-groove structure and dynamics. *Journal of the American Chemical Society* **2000,** *122* (43), 10513-10520.

26. Chiu, T. K.; Dickerson, R. E., 1 Å crystal structures of B-DNA reveal sequence-specific binding and groove-specific bending of DNA by magnesium and calcium. *Journal of Molecular Biology* **2000,** *301* (4), 915-945.

27. Auffinger, P.; Westhof, E., Water and ion binding around RNA and DNA (C,G) oligomers. *Journal of Molecular Biology* **2000,** *300* (5), 1113-1131.

28. Woods, K. K.; McFail-Isom, L.; Sines, C. C.; Howerton, S. B.; Stephens, R. K.; Williams, L. D., Monovalent cations sequester within the A-tract minor groove of $[d(CGCGAATTCGCG)]_2$. *Journal of the American Chemical Society* **2000,** *122* (7), 1546-1547.

29. Denisov, V. P.; Halle, B., Sequence-specific binding of counterions to B-DNA. *Proceedings of the National Academy of Sciences of the United States of America* **2000,** *97* (2), 629-633.

30. Howerton, S. B.; Sines, C. C.; VanDerveer, D.; Williams, L. D., Locating monovalent cations in the grooves of B-DNA. *Biochemistry* **2001,** *40* (34), 10023-10031.

31. Tereshko, V.; Wilds, C. J.; Minasov, G.; Prakash, T. P.; Maier, M. A.; Howard, A.; Wawrzak, Z.; Manoharan, M.; Egli, M., Detection of alkali metal ions in DNA crystals using state-of-the-art X-ray diffraction experiments. *Nucleic Acids Research* **2001,** *29* (5), 1208-1215.

32. Storhoff, J. J.; Lucas, A. D.; Garimella, V.; Bao, Y. P.; Muller, U. R., Homogeneous detection of unamplified genomic DNA sequences based on colorimetric scatter of gold nanoparticle probes. *Nature Biotechnology* **2004,** *22* (7), 883-887.

33. Bao, Y. P.; Huber, M.; Wei, T.-F.; Marla, S. S.; Storhoff, J. J.; Muller, U. R., SNP identification in unamplified human genomic DNA with gold nanoparticle probes. *Nucleic Acids Research* **2005,** *33* (2), e15/11-e15/17.

34. Zhao, J.; Tang, S.; Storhoff, J.; Marla, S.; Bao, Y. P.; Wang, X.; Wong, E.; Ragupathy, V.; Ye, Z.; Hewlett, I., Multiplexed, rapid detection of H5N1 using a PCR-free nanoparticle-based genomic microarray assay. *BMC Biotechnology* **2010,** *10* (1), 74.

35. Taton, T. A.; Mirkin, C. A.; Letsinger, R. L., Scanometric DNA Array Detection with Nanoparticle Probes. *Science* **2000,** *289* (5485), 1757-1760.

36. Alivisatos, A. P.; Johnsson, K. P.; Peng, X.; Wilson, T. E.; Loweth, C. J.; Schultz, P. G., Organization of 'nanocrystal molecules' using DNA. *Nature* **1996,** *382* (6592), 609-611.

37. Mirkin, C. A.; Letsinger, R. L.; Mucic, R. C.; Storhoff, J. J., A DNA-based method for rationally assembling nanoparticles into macroscopic materials. *Nature* **1996,** *382* (6592), 607-609.

38. Sikder, M. D. H.; Gibbs-Davis, J. M., The Influence of Gap Length on Cooperativity and Rate of Association in DNA-Modified Gold Nanoparticle Aggregates. *The Journal of Physical Chemistry C* **2012,** *116* (21), 11694-11701.

39. Jin, R.; Wu, G.; Li, Z.; Mirkin, C. A.; Schatz, G. C., What Controls the Melting Properties of DNA-Linked Gold Nanoparticle Assemblies? *Journal of the American Chemical Society* **2003,** *125* (6), 1643-1654.

40. Solie, T. N.; Schellman, J. A., The interaction of nucleosides in aqueous solution. *Journal of Molecular Biology* **1968,** *33* (1), 61-77.

41. Zheng, B.; Cheng, S.; Liu, W.; Lam, M. H.-W.; Liang, H., A simple colorimetric pH alarm constructed from DNA–gold nanoparticles. *Analytica Chimica Acta* **2012,** *741* (0), 106-113.

42. Aalberts, D. P.; Parman, J. M.; Goddard, N. L., Single-Strand Stacking Free Energy from DNA Beacon Kinetics. *Biophysical Journal* **2003,** *84* (5), 3212-3217.

43. Stoeva, S. I.; Lee, J.-S.; Thaxton, C. S.; Mirkin, C. A., Multiplexed DNA Detection with Biobarcoded Nanoparticle Probes. *Angewandte Chemie International Edition* **2006,** *45* (20), 3303-3306.

44. Gibbs-Davis, J. M.; Schatz, G. C.; Nguyen, S. T., Sharp Melting Transitions in DNA Hybrids without Aggregate Dissolution: Proof of Neighboring-Duplex Cooperativity. *Journal of the American Chemical Society* **2007,** *129* (50), 15535-15540.

45. Gruenwedel, D. W.; Hsu, C. H.; Lu, D. S., The effects of aqueous neutral-salt solutions on the melting temperatures of deoxyribonucleic acids. *Biopolymers* **1971,** *10* (1), 47-68.

46. Korolev, N.; Nordenskiöld, L., Influence of Alkali Cation Nature on Structural Transitions and Reactions of Biopolyelectrolytes. *Biomacromolecules* **2000,** *1* (4), 648-655.

47. Marky, L. A.; Breslauer, K. J., Calculating thermodynamic data for transitions of any molecularity from equilibrium melting curves. *Biopolymers* **1987,** *26* (9), 1601-1620.

48. Korolev, N. I.; Vlasov, A. P.; Kuznetsov, I. A., Thermal denaturation of Na- and Li-DNA in salt-free solutions. *Biopolymers* **1994,** *34* (9), 1275-1290.

49. Burda, J. V.; Šponer, J.; Leszczynski, J.; Hobza, P., Interaction of DNA Base Pairs with Various Metal Cations (Mg^{2+}, Ca^{2+}, Sr^{2+}, Ba^{2+}, Cu^{+}, Ag^{+}, Au^{+}, Zn^{2+}, Cd^{2+}, and Hg^{2+}): Nonempirical ab Initio Calculations on Structures, Energies, and Nonadditivity of the Interaction. *The Journal of Physical Chemistry B* **1997,** *101* (46), 9670-9677.

50. Sundaresan, N.; Thomas, T.; Thomas, T. J.; Pillai, C. K. S., Lithium Ion Induced Stabilization of the Liquid Crystalline DNA. *Macromolecular Bioscience* **2006,** *6* (3), 250-250.

51. Oh, J.-H.; Lee, J.-S., Designed Hybridization Properties of DNA–Gold Nanoparticle Conjugates for the Ultraselective Detection of a Single-Base Mutation in the Breast Cancer Gene BRCA1. *Analytical Chemistry* **2011,** *83* (19), 7364-7370.

52. Smith, B. D.; Dave, N.; Huang, P.-J. J.; Liu, J., Assembly of DNA-Functionalized Gold Nanoparticles with Gaps and Overhangs in Linker DNA. *The Journal of Physical Chemistry C* **2011,** *115* (16), 7851-7857.

53. Storhoff, J. J.; Lazarides, A. A.; Mucic, R. C.; Mirkin, C. A.; Letsinger, R. L.; Schatz, G. C., What Controls the Optical Properties of DNA-Linked Gold Nanoparticle Assemblies? *Journal of the American Chemical Society* **2000,** *122* (19), 4640-4650.

54. Cho, M.; Han, M. S.; Ban, C., Detection of mismatched DNAsvia the binding affinity of MutS using a gold nanoparticle-based competitive colorimetric method. *Chemical Communications* **2008,** (38), 4573-4575.

55. Azam, M. S.; Weeraman, C. N.; Gibbs-Davis, J. M., Halide-Induced Cooperative Acid–Base Behavior at a Negatively Charged Interface. *The Journal of Physical Chemistry C* **2013,** *117* (17), 8840-8850.

56. Cheng, W.; Dong, S.; Wang, E., Iodine-Induced Gold-Nanoparticle Fusion/Fragmentation/Aggregation and Iodine-Linked Nanostructured Assemblies on a Glass Substrate. *Angewandte Chemie International Edition* **2003,** *42* (4), 449-452.

57. Wei, S.-C.; Hsu, P.-H.; Lee, Y.-F.; Lin, Y.-W.; Huang, C.-C., Selective Detection of Iodide and Cyanide Anions Using Gold-Nanoparticle-Based Fluorescent Probes. *ACS Applied Materials & Interfaces* **2012,** *4* (5), 2652-2658.

58. Lee, I. L.; Sung, Y.-M.; Wu, C.-H.; Wu, S.-P., Colorimetric sensing of iodide based on triazole-acetamide functionalized gold nanoparticles. *Microchimica Acta* **2014,** *181* (5-6), 573-579.

CHAPTER 5

The Influence of Divalent Cations on the Acid-Base Behavior of the Silica/Water Interface

Sum Frequency Generation experiments (**Figure 5.8**) were performed by Dr. Md Shafiul Azam, Post Doctoral Fellow, Department of Chemical Engineering, University of Alberta.

5.1 Introduction

Being one of the most abundant mineral oxides in the earth's crust, the silica/water interface plays a major role in nature. The hydrogen-bonded network of water undergoes serious perturbation in the presence of silica, due to the inherent negative charge of the silica surface in the presence of water of pH > 3 and gives rise to important interfacial properties like the interfacial potential that in turn influences surface-specific processes such as dissolution,[1-5] adsorption,[4, 6-11] precipitation,[12] oxidation,[13] reduction,[14] and photolytic water splitting reactions.[15] Processes involving interfacial interactions with water also depend on the acid-base chemistry of the silica/water interface.[16-18] To better comprehend interfacial chemical processes a thorough understanding of the water/silica structure and the extent of charging at these surfaces is, therefore, very important.[1, 4-6, 9, 19-31]

The surface acidity based on the deprotonation of silanol groups results in a net change in the surface charge over a broad range of pH. The deprotonation of the silica surface perturbs the hydrogen-bonded structure of water at the interface. Moreover, the water structure is also proposed to be partly responsible for the pK_a values of the surface sites, which are different from their bulk analogs.[31-36] The interaction of silica and water also depends on the presence of foreign electrolytes as well as the surface charge density. Owing to the complex relationship between the surface acidity and the water structure, one would expect that the intrusion of such electrolytes should have a great effect on the surface charge density or more simply the acid-base behavior of the interface, which has indeed been observed.[37-

[38] Interestingly, the planar silica surface has been found to possess two distinct equilibria giving rise to two pK_a values over a broad pH range that are both attributed to silanol groups that differ because of the local hydrogen-bonding environment.[33, 39-40, 41]

Studying the acid-base equilibria of silica particles is particularly difficult because of the colloidal instability at lower pH.[32] Therefore, the utilization of silica particles in potentiometric titrations was reported for a limited pH range, resulting in a limited understanding of the overall acid-base properties. One solution to address the difficulty in working with colloidal silica is to utilize flat silica surfaces made of fused silica as a bulk material. Studying the silica/water interface with such macroscopic silica samples is particularly difficult as most techniques for colloidal samples are not well-suited for large planar silica samples. However, nonlinear optical processes like second harmonic generation (SHG) and sum frequency generation (SFG) are sensitive to the non-centrosymmetric structure of the solid/liquid interface allowing one to study the interface over a broad pH range.[11, 33, 42-44] SHG makes use of that fact that the second harmonic electric field can only be generated from a material or interface where inversion symmetry is broken. For the silica/water system, the non-resonant SHG signal produced from the interface is related to the extent of ordered water molecules at the interface. Since the ordered structure of the water at the interface is largely dependent on the surface charge density of the solid surface, SHG can probe changes in the interfacial charge, therefore, the acid-base properties of the planar silica surface.[37, 39-40] SFG on the other hand probes the vibrational modes of the ordered water molecules at the interface and the extent of the hydrogen-bonding network, which is strongly influenced by the interfacial potential that stems from the charged surface.[45-50] SFG studies have shown that two distinct water structures are present at the silica/water interface. These differing structures are strongly and weakly coordinated water molecules at the interface based on the extent of hydrogen bonding.[45] The corresponding distinct vibrational modes were found to vary significantly over a broad pH range.

Surface deprotonation has been found to be very sensitive to the electrolyte composition[18, 26-29] and ionic strength.[3, 35, 48-49] Such sensitivity has been shown to be highly specific to the polarizability of the ions present, or more specifically the identity of the ions present.[2-3, 51-53] Recently, our group monitored the deprotonation of the two distinct acidic sites of silica in the presence of different alkali chloride electrolytes over a wide pH range using SHG,[37] where it was shown that the surface pK_a was largely modulated by the size of the alkali metal cations. Understanding such behavior is very important to map the surface charge density and electronic structure of silica over a wide pH range, which in turn is important for accurate environmental modeling and technological applications where silica is used as a major component. In this study, we have aimed to understand the acid-base properties of the silica surface in the presence of smaller divalent cations at the buried silica/water interface as these cations have been shown to play an important role in the separation of oil from sand in the oil-sand industry.[54-55]

5.2 Experimental Section

5.2.1 General Data

Calcium chloride hexahydrate (Fluka Chemika, >99%), Magnesium chloride hexahydrate (Caledon Laboratory, >99%), Sodium chloride (EMD Chemicals, ≥99%), sodium hydroxide (Sigma-Aldrich, ≥97%) and sulfuric acid (Caledon Laboratory) were used in the SHG and SFG experiments. Freshly purified ultrapure deionized water (18.2 MΩ·cm water form a MilliQ-Plus ultrapure water purification systems by the Millipore corporation) was used in all experiments. The pH of all the solutions was measured using an Orion 2–Star Benchtop pH meter (Thermo scientific) with a double-junction Ag/AgCl (Orion, 9107APMD). The pH meter was calibrated with pH 4.00 and pH 7.00 buffers for the pH variation experiments ranging pH 7 – 2 and calibration was performed with pH 7.00 and pH 10.00 buffers for those ranging pH 7 – 13.

A UV-grade fused silica (SiO_2) hemisphere was used in the SHG experiments, whereas an IR grade SiO_2 hemisphere was used in the SFG experiments. Both types of hemispheres were 1 inch in diameter and purchased from ISP Optics. The hemispheres were cleaned prior to mounting on a custom-built Teflon cell assembly with translational stages. These translational stages can be moved in three dimensions in space (x,y,z–directions). The position of the interface was perpendicular with respect to the laser table. Filling the Teflon cell with ultrapure Milli-Q water formed the silica/water interface. The pH and the salt concentrations were routinely changed during the pH titration and salt titration experiments, therefore, the aqueous phase was purposefully exposed to easily change and monitor the pH and the salt concentration in all experiments. The design of this cell has been previously reported by our group.[37] The hemisphere cleaning process comprised sonication in freshly produced ultrapure Milli-Q water and methanol followed by Nochromix treatment and plasma cleaning. The flat surface of the hemisphere was treated with Nochromix solution (Godax Laboratories, 5% w/v solution in H_2SO_4; added dropwise onto the hemisphere surface) for 1 hour followed by extensive rinsing and sonication in Milli-Q water to avoid traces of leftover acid. The hemisphere was finally sonicated in methanol and dried in an oven at 100 ºC for 30 minutes. The lens was then cooled to room temperature and plasma cleaning performed using a *Harrick Plasma* plasma cleaner (PDC-32G) in the air for 3 minutes.

5.2.2 Femtosecond (fs) Laser System Setup

A femtosecond pulsed laser system was used to generate visible laser light (λ = 550 – 580 nm) for the SHG experiments and tunable, broadband IR light (2850 – 3650 cm^{-1}) for the SFG experiments. The laser system consists of a Ti:Sapphire oscillator (Spectra Physics, Mai Tai, 80 MHz, 1.0 W) which produces 800-nm pulses (<100 fs, FWHM ~12 nm). Pulses produced from the Mai Tai were used as the seed pulses in a regenerative amplifier (Spitfire Pro, Spectra Physics) pumped by a Nd:YLF laser (Spectra Physics, Empower, 11.5 W) to give femtosecond pulses with high peak power (1 kHz, 3.5 mJ per pulse). This Spitfire output was split using a 30/70 beam splitter to provide input (1 kHz, 1.1 mJ) to an optical parametric amplifier (Spectra Physics OPA-800CF) for generating light tunable in the visible region. In the SHG experiments, the wavelength of the incident light was tuned to either 550 ± 2 nm or 580 ± 2 nm. The 70% reflected light (1 kHz, 2.4 mJ) was used to pump a computer-controlled optical parametric amplifier (Coherent, TOPAS) to generate tunable IR light for SFG experiments. A schematic representation of the entire laser system is shown in Figure 5.1.

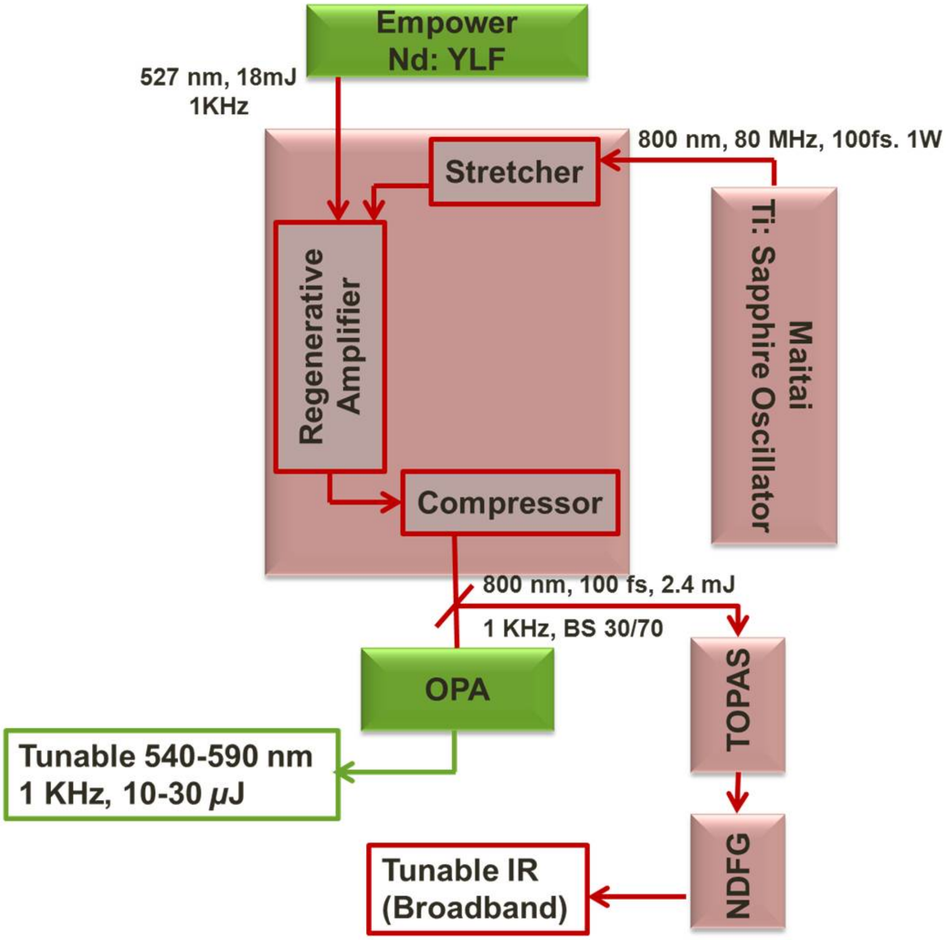

Figure 5.1. Schematic representation of the femtosecond laser system used for the SHG and SFG experiments performed in this study. The Ti:Sapphire oscillator produces femtosecond pulses that are used as seeds in a regenerative amplifier pumped by a Nd:YLF laser. The amplified beam is split by passing through a 30/70 beam splitter (BS 30/70) and the transmitted lights are used to pump an

optical parametric amplifier (OPA) to generate visible light tunable in the 540 – 590 nm ranges and a computer controlled OPA to produce the broadband IR (770 – 9090 cm^{-1}).

5.2.3 Second Harmonic Generation Experiments

The 550 ± 2 nm or 580 ± 2 nm OPA output (10 – 30 μJ) was attenuated by a dual wheel neutral-density filter (New Focus) to 300 – 600 nJ prior to focusing onto the hemispherical surface of the lens. A $\lambda/2$ wave plate and Glen-Thompson polarizer (B. Halle, UV-grade Calcite, PGT 4.10) were used to generate p-polarized light (right after attenuation) to focus on the silica/water interface. Experiments performed with s-polarized light have been shown to have similar pH-dependence as p-polarized light.[56] SHG was monitored in reflection geometry with the incident beam 62° from surface normal (Figure 5.2). Incident light with power > 750 nJ per pulse led to deviations from the quadratic relationship between incident power and SHG signal intensity; therefore, all experiments were performed below this critical power. The SHG light (λ_{SHG} = 275 nm or 290 nm) reflected from the interface was recollimated and focused onto a monochromator (Optometrics Corp., Mini-Chrom MC1-02) coupled to a photomultiplier tube (PMT, Hamamatsu Photonics). A bandpass colored glass filter (Thorlabs, UG5) was used to filter out the reflected fundamental (550 nm or 580 nm). The electrical response of the PMT was then amplified with a pre-amplifier and counted with a gated photon counter (Stanford Research Systems). The SHG light shows a quadratic power dependence and itself is monochromatic in nature. Therefore, prior to performing all pH-titration and salt titration experiments we examined the power dependence and wavelength dependence for the final confirmation of SHG.

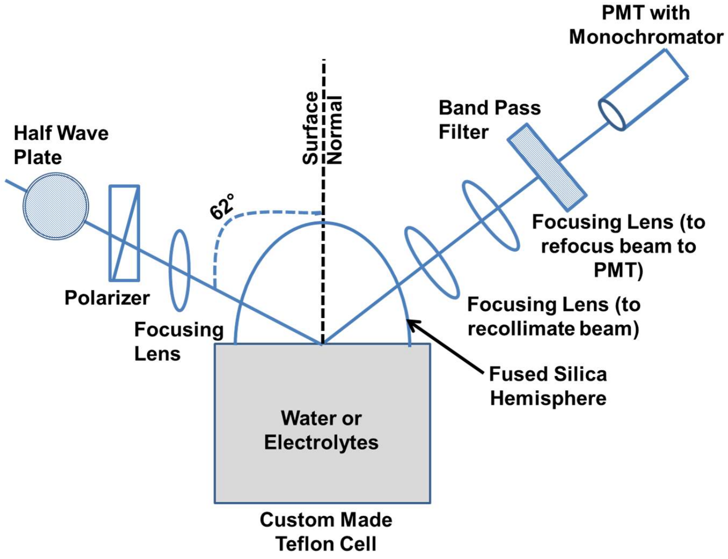

Figure 5.2. Top view of the second harmonic generation assembly in our laboratory. The fundamental light is processed through a half wave plate and a polarizer to select p- polarization. The beam was focused on a fused silica hemisphere surface, assembled with a custom made Teflon cell assembly and in direct contact with the aqueous phase, at 62° with respect to the surface normal. The SHG was reflected through a recollimating lens, passed through a band pass filter to remove residual fundamental light from the laser and focused on a PMT (photomultiplier tube) using focusing lens and a monochromator.

5.2.4 pH Titration SHG Experiments

The properly cleaned sample hemisphere was assembled with the Teflon cell assembly to complete the SHG set up. Prior to performing a pH variation experiment, the cell was rinsed three times with Milli-Q water to condition the sample. The laser beam was properly aligned in the presence of Milli-Q water to optimize the SHG set up for maximum signal intensity. Finally, the Teflon cell was flushed one more time with the background solution (aqueous 0.1 M $CaCl_2$ or $MgCl_2$) right before performing an equilibration run for 30 min with 10 mL electrolyte solution. Each experiment was performed using a freshly cleaned hemisphere. Such caution is crucial to study the silica/water interface at both high and low pH to avoid hysteresis.[57] The pH variation experiments were performed in two distinct stages. The low pH experiments were started at pH 7 followed by addition of acid to lower pH to ~ 2. The high pH experiments were started at the pH of electrolyte solution followed by addition of base to increase pH to ~ 13 or until the solution appeared cloudy. The pH of freshly produced Milli-Q water and that of the background electrolyte solution was below 7, therefore, the starting value for the low pH experiments were always adjusted with NaOH solution prepared with the same sample solutions. Due to poor solubility of $Ca(OH)_2$ and $Mg(OH)_2$ at room temperature and high concentrations, we used NaOH as a base to increase the pH of solutions in all experiments. Since NaOH provides Na^+ ions in an aqueous medium, the question was raised if such a small amount of Na^+ ions could influence the experimental results. To resolve this issue, we have used 10 mM concentration of NaCl in the background for all solutions of 100 mM $CaCl_2$ and $MgCl_2$. Therefore, such small contribution of Na^+ from the alkaline solution shall have a negligent effect on all experiments. SHG was monitored for the first 30 minutes period to confirm that the silica/electrolyte interface had reached equilibrium. Aqueous 10 mM NaCl and 100 mM MCl_2 ($M = Ca^{2+}$ or Mg^{2+})

solutions were used for preparing the dilute HCl solution, which was then added in μL aliquots to lower the pH of the sample. The resulting acidified solution was allowed to equilibrate for 3 minutes, and the bulk pH was then measured with the benchtop pH meter followed by recording SHG for ~ 2 minutes. These steps were repeated until the bulk pH solution reached a value of ~ 2. The SHG data for the high pH experiments were recorded in a similar fashion to the low pH experiments where NaOH dissolved in 10 mM NaCl and 100 mM MCl_2 solution was used to increase the pH until it reached a value of ~ 13 or the solution appeared to be cloudy due the formation of insoluble $Ca(OH)_2$ and $Mg(OH)_2$.

5.2.5 Salt Concentration Variation SHG Experiments

The salt titration experiments were performed in a similar fashion to the pH titration experiments. The sample was conditioned with Milli-Q water, and the SHG was optimized. The background solution for these experiments was aqueous 10 mM NaCl. SHG was recorded for 30 minutes with the background solution to allow complete equilibration. Aqueous 10 mM NaCl solution was used to prepare 1.0 M MCl_2 samples for the titration experiments. Small aliquots of sample solutions of 1.0 M MCl_2 were added to the initial 10 mL background solution in μL and allowed to equilibrate for 3 minutes followed by recording the SHG data for ~ 2 minutes. The experiments were continued until the concentration of Ca^{2+} or Mg^{2+} reached ~ 0.4 M, or the SHG signal leveled off.

5.2.6 Broadband Vibrational Sum Frequency Generation Experiments

All of the sum frequency generation experiments were performed and analyzed by Dr. Md Shafiul Azam a postdoctoral fellow in the groups of Prof. Chad Liu and Prof. Hongbo Zeng in the Department of Chemistry and Materials Engineering at the University of Alberta. The reflected 70% of the amplified Spitfire Pro output (2.4 W) was used to pump a computer controlled TOPAS-C/NDFG optical parametric amplifier (Light Conversion) to generate broadband infrared light. The resulting IR was tuned in the 3000 – 3600 cm^{-1} ranges for probing the resonant O-H stretch of water molecules at the interface. Spitfire regeneratively amplified 800 nm (120 fs) visible light was broadened to a picosecond (ps) pulse using a Fabry-perot etalon (FWHM ~ 10 cm^{-1}). The p-polarized fs IR (~ 10 – 12 mJ/pulse) and the p-polarized ps visible beam (~ 10 mJ /pulse) were focused on a fused silica hemisphere (ISP optics, 1 inch diameter, IR-grade SiO_2), assembled in a similar type of custom made Teflon cell assembly to the SHG setup. The incident angles of the IR and visible beam onto the silica/water interface were kept 66° and 64°, respectively, from the surface normal. The two beams were aligned spatially and temporally to achieve maximum sum frequency generation. The resulting SFG emitted from the interface was recollimated, filtered with a bandpass filter to remove residual 800 nm incident light (Chroma, HQ 617/70 M), passed through a polarizer to select the s-polarized SFG, and focused onto a spectrograph (Acton SP-2556 Imaging Spectrograph, grating: 1800 G/mm with 500-nm blaze wavelength) connected to a thermoelectrically cooled, back-illuminated, charge coupled device camera

(Acton PIXIS 100B CCD digital camera system, 1340 x 100 pixels, 20 mm x 20 mm pixel size, Princeton Instruments). A reference spectrum was recorded with a gold-coated IR grade silica hemisphere with infra-red absorption maxima at 3160 cm^{-1}, 3280 cm^{-1}, 3390 cm^{-1} and 3500 cm^{-1}. All spectra were recorded using these wavelengths for the silica/water interface. The final spectra of the silica/water interface were obtained by adding the recorded spectra at above mentioned wavelengths and normalizing with respect to the summed gold-coated reference spectra.[58]

5.2.7 Data Processing

At least two sets of data were reproduced for all the experiments. The SHG intensity was recorded with a LabVIEW 2009 (National Instruments) data acquisition program. The average SHG intensity for a particular MCl$_2$ concentration or pH data point was measured from at least 120 counts (~1 count per second) and the SHG E-field ($E_{2\omega}$) was determined by taking the square root of this average intensity. The resulting $E_{2\omega}$ values were plotted against pH or MCl$_2$ concentration and shown in Figure 5.5 and 5.7, respectively. A sigmoidal function (equation 5.1) was used to fit the $E_{2\omega}$ versus pH plot for determination of the pH$_{0.5}$ at which half of the silanol groups were deprotonated in the low pH region, using Igor Pro (version 6.30):

$$f = base + \frac{\max}{1 + \exp(\frac{x_{half} - x}{rate})} \tag{5.1}$$

where x_{half} is pH$_{0.5}$, *rate* is the sharpness of the transition, and *max* and *base* are maximum and minimum, respectively. The resulting data were smoothed using the Binomial smoothing function in Igor Pro (version 6.30) with a smoothing factor of 2 for all of the SHG experiments.

5.3 Using Second Harmonic Generation to Study the Acid-Base Chemistry of the Silica/Water Interface

Interfacial acid-base chemistry remains a challenging task to study although there are ample methods to probe the acid-base properties of bulk materials. SHG, however, is a surface specific technique and is highly selective and sensitive to interfacial charges, so it was selected for this study of the effect of divalent cations on the acid-base chemistry of planar silica. The second harmonic electric field is dependent on the second order susceptibility, $\chi^{(2)}$ and the incident electric field, E_ω according to:

$$E_{2\omega} = \chi^{(2)} E_\omega E_\omega \tag{5.2}$$

The second order susceptibility, $\chi^{(2)}$ is a bulk quantity that is related to its molecular level property, the molecular hyperpolarizability, $\beta^{(2)}$ by

$$\chi^{(2)} = N \cdot \langle \beta^{(2)} \rangle \tag{5.3}$$

where N is the total number of molecules. The molecular hyperpolarizability, $\beta^{(2)}$ is the property of a molecule that determines its ability to induce polarization in the presence of an electric field at an oscillation frequency that is twice the frequency of the incident electric field ($P_{2\omega}$). The term $\langle \beta^{(2)} \rangle$ refers to an orientational average of the all the molecules in the bulk material. Therefore, a system with centrosymmetry or inversion symmetry will give rise to $\langle \beta^{(2)} \rangle = 0$, which in turn makes $\chi^{(2)} = 0$ and $E_{2\omega} = 0$, leading to no second harmonic generation.[33] The silica/water interface does not possess inversion symmetry, unlike the bulk fused silica and water phases. Therefore, any SHG signal arising from the sample is specific for interfacial processes. SHG is also influenced by the presence of a static electric field. This static field arises at the silica/water interface when the surface silanol groups undergo deprotonation resulting in an overall negative charge at the silica surface. Specifically, the contribution of the static field generated by interfacial charges depends on the third-order susceptibility, $\chi^{(3)}$,[39-40] which changes the expression of the second-order electric field,

$$E_{2\omega} \propto P_{2\omega} = \chi^{(2)} E_{\omega} E_{\omega} + \chi^{(3)} E_{\omega} E_{\omega} \Phi_0 \qquad (5.4)$$

where Φ_0 is the interfacial potential. At high salt concentrations, this interfacial potential Φ_0 has been shown to depend directly on the surface charge density, therefore, it is sensitive to pH changes.[33, 59] On the other hand the second and third order susceptibilities, $\chi^{(2)}$ and $\chi^{(3)}$ respectively are shown to be much less pH sensitive, and thus assumed to have a negligible contribution.[33, 60] Therefore, the change in the SHG intensity can be directly correlated with the extent of protonation and deprotonation of the surface when the bulk pH is varied.[33, 35]

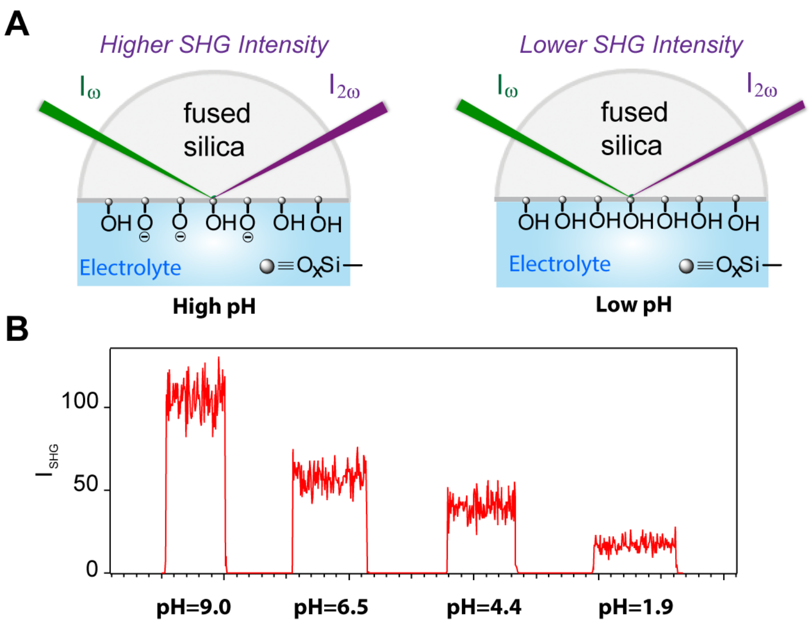

Figure 5.3. A.) Surface silanol functional groups are mostly deprotonated at high pH that results in an increase in the SHG intensity (on the left). At low pH, protonation of the surface siloxides results in a decrease in the SHG signal (on the right). B.) SHG intensity increases as pH is increased, as it is proportional to the number of interfacial charges. The data at pH 9.0 were recorded on a different sample and so represent the relative increase in the SHG signal rather than absolute comparison to the other lower pH values.

The change in SHG intensity is shown in Figure 5.3 as the pH of the medium was varied. The source of this increase was the pH induced deprotonation of the surface silanol groups.[39] The expectation from the pH variation experiments was to obtain two sigmoidal transitions as the silica/water interface possesses two distinct acidic sites, attributed to a more acidic silanols in contact with weakly hydrogen-bonded water and the less acidic silanols in contact with strongly hydrogen-bonded water.[8, 39-40, 45, 47, 61-63] Previous work in our group showed that these two distinct pK_a values were strongly dependent on the identity of cations present in the aqueous phase (Figure 5.4).[37]

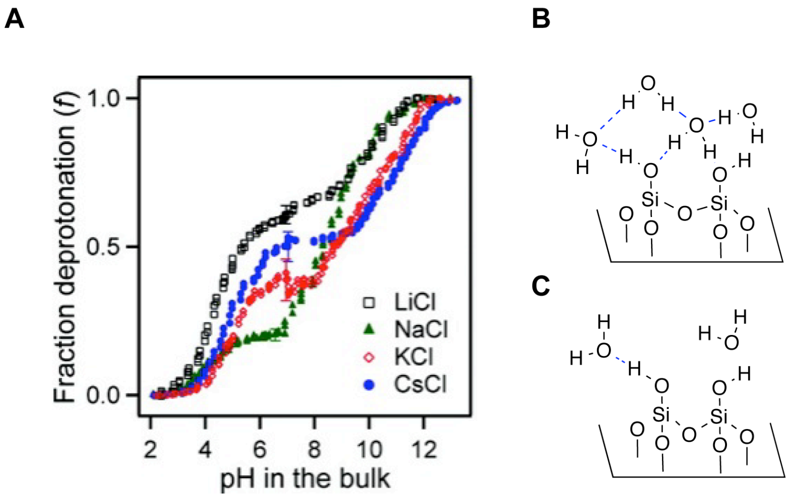

Figure 5.4. A.) pH titration experiments on silica/water interface exhibit two distinct sigmoidal transitions. The lower transition is for surface silanols coordinated with weakly hydrogen-bonded water molecules at the interface, and the upper transition corresponds to silanol groups associated with the strongly hydrogen bonded-water molecules. The SHG E-field was correlated to the fraction deprotonated in this figure. Strongly and weakly hydrogen-bonded water molecules at the silica/water interface are depicted in (B) and (C) respectively. A portion of the figure was adapted and modified with permission from reference 37.[37]

Specifically, according to the work of our lab,[37] the affinity of the alkali ions for the siloxide functional groups was very different, particularly for the silanol sites deprotonated at high pH. The extent of deprotonation was shown to increase in the presence of smaller monovalent cations. These cations do not necessarily neutralize the surface but rather screen the surface negative charges resulting in increased deprotonation.[35] The silanol deprotonation at the silica surface can be expressed as:

$$SiOH + H_2O \underset{}{\overset{K_a}{\rightleftharpoons}} SiO^- + H_3O^+ \qquad (5.5)$$

where K_a is the deprotonation constant. The surface siloxides underwent electrostatic interaction in the presence of a monovalent cation M^+,

$$SiO^- + M^+ \overset{K_b}{\rightleftharpoons} SiO^- \cdot M^+ \qquad (5.6)$$

where K_b is the binding constant of the cations. The overall equilibrium becomes:

$$K_a^{effective} = K_a \cdot K_b = \frac{\left[SiO^- \cdot M^+\right]\left[H_3O^+\right]}{\left[SiOH\right]\left[M^+\right]} \qquad (5.7)$$

The value of $pK_a^{effective}$ can be determined from the $pH_{0.5}$ that corresponds to the x_{half} from equation 5.1 and the cation concentration M^+ by

$$pK_a^{effective} = p(K_a \cdot K_b) = pH_{0.5} - pM^+ \qquad (5.8)$$

The ability of ions to disrupt the structure of interfacial water[50] makes it interesting to study the water structure in the presence of cations of various sizes. Small and hard cations[64] are expected to strongly interact with the surface siloxides leading to more deprotonation of the surface silanol groups. Indeed, our group reported that Na^+ causes a more acidic surface than Cs^+ does.[37] A higher deprotonation represents a higher K_a, which in turn lowers the pK_a of the surface. Unfortunately, the effects of the smaller divalent cations on these electrolyte-surface interactions still remain undiscovered over a large pH range.

5.4 Effect of MCl_2 ($M = Ca^{2+}$ or Mg^{2+}) on the Acid-Base Equilibria of Silica/Water Interface

Figure 5.5 shows the pH dependence of the SHG electric field for the silica/water interface in the presence of 0.1 M $CaCl_2$ (Figure 5.5, A and B) and 0.1 M $MgCl_2$ (Figure 5.5 C and D) with a background concentration of 10 mM NaCl (see section 5.2.4.). The E_{SHG} or $E_{2\omega}$ measured in these experiments is proportional to the fraction of deprotonated silanols at the interface according to equation 5.4 and the constant capacitance model.[59] The low pH titration in the presence of $CaCl_2$ revealed a sigmoidal transition with a $pH_{0.5}$ value of 4.25 ± 0.04. This value was consistent with earlier work from our lab[37] that reported similar results for the chloride salts of other monovalent cations (Li^+, Na^+, K^+, and Cs^+).

The high pH dependence of the SHG signal in the presence of Ca^{2+} or Mg^{+2}, however, was highly unexpected as the SHG intensity increased with increasing pH followed by a gradual decrease with further increase in pH (Figure 5.5, B and D). For the high pH titration with $CaCl_2$, the SHG signal increased with increasing pH of the aqueous medium until it reached a plateau at pH ~ 10. This suggested saturation of deprotonation under the influence of Ca^{2+}'s screening interaction. As the pH was increased to further higher values, the SHG signal started dropping. This decrease in the SHG intensity was suggestive of partial neutralization of the surface charges. Such neutralization is indicative of a stronger silica-Ca^{2+} interaction than simple screening, where ion-pair formation takes place rather than long-range electrostatic interactions. Complete neutralization was expected when the final SHG intensity was equal to the initial SHG intensity at pH 2. For this system, we could not proceed to further higher pH to see if the signal dropped down to the initial intensity due to the low solubility of the $CaCl_2$ electrolyte solution at pH > 12 (Figure 5.6).

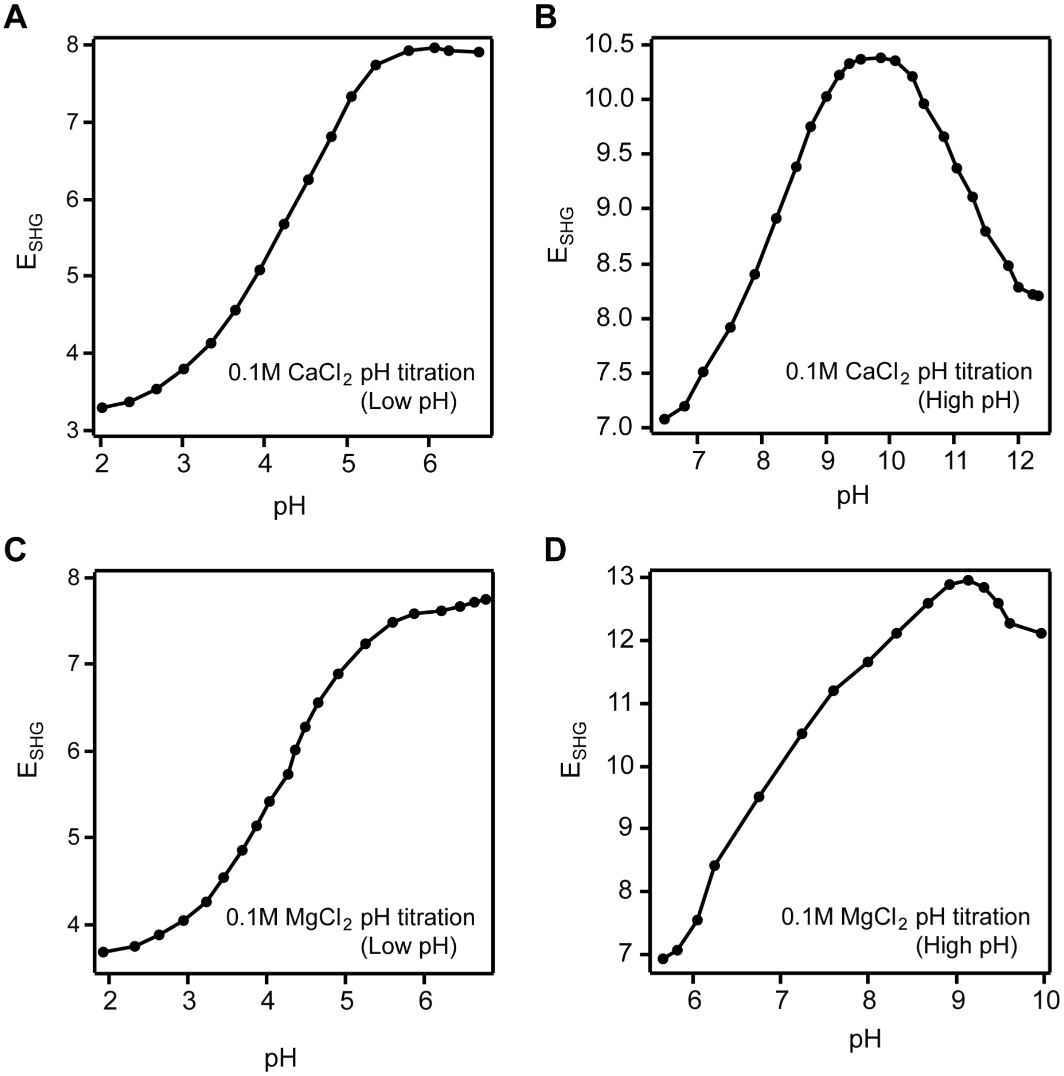

Figure 5.5. The pH titration curves of the silica/water interface in the presence of 0.1 M $CaCl_2$.: A.) at low pH and B.) at high pH.. The pH titration curves of

silica/water interface in the presence of 0.1 M $MgCl_2$: C.) at low pH and D.) at high pH.

We found that $MgCl_2$ also exhibited a sigmoidal transition for the low pH titration with a $pH_{0.5}$ value of 4.17 ± 0.01 (Figure 5.5C). Similar to $CaCl_2$, we observed an unusual decrease in $E_{2\omega}$ when the pH was greater than 9 in the high pH titration experiments. Reaching the plateau at a lower pH value than was observed for the Ca^{2+} system indicated the stronger affinity of Mg^{2+} towards SiO^- compared to that of Ca^{2+}, which was also supported by the lower $pH_{0.5}$ value for $MgCl_2$ than $CaCl_2$ in the low pH titration. At pH > 10 the $MgCl_2$ solution became cloudy, therefore, limiting the pH range that was explored.

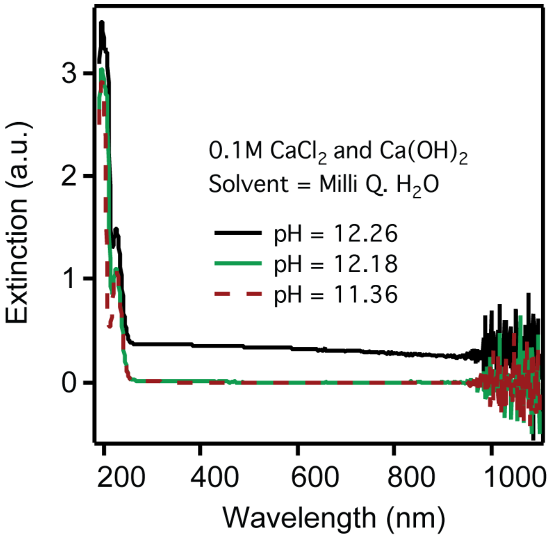

Figure 5.6. UV-vis absorption spectra of post-SHG experiment of $CaCl_2$ sample solutions; the solution remained clear at pH 12.2 and turned cloudy at pH 12.3. The scattering in the UV-vis spectrum for the pH 12.3 sample was indicative of precipitation.

5.5 M^{2+} Binding Equilibria at the Silica/Water Interface

The unusual pH dependent intensity decrease at higher pH was explored further by probing the salt-concentration dependent surface behavior at a particular pH. For most surfaces at low pH, the total number of charges on the surface is less than that at higher pH. Therefore, the addition of only a small concentration of cations should screen the entire surface charge when the pH is low compared to when the pH is high, and more surface charges are present. Such phenomena were observed for the silica/water interface in the presence of NaCl (Figure 5.7C). Specifically, we performed two salt titration experiments at pH 6 and 10.5. We observed a steeper screening curve for NaCl at lower pH than that at higher pH as expected. However, we observed the opposite trend for Ca^{2+} (Figure 5.7A). At pH 10.5, we found the salt titration curve was steeper than that at pH 6. This data suggested that the surface siloxides at pH underwent partial neutralization in the presence of the divalent ions. Therefore, at pH 10.5, the surface possessed less negative charge than pH 6 for the interface in the presence of $CaCl_2$ and $MgCl_2$. A simple screening process was not enough to explain the increase in the affinity of these divalent cations in neutralizing the interfacial negative charges. The lower charge density at higher pH is indicative of a more complex interaction and possibly direct bonding of the silica and calcium. We observed similar titration curves for Mg^{2+} (Figure 5.7B) as well, where the titration curve at pH 9.5 was steeper than pH 6. Moreover, according to equation 5.4, a surface with a larger number of charges should result in higher SHG intensity. Indeed, from the salt variation experiments, we observed a higher final

E_{SHG} at pH 10.5 than at pH 6 for NaCl at the same electrolyte concentration. This indicated that the surface possessed more negative charges at pH 10.5 even after screening interaction with Na^+ than at pH 6. On the contrary, we found that for $CaCl_2$ and $MgCl_2$, the final value of E_{SHG} was lower at pH 10.5 than at pH 6. These observations further confirmed that the net negative charge at high pH for $CaCl_2$ and $MgCl_2$ was less compared to that of the low pH.

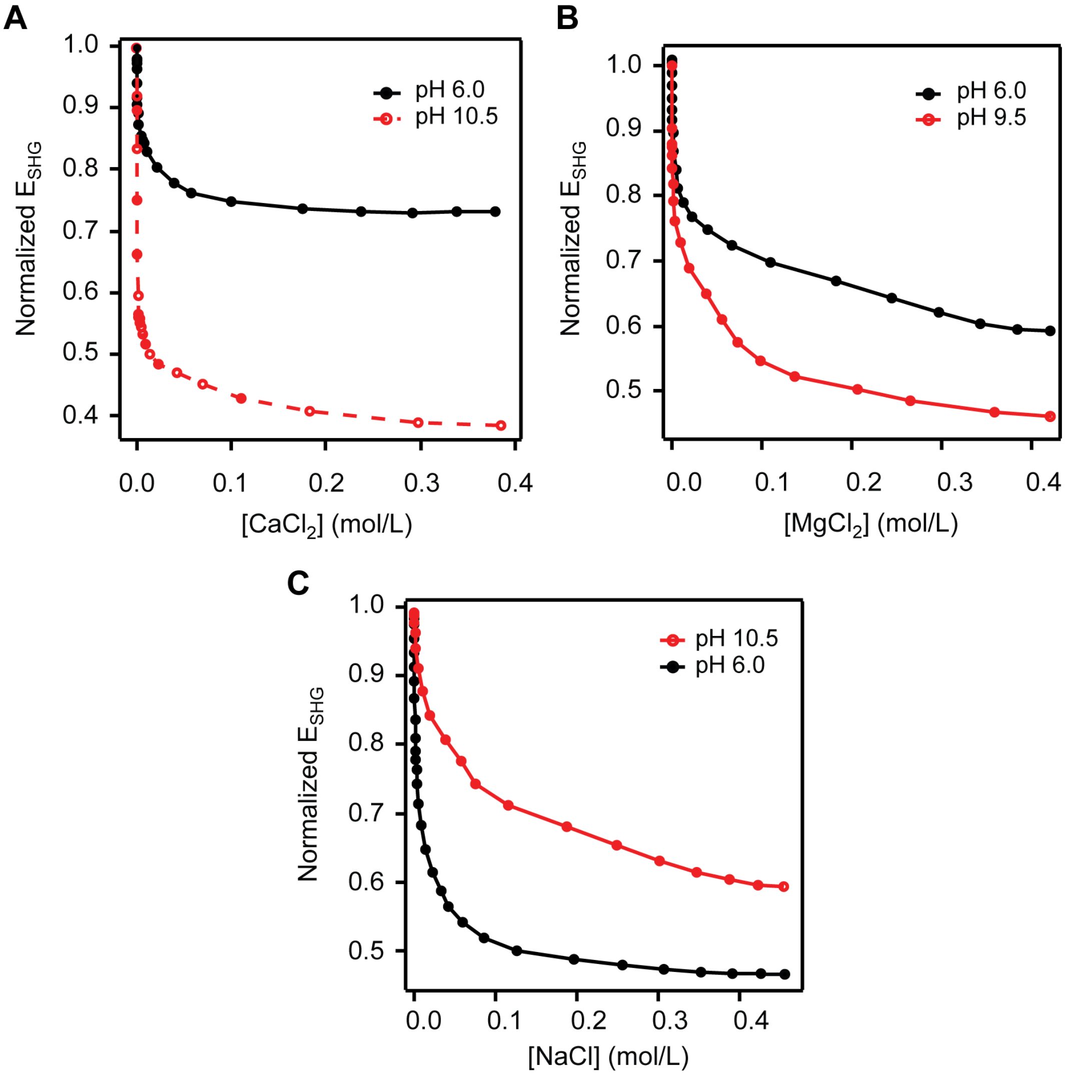

Figure 5.7. A.) Normalized E_{SHG} of the silica/water interface as a function of $CaCl_2$ concentration at pH 6 and 10.5. B.) Normalized E_{SHG} of the silica/water interface as a function of $MgCl_2$ concentration at pH 6 and 9.5. C.) Normalized E_{SHG} of the silica/water interface as a function of NaCl concentration at pH 6 and 10.5.

5.6 Vibrational Sum Frequency Generation Spectroscopic Analysis

Vibrational sum frequency generation (SFG) is a very useful nonlinear optical spectroscopic technique to probe changes in the amount of ordered water molecules at the interface. These experiments are performed in the presence of two distinct incident electric fields on the interface with frequencies in the visible and infrared region. A large increase in the second-order susceptibility $\chi^{(2)}$ is observed when the vibrational frequency of the water molecules is in resonance with the incident infrared field. The second-order electric field E_{SFG} has a similar relationship as E_{SHG} to $\chi^{(2)}$:

$$E_{SFG} = \chi^{(2)} E_{Vis} E_{IR} + \chi^{(3)} E_{Vis} E_{IR} \Phi_0 \tag{5.9}$$

where Φ_0 is the interfacial potential, E_{Vis} and E_{IR} are the incident visible and IR electric fields, respectively, and $\chi^{(2)}$ and $\chi^{(3)}$ are the second and third order susceptibilities, respectively. An increase in $\chi^{(2)}$ will lead to an increase in the electric field at the sum of the two incident frequencies (E_{SFG}). Like SHG, the second-order susceptibility $\chi^{(2)}$ is non-zero for noncentrosymmetric medium. Therefore, only ordered water molecules contribute to the resonantly enhanced part of the $\chi^{(2)}$ term. The addition of alkali chlorides to the silica/water interface has been shown to decrease the SFG intensity. [45, 48-49] Such a decrease was attributed to screening of interfacial charges in the diffuse and compact double layer, which led to a decrease in the amount of ordered water molecules. To determine the amount of the ordered water molecules at the silica/water interface in the presence of Ca^{2+} and Mg^{2+}, we monitored the resonantly enhanced vibrational sum frequency generation (SFG) signal in the absence and presence of these electrolytes.

In the SFG spectra, we observed two peaks at ~ 3200 cm^{-1} and at ~ 3400 cm^{-1}, which is typical of the SFG spectrum observed for the silica/water interface.

Figure 5.8 shows the SFG spectra of the silica/water interface at three different pH values in the presence and absence of 0.1 M $CaCl_2$ and $MgCl_2$. As we have seen, the behavior of calcium at high pH is very different from that in the low pH range. Due to this unusual pH dependence, monitoring SFG in the presence of Ca^{2+} at pH 6, 10, and 12 provides important insights into the SHG results. The spectrum at pH 6 illustrated the water structure at the beginning of the titration curve for the silica sites deprotonated above pH 7, whereas pH 10 represented the plateau of the pH titration curve. We also were interested to see how the ordered water structure behaved at pH 12, past the plateau of the titration curve. Near neutral pH, the addition of 0.1 M $CaCl_2$ resulted in a ~ 4-fold decrease in the SFG signal intensity. Shen[37] and Hore[45, 48-49] have previously reported similar decreases in SFG intensity for NaCl. Remarkably, at pH 10, the SFG signal intensity decreased nearly to 0 in the presence of $CaCl_2$, which was very surprising and very different from what was observed for the silica/water interface in the presence of NaCl.[38]

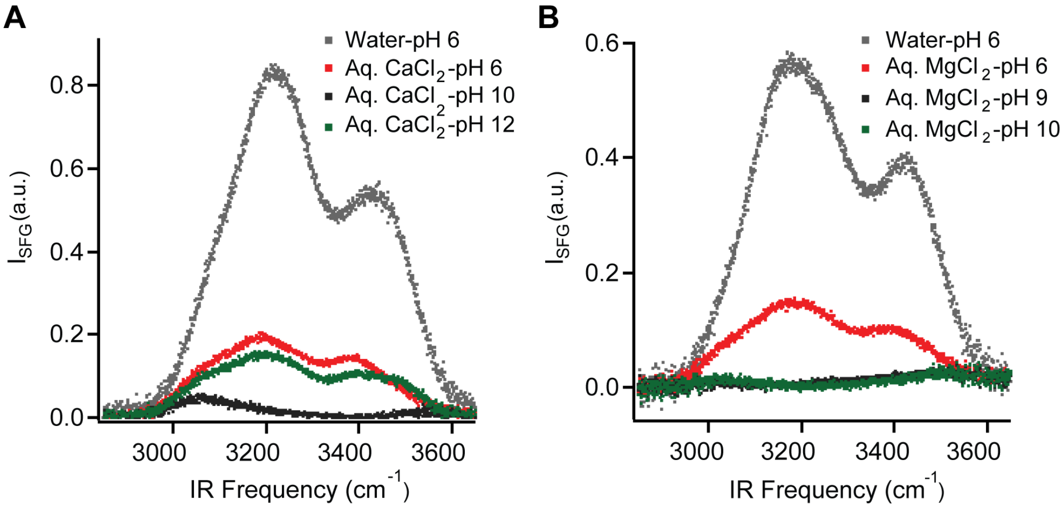

Figure 5.8. (A) Sum frequency generation spectra of water at the aqueous $CaCl_2$/silica interface at various pH. (B) Sum frequency generation spectra of

water at the aqueous $MgCl_2$/silica interface at various pH. The aqueous phase consisted of 0.1 M MCl_2 and 10 mM NaCl, and the pH was adjusted with NaOH. We have used the ssp-polarization combination to monitor the amount of ordered water molecules in all SFG experiments.[65]

We attribute this drop in signal to charge neutralization of the surface, which led to a lack of the net order in the interfacial water molecules. Yet the SFG signal increased when the pH was further increase to 12, indicating that the surface became charged again. These results strongly suggest a complete charge reversal at the silica/water interface, which has been observed in the zeta potential of silica particles in the presence of 0.01 M $Ca(NO_3)_2$ but never before observed at the planar silica/water interface.[66] When compared to the SHG results described in section 5.4, the SFG spectra is a confirmation of Ca^{2+} binding to the silica surface. The structure of the silica/Ca^{2+} adduct is yet to be discovered, but it is proposed to consist of $CaOH^+$ coordinated directly to the surface.[67] A schematic depiction of this charge reversal process is shown in Figure 5.9.

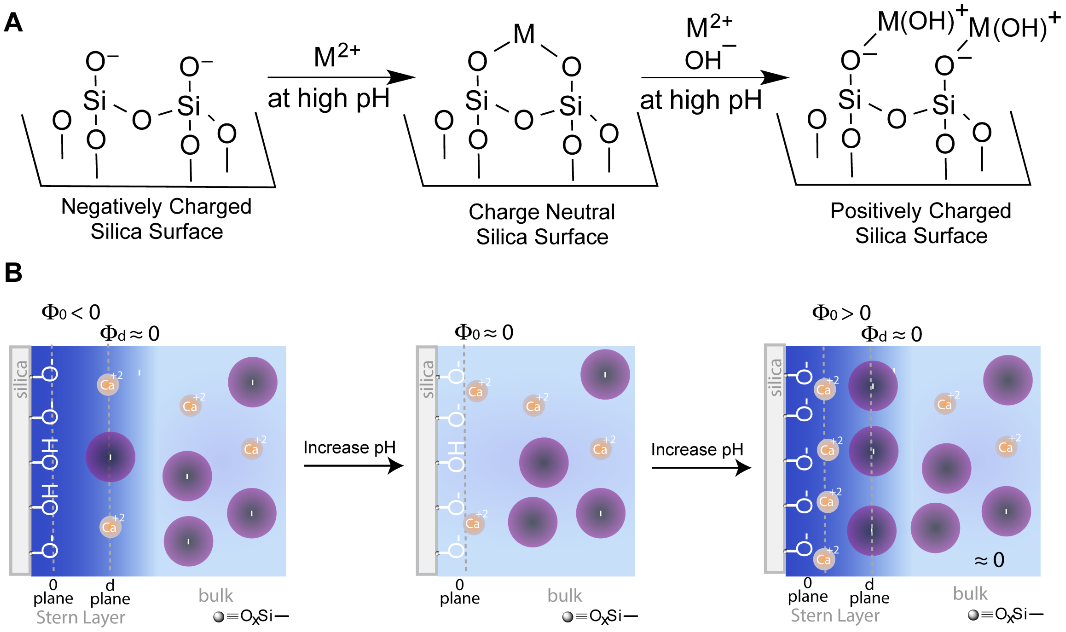

Figure 5.9. A.) At pH 9 – 10, the divalent cations completely neutralize the surface charge to form a charge neutral specifies. Further increase in the pH facilitates formation of the positively charged species MOH^+ directly coordinated to the silica surface, which eventually reverses the net negative charge of the surface to a net positive charge. B.) At low pH the interfacial potential, $\Phi_0 < 0$ due to the siloxide negative charges. In the presence of divalent cations, as pH is increased, the cations can form a strong ion-pair with the siloxides that results in charge neutralization, therefore, $\Phi_0 = 0$. When the pH is further increased, more divalent cations interact with the siloxides resulting in a net positive charge.

For Mg^{2+}, we performed the SFG experiments at pH 6, 9 and 10. Similar to Ca^{2+}, we observed a signal intensity decrease when the pH was greater than 9 for $MgCl_2$. At pH 9 the intensity of the SFG was ~ 0, indicative of charge neutralization of the silica/water interface as well. In the case of Mg^{2+}, we could not probe the interface at pH > 10 due to poor solubility of the sample solution. At pH 10 we found the SFG signal intensity was very similar to that of pH 9, which did not reveal whether the charge was reversed in the presence of Mg^{2+} at even higher pH, although the slight decrease in SHG supported charge reversal.

5.7 Conclusions

The acid-base property of silica/water interface is highly modulated by the identity of the cations. The behavior of the charged interface in the presence of divalent cations at high pH was a dramatic discovery to the yet known surface properties of silica/water interface. The aqueous/silica interface in the presence of Ca^{2+} possessed a similar surface $pH_{0.5}$ to the monovalent Na^+ at pH range 7–2.[37] At high pH the siloxides exhibited a higher affinity for Ca^{2+}, which we propose resulted in charge neutralization of the silica surface. From the SHG study, we originally proposed that at pH > 10.5, the interface experienced a change from a more negative to a less negative charge density, supported qualitatively by salt-variation experiments and comparison with the aqueous NaCl/silica interface. The SFG study of the interface in the presence of Ca^{2+}, however, showed a complete charge reversal when the pH was greater than 10. In the case of Mg^{2+}, similar observations were found. In this case, the SHG intensity decrease with increasing pH was observed at pH > 9, which was less than that for Ca^{2+}. Similar to Ca^{2+}, Mg^{2+} also showed a higher binding affinity toward the silica surface at high pH. From the SFG experiments, we also found Mg^{2+} to undergo charge neutralization but, unfortunately, the charge reversal could not be completely probed due to poor solubility of Mg^{2+} at $pH > 10$ in the presence of OH^-.

5.8 References

1. Casey, W. H.; Ludwig, C., The mechanism of dissolution of oxide minerals. *Nature* **1996,** *381*, 506.

2. Dove, P. M., The dissolution kinetics of quartz in aqueous mixed cation solutions. *Geochimica et Cosmochimica Acta* **1999,** *63*, 3715–3727.

3. Icenhower, J. P.; Dove, P. M., The dissolution kinetics of amorphous silica into sodium chloride solutions: Effects of temperature and ionic strength. *Geochimica et Cosmochimica Acta* **2000,** *64*, 4193-4203.

4. Karlsson, M.; Craven, C.; Dove, P. M.; Casey, W. H., Surface charge concentrations on silica in different 1.0 M metal-chloride background electrolytes and implications for dissolution rates. *Aquatic Geochemistry* **2001,** *7* (1), 13-32.

5. Ohlin, C. A.; Villa, E. M.; Rustad, J. R.; Casey, W. H., Dissolution of insulating oxide materials at the molecular scale. *Nature Materials* **2010,** *9*, 11.

6. Borah, J. M.; Mahiuddin, S.; Sarma, N.; Parsons, D. F.; Ninham, B. W., Specific Ion Effects on Adsorption at the Solid/Electrolyte Interface: A Probe into the Concentration Limit. *Langmuir* **2011,** *27* (14), 8710-8717.

7. Cacace, M. G.; Landau, E. M.; Ramsden, J. J., The Hofmeister series: salt and solvent effects on interfacial phenomena. *Quarterly Reviews of Biophysics* **1997,** *30* (3), 241-277.

8. Fisk, J. D.; Batten, R.; Jones, G.; O'Reill, J. P.; Shaw, A. M., pH Dependence of the Crystal Violet Adsorption Isotherm at the Silica/Water Interface. *The Journal of Physical Chemistry B* **2005,** *109* (30), 14475-14480.

9. Hodgson, A.; Haq, S., Water adsorption and the wetting of metal surfaces. *Surface Science Reports* **2009,** *64*, 381.

10. Onorato, R. M.; Otten, D. E.; Saykally, R. J., Adsorption of thiocyanate ions to the dodecanol/water interface characterized by UV second harmonic generation. *Proceedings of the National Academy of Sciences* **2009,** *106* (36), 15176-15180.

11. Schr¨odle, S.; Richmond, G. L., In situ non-linear spectroscopic approaches to understanding adsorption at mineral–water interfaces. *Journal of Physics D: Applied Physics* **2008,** *41*.

12. Kellermeier, M.; Glaab, F.; Klein, R.; Melero-Garcia, E.; Kunz, W.; Garcia-Ruiz, J. M., The effect of silica on polymorphic precipitation of calcium carbonate: an on-line energy-dispersive X-ray diffraction (EDXRD) study. *Nanoscale* **2013,** *5* (15), 7054-7065.

13. Tsoncheva, T.; Issa, G.; Blasco, T.; Concepcion, P.; Dimitrov, M.; Hernández, S.; Kovacheva, D.; Atanasova, G.; López Nieto, J. M., Silica supported copper and cerium oxide catalysts for ethyl acetate oxidation. *Journal of Colloid and Interface Science* **2013,** *404* (0), 155-160.

14. Denton, P.; Giroir-Fendler, A.; Praliaud, H.; Primet, M., Role of the Nature of the Support (Alumina or Silica), of the Support Porosity, and of the Pt Dispersion in the Selective Reduction of NO by C3H6 under Lean-Burn Conditions. *Journal of Catalysis* **2000,** *189* (2), 410-420.

15. Xiong, A.; Ma, G.; Maeda, K.; Takata, T.; Hisatomi, T.; Setoyama, T.; Kubota, J.; Domen, K., Fabrication of photocatalyst panels and the factors

determining their activity for water splitting. *Catalysis Science & Technology* **2014,** *4* (2), 325-328.

16. Sposito, G., *The Surface Chemistry of Soils*. Oxford University Press: 1984; p 234.

17. Stumm, W.; Morgan, J. J., *Aquatic Chemistry: Chemical Equilibria and Rates in Natural Waters; Third Edition*. Wiley: 1995; p 1022 pp.

18. Langmuir, D., *Aqueous Environmental Geochemistry*. Prentice Hall: 1997; p 600.

19. Enterkin, J. A.; Subramanian, A. K.; Russell, B. C.; Castell, M. R.; Poeppelmeier, K. R.; Marks, L. D., A homologous series of structures on the surface of $SrTiO_3$(110). *Nature Materials* **2010,** *9*, 245.

20. Diebold, U., Oxide surfaces: Surface science goes inorganic. *Nature Materials* **2010,** *9*, 185.

21. He, Y.; Tilocca, A.; Dulub, O.; Selloni, A.; Diebold, U., Local ordering and electronic signatures of submonolayer water on anatase TiO_2(101). *Nature Materials* **2009,** *8*, 585.

22. Maccarini, M., Water at solid surfaces: A review of selected theoretical aspects and experiments on the subject. *Biointerphases* **2007,** *2*, MR1.

23. Ball, P., Water as an Active Constituent in Cell Biology. *Chemical Reviews* **2008,** *108*, 74.

24. Ball, P., Water: Water - an enduring mystery. *Nature* **2008,** *452* (7185), 291-292.

25. Grassian, V. H., *Environmental catalysis*. 2005.

26. Michaelides, A.; Morgenstern, K., Ice nanoclusters at hydrophobic metal surfaces. *Nature Materials* **2007,** *6*, 597.

27. Nilsson, A.; Pettersson, L. G. M.; Norskov, J. K., *Chemical bonding at surfaces and interfaces*. 2008.

28. Jena, K. C.; Hore, D. K., Variation of Ionic Strength Reveals the Interfacial Water Structure at a Charged Mineral Surface. *The Journal of Physical Chemistry C* **2009,** *113*, 15364.

29. Somorjai, G.; Frei, H.; Park, J., Advancing the Frontiers in Nanocatalysis, Biointerfaces, and Renewable Energy Conversion by Innovations of Surface Techniques. *Journal of the American Chemical Society* **2009,** *131*, 16589.

30. Gray, J., The interaction of proteins with solid surfaces. *Current Opinion in Structural Biology* **2004,** *14*, 110.

31. Dove, P.; Craven, C., Surface charge density on silica in alkali and alkaline earth chloride electrolyte solutions. *Geochimica et Cosmochimica Acta* **2005,** *69* (21), 4963-4970.

32. Iler, R. K., *Chemistry of Silica - Solubility, Polymerization, Colloid and Surface Properties and Biochemistry*. John Wiley & Sons: 1979.

33. Eisenthal, K. B., Liquid interfaces probed by second-harmonic and sum-frequency spectroscopy. *Chemical Reviews* **1996,** *96* (4), 1343-1360.

34. Leung, K.; Nielsen, I. M. B.; Criscenti, L. J., Elucidating the Bimodal Acid−Base Behavior of the Water−Silica Interface from First Principles. *Journal of the American Chemical Society* **2009,** *131* (51), 18358-18365.

35. Campen, R. K.; Pymer, A. K.; Nihonyanagi, S.; Borguet, E., Linking Surface Potential and Deprotonation in Nanoporous Silica: Second Harmonic Generation and Acid/Base Titration. *The Journal of Physical Chemistry C* **2010,** *114*, 8465–18473.

36. de Beer, A.; Campen, R.; Roke, S., Separating surface structure and surface charge with second-harmonic and sum-frequency scattering. *Physical Review B* **2010,** *82* (23).

37. Azam, M. S.; Weeraman, C. N.; Gibbs-Davis, J. M., Specific Cation Effects on the Bimodal Acid–Base Behavior of the Silica/Water Interface. *The Journal of Physical Chemistry Letters* **2012**, 1269-1274.

38. Azam, M. S.; Weeraman, C. N.; Gibbs-Davis, J. M., Halide-Induced Cooperative Acid–Base Behavior at a Negatively Charged Interface. *The Journal of Physical Chemistry C* **2013,** *117* (17), 8840-8850.

39. Ong, S.; Zhao, X.; Eisenthal, K. B., Polarization of water molecules at a charged interface: second harmonic studies of the silica/water interface. *Chemical Physics Letters* **1992,** *191* (3,4), 327-335.

40. Zhao, X.; Ong, S.; Wang, H.; Eisenthal, K. B., New method for determination of surface pKa using second harmonic generation. *Chemical Physics Letters* **1993,** *214* (2), 203-207.

41. Appelo, C. A. J.; Postma, D., *Geochemistry, Groundwater and Pollution*. 2 ed.; A. A. Balkema Publishers: Amsterdam, 2005.

42. Corn, R. M.; Higgins, D. A., Optical Second Harmonic Generation as a Probe of Surface Chemistry. *Chemical Reviews* **1994,** *94*, 107-125.

43. Gopalakrishnan, S.; Liu, D.; Allen, H. C.; Kuo, M.; Shultz, M. J., Vibrational Spectroscopic Studies of Aqueous Interfaces: Salts, Acids, Bases, and Nanodrops. *Chemical Reviews* **2006,** *106* (4), 1155-1175.

44. Verreault, D.; Hua, W.; Allen, H. C., From Conventional to Phase-Sensitive Vibrational Sum Frequency Generation Spectroscopy: Probing Water Organization at Aqueous Interfaces. *The Journal of Physical Chemistry Letters* **2012,** *3*, 3012-3028.

45. Du, Q.; Freysz, E.; Shen, Y., Vibrational spectra of water molecules at quartz/water interfaces. *Physical Review Letters* **1994,** *72* (2), 238-241.

46. Li, I.; Bandara, J.; Shultz, M. J., Time Evolution Studies of the H2O/Quartz Interface Using Sum Frequency Generation, Atomic Force Microscopy, and Molecular Dynamics. *Langmuir* **2004,** *20* (24), 10474-10480.

47. Ostroverkhov, V.; Waychunas, G.; Shen, Y., New Information on Water Interfacial Structure Revealed by Phase-Sensitive Surface Spectroscopy. *Physical Review Letters* **2005,** *94* (4).

48. Jena, K. C.; Hore, D. K., Variation of Ionic Strength Reveals the Interfacial Water Structure at a Charged Mineral Surface. *The Journal of Physical Chemistry C* **2009,** *113*, 15364-15372.

49. Jena, K. C.; Covert, P. A.; Hore, D. K., The Effect of Salt on the Water Structure at a Charged Solid Surface: Differentiating Second- and Third-order Nonlinear Contributions. *The Journal of Physical Chemistry Letters* **2011,** *2* (9), 1056-1061.

50. Yang, Z.; Li, Q.; Chou, K. C., Structures of Water Molecules at the Interfaces of Aqueous Salt Solutions and Silica: Cation Effects. *The Journal of Physical Chemistry C* **2009,** *113*, 8201–8205.

51. Lyklema, J., Simple Hofmeister series. *Chemical Physics Letters* **2009,** *467*, 217-222.

52. Parsons, D. F.; Bostrom, M.; Nostro, P. L.; Ninham, B. W., Hofmeister effects: interplay of hydration, nonelectrostatic potentials, and ion size. *Physical Chemistry Chemical Physics* **2011,** *13* (27), 12352-12367.

53. Wallace, A. F.; Gibbs, G. V.; Dove, P. M., Influence of Ion-Associated Water on the Hydrolysis of Si-O Bonded Interactions. *The Journal of Physical Chemistry A* **2010,** *114*, 2534-2542.

54. Liu, J.; Xu, Z.; Masliyah, J., Studies on Bitumen−Silica Interaction in Aqueous Solutions by Atomic Force Microscopy. *Langmuir* **2003,** *19* (9), 3911-3920.

55. Zhao, H.; Long, J.; Masliyah, J. H.; Xu, Z., Effect of Divalent Cations and Surfactants on Silica−Bitumen Interactions. *Industrial & Engineering Chemistry Research* **2006,** *45* (22), 7482-7490.

56. Azam, M. S.; Weeraman, C. N.; Gibbs-Davis, J. M., Specific Cation Effects on the Bimodal Acid–Base Behavior of the Silica/Water Interface. *The Journal of Physical Chemistry Letters* **2012,** *3* (10), 1269-1274.

57. Gibbs-Davis, J. M.; Kruk, J. J.; Konek, C. T.; Scheidt, K. A.; Geiger, F. M., Jammed Acid-Base Reactions at Interfaces. *Journal of the American Chemical Society* **2008,** *130*, 15444–15447.

58. Ding, F.; Hu, Z.; Zhong, Q.; Manfred, K.; Gattass, R. R.; Brindza, M. R.; Fourkas, J. T.; Walker, R. A.; Weeks, J. D., Interfacial Organization of Acetonitrile: Simulation and Experiment. *The Journal of Physical Chemistry C* **2010,** *114*, 17651–17659.

59. Lützenkirchen, J., The Constant Capacitance Model and Variable Ionic Strength: An Evaluation of Possible Applications and Applicability. *Journal of Colloid and Interface Science* **1999,** *217* (1), 8-18.

60. Konek, C. T.; Musorrafiti, M. J.; Al-Abadleh, H. A.; Bertin, P. A.; Nguyen, S. T.; Geiger, F. M., Interfacial Acidities, Charge Densities, Potentials, and Energies of Carboxylic Acid-Functionalized Silica/Water Interfaces Determined by Second Harmonic Generation. *Journal of the American Chemical Society* **2004,** *126*, 11754-11755.

61. Dong, Y.; Pappu, S. V.; Xu, Z., Detection of Local Density Distribution of Isolated Silanol Groups on Planar Silica Surfaces Using Nonlinear Optical Molecular Probes. *Analytical Chemistry* **1998,** *70* (22), 4730-4735.

62. Du, Q.; Freysz, E.; Shen, Y. R., Vibrational spectra of water molecules at quartz/water interfaces. *Physical Review Letters* **1994,** *72* (2), 238-241.

63. Duval, Y.; Mielczarski, J. A.; Pokrovsky, O. S.; Mielczarski, E.; Ehrhardt, J. J., Evidence of the Existence of Three Types of Species at the Quartz–Aqueous Solution Interface at pH 0–10: XPS Surface Group Quantification and Surface Complexation Modeling. *The Journal of Physical Chemistry B* **2002,** *106* (11), 2937-2945.

64. Pearson, R. G., Hard and soft acids and bases, HSAB, part 1: Fundamental principles. *Journal of Chemical Education* **1968,** *45* (9), 581.

65. Yeganeh, M. S.; Dougal, S. M.; Pink, H. S., Vibrational Spectroscopy of Water at Liquid Solid Interfaces: Crossing the Isoelectric Point of a Solid Surface. *Physical Review Letters* **1999,** *83*, 1180-1182.

66. Rashchi, F.; Xu, Z.; Finch, J. A., Adsorption on silica in Pb- and Ca-SO4-CO3 systems. *Colloids and Surfaces A: Physicochemical and Engineering Aspects* **1998,** *132* (2–3), 159-171.

67. Dove, P. M.; Craven, C. M., Surface charge density on silica in alkali and alkaline earth chloride electrolyte solutions. *Geochimica et Cosmochimica Acta* **2005,** *69* (21), 4963-4970.

CHAPTER 6

General Conclusions

6.1 General Conclusions

Molecular recognition of small molecules, ions and biopolymers has gained a high degree of attention over many years.[1-3] Particularly, nucleic acid detection has shown tremendous promise in genetic profiling, disease diagnostics, and forensic applications.[1, 4] For example the detection of short tandem repeat (STR) sequences can be useful for identifying individuals for crime investigations and cancer diagnosis.[5-7] The aim of this thesis was to ascertain a comprehensive understanding of the molecular level processes relevant to nucleic acid sensing assays. The main focus has been the study of DNA modified gold nanoparticles (GNP–DNA) and the influence of probe:target DNA complex and aqueous electrolyte composition on cooperativity, the thermodynamics and kinetics of their recognition behavior.

GNP–DNA conjugates offer easy colorimetric DNA detection with a high degree of selectivity that can detect mutations with very subtle anomalies arising from a single base pair mismatch. We have evaluated the effect of the DNA structure and the polarizability of the electrolyte on the cooperativity, which promotes selectivity. These findings are not only important to better understand these materials but also aids in the design and optimization of nucleic acid detection assays. We have also reported some very interesting properties of buried fused silica surfaces, relevant to microarray based DNA detection assays where DNA is immobilized onto solid silica chips.[8-9]

In the second chapter of this thesis, we have evaluated the effect of flexible DNA structures on the cooperative, thermodynamic and kinetic behavior of GNP–DNA assemblies. Such information is particularly important in the detection of very long DNA sequences, such as genomic DNA,[10] where a large portion of the target DNA is exposed as single strands giving rise to DNA gaps. According to our study, gap sequences can strongly hinder the selectivity of DNA with subtle anomalies like single nucleotide insertion. We showed that the introduction of one single DNA gap can significantly reduce the thermodynamic stability of the aggregates formed by the target linked GNP–DNA probes. The presence of single DNA gap also imparted a significant reduction in cooperativity by a factor of two. This result strongly suggested that detection assays can be highly affected by the presence of gaps through a reduction of selectivity of these GNP–DNA probes. Another striking effect of DNA gaps on the aggregates was their rate of aggregation. We showed that the aggregation rate is inversely proportional to the gap size present on the target DNA strands. Such information is particularly important to address the challenge of disconcertingly slow aggregation; therefore, implementation of a nicked site. Finally, we also reported that the presence of the gap significantly reduced the size of the aggregates. These aggregate sizes can be used as a sensing standard.

Gold nanorods have shown a lot of interest in therapeutics and diagnostics.[11] It would be particularly interesting to see if cooperativity would persist in nanorod conjugates at higher DNA density improving their selectivity for mutations in the target. Additionally, as a continuation of this current work, DNA gaps can be studied in DNA functionalized gold nanorod assemblies.

In the third chapter of this thesis, we evaluated the effect of structural diversity of DNA linker strands on the cooperativity, thermodynamics, and kinetics. Here we studied DNA hairpins as linkers and varied their loop and stem size to determine changes in the GNP–DNA assemblies. In this study, we observed that an increase in the stem size increased cooperativity but decreased the thermodynamic stability, aggregation kinetics and aggregate size. However, increasing the loop size decreased the thermodynamic stability, cooperativity, rate of aggregation and the aggregate size. These results are strongly indicative of the influence of bulky secondary structures that can significantly modulate the thermodynamic stability, cooperativity and kinetics of the associated macroscopic aggregates.

Telomeres are important DNA sequences that can provide information about health and diseases.[12-14] A short length telomere is indicative of poor health whereas inheriting longer telomeres can cause increased cancer rates. Telomeric repeats in many organisms have shown G-quadruplex structures, a secondary DNA structure composed of polyguanosine bases.[15-16] Consequently, detection of these telomeric repeats using GNP–DNA assemblies can give rise to G-quadruplexes. As a continuation of this work, it would be interesting to see how the bulky guanosine secondary structure effect the cooperativity and assembly kinetics in these materials. Such quadruplex structures are stabilized by the presence of cations (Figure 6.1).[17-18] Hence, studying a variety of cation sizes would also be interesting to see specific ion effect on these nucleic acid nanoparticle conjugates.

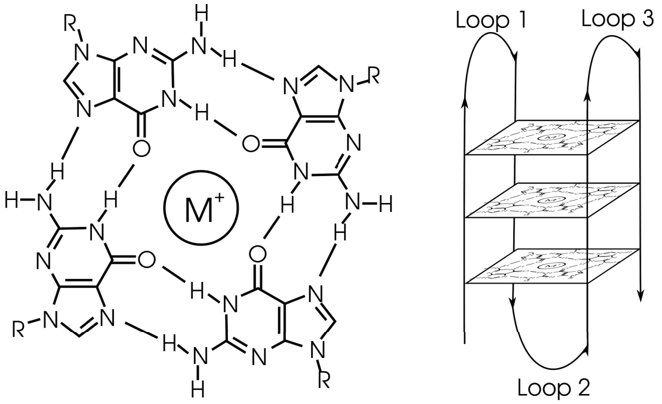

Figure 6.1. Polyguianidine induced G- quadruplex: A secondary structure of DNA. A metal cation is trapped in the cavity created by the quadruplex. Figure adapted from reference 18.[18]

Another important extension of the current work would be to optimize DNA detection assays based on strand displacement reactions (SDR) in the GNP–DNA assemblies. Temperature dependent SDR for DNA detection is currently in progress in our group. These reactions are slow at temperatures much lower than the T_m of the GNP–DNA aggregates. However, SDR are significantly faster at temperatures closer to the T_m. Consequently, at room temperature, these SDR are not simplistic in DNA detection using high temperature aggregates. Due to the lower thermodynamic stability, the hairpin linked GNP–DNA assemblies are, therefore, excellent candidates for fast, accurate and simplified detection of DNA at room temperature. Moreover, short tandem repeat (STR) detection assays could be another potential future work of this project. STR analysis has become routine in modern forensic work since 1991.[6-7] Introducing such STR in the hairpin linked

GNP–DNA assemblies would be very interesting to see if those sequences can be selectively detected.

In the fourth chapter of this thesis, we showed the effect of cation size on the cooperative, thermodynamic and kinetic behavior of GNP–DNA assemblies. Such information is particularly important because of DNA's polyelectrolyte nature stemming from the negative charges of the phosphate groups on the DNA backbone. An electrostatic interaction is highly expected when DNA is introduced to an electrolyte solution like those found in the buffers used in the sensing assays. The presence of strongly interfering ions can alter the behavior of these materials. We chose the alkali metal cations for studying the specific ion effect on these assemblies. We observed that the size of the cations is significantly important in cooperativity in these materials. For the largest cations, Cs^+, we found that it highly influenced the cooperativity by increasing the number of cooperative DNA strands in the aggregates. Such an increase in cooperativity is highly suggestive of this polarizable cation's ability to construct materials with a high degree of selectivity in single nucleotide polymorphism detection. In this study, we also showed that a decrease in cation size significantly increased the size of the aggregates (Figure 6.2). Therefore, this result again can be applied as a standard for detection of metal cations for profiling and perhaps heavy metal sensing such as As^{3+}. We also showed that decreasing the cation size enhances the assembly kinetics.

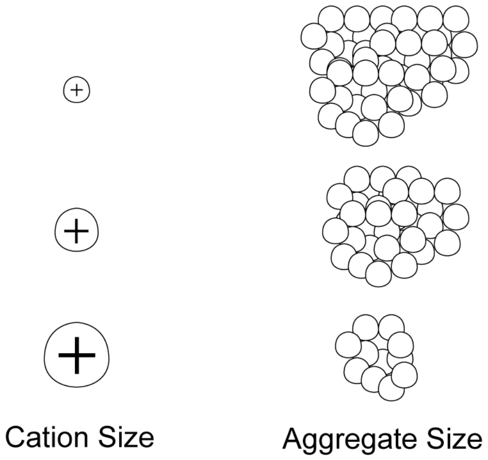

Figure 6.2. Schematic demonstration of aggregates formed from monomeric GNP-DNA conjugates. Larger aggregates are formed in the presence of smaller cations. Size of the cations and aggregates in this an approximate representation and are not actual sizes.

GNP–DNA melting transition shows hysteresis. These assemblies dissociate over a very narrow temperature range, but the temperature-induced association is very slow. We have shown that the presence of smaller cations enhances the aggregation kinetics. The evaluation of divalent or trivalent cations in these systems will be very interesting to see if rate of aggregation can be promoted to such acceleration that will overcome the hysteresis in these transitions.

Moreover, we studied the effect of some anions on the GNP–DNA assemblies. The results showed a dramatic anionic effect on the thermodynamic stability of the aggregates. In the presence of iodide (I^-) we found irreversible aggregate formation. Such result indicates oxidation of thiol anchored probe sequences from the nanoparticle surface that caused a potential drop followed by irreversible aggregation. On the other hand, in the presence of bromide (Br^-) we observed no reversible aggregate formation. Such effect of Br^- was very interesting and requires further investigation to evaluate the molecular level understanding. Completion of this anion project and studying larger anions to see the effect of polarizability on cooperativity can be another future work of this thesis.

In the fifth chapter, being inspired by the specific cation effect on the gold nanoparticle surface, we were interested to see the effect of specific cations on a planar surface. We chose silica because of its important applications in DNA microarray detection. Our group previously reported the effect of monovalent cations on the surface charge and acid-base behavior of silica/water interface. In this chapter, we aimed to study divalent cations Ca^{2+} and Mg^{2+} to evaluate their effect and compare them with their monovalent counterparts. In our study, we showed that the bimodal behavior of silica/water interface is drastically altered when monovalent cations are replaced with Ca^{2+} or Mg^{2+}. We observed a dramatic increase in the binding affinity of Ca^{2+} and Mg^{2+} at particularly higher pH, which is strongly suggestive of silica surface charge neutralization and charge reversal where a simple screening effect is expected under such circumstances. These results are highly important and have important implications in the oil–sand industry. The presence of many trivalent cations such as Al^{3+} and Fe^{3+} can also influence the properties of oil sand. It is important to understand these properties better for the construction of an easy and cost effective oil/sand separation method. Therefore, as a continuation of this project, it would be very interesting to see how buried silica surface behaves in the presence of higher valence cations.

6.2 References

1. Rosi, N. L.; Mirkin, C. A., Nanostructures in Biodiagnostics. *Chemical Reviews* **2005,** *105* (4), 1547-1562.

2. Daniel, M.-C.; Astruc, D., Gold Nanoparticles: Assembly, Supramolecular Chemistry, Quantum-Size-Related Properties, and Applications toward Biology, Catalysis, and Nanotechnology. *Chemical Reviews* **2003,** *104* (1), 293-346.

3. Wilson, R., The use of gold nanoparticles in diagnostics and detection. *Chemical Society Reviews* **2008,** *37* (9), 2028-2045.

4. Fehrmann, R. S. N.; Li, X.-y.; van der Zee, A. G. J.; de Jong, S.; te Meerman, G. J.; de Vries, E. G. E.; Crijns, A. P. G., Profiling Studies in Ovarian Cancer: A Review. *The Oncologist* **2007,** *12* (8), 960-966.

5. Wooster, R.; Cleton-Jansen, A. M.; Collins, N.; Mangion, J.; Cornelis, R. S.; Cooper, C. S.; Gusterson, B. A.; Ponder, B. A. J.; von Deimling, A.; Wiestler, O. D.; Cornelisse, C. J.; Devilee, P.; Stratton, M. R., Instability of short tandem repeats (microsatellites) in human cancers. *Nature Genetics* **1994,** *6* (2), 152-156.

6. Phil, R., Legal and public policy issues in DNA forensics. *Nature Reviews Genetics* **2001,** *2* (4), 313-317.

7. Jobling, M. A.; Gill, P., Encoded evidence: DNA in forensic analysis. *Nature Reviews Genetics* **2005,** *6* (3), 246-246.

8. Stoughton, R. B., APPLICATIONS OF DNA MICROARRAYS IN BIOLOGY. *Annual Review of Biochemistry* **2005,** *74* (1), 53-82.

9. Smith, L.; Greenfield, A., DNA microarrays and development. *Human Molecular Genetics* **2003,** *12* (suppl 1), R1-R8.

10. Storhoff, J. J.; Lucas, A. D.; Garimella, V.; Bao, Y. P.; Muller, U. R., Homogeneous detection of unamplified genomic DNA sequences based on colorimetric scatter of gold nanoparticle probes. *Nature Biotechnology* **2004,** *22* (7), 883-887.

11. Pissuwan, D.; Valenzuela, S. M.; Cortie, M. B., Prospects for gold nanorod particles in diagnostic and therapeutic applications. *Biotechnology & Genetic Engineering Reviews* **2008,** *25*, 93-112.

12. Burge, S.; Parkinson, G. N.; Hazel, P.; Todd, A. K.; Neidle, S., Quadruplex DNA: sequence, topology and structure. *Nucleic Acids Research* **2006,** *34* (19), 5402-5415.

13. Bailey, S. M.; Murnane, J. P., Telomeres, chromosome instability and cancer. *Nucleic Acids Research* **2006,** *34* (8), 2408-2417.

14. Tran, P. L. T.; Mergny, J.-L.; Alberti, P., Stability of telomeric G-quadruplexes. *Nucleic Acids Research* **2011,** *39* (8), 3282-3294.

15. Davis, J. T.; Spada, G. P., Supramolecular architectures generated by self-assembly of guanosine derivatives. *Chemical Society Reviews* **2007,** *36* (2), 296-313.

16. Wu, Z.-S.; Guo, M.-M.; Shen, G.-L.; Yu, R.-Q., G-rich oligonucleotide-functionalized gold nanoparticle aggregation. *Analytical and Bioanalytical Chemistry* **2007,** *387* (8), 2623-2626.

17. Hurst, S. J.; Hill, H. D.; Macfarlane, R. J.; Wu, J.; Dravid, V. P.; Mirkin, C. A., Synthetically Programmable DNA Binding Domains in Aggregates of DNA-Functionalized Gold Nanoparticles. *Small* **2009,** *5* (19), 2156-2161.

18. Campbell, N.; Neidle, S., G-Quadruplexes and Metal Ions. In *Interplay between Metal Ions and Nucleic Acids*, Sigel, A.; Sigel, H.; Sigel, R. K. O., Eds. Springer Netherlands: 2012; Vol. 10, pp 119-134.

BIBLIOGRAPHY

1. Chris R. Calladine, H. D., Ben Luisi, Andrew Travers, *Understanding DNA: The Molecule and How it Works*. 3rd ed.; Elsevier Academic Press: 2004.

2. Drummond, T. G.; Hill, M. G.; Barton, J. K., Electrochemical DNA sensors. *Nature Biotechnology* **2003,** *21* (10), 1192-1199.

3. Taton, T. A.; Mirkin, C. A.; Letsinger, R. L., Scanometric DNA Array Detection with Nanoparticle Probes. *Science* **2000,** *289* (5485), 1757-1760.

4. Dai, N.; Kool, E. T., Fluorescent DNA-based enzyme sensors. *Chemical Society Reviews* **2011,** *40* (12), 5756-5770.

5. Xiang, Y.; Lu, Y., DNA as Sensors and Imaging Agents for Metal Ions. *Inorganic Chemistry* **2013,** *53* (4), 1925-1942.

6. Zhang, X.-B.; Kong, R.-M.; Lu, Y., Metal Ion Sensors Based on DNAzymes and Related DNA Molecules. *Annual Review of Analytical Chemistry* **2011,** *4* (1), 105-128.

7. Storhoff, J. J.; Mirkin, C. A., Programmed Materials Synthesis with DNA. *Chemical Reviews* **1999,** *99* (7), 1849-1862.

8. Mao, X.; Liu, G., Nanomaterial based electrochemical DNA biosensors and bioassays. *Journal of Biomedical Nanotechnology* **2008,** *4* (4), 419-431.

9. Seeman, N. C., Nanomaterials based on DNA. *Annual Review of Biochemistry* **2010,** *79*, 65-87.

10. Park, S. Y.; Lytton-Jean, A. K. R.; Lee, B.; Weigand, S.; Schatz, G. C.; Mirkin, C. A., DNA-programmable nanoparticle crystallization. *Nature* **2008,** *451* (7178), 553-556.

11. Andersen, E. S.; Dong, M.; Nielsen, M. M.; Jahn, K.; Subramani, R.; Mamdouh, W.; Golas, M. M.; Sander, B.; Stark, H.; Oliveira, C. L. P.; Pedersen, J. S.; Birkedal, V.; Besenbacher, F.; Gothelf, K. V.; Kjems, J., Self-assembly of a nanoscale DNA box with a controllable lid. *Nature* **2009,** *459* (7243), 73-76.

12. Niemeyer, C. M.; Simon, U., DNA-Based Assembly of Metal Nanoparticles. *European Journal of Inorganic Chemistry* **2005,** *2005* (18), 3641-3655.

13. Park, S. Y.; Gibbs-Davis, J. M.; Nguyen, S. T.; Schatz, G. C., Sharp Melting in DNA-Linked Nanostructure Systems: Thermodynamic Models of DNA-Linked Polymers. *The Journal of Physical Chemistry B* **2007,** *111* (30), 8785-8791.

14. Eryazici, I.; Prytkova, T. R.; Schatz, G. C.; Nguyen, S. T., Cooperative Melting in Caged Dimers with Only Two DNA Duplexes. *Journal of the American Chemical Society* **2010,** *132* (48), 17068-17070.

15. Ellington, A. D.; Szostak, J. W., In vitro selection of RNA molecules that bind specific ligands. *Nature* **1990,** *346* (6287), 818-822.

16. Ellington, A. D.; Szostak, J. W., Selection in vitro of single-stranded DNA molecules that fold into specific ligand-binding structures. *Nature* **1992,** *355* (6363), 850-852.

17. Rosi, N. L.; Mirkin, C. A., Nanostructures in Biodiagnostics. *Chemical Reviews* **2005,** *105* (4), 1547-1562.

18. Giljohann, D. A.; Seferos, D. S.; Patel, P. C.; Millstone, J. E.; Rosi, N. L.; Mirkin, C. A., Oligonucleotide loading determines cellular uptake of DNA-modified gold nanoparticles. *Nano Letters* **2007,** *7* (12), 3818-3821.

19. Chiu, T.-C.; Huang, C.-C., Aptamer-Functionalized Nano-Biosensors. *Sensors* **2009,** *9* (12), 10356-10388.

20. Giljohann, D. A.; Seferos, D. S.; Daniel, W. L.; Massich, M. D.; Patel, P. C.; Mirkin, C. A., Gold Nanoparticles for Biology and Medicine. *Angewandte Chemie International Edition* **2010,** *49* (19), 3280-3294.

21. Zhao, W.; Brook, M. A.; Li, Y., Design of Gold Nanoparticle-Based Colorimetric Biosensing Assays. *ChemBioChem* **2008,** *9* (15), 2363-2371.

22. Quinten, M., *Optical Properties of Nanoparticle Systems: Mie and Beyond*. Wiley-VCH, Weinheim, Germany: 2011.

23. Daniel, M.-C.; Astruc, D., Gold nanoparticles: assembly, supramolecular chemistry, quantum-size-related properties, and applications toward biology, catalysis, and nanotechnology. *Chemical Reviews* **2004,** *104* (1), 293-346.

24. Cai, W.; Gao, T.; Hong, H.; Sun, J., Applications of gold nanoparticles in cancer nanotechnology. *Nanotechnology, science and applications* **2008,** *1*, 17.

25. Turkevich, J.; Stevenson, P. C.; Hillier, J., A study of the nucleation and growth processes in the synthesis of colloidal gold. *Discussions of the Faraday Society* **1951,** *11* (0), 55-75.

26. Frens, G., Particle size and sol stability in metal colloids. *Kolloid-Zeitschrift und Zeitschrift für Polymere* **1972,** *250* (7), 736-741.

27. Frens, G., Controlled Nucleation for the Regulation of the Particle Size in Monodisperse Gold Suspensions. *Nature* **1973,** *241* (105), 20-22.

28. Brust, M.; Walker, M.; Bethell, D.; Schiffrin, D. J.; Whyman, R., Synthesis of thiol-derivatised gold nanoparticles in a two-phase Liquid-Liquid system. *Journal of the Chemical Society, Chemical Communications* **1994,** (7), 801-802.

29. Kelly, K. L.; Coronado, E.; Zhao, L. L.; Schatz, G. C., The Optical Properties of Metal Nanoparticles: The Influence of Size, Shape, and Dielectric Environment. *The Journal of Physical Chemistry B* **2002,** *107* (3), 668-677.

30. Mirkin, C. A.; Letsinger, R. L.; Mucic, R. C.; Storhoff, J. J., A DNA-based method for rationally assembling nanoparticles into macroscopic materials. *Nature* **1996,** *382* (6592), 607-609.

31. Alivisatos, A. P.; Johnsson, K. P.; Peng, X.; Wilson, T. E.; Loweth, C. J.; Bruchez, M. P.; Schultz, P. G., Organization of 'nanocrystal molecules' using DNA. *Nature* **1996,** *382* (6592), 609-611.

32. Song, Y.; Wei, W.; Qu, X., Colorimetric Biosensing Using Smart Materials. *Advanced Materials* **2011,** *23* (37), 4215-4236.

33. Love, J. C.; Estroff, L. A.; Kriebel, J. K.; Nuzzo, R. G.; Whitesides, G. M., Self-Assembled Monolayers of Thiolates on Metals as a Form of Nanotechnology. *Chemical Reviews* **2005,** *105* (4), 1103-1170.

34. Hurst, S. J.; Lytton-Jean, A. K. R.; Mirkin, C. A., Maximizing DNA Loading on a Range of Gold Nanoparticle Sizes. *Analytical Chemistry* **2006,** *78* (24), 8313-8318.

35. Storhoff, J. J.; Lazarides, A. A.; Mucic, R. C.; Mirkin, C. A.; Letsinger, R. L.; Schatz, G. C., What Controls the Optical Properties of DNA-Linked Gold Nanoparticle Assemblies? *Journal of the American Chemical Society* **2000,** *122* (19), 4640-4650.

36. Jain, P. K.; Lee, K. S.; El-Sayed, I. H.; El-Sayed, M. A., Calculated Absorption and Scattering Properties of Gold Nanoparticles of Different Size, Shape, and Composition: Applications in Biological Imaging and Biomedicine. *The Journal of Physical Chemistry B* **2006,** *110* (14), 7238-7248.

37. Stoeva, S. I.; Lee, J.-S.; Thaxton, C. S.; Mirkin, C. A., Multiplexed DNA Detection with Biobarcoded Nanoparticle Probes. *Angewandte Chemie International Edition* **2006,** *45* (20), 3303-3306.

38. De Long, R. K.; Reynolds, C. M.; Malcolm, Y.; Schaeffer, A.; Severs, T.; Wanekaya, A., Functionalized gold nanoparticles for the binding, stabilization, and delivery of therapeutic DNA, RNA, and other biological macromolecules. *Nanotechnology, Science and Applications* **2010,** *3*, 53-63.

39. Elghanian, R.; Storhoff, J. J.; Mucic, R. C.; Letsinger, R. L.; Mirkin, C. A., Selective Colorimetric Detection of Polynucleotides Based on the Distance-Dependent Optical Properties of Gold Nanoparticles. *Science* **1997,** *277* (5329), 1078-1081.

40. Tyagi, S.; Kramer, F. R., Molecular Beacons: Probes that Fluoresce upon Hybridization. *Nature Biotechnology* **1996,** *14* (3), 303-308.

41. Lander, E. S., Array of hope. *Nature Genetics* **1999,** *21*, 3-4.

42. Duggan, D. J.; Bittner, M.; Chen, Y.; Meltzer, P.; Trent, J. M., Expression profiling using cDNA microarrays. *Nature Genetics* **1999,** *21* (1, Suppl.), 10-14.

43. Fang, X.; Liu, X.; Schuster, S.; Tan, W., Designing a Novel Molecular Beacon for Surface-Immobilized DNA Hybridization Studies. *Journal of the American Chemical Society* **1999,** *121* (12), 2921-2922.

44. Lee, O.-S.; Prytkova, T. R.; Schatz, G. C., Using DNA to Link Gold Nanoparticles, Polymers, and Molecules: A Theoretical Perspective. *The Journal of Physical Chemistry Letters* **2010,** *1* (12), 1781-1788.

45. Park, S. Y.; Stroud, D., Theory of melting and the optical properties of gold/DNA nanocomposites. *Physical Review B* **2003,** *67* (21), 212202.

46. Lukatsky, D. B.; Frenkel, D., Phase Behavior and Selectivity of DNA-Linked Nanoparticle Assemblies. *Physical Review Letters* **2004,** *92* (6), 068302.

47. Lukatsky, D. B.; Frenkel, D., Surface and bulk dissolution properties, and selectivity of DNA-linked nanoparticle assemblies. *The Journal of Chemical Physics* **2005,** *122* (21), 214904/214901-214904/214911.

48. Jin, R.; Wu, G.; Li, Z.; Mirkin, C. A.; Schatz, G. C., What Controls the Melting Properties of DNA-Linked Gold Nanoparticle Assemblies? *Journal of the American Chemical Society* **2003,** *125* (6), 1643-1654.

49. Prytkova, T. R.; Eryazici, I.; Stepp, B.; Nguyen, S.-B.; Schatz, G. C., DNA Melting in Small-Molecule−DNA-Hybrid Dimer Structures: Experimental Characterization and Coarse-Grained Molecular Dynamics Simulations. *The Journal of Physical Chemistry B* **2010,** *114* (8), 2627-2634.

50. Long, H.; Kudlay, A.; Schatz, G. C., Molecular Dynamics Studies of Ion Distributions for DNA Duplexes and DNA Clusters: Salt Effects and Connection to DNA Melting. *The Journal of Physical Chemistry B* **2006,** *110* (6), 2918-2926.

51. Kudlay, A.; Gibbs, J. M.; Schatz, G. C.; Nguyen, S. T.; Olvera de la Cruz, M., Sharp Melting of Polymer−DNA Hybrids: An Associative Phase Separation Approach. *The Journal of Physical Chemistry B* **2007,** *111* (7), 1610-1619.

52. Park, S. Y.; Stroud, D., Theory of melting and the optical properties of gold/DNA nanocomposites. *Physical Review B: Condensed Matter and Materials Physics* **2003,** *67* (21), 212202/212201-212202/212204.

53. Park, S. Y.; Stroud, D., Theory of the optical properties of a DNA-modified gold nanoparticle system. *Physica B (Amsterdam, Neth.)* **2003,** *338* (1-4), 353-356.

54. Park, S. Y.; Stroud, D., Structure formation, melting, and optical properties of gold/DNA nanocomposites: Effects of relaxation time. *Physical Review B: Condensed Matter and Materials Physics* **2003,** *68* (22), 224201/224201-224201/224211.

55. Stauffer, D.; Aharony, A., *Introduction to Percolation Theory*. Revised Second Edition ed.; Taylor & Francis: 1994.

56. Karplus, M.; Kushick, J. N., Method for estimating the configurational entropy of macromolecules. *Macromolecules* **1981,** *14* (2), 325-332.

57. Gibbs-Davis, J. M.; Schatz, G. C.; Nguyen, S. T., Sharp Melting Transitions in DNA Hybrids without Aggregate Dissolution: Proof of Neighboring-Duplex Cooperativity. *Journal of the American Chemical Society* **2007,** *129* (50), 15535-15540.

58. Harris, N. C.; Kiang, C.-H., Defects Can Increase the Melting Temperature of DNA−Nanoparticle Assemblies. *The Journal of Physical Chemistry B* **2006,** *110* (33), 16393-16396.

59. Y. Paul Bao, M. H., Tai-Fen Wei, Sudhakar S. Marla, James J. Storhoff, and Uwe R. Müller, SNP identification in unamplified human genomic DNA with gold nanoparticle probes. *Nucleic Acids Research* **2005,** *33(2)*.

60. Storhoff, J. J.; Lucas, A. D.; Garimella, V.; Bao, Y. P.; Muller, U. R., Homogeneous detection of unamplified genomic DNA sequences based on colorimetric scatter of gold nanoparticle probes. *Nature Biotechnology* **2004,** *22* (7), 883-887.

61. Zhao, J.; Tang, S.; Storhoff, J.; Marla, S.; Bao, Y. P.; Wang, X.; Wong, E.; Ragupathy, V.; Ye, Z.; Hewlett, I., Multiplexed, rapid detection of H5N1 using a PCR-free nanoparticle-based genomic microarray assay. *BMC Biotechnology* **2010,** *10* (1), 74.

62. Hill, H. D.; Vega, R. A.; Mirkin, C. A., Nonenzymatic Detection of Bacterial Genomic DNA Using the Bio Bar Code Assay. *Analytical Chemistry* **2007,** *79* (23), 9218-9223.

63. Smith, B. D.; Dave, N.; Huang, P.-J. J.; Liu, J., Assembly of DNA-Functionalized Gold Nanoparticles with Gaps and Overhangs in Linker DNA. *The Journal of Physical Chemistry C* **2011,** *115* (16), 7851-7857.

64. Liu, J.; Lu, Y., A Colorimetric Lead Biosensor Using DNAzyme-Directed Assembly of Gold Nanoparticles. *Journal of the American Chemical Society* **2003,** *125* (22), 6642-6643.

65. Liu, J.; Lu, Y., Accelerated Color Change of Gold Nanoparticles Assembled by DNAzymes for Simple and Fast Colorimetric Pb2+ Detection. *Journal of the American Chemical Society* **2004,** *126* (39), 12298-12305.

66. Maye, M. M.; Kumara, M. T.; Nykypanchuk, D.; Sherman, W. B.; Gang, O., Switching binary states of nanoparticle superlattices and dimer clusters by DNA strands. *Nature Nanotechnology* **2010,** *5* (2), 116-120.

67. Hill, H. D.; Macfarlane, R. J.; Senesi, A. J.; Lee, B.; Park, S. Y.; Mirkin, C. A., Controlling the Lattice Parameters of Gold Nanoparticle FCC Crystals with Duplex DNA Linkers. *Nano Letters* **2008,** *8* (8), 2341-2344.

68. Macfarlane, R. J.; Lee, B.; Hill, H. D.; Senesi, A. J.; Seifert, S.; Mirkin, C. A., Assembly and organization processes in DNA-directed colloidal crystallization. *Proceedings of the National Academy of Sciences* **2009,** *106* (26), 10493-10498.

69. Shchepinov, M. S.; Mir, K. U.; Elder, J. K.; Frank-Kamenetskii, M. D.; Southern, E. M., Oligonucleotide dendrimers: stable nano-structures. *Nucleic Acids Research* **1999,** *27* (15), 3035-3041.

70. Lytton-Jean, A. K. R.; Mirkin, C. A., A Thermodynamic Investigation into the Binding Properties of DNA Functionalized Gold Nanoparticle Probes and

Molecular Fluorophore Probes. *Journal of the American Chemical Society* **2005,** *127* (37), 12754-12755.

71. Xu, J.; Craig, S. L., Thermodynamics of DNA Hybridization on Gold Nanoparticles. *Journal of the American Chemical Society* **2005,** *127* (38), 13227-13231.

72. Anderson, C. F.; Record, M. T., Polyelectrolyte Theories and their Applications to DNA. *Annual Review of Physical Chemistry* **1982,** *33* (1), 191-222.

73. Grabar, K. C.; Freeman, R. G.; Hommer, M. B.; Natan, M. J., Preparation and Characterization of Au Colloid Monolayers. *Analytical Chemistry* **1995,** *67* (4), 735-743.

74. Kibbe, W. A., OligoCalc: an online oligonucleotide properties calculator. *Nucleic Acids Research* **2007,** *35* (suppl 2), W43-W46.

75. Aalberts, D. P.; Parman, J. M.; Goddard, N. L., Single-Strand Stacking Free Energy from DNA Beacon Kinetics. *Biophysical Journal* **2003,** *84* (5), 3212-3217.

76. Mills, J. B.; Cooper, J. P.; Hagerman, P. J., Electrophoretic Evidence that Single-Stranded Regions of 1 or More Nucleotides Dramatically Increase the Flexibility of DNA. *Biochemistry* **1994,** *33* (7), 1797-1803.

77. Rivetti, C.; Walker, C.; Bustamante, C., Polymer chain statistics and conformational analysis of DNA molecules with bends or sections of different flexibility. *Journal of Molecular Biology* **1998,** *280* (1), 41-59.

78. Lane, M. J.; Paner, T.; Kashin, I.; Faldasz, B. D.; Li, B.; Gallo, F. J.; Benight, A. S., The Thermodynamic Advantage of DNA Oligonucleotide ‘Stacking Hybridization’ Reactions: Energetics of a DNA Nick. *Nucleic Acids Research* **1997,** *25* (3), 611-616.

79. Marky, L. A.; Breslauer, K. J., Calculating thermodynamic data for transitions of any molecularity from equilibrium melting curves. *Biopolymers* **1987,** *26* (9), 1601-1620.

80. Tan, Z.-J.; Chen, S.-J., Nucleic Acid Helix Stability: Effects of Salt Concentration, Cation Valence and Size, and Chain Length. *Biophysical Journal* **2006,** *90* (4), 1175-1190.

81. Korolev, N. I.; Vlasov, A. P.; Kuznetsov, I. A., Thermal denaturation of Na- and Li-DNA in salt-free solutions. *Biopolymers* **1994,** *34* (9), 1275-1290.

82. Oh, J.-H.; Lee, J.-S., Designed Hybridization Properties of DNA–Gold Nanoparticle Conjugates for the Ultraselective Detection of a Single-Base Mutation in the Breast Cancer Gene BRCA1. *Analytical Chemistry* **2011,** *83* (19), 7364-7370.

83. Maye, M. M.; Nykypanchuk, D.; van der Lelie, D.; Gang, O., A Simple Method for Kinetic Control of DNA-Induced Nanoparticle Assembly. *Journal of the American Chemical Society* **2006,** *128* (43), 14020-14021.

84. Prigodich, A. E.; Lee, O.-S.; Daniel, W. L.; Seferos, D. S.; Schatz, G. C.; Mirkin, C. A., Tailoring DNA Structure To Increase Target Hybridization Kinetics on Surfaces. *Journal of the American Chemical Society* **2010,** *132* (31), 10638-10641.

85. Chen, C.; Wang, W.; Ge, J.; Zhao, X. S., Kinetics and thermodynamics of DNA hybridization on gold nanoparticles. *Nucleic Acids Research* **2009,** *37* (11), 3756-3765.

86. O'Meara, D.; Nilsson, P.; Nygren, P.-Å.; Uhlén, M.; Lundeberg, J., Capture of Single-Stranded DNA Assisted by Oligonucleotide Modules. *Analytical Biochemistry* **1998,** *255* (2), 195-203.

87. Riccelli, P. V.; Merante, F.; Leung, K. T.; Bortolin, S.; Zastawny, R. L.; Janeczko, R.; Benight, A. S., Hybridization of single-stranded DNA targets to immobilized complementary DNA probes: comparison of hairpin versus linear capture probes. *Nucleic Acids Research* **2001,** *29* (4), 996-1004.

88. Akamatsu, K.; Kimura, M.; Shibata, Y.; Nakano, S.-i.; Miyoshi, D.; Nawafune, H.; Sugimoto, N., A DNA Duplex with Extremely Enhanced Thermal Stability Based on Controlled Immobilization on Gold Nanoparticles. *Nano Letters* **2006,** *6* (3), 491-495.

89. Lee, J. S.; Ulmann, P. A.; Han, M. S.; Mirkin, C. A., A DNA-gold nanoparticle-based colorimetric competition assay for the detection of cysteine. *Nano Letters* **2008,** *8* (2), 529-533.

90. Han, M. S.; Lytton-Jean, A. K. R.; Mirkin, C. A., A Gold Nanoparticle Based Approach for Screening Triplex DNA Binders. *Journal of the American Chemical Society* **2006,** *128* (15), 4954-4955.

91. Han, M. S.; Lytton-Jean, A. K. R.; Oh, B.-K.; Heo, J.; Mirkin, C. A., Colorimetric Screening of DNA-Binding Molecules with Gold Nanoparticle Probes. *Angewandte Chemie* **2006,** *118* (11), 1839-1842.

92. Hurst, S. J.; Han, M. S.; Lytton-Jean, A. K. R.; Mirkin, C. A., Screening the Sequence Selectivity of DNA-Binding Molecules Using a Gold Nanoparticle-Based Colorimetric Approach. *Analytical Chemistry* **2007,** *79* (18), 7201-7205.

93. Thanh, N. T. K.; Rosenzweig, Z., Development of an Aggregation-Based Immunoassay for Anti-Protein A Using Gold Nanoparticles. *Analytical Chemistry* **2002,** *74* (7), 1624-1628.

94. Zhang, J.; Wang, L.; Pan, D.; Song, S.; Boey, F. Y. C.; Zhang, H.; Fan, C., Visual Cocaine Detection with Gold Nanoparticles and Rationally Engineered Aptamer Structures. *Small* **2008,** *4* (8), 1196-1200.

95. Liu, J.; Lu, Y., Fast Colorimetric Sensing of Adenosine and Cocaine Based on a General Sensor Design Involving Aptamers and Nanoparticles. *Angewandte Chemie International Edition* **2006,** *45* (1), 90-94.

96. Li, W.; Feng, L.; Ren, J.; Wu, L.; Qu, X., Visual Detection of Glucose Using Conformational Switch of i-Motif DNA and Non-Crosslinking Gold Nanoparticles. *Chemistry – A European Journal* **2012,** *18* (40), 12637-12642.

97. Hone, D. C.; Haines, A. H.; Russell, D. A., Rapid, Quantitative Colorimetric Detection of a Lectin Using Mannose-Stabilized Gold Nanoparticles. *Langmuir* **2003,** *19* (17), 7141-7144.

98. Otsuka, H.; Akiyama, Y.; Nagasaki, Y.; Kataoka, K., Quantitative and Reversible Lectin-Induced Association of Gold Nanoparticles Modified with α-Lactosyl-ω-mercapto-poly(ethylene glycol). *Journal of the American Chemical Society* **2001,** *123* (34), 8226-8230.

99. Pavlov, V.; Xiao, Y.; Shlyahovsky, B.; Willner, I., Aptamer-Functionalized Au Nanoparticles for the Amplified Optical Detection of Thrombin. *Journal of the American Chemical Society* **2004,** *126* (38), 11768-11769.

100. Nam, J.-M.; Wise, A. R.; Groves, J. T., Colorimetric Bio-Barcode Amplification Assay for Cytokines. *Analytical Chemistry* **2005,** *77* (21), 6985-6988.

101. Sudeep, P. K.; Joseph, S. T. S.; Thomas, K. G., Selective Detection of Cysteine and Glutathione Using Gold Nanorods. *Journal of the American Chemical Society* **2005,** *127* (18), 6516-6517.

102. Wu, P.; Hwang, K.; Lan, T.; Lu, Y., A DNAzyme-Gold Nanoparticle Probe for Uranyl Ion in Living Cells. *Journal of the American Chemical Society* **2013,** *135* (14), 5254-5257.

103. Xue, X.; Wang, F.; Liu, X., One-Step, Room Temperature, Colorimetric Detection of Mercury (Hg2+) Using DNA/Nanoparticle Conjugates. *Journal of the American Chemical Society* **2008,** *130* (11), 3244-3245.

104. Lee, J.-S.; Han, M. S.; Mirkin, C. A., Colorimetric Detection of Mercuric Ion (Hg2+) in Aqueous Media using DNA-Functionalized Gold Nanoparticles. *Angewandte Chemie* **2007,** *119* (22), 4171-4174.

105. Chung, C. H.; Kim, J. H.; Jung, J.; Chung, B. H., Nuclease-resistant DNA aptamer on gold nanoparticles for the simultaneous detection of Pb2+ and Hg2+ in human serum. *Biosensors and Bioelectronics* **2013,** *41* (0), 827-832.

106. Kim, Y.; Johnson, R. C.; Hupp, J. T., Gold Nanoparticle-Based Sensing of "Spectroscopically Silent" Heavy Metal Ions. *Nano Letters* **2001,** *1* (4), 165-167.

107. Wang, Z.; Lee, J. H.; Lu, Y., Label-Free Colorimetric Detection of Lead Ions with a Nanomolar Detection Limit and Tunable Dynamic Range by using Gold Nanoparticles and DNAzyme. *Advanced Materials* **2008,** *20* (17), 3263-3267.

108. Zhao, W.; Chiuman, W.; Lam, J. C. F.; McManus, S. A.; Chen, W.; Cui, Y.; Pelton, R.; Brook, M. A.; Li, Y., DNA Aptamer Folding on Gold

Nanoparticles: From Colloid Chemistry to Biosensors. *Journal of the American Chemical Society* **2008,** *130* (11), 3610-3618.

109. Huang, Y.-F.; Chang, H.-T., Analysis of Adenosine Triphosphate and Glutathione through Gold Nanoparticles Assisted Laser Desorption/Ionization Mass Spectrometry. *Analytical Chemistry* **2007,** *79* (13), 4852-4859.

110. Wang, Z.; Sun, N.; He, Y.; Liu, Y.; Li, J., DNA Assembled Gold Nanoparticles Polymeric Network Blocks Modular Highly Sensitive Electrochemical Biosensors for Protein Kinase Activity Analysis and Inhibition. *Analytical Chemistry* **2014**.

111. Song, G.; Chen, C.; Ren, J.; Qu, X., A Simple, Universal Colorimetric Assay for Endonuclease/Methyltransferase Activity and Inhibition Based on an Enzyme-Responsive Nanoparticle System. *ACS Nano* **2009,** *3* (5), 1183-1189.

112. Zhao, W.; Lam, J. C. F.; Chiuman, W.; Brook, M. A.; Li, Y., Enzymatic Cleavage of Nucleic Acids on Gold Nanoparticles: A Generic Platform for Facile Colorimetric Biosensors. *Small* **2008,** *4* (6), 810-816.

113. Wang, C.; Chen, Y.; Wang, T.; Ma, Z.; Su, Z., Biorecognition-Driven Self-Assembly of Gold Nanorods: A Rapid and Sensitive Approach toward Antibody Sensing. *Chemistry of Materials* **2007,** *19* (24), 5809-5811.

114. Beissenhirtz, M. K.; Elnathan, R.; Weizmann, Y.; Willner, I., The Aggregation of Au Nanoparticles by an Autonomous DNA Machine Detects Viruses. *Small* **2007,** *3* (3), 375-379.

115. Souza, G. R.; Christianson, D. R.; Staquicini, F. I.; Ozawa, M. G.; Snyder, E. Y.; Sidman, R. L.; Miller, J. H.; Arap, W.; Pasqualini, R., Networks of gold nanoparticles and bacteriophage as biological sensors and cell-targeting agents. *Proceedings of the National Academy of Sciences of the United States of America* **2006,** *103* (5), 1215-1220.

116. Schofield, C. L.; Field, R. A.; Russell, D. A., Glyconanoparticles for the Colorimetric Detection of Cholera Toxin. *Analytical Chemistry* **2007,** *79* (4), 1356-1361.

117. Medley, C. D.; Smith, J. E.; Tang, Z.; Wu, Y.; Bamrungsap, S.; Tan, W., Gold Nanoparticle-Based Colorimetric Assay for the Direct Detection of Cancerous Cells. *Analytical Chemistry* **2008,** *80* (4), 1067-1072.

118. Huang, C.-C.; Huang, Y.-F.; Cao, Z.; Tan, W.; Chang, H.-T., Aptamer-Modified Gold Nanoparticles for Colorimetric Determination of Platelet-Derived Growth Factors and Their Receptors. *Analytical Chemistry* **2005,** *77* (17), 5735-5741.

119. Wu, Z.-S.; Lu, H.; Liu, X.; Hu, R.; Zhou, H.; Shen, G.; Yu, R.-Q., Inhibitory Effect of Target Binding on Hairpin Aptamer Sticky-End Pairing-Induced Gold Nanoparticle Assembly for Light-up Colorimetric Protein Assay. *Analytical Chemistry* **2010,** *82* (9), 3890-3898.

120. Dubertret, B.; Calame, M.; Libchaber, A. J., Single-mismatch detection using gold-quenched fluorescent oligonucleotides. *Nature Biotechnology* **2001,** *19* (4), 365-370.

121. Harry, S. R.; Hicks, D. J.; Amiri, K. I.; Wright, D. W., Hairpin DNA coated gold nanoparticles as intracellular mRNA probes for the detection of tyrosinase gene expression in melanoma cells. *Chemical Communications* **2010,** *46* (30), 5557-5559.

122. Sikder, M. D. H.; Gibbs-Davis, J. M., The Influence of Gap Length on Cooperativity and Rate of Association in DNA-Modified Gold Nanoparticle Aggregates. *The Journal of Physical Chemistry C* **2012,** *116* (21), 11694-11701.

123. Elghanian, R. J. J., Selective colorimetric detection of polynucleotides based on the distance-dependent optical properti. *Science* **1997,** *277* (5329), 1078.

124. Mucic, R. C.; Storhoff, J. J.; Mirkin, C. A.; Letsinger, R. L., DNA-Directed Synthesis of Binary Nanoparticle Network Materials. *Journal of the American Chemical Society* **1998,** *120* (48), 12674-12675.

125. Sidhaye, D. S.; Kashyap, S.; Sastry, M.; Hotha, S.; Prasad, B. L. V., Gold Nanoparticle Networks with Photoresponsive Interparticle Spacings. *Langmuir* **2005,** *21* (17), 7979-7984.

126. Seela, F.; Budow, S., pH-Dependent Assembly of DNA–Gold Nanoparticles Based on the i-Motif: A Switchable Device with the Potential of a Nanomachine. *Helvetica Chimica Acta* **2006,** *89* (9), 1978-1985.

127. Liu, J.; Lu, Y., Stimuli-Responsive Disassembly of Nanoparticle Aggregates for Light-Up Colorimetric Sensing. *Journal of the American Chemical Society* **2005,** *127* (36), 12677-12683.

128. Li, J.; Fu, H.-E.; Wu, L.-J.; Zheng, A.-X.; Chen, G.-N.; Yang, H.-H., General Colorimetric Detection of Proteins and Small Molecules Based on Cyclic Enzymatic Signal Amplification and Hairpin Aptamer Probe. *Analytical Chemistry* **2012,** *84* (12), 5309-5315.

129. Xiang, S.; Fruehauf, J.; Li, C. J., Short hairpin RNA-expressing bacteria elicit RNA interference in mammals. *Nature Biotechnology* **2006,** *24* (6), 697-702.

130. Davison, A.; Leach, D. R. F., Two-base DNA hairpin-loop structures in vivo. *Nucleic Acids Research* **1994,** *22* (21), 4361-4363.

131. Rentzeperis, D.; Alessi, K.; Marky, L. A., Thermodynamics of DNA hairpins: Contribution of loop size to hairpin stability and ethidium binding. *Nucleic Acids Research* **1993,** *21* (11), 2683-2689.

132. Lai, Y.-J.; Tseng, W.-L., Role of 5-thio-(2-nitrobenzoic acid)-capped gold nanoparticles in the sensing of chromium(vi): remover and sensor. *Analyst* **2011,** *136* (13), 2712-2717.

133. Antao, V. P.; Tinoco, I. J., Thermodynamic parameters for loop formation in RNA and DNA hairpin tetraloops. *Nucleic Acids Research* **1992,** *20* (4), 819-824.

134. Groebe, D. R.; Uhlenbeck, O. C., Characterization of RNA hairpin loop stability. *Nucleic Acids Research* **1988,** *16* (24), 11725-11735.

135. Record, M. T.; Anderson, C. F.; Lohman, T. M., Thermodynamic analysis of ion effects on the binding and conformational equilibria of proteins and nucleic acids: the roles of ion association or release, screening, and ion effects on water activity. *Quarterly Reviews of Biophysics* **1978,** *11* (02), 103-178.

136. Sabbagh, I.; Delsanti, M., Solubility of highly charged anionic polyelectrolytes in presence of multivalent cations: Specific interaction effect. *The European Physical Journal E* **2000,** *1* (1), 75-86.

137. Hugerth, A.; Sundelöf, L.-O., The effect of polyelectrolyte counterion specificity, charge density, and conformation on polyelectrolyte–amphiphile interaction: The carrageenan/furcellaran–amitriptyline system. *Biopolymers* **2001,** *58* (2), 186-194.

138. Ludwig, H.; Loebel, K. H., Interaction of polyelectrolytes with mono- and divalent cations. *Berichte der Bunsengesellschaft für physikalische Chemie* **1996,** *100* (6), 863-868.

139. Springer, T.; Sipova, H.; Vaisocherova, H.; Stepanek, J.; Homola, J., Shielding effect of monovalent and divalent cations on solid-phase DNA hybridization: surface plasmon resonance biosensor study. *Nucleic Acids Research* **2010,** *38* (20), 7343-7351.

140. Plum, G. E.; Arscott, P. G.; Bloomfield, V. A., Condensation of DNA by trivalent cations. 2. Effects of cation structure. *Biopolymers* **1990,** *30* (5-6), 631-643.

141. He, S.; Arscott, P. G.; Bloomfield, V. A., Condensation of DNA by multivalent cations: experimental studies of condensation kinetics. *Biopolymers* **2000,** *53* (4), 329-341.

142. Bloomfield, V. A., Condensation of DNA by multivalent cations: considerations on mechanism. *Biopolymers* **1991,** *31* (13), 1471-1481.

143. Soto, A. M.; Misra, V.; Draper, D. E., Tertiary Structure of an RNA Pseudoknot Is Stabilized by "Diffuse" Mg2+ Ions. *Biochemistry* **2007,** *46* (11), 2973-2983.

144. Anderson, C. F.; Record, M. T., Salt-Nucleic Acid Interactions. *Annual Review of Physical Chemistry* **1995,** *46* (1), 657-700.

145. Misra, V. K.; Sharp, K. A.; Friedman, R. A.; Honig, B., Salt Effects on Ligand-DNA Binding: Minor Groove Binding Antibiotics. *Journal of Molecular Biology* **1994,** *238* (2), 245-263.

146. Chu, V. B.; Bai, Y.; Lipfert, J.; Herschlag, D.; Doniach, S., Evaluation of ion binding to DNA duplexes using a size-modified Poisson-Boltzmann theory. *Biophysical Journal* **2007,** *93* (9), 3202-3209.

147. Hud, N. V.; Feigon, J., Localization of divalent metal ions in the minor groove of DNA A-tracts. *Journal of the American Chemical Society* **1997,** *119* (24), 5756-5757.

148. Young, M. A.; Jayaram, B.; Beveridge, D. L., Intrusion of counterions into the spine of hydration in the minor groove of B-DNA: Fractional occupancy of electronegative pockets. *Journal of the American Chemical Society* **1997,** *119* (1), 59-69.

149. Shui, X.; McFail-Isom, L.; Hu, G. G.; Williams, L. D., The B-DNA dodecamer at high resolution reveals a spine of water on sodium. *Biochemistry* **1998,** *37* (23), 8341-8355.

150. Berger, I.; Tereshko, V.; Ikeda, H.; Marquez, V. E.; Egli, M., Crystal structures of B-DNA with incorporated 2'-deoxy-2'-fluoro-arabino-furanosyl thymines: Implications of conformational preorganization for duplex stability. *Nucleic Acids Research* **1998,** *26* (10), 2473-2480.

151. Feig, M.; Pettitt, B. M., Sodium and chlorine ions as part of the DNA solvation shell. *Biophysical Journal* **1999,** *77* (4), 1769-1781.

152. Chiu, T. K.; Kaczor-Grzeskowiak, M.; Dickerson, R. E., Absence of minor groove monovalent cations in the crosslinked dodecamer C-G-C-G-A-A-T-T-C-G-C-G. *Journal of Molecular Biology* **1999,** *292* (3), 589-608.

153. Minasov, G.; Tereshko, V.; Egli, M., Atomic-resolution crystal structures of B-DNA reveal specific influences of divalent metal ions an conformation and packing. *Journal of Molecular Biology* **1999,** *291* (1), 83-99.

154. Tereshko, V.; Minasov, G.; Egli, M., A 'Hydrat-ion' spine in a B-DNA minor groove. *Journal of the American Chemical Society* **1999,** *121* (15), 3590-3595.

155. Hud, N. V.; Sklenář, V.; Feigon, J., Localization of ammonium ions in the minor groove of DNA duplexes in solution and the origin of DNA A-tract bending. *Journal of Molecular Biology* **1999,** *286* (3), 651-660.

156. Tereshko, V.; Minasov, G.; Egli, M., The Dickerson-Drew B-DNA dodecamer revisited at atomic resolution. *Journal of the American Chemical Society* **1999,** *121* (2), 470-471.

157. Hamelberg, D.; McFail-Isom, L.; Williams, L. D.; David Wilson, W., Flexible structure of DNA: Ion dependence of minor-groove structure and dynamics. *Journal of the American Chemical Society* **2000,** *122* (43), 10513-10520.

158. Chiu, T. K.; Dickerson, R. E., 1 Å crystal structures of B-DNA reveal sequence-specific binding and groove-specific bending of DNA by magnesium and calcium. *Journal of Molecular Biology* **2000,** *301* (4), 915-945.

159. Auffinger, P.; Westhof, E., Water and ion binding around RNA and DNA (C,G) oligomers. *Journal of Molecular Biology* **2000,** *300* (5), 1113-1131.

160. Woods, K. K.; McFail-Isom, L.; Sines, C. C.; Howerton, S. B.; Stephens, R. K.; Williams, L. D., Monovalent cations sequester within the A-tract minor groove of [d(CGCGAATTCGCG)]2. *Journal of the American Chemical Society* **2000,** *122* (7), 1546-1547.

161. Denisov, V. P.; Halle, B., Sequence-specific binding of counterions to B-DNA. *Proceedings of the National Academy of Sciences of the United States of America* **2000,** *97* (2), 629-633.

162. Howerton, S. B.; Sines, C. C.; VanDerveer, D.; Williams, L. D., Locating monovalent cations in the grooves of B-DNA. *Biochemistry* **2001,** *40* (34), 10023-10031.

163. Tereshko, V.; Wilds, C. J.; Minasov, G.; Prakash, T. P.; Maier, M. A.; Howard, A.; Wawrzak, Z.; Manoharan, M.; Egli, M., Detection of alkali metal ions in DNA crystals using state-of-the-art X-ray diffraction experiments. *Nucleic Acids Research* **2001,** *29* (5), 1208-1215.

164. Bao, Y. P.; Huber, M.; Wei, T.-F.; Marla, S. S.; Storhoff, J. J.; Muller, U. R., SNP identification in unamplified human genomic DNA with gold nanoparticle probes. *Nucleic Acids Research* **2005,** *33* (2), e15/11-e15/17.

165. Alivisatos, A. P.; Johnsson, K. P.; Peng, X.; Wilson, T. E.; Loweth, C. J.; Schultz, P. G., Organization of 'nanocrystal molecules' using DNA. *Nature* **1996,** *382* (6592), 609-611.

166. Solie, T. N.; Schellman, J. A., The interaction of nucleosides in aqueous solution. *Journal of Molecular Biology* **1968,** *33* (1), 61-77.

167. Zheng, B.; Cheng, S.; Liu, W.; Lam, M. H.-W.; Liang, H., A simple colorimetric pH alarm constructed from DNA–gold nanoparticles. *Analytica Chimica Acta* **2012,** *741* (0), 106-113.

168. Gruenwedel, D. W.; Hsu, C. H.; Lu, D. S., The effects of aqueous neutral-salt solutions on the melting temperatures of deoxyribonucleic acids. *Biopolymers* **1971,** *10* (1), 47-68.

169. Korolev, N.; Nordenskiöld, L., Influence of Alkali Cation Nature on Structural Transitions and Reactions of Biopolyelectrolytes. *Biomacromolecules* **2000,** *1* (4), 648-655.

170. Burda, J. V.; Šponer, J.; Leszczynski, J.; Hobza, P., Interaction of DNA Base Pairs with Various Metal Cations (Mg^{2+}, Ca^{2+}, Sr^{2+}, Ba^{2+}, Cu^{+}, Ag^{+}, Au^{+}, Zn^{2+}, Cd^{2+}, and Hg^{2+}): Nonempirical ab Initio Calculations on Structures, Energies, and Nonadditivity of the Interaction. *The Journal of Physical Chemistry B* **1997,** *101* (46), 9670-9677.

171. Sundaresan, N.; Thomas, T.; Thomas, T. J.; Pillai, C. K. S., Lithium Ion Induced Stabilization of the Liquid Crystalline DNA. *Macromolecular Bioscience* **2006,** *6* (3), 250-250.

172. Cho, M.; Han, M. S.; Ban, C., Detection of mismatched DNAsvia the binding affinity of MutS using a gold nanoparticle-based competitive colorimetric method. *Chemical Communications* **2008,** (38), 4573-4575.

173. Azam, M. S.; Weeraman, C. N.; Gibbs-Davis, J. M., Halide-Induced Cooperative Acid–Base Behavior at a Negatively Charged Interface. *The Journal of Physical Chemistry C* **2013,** *117* (17), 8840-8850.

174. Cheng, W.; Dong, S.; Wang, E., Iodine-Induced Gold-Nanoparticle Fusion/Fragmentation/Aggregation and Iodine-Linked Nanostructured Assemblies on a Glass Substrate. *Angewandte Chemie International Edition* **2003,** *42* (4), 449-452.

175. Wei, S.-C.; Hsu, P.-H.; Lee, Y.-F.; Lin, Y.-W.; Huang, C.-C., Selective Detection of Iodide and Cyanide Anions Using Gold-Nanoparticle-Based Fluorescent Probes. *ACS Applied Materials & Interfaces* **2012,** *4* (5), 2652-2658.

176. Lee, I. L.; Sung, Y.-M.; Wu, C.-H.; Wu, S.-P., Colorimetric sensing of iodide based on triazole-acetamide functionalized gold nanoparticles. *Microchimica Acta* **2014,** *181* (5-6), 573-579.

177. Casey, W. H.; Ludwig, C., The mechanism of dissolution of oxide minerals. *Nature* **1996,** *381*, 506.

178. Dove, P. M., The dissolution kinetics of quartz in aqueous mixed cation solutions. *Geochimica et Cosmochimica Acta* **1999,** *63*, 3715–3727.

179. Icenhower, J. P.; Dove, P. M., The dissolution kinetics of amorphous silica into sodium chloride solutions: Effects of temperature and ionic strength. *Geochimica et Cosmochimica Acta* **2000,** *64*, 4193-4203.

180. Karlsson, M.; Craven, C.; Dove, P. M.; Casey, W. H., Surface charge concentrations on silica in different 1.0 M metal-chloride background electrolytes and implications for dissolution rates. *Aquatic Geochemistry* **2001,** *7* (1), 13-32.

181. Ohlin, C. A.; Villa, E. M.; Rustad, J. R.; Casey, W. H., Dissolution of insulating oxide materials at the molecular scale. *Nature Materials* **2010,** *9*, 11.

182. Borah, J. M.; Mahiuddin, S.; Sarma, N.; Parsons, D. F.; Ninham, B. W., Specific Ion Effects on Adsorption at the Solid/Electrolyte Interface: A Probe into the Concentration Limit. *Langmuir* **2011,** *27* (14), 8710-8717.

183. Cacace, M. G.; Landau, E. M.; Ramsden, J. J., The Hofmeister series: salt and solvent effects on interfacial phenomena. *Quarterly Reviews of Biophysics* **1997,** *30* (3), 241-277.

184. Fisk, J. D.; Batten, R.; Jones, G.; O'Reill, J. P.; Shaw, A. M., pH Dependence of the Crystal Violet Adsorption Isotherm at the Silica/Water Interface. *The Journal of Physical Chemistry B* **2005,** *109* (30), 14475-14480.

185. Hodgson, A.; Haq, S., Water adsorption and the wetting of metal surfaces. *Surface Science Reports* **2009,** *64*, 381.

186. Onorato, R. M.; Otten, D. E.; Saykally, R. J., Adsorption of thiocyanate ions to the dodecanol/water interface characterized by UV second harmonic generation. *Proceedings of the National Academy of Sciences* **2009,** *106* (36), 15176-15180.

187. Schr¨odle, S.; Richmond, G. L., In situ non-linear spectroscopic approaches to understanding adsorption at mineral–water interfaces. *Journal of Physics D: Applied Physics* **2008,** *41*.

188. Kellermeier, M.; Glaab, F.; Klein, R.; Melero-Garcia, E.; Kunz, W.; Garcia-Ruiz, J. M., The effect of silica on polymorphic precipitation of calcium carbonate: an on-line energy-dispersive X-ray diffraction (EDXRD) study. *Nanoscale* **2013,** *5* (15), 7054-7065.

189. Tsoncheva, T.; Issa, G.; Blasco, T.; Concepcion, P.; Dimitrov, M.; Hernández, S.; Kovacheva, D.; Atanasova, G.; López Nieto, J. M., Silica supported copper and cerium oxide catalysts for ethyl acetate oxidation. *Journal of Colloid and Interface Science* **2013,** *404* (0), 155-160.

190. Denton, P.; Giroir-Fendler, A.; Praliaud, H.; Primet, M., Role of the Nature of the Support (Alumina or Silica), of the Support Porosity, and of the Pt Dispersion in the Selective Reduction of NO by C3H6 under Lean-Burn Conditions. *Journal of Catalysis* **2000,** *189* (2), 410-420.

191. Xiong, A.; Ma, G.; Maeda, K.; Takata, T.; Hisatomi, T.; Setoyama, T.; Kubota, J.; Domen, K., Fabrication of photocatalyst panels and the factors

determining their activity for water splitting. *Catalysis Science & Technology* **2014,** *4* (2), 325-328.

192. Sposito, G., *The Surface Chemistry of Soils*. Oxford University Press: 1984; p 234.

193. Stumm, W.; Morgan, J. J., *Aquatic Chemistry: Chemical Equilibria and Rates in Natural Waters; Third Edition*. Wiley: 1995; p 1022 pp.

194. Langmuir, D., *Aqueous Environmental Geochemistry*. Prentice Hall: 1997; p 600.

195. Enterkin, J. A.; Subramanian, A. K.; Russell, B. C.; Castell, M. R.; Poeppelmeier, K. R.; Marks, L. D., A homologous series of structures on the surface of $SrTiO_3$(110). *Nature Materials* **2010,** *9*, 245.

196. Diebold, U., Oxide surfaces: Surface science goes inorganic. *Nature Materials* **2010,** *9*, 185.

197. He, Y.; Tilocca, A.; Dulub, O.; Selloni, A.; Diebold, U., Local ordering and electronic signatures of submonolayer water on anatase TiO_2(101). *Nature Materials* **2009,** *8*, 585.

198. Maccarini, M., Water at solid surfaces: A review of selected theoretical aspects and experiments on the subject. *Biointerphases* **2007,** *2*, MR1.

199. Ball, P., Water as an Active Constituent in Cell Biology. *Chemical Reviews* **2008,** *108*, 74.

200. Ball, P., Water: Water - an enduring mystery. *Nature* **2008,** *452* (7185), 291-292.

201. Grassian, V. H., *Environmental Catalysis*. 2005.

202. Michaelides, A.; Morgenstern, K., Ice nanoclusters at hydrophobic metal surfaces. *Nature Materials* **2007,** *6*, 597.

203. Nilsson, A.; Pettersson, L. G. M.; Norskov, J. K., *Chemical Bonding at Surfaces and Interfaces*. 2008.

204. Jena, K. C.; Hore, D. K., Variation of Ionic Strength Reveals the Interfacial Water Structure at a Charged Mineral Surface. *The Journal of Physical Chemistry C* **2009,** *113*, 15364.

205. Somorjai, G.; Frei, H.; Park, J., Advancing the Frontiers in Nanocatalysis, Biointerfaces, and Renewable Energy Conversion by Innovations of Surface Techniques. *Journal of the American Chemical Society* **2009,** *131*, 16589.

206. Gray, J., The interaction of proteins with solid surfaces. *Current Opinion in Structural Biology* **2004,** *14*, 110.

207. Dove, P.; Craven, C., Surface charge density on silica in alkali and alkaline earth chloride electrolyte solutions. *Geochimica et Cosmochimica Acta* **2005,** *69* (21), 4963-4970.

208. Iler, R. K., *Chemistry of Silica - Solubility, Polymerization, Colloid and Surface Properties and Biochemistry*. John Wiley & Sons: 1979.

209. Eisenthal, K. B., Liquid interfaces probed by second-harmonic and sum-frequency spectroscopy. *Chemical Reviews* **1996,** *96* (4), 1343-1360.

210. Leung, K.; Nielsen, I. M. B.; Criscenti, L. J., Elucidating the Bimodal Acid−Base Behavior of the Water−Silica Interface from First Principles. *Journal of the American Chemical Society* **2009,** *131* (51), 18358-18365.

211. Campen, R. K.; Pymer, A. K.; Nihonyanagi, S.; Borguet, E., Linking Surface Potential and Deprotonation in Nanoporous Silica: Second Harmonic Generation and Acid/Base Titration. *The Journal of Physical Chemistry C* **2010,** *114*, 8465–18473.

212. de Beer, A.; Campen, R.; Roke, S., Separating surface structure and surface charge with second-harmonic and sum-frequency scattering. *Physical Review B* **2010,** *82* (23).

213. Azam, M. S.; Weeraman, C. N.; Gibbs-Davis, J. M., Specific Cation Effects on the Bimodal Acid–Base Behavior of the Silica/Water Interface. *The Journal of Physical Chemistry Letters* **2012**, 1269-1274.

214. Ong, S.; Zhao, X.; Eisenthal, K. B., Polarization of water molecules at a charged interface: second harmonic studies of the silica/water interface. *Chemical Physics Letters* **1992,** *191* (3,4), 327-335.

215. Zhao, X.; Ong, S.; Wang, H.; Eisenthal, K. B., New method for determination of surface pKa using second harmonic generation. *Chemical Physics Letters* **1993,** *214* (2), 203-207.

216. Appelo, C. A. J.; Postma, D., *Geochemistry, Groundwater and Pollution*. 2 ed.; A. A. Balkema Publishers: Amsterdam, 2005.

217. Corn, R. M.; Higgins, D. A., Optical Second Harmonic Generation as a Probe of Surface Chemistry. *Chemical Reviews* **1994,** *94*, 107-125.

218. Gopalakrishnan, S.; Liu, D.; Allen, H. C.; Kuo, M.; Shultz, M. J., Vibrational Spectroscopic Studies of Aqueous Interfaces: Salts, Acids, Bases, and Nanodrops. *Chemical Reviews* **2006,** *106* (4), 1155-1175.

219. Verreault, D.; Hua, W.; Allen, H. C., From Conventional to Phase-Sensitive Vibrational Sum Frequency Generation Spectroscopy: Probing Water Organization at Aqueous Interfaces. *The Journal of Physical Chemistry Letters* **2012,** *3*, 3012-3028.

220. Du, Q.; Freysz, E.; Shen, Y., Vibrational spectra of water molecules at quartz/water interfaces. *Physical Review Letters* **1994,** *72* (2), 238-241.

221. Li, I.; Bandara, J.; Shultz, M. J., Time Evolution Studies of the H2O/Quartz Interface Using Sum Frequency Generation, Atomic Force Microscopy, and Molecular Dynamics. *Langmuir* **2004,** *20* (24), 10474-10480.

222. Ostroverkhov, V.; Waychunas, G.; Shen, Y., New Information on Water Interfacial Structure Revealed by Phase-Sensitive Surface Spectroscopy. *Physical Review Letters* **2005,** *94* (4).

223. Jena, K. C.; Hore, D. K., Variation of Ionic Strength Reveals the Interfacial Water Structure at a Charged Mineral
Surface. *The Journal of Physical Chemistry C* **2009,** *113*, 15364-15372.

224. Jena, K. C.; Covert, P. A.; Hore, D. K., The Effect of Salt on the Water Structure at a Charged Solid Surface: Differentiating Second- and Third-order Nonlinear Contributions. *The Journal of Physical Chemistry Letters* **2011,** *2* (9), 1056-1061.

225. Yang, Z.; Li, Q.; Chou, K. C., Structures of Water Molecules at the Interfaces of Aqueous Salt Solutions and Silica: Cation Effects. *The Journal of Physical Chemistry C* **2009,** *113*, 8201–8205.

226. Lyklema, J., Simple Hofmeister series. *Chemical Physics Letters* **2009,** *467*, 217-222.

227. Parsons, D. F.; Bostrom, M.; Nostro, P. L.; Ninham, B. W., Hofmeister effects: interplay of hydration, nonelectrostatic potentials, and ion size. *Physical Chemistry Chemical Physics* **2011,** *13* (27), 12352-12367.

228. Wallace, A. F.; Gibbs, G. V.; Dove, P. M., Influence of Ion-Associated Water on the Hydrolysis of Si-O Bonded Interactions. *The Journal of Physical Chemistry A* **2010,** *114*, 2534-2542.

229. Liu, J.; Xu, Z.; Masliyah, J., Studies on Bitumen−Silica Interaction in Aqueous Solutions by Atomic Force Microscopy. *Langmuir* **2003,** *19* (9), 3911-3920.

230. Zhao, H.; Long, J.; Masliyah, J. H.; Xu, Z., Effect of Divalent Cations and Surfactants on Silica−Bitumen Interactions. *Industrial & Engineering Chemistry Research* **2006,** *45* (22), 7482-7490.

231. Azam, M. S.; Weeraman, C. N.; Gibbs-Davis, J. M., Specific Cation Effects on the Bimodal Acid–Base Behavior of the Silica/Water Interface. *The Journal of Physical Chemistry Letters* **2012,** *3* (10), 1269-1274.

232. Gibbs-Davis, J. M.; Kruk, J. J.; Konek, C. T.; Scheidt, K. A.; Geiger, F. M., Jammed Acid-Base Reactions at Interfaces. *Journal of the American Chemical Society* **2008,** *130*, 15444–15447.

233. Ding, F.; Hu, Z.; Zhong, Q.; Manfred, K.; Gattass, R. R.; Brindza, M. R.; Fourkas, J. T.; Walker, R. A.; Weeks, J. D., Interfacial Organization of Acetonitrile: Simulation and Experiment. *The Journal of Physical Chemistry C* **2010,** *114*, 17651–17659.

234. Lützenkirchen, J., The Constant Capacitance Model and Variable Ionic Strength: An Evaluation of Possible Applications and Applicability. *Journal of Colloid and Interface Science* **1999,** *217* (1), 8-18.

235. Konek, C. T.; Musorrafiti, M. J.; Al-Abadleh, H. A.; Bertin, P. A.; Nguyen, S. T.; Geiger, F. M., Interfacial Acidities, Charge Densities, Potentials, and Energies of Carboxylic Acid-Functionalized Silica/Water Interfaces Determined by Second Harmonic Generation. *Journal of the American Chemical Society* **2004,** *126*, 11754-11755.

236. Dong, Y.; Pappu, S. V.; Xu, Z., Detection of Local Density Distribution of Isolated Silanol Groups on Planar Silica Surfaces Using Nonlinear Optical Molecular Probes. *Analytical Chemistry* **1998,** *70* (22), 4730-4735.

237. Du, Q.; Freysz, E.; Shen, Y. R., Vibrational spectra of water molecules at quartz/water interfaces. *Physical Review Letters* **1994,** *72* (2), 238-241.

238. Duval, Y.; Mielczarski, J. A.; Pokrovsky, O. S.; Mielczarski, E.; Ehrhardt, J. J., Evidence of the Existence of Three Types of Species at the Quartz–Aqueous Solution Interface at pH 0–10: XPS Surface Group Quantification and Surface Complexation Modeling. *The Journal of Physical Chemistry B* **2002,** *106* (11), 2937-2945.

239. Pearson, R. G., Hard and soft acids and bases, HSAB, part 1: Fundamental principles. *Journal of Chemical Education* **1968,** *45* (9), 581.

240. Yeganeh, M. S.; Dougal, S. M.; Pink, H. S., Vibrational Spectroscopy of Water at Liquid Solid Interfaces: Crossing the Isoelectric Point of a Solid Surface. *Physical Review Letters* **1999,** *83*, 1180-1182.

241. Rashchi, F.; Xu, Z.; Finch, J. A., Adsorption on silica in Pb- and Ca-SO4-CO3 systems. *Colloids and Surfaces A: Physicochemical and Engineering Aspects* **1998,** *132* (2–3), 159-171.

242. Dove, P. M.; Craven, C. M., Surface charge density on silica in alkali and alkaline earth chloride electrolyte solutions. *Geochimica et Cosmochimica Acta* **2005,** *69* (21), 4963-4970.

243. Daniel, M.-C.; Astruc, D., Gold Nanoparticles: Assembly, Supramolecular Chemistry, Quantum-Size-Related Properties, and Applications toward Biology, Catalysis, and Nanotechnology. *Chemical Reviews* **2003,** *104* (1), 293-346.

244. Wilson, R., The use of gold nanoparticles in diagnostics and detection. *Chemical Society Reviews* **2008,** *37* (9), 2028-2045.

245. Fehrmann, R. S. N.; Li, X.-y.; van der Zee, A. G. J.; de Jong, S.; te Meerman, G. J.; de Vries, E. G. E.; Crijns, A. P. G., Profiling Studies in Ovarian Cancer: A Review. *The Oncologist* **2007,** *12* (8), 960-966.

246. Wooster, R.; Cleton-Jansen, A. M.; Collins, N.; Mangion, J.; Cornelis, R. S.; Cooper, C. S.; Gusterson, B. A.; Ponder, B. A. J.; von Deimling, A.; Wiestler, O. D.; Cornelisse, C. J.; Devilee, P.; Stratton, M. R., Instability of short tandem repeats (microsatellites) in human cancers. *Nature Genetics* **1994,** *6* (2), 152-156.

247. Phil, R., Legal and public policy issues in DNA forensics. *Nature Reviews Genetics* **2001,** *2* (4), 313-317.

248. Jobling, M. A.; Gill, P., Encoded evidence: DNA in forensic analysis. *Nature Reviews Genetics* **2005,** *6* (3), 246-246.

249. Stoughton, R. B., APPLICATIONS OF DNA MICROARRAYS IN BIOLOGY. *Annual Review of Biochemistry* **2005,** *74* (1), 53-82.

250. Smith, L.; Greenfield, A., DNA microarrays and development. *Human Molecular Genetics* **2003,** *12* (suppl 1), R1-R8.

251. Pissuwan, D.; Valenzuela, S. M.; Cortie, M. B., Prospects for gold nanorod particles in diagnostic and therapeutic applications. *Biotechnology & Genetic Engineering Reviews* **2008,** *25*, 93-112.

252. Burge, S.; Parkinson, G. N.; Hazel, P.; Todd, A. K.; Neidle, S., Quadruplex DNA: sequence, topology and structure. *Nucleic Acids Research* **2006,** *34* (19), 5402-5415.

253. Bailey, S. M.; Murnane, J. P., Telomeres, chromosome instability and cancer. *Nucleic Acids Research* **2006,** *34* (8), 2408-2417.

254. Tran, P. L. T.; Mergny, J.-L.; Alberti, P., Stability of telomeric G-quadruplexes. *Nucleic Acids Research* **2011,** *39* (8), 3282-3294.

255. Davis, J. T.; Spada, G. P., Supramolecular architectures generated by self-assembly of guanosine derivatives. *Chemical Society Reviews* **2007,** *36* (2), 296-313.

256. Wu, Z.-S.; Guo, M.-M.; Shen, G.-L.; Yu, R.-Q., G-rich oligonucleotide-functionalized gold nanoparticle aggregation. *Analytical and Bioanalytical Chemistry* **2007,** *387* (8), 2623-2626.

257. Hurst, S. J.; Hill, H. D.; Macfarlane, R. J.; Wu, J.; Dravid, V. P.; Mirkin, C. A., Synthetically Programmable DNA Binding Domains in Aggregates of DNA-Functionalized Gold Nanoparticles. *Small* **2009,** *5* (19), 2156-2161.

258. Campbell, N.; Neidle, S., G-Quadruplexes and Metal Ions. In *Interplay between Metal Ions and Nucleic Acids*, Sigel, A.; Sigel, H.; Sigel, R. K. O., Eds. Springer Netherlands: 2012; Vol. 10, pp 119-134.